Numerical modelling of the oceanic circulation

Laurent Debreu

Mémoire pour l'obtention du diplôme d'Habilitation à Diriger des Recherches

Université Grenoble Rhône-Alpes, spécialité : Mathématiques Appliquées

Modélisation numérique de la circulation océanique

présenté par

Laurent Debreu

Inria, Laboratoire Jean Kuntzmann

de l'Université de Grenoble Rhône-Alpes

Jean Marie Beckers	Professeur, University of Liège	Rapporteur
Serge Gratton	Professeur, INPT/ENSEEIHT, Toulouse	Rapporteur
John Thuburn	Professeur, University of Exeter	Rapporteur
Eric Blayo	Professeur, Université Grenoble Rhône-Alpes	Examinateur
François-Xavier Le Dimet	Professeur, Université Grenoble Rhône-Alpes	Président du jury
Yves Morel	Directeur de recherche CNRS, LEGOS, Toulouse	Examinateur

Soutenue le 17 décembre 2015

Contents

Part I

Curriculum Vitae

Laurent Debreu

Research scientist at Inria (CR1), HDR
Head of the AIRSEA (Inria / Laboratoire Jean Kuntzmann) team
Address : Laboratoire Jean Kuntzmann, Batiment IMAG, 700 avenue centrale, 38400 St Martin d'Hères
Phone: +33 4 57 42 17 25, e-mail: Laurent.Debreu@inria.fr
Web Page: http://team.inria.fr/airsea/laurent-debreu

Date of birth: 30-06-1971
Hometown: Lille, France
Citizenship: French

Work Experience

- 2001- : Research scientist at Inria

- 2000-2001 : Postdoctoral Research Associate, Laboratory of Geophysical and Industrial Flows (LEGI, Grenoble)

Education

- 1997-2000 : PhD in Applied Mathematics, Joseph Fourier University, Grenoble

- 1996 : Engineer degree in scientific computation (ENSIMAG, Grenoble)

Stays Abroad (> 3 months)

- University of California at Los Angeles, USA, Jim Mc Williams, 2009

- Florida State University, Tallahassee, USA, M.Y. Hussaini, 2002

- University of California at Los Angeles, USA, Jim Mc Williams, 2000

Research topics

- Numerical methods for ocean and atmosphere modelling

- Local mesh refinement (structured meshes)

- Model coupling

- Variational data assimilation

PhD students

- 2011-2015: Jérémie Demange, Numerical schemes for tracers advection and gravity waves propagation in ocean models. Co-supervisors : E. Blayo (Joseph Fourier University), P. Marchesiello (IRD, Toulouse).

- 2011-2013: Xavier Meunier, Learning techniques for subgrid-scale parameterizations. Co-supervisors : B. Barnier (CNRS, Grenoble), J. Le Sommer (CNRS, Grenoble).

- 2007-2010: Emilie Neveu, Application of multigrid methods to variational data assimilation. Co-supervisor : F.-X. LeDimet (Joseph Fourier University).

- 2005-2008: Florian Lemarié, Mathematical and numerical aspects of ocean atmosphere coupling. Co-supervisor : E. Blayo (Joseph Fourier University).

- 2004-2007: Ehouarn Simon, Variational data assimilation and local mesh refinement. Co-supervisor : E. Blayo (Joseph Fourier University).

Teaching and training experience

- Numerical ocean modelling, ENSTA engineer school Bretagne and M2R Oceanography, Brest, France, 2011-

- Numerous teachings between 2001 and 2010 at the Joseph Fourier University and at the ENSIMAG engineer school : Mathematical Modelling, Finite Element methods, Finite Volume methods, Models and Data for geophysical fluids.

- PhD training: Numerical ocean and atmosphere modelling (with T. Dubos (Ecole Polytechnique, Paris), F. Hourdin (CNRS, Paris), G. Roullet (Université de Bretagne Occidentale, Brest)), 2014- (annual training)

- Multiresolution methods and data assimilation, Advanced Data Assimilation for Geosciences, Les Houches, May 2010.

- Tutorial *Realistic numerical models of the ocean and the atmosphere: principles and practice*, African Conference on Research in Computer Science and Applied Mathematics (CARI), Alger, Algeria, September 2012. (with P. Marchesiello, G. Cambon (IRD, Toulouse) and R. Benshila (CNRS, Paris)

- AGRIF Training workshop : *AGRIF developers Training*, June 2012, Grenoble. 60 participants.

- Data assimilation course, Data assimilation for geophysical fluids, CIMPA-UNESCO Thematic school, Wuhan, Chine, May 2010.

- Tutorial *An introduction to data assimilation and environmental applications*, African Conference on Research in Computer Science and Applied Mathematics (CARI), Cotonou, Bnin, 2008. (with F.-X. LeDimet (Joseph Fourier University))

Responsibilities

- Head of the AIRSEA Inria team, 2015- : Mathematics and computing applied to oceanic and atmospheric flows (12 permanent members)

- Leader of the NEMO AGRIF Working Group

- Member of the IRD scientific evaluation committee (2016-)

- Invited member of the Ifremer scientific committee (2015)

- Coordinator of the COMODO ANR[1] project (bringing together the whole French community in numerical ocean modelling), 2011-2016.

- Member of scientific committee of operational oceanography (Mercator-Ocean) : 2010-2014

- Member of scientific committee of the African Conference on Research in Computer Science and Applied Mathematics (CARI). 2010-

- Member of scientific committee CORDI-S (Inria PhD grants), 2008-2012

- Member of the steering comittee of the CROCO (Coastal and Regional ocean) model (2015-)

- Head (with E. Blayo) of the Inria international team NMOM (Numerical Methods for Ocean Modelling). Partners : UCLA/USA, CICESE/Mexico. 2008-2012.

Responsibility of research contracts (*after 2005*)

Main contracts only (> 100k€).

- ANR[1] HEAT (Highly Efficient Atmospheric Modeling), 2014-2018. Coordinator for the Inria AIRSEA team partner (Other partners : LMD, Meteofrance, CERFACS, LSCE, LAGGA). PI. T. Dubos (Ecole Polytechnique, France).

- ANR[1] COMODO (French Ocean Modelling Community), 2011-2015. PI. (Other partners : CNRS/LGGE, CNRS/LOCEAN, CNRS/LPO, CNRS/LA, CNRS/LEGOS, IFREMER, SHOM, IRD, Université Paul Sabatier)

- ANR[1] MSDAG (Multiscale Data Assimilation in Geophysics), 2009-2011. Coordinator for the Inria AIRSEA team partner (Other partners: Inria/Clime, Inria/Fluminance, LSCE). PI: M. Bocquet (Inria/Clime, CEREA).

---

[1]French National Research Agency

Responsibility of industrial contracts (*after 2005*)

- NOVELTIS, 2014: Expertise on the AGRIF software. Use in the HYCOM ocean model.

- CLIMPACT/METNEXT, 2012: Evaluation of the MeteoDC (Meteorology on Distributed Computers) software.

- ALYOTECH, 2011: Expertise on the AGRIF software. Use in the HYCOM ocean model.

- IFREMER, 2011 : Expertise on the AGRIF software. Use in the MARS3D IFREMER ocean model.

- GRAVIT (Grenoble Alpes Valorisation Innovation Technologies)(2008-2009) : Computation on heterogeneous networks: application to weather forecasts (METEODC).

- IFREMER, 2006-2008: Numerical developments in the MARS3D IFREMER model.

Software developments

- AGRIF: Adaptive Grid Refinement In Fortran (main developer). I am the main developer of the AGRIF software. AGRIF is a sofware for the integration of full adaptive mesh refinement (AMR) features within a multidimensional finite difference/finite volume numerical model written in the Fortran language. AGRIF is routinely used in several state of the art ocean models. The software is divided in two parts. A library composed of the main functions for grid hierarchy management (potentially adaptively) and for grid interactions between the grids of the hierarchy. The other part of the software deals with code translation and allows an automatic extension of a mono-grid code to a multi-grid code. This last part is using Fortran lexical and syntaxic analysis (implemented using the Flex and Yacc software packages). AGRIF is mainly designed for existing large codes. It is then used to minimize the required changes and to allow a simple integration of local mesh refinement features.
  AGRIF deals with 1, 2 or 3D mesh refinement of structured (staggered or collocated) grids, allows static and/or dynamic grid refinement and is fully parallelized.
  As of july 2015, more than 200 scientific publications mention the use of the AGRIF software.

- METEODC: METEOrology on Distributed Computers. METEODC is based on a Python library developed by the AIRSEA INRIA team and specially designed for the deployment of numerical computations on heterogeneous clusters of computers. Based on advanced applied mathematics methods (Schwarz waveform relaxation methods), it allows for an efficient parallelization and an original treatment of fault tolerance and load balancing issues. Using a client/server approach, the computations are divided into independent tasks that are distributed over the existing cluster. Almost no changes are required to the original application to take advantage of the Python library. Only a few interfaces have to be developed following the software specifications. Current developments are focused on the integration of parallel in time algorithms for a finer parallel grain.

Publications

Submitted and In revision papers

Burchard, Hans, Laurent Debreu, Knut Klingbeil, and Florian Lemarié (2016). "The numerics of hydrostatic structured-grid coastal ocean models: state of the art and future perspectives". In: *Ocean Modelling*.

Demange, Jérémie, Laurent Debreu, Patrick Marchesiello, Florian Lemarié, and Eric Blayo (2014a). *Numerical representation of internal waves propagation*. Research Report RR-8590. URL: https://hal.inria.fr/hal-01063417.

— (2014b). *On the use of a depth-dependent barotropic mode in ocean models: impact on the stability of the coupled barotropic/baroclinic system*. Research Report RR-8589. URL: https://hal.inria.fr/hal-01063414.

Published papers

Soufflet, Yves, Patrick Marchesiello, Julien Jouanno, Xavier Capet, Laurent Debreu, and Florian Lemarié (2016). "On effective resolution in ocean models". In: *Ocean Modelling* 98, pp. 36–50.

Debreu, Laurent, Emilie Neveu, Ehouarn Simon, François-Xavier Le Dimet, and Arthur Vidard (2015). "Multigrid solvers and multigrid preconditioners for the solution of variational data assimilation problems". In: *Quarterly Journal of the Royal Meteorological Society*. QJ-14-0040.R2, n/a–n/a. DOI: 10.1002/qj.2676. URL: http://dx.doi.org/10.1002/qj.2676.

Lemarié, Florian, Eric Blayo, and Laurent Debreu (2015). "Analysis of Ocean-atmosphere Coupling Algorithms: Consistency and Stability". In: *Procedia Computer Science*. International Conference On Computational Science, ICCS 2015 - Computational Science at the Gates of Nature 51, pp. 2066–2075. DOI: 10.1016/j.procs.2015.05.473. URL: https://hal.inria.fr/hal-01158776.

Lemarié, Florian, Laurent Debreu, Jérémie Demange, Gurvan Madec, Jean-Marc Molines, and Marc Honnorat (2015). "Stability constraints for oceanic numerical models: implications for the formulation of time and space discretizations". In: *Ocean Modelling* 92, pp. 124–148.

Djath, Natacha, Angelique Melet, Jacques Verron, Jean-Marc Molines, Bernard Barnier, Lionel Gourdeau, and Laurent Debreu (2014). "A 1/36 degrees model of the Solomon Sea embedded into a global ocean model : on the setting up of an interactive open boundary nested model system". In: *Journal of Operational Oceanography* 7.1, p. 13. URL: https://hal.inria.fr/hal-01095929.

Talandier, Claude, Julie Deshayes, Anne-Marie Tréguier, Xavier Capet, Rachid Benshila, Laurent Debreu, Raphaël Dussin, Jean-Marc Molines, and Gurvan Madec (2014). "Improvements of simulated Western North Atlantic current system and impacts on the AMOC". In: *Ocean Modelling* 79, pp. 1–19. DOI: 10.1016/j.ocemod.2013.12.007. URL: https://hal.inria.fr/hal-00944219.

Lemarié, Florian, Laurent Debreu, and Eric Blayo (2013b). "Toward an Optimized Global-in-Time Schwarz Algorithm for Diffusion Equations with Discontinuous and Spatially Variable Coefficients, Part 1: The Constant Coefficients Case". In: *Electronic Transactions on*

Numerical Analysis 40, pp. 148–169. URL: https://hal.archives-ouvertes.fr/hal-00661977.

Lemarié, Florian, Laurent Debreu, and Eric Blayo (2013c). "Toward an Optimized Global-in-Time Schwarz Algorithm for Diffusion Equations with Discontinuous and Spatially Variable Coefficients, Part 2: the Variable Coefficients Case". In: *Electronic Transactions on Numerical Analysis* 40, pp. 170–186. URL: https://hal.archives-ouvertes.fr/hal-00661978.

Debreu, Laurent, Patrick Marchesiello, Pierrick Penven, and Gildas Cambon (2012). "Two-way nesting in split-explicit ocean models: Algorithms, implementation and validation". In: *Ocean Modelling* 49-50, pp. 1–21. DOI: 10.1016/j.ocemod.2012.03.003. URL: https://hal.archives-ouvertes.fr/hal-00690731.

Lemarié, Florian, Laurent Debreu, Alexander F. Shchepetkin, and Jim Mcwilliams (2012). "On the Stability and Accuracy of the Harmonic and Biharmonic Isoneutral Mixing Operators in Ocean Models". In: *Ocean Modelling* 52-53, pp. 9–35. DOI: 10.1016/j.ocemod.2012.04.007. URL: https://hal.archives-ouvertes.fr/hal-00665826.

Neveu, Emilie, Laurent Debreu, and François-Xavier Le Dimet (2011). "Multigrid methods and data assimilation - Convergence study and first experiments on non-linear equations". In: *ARIMA* 14, pp. 63–80. URL: https://hal.inria.fr/hal-00658106.

Simon, Ehouarn, Laurent Debreu, and Eric Blayo (2011). "4D Variational Data Assimilation for Locally Nested Models : complementary theoretical aspects and application to a 2D shallow water model". In: *International Journal for Numerical Methods in Fluids* 66.2, pp. 135–161. DOI: 10.1002/fld.2244. URL: https://hal.inria.fr/hal-00658105.

Marchesiello, Patrick, Laurent Debreu, and Xavier Couvelard (2009). "Spurious diapycnal mixing in terrain-following coordinate models: The problem and a solution". In: *Ocean Modelling* 26.3-4, pp. 156–169. DOI: 10.1016/j.ocemod.2008.09.004. URL: https://hal.archives-ouvertes.fr/hal-00409317.

Cailleau, Sylvain, Veronika Fedorenko, Bernard Barnier, Eric Blayo, and Laurent Debreu (2008). "Comparison of different numerical methods used to handle the open boundary of a regional ocean circulation model of the Bay of Biscay". In: *Ocean Modelling* 25.1-2, pp. 1–16. DOI: 10.1016/j.ocemod.2008.05.009. URL: https://hal.archives-ouvertes.fr/hal-00387446.

Chanut, Jérôme, Bernard Barnier, William Large, Laurent Debreu, Thierry Penduff, Jean-Marc Molines, and Pierre Mathiot (2008a). "Mesoscale Eddies in the Labrador Sea and Their Contribution to Convection and Restratification". In: *Journal of Physical Oceanography* 38.8, pp. 1617–1643. DOI: 10.1175/2008JPO3485.1. URL: https://hal.archives-ouvertes.fr/hal-00786837.

Debreu, Laurent and Eric Blayo (2008). "Two-way embedding algorithms: a review". In: *Ocean Dynamics* 58.5-6, pp. 415–428. DOI: 10.1007/s10236-008-0150-9. URL: https://hal.archives-ouvertes.fr/hal-00387449.

Debreu, Laurent, Christophe Vouland, and Eric Blayo (2008). "AGRIF: Adaptive Grid Refinement in Fortran". In: *Computers and Geosciences* 34.1, pp. 8–13. DOI: 10.1016/j.cageo.2007.01.009. URL: https://hal.archives-ouvertes.fr/hal-00387435.

Penven, Pierrick, Patrick Marchesiello, Laurent Debreu, and Jérome Lefèvre (2008). "Software tools for pre- and post-processing of oceanic regional simulations." In: *Environmental Modelling and Software* 23.5, pp. 660–662. DOI: 10.1016/j.envsoft.2007.07.004. URL: https://hal.archives-ouvertes.fr/hal-00388202.

Ngnepieba, Pierre, M.Yussuf Hussaini, and Laurent Debreu (2006). "Optimal Control and Stochastic Parameter Estimation". In: *Monte Carlo Methods Appl.* 12.5/6, pp. 461–476. URL: https://hal.archives-ouvertes.fr/hal-00171447.

Penven, Pierrick, Laurent Debreu, Patrick Marchesiello, and C. Mcwilliams James (2006). "Evaluation and application of the ROMS 1-way embedding procedure to the central california upwelling system". In: *Ocean Modelling* 12, pp. 157–187. DOI: 10.1016/j.ocemod.2005.05.002. URL: https://hal.archives-ouvertes.fr/hal-00280334.

Blayo, Eric and Laurent Debreu (2005). "Revisiting open boundary conditions from the point of view of characteristic variables". In: *Ocean Modelling*. URL: https://hal.inria.fr/inria-00134856.

Blayo, Eric, Laurent Debreu, Grégory Mounié, and Denis Trystram (2000). "Dynamic Load Balancing for Adaptive Mesh Ocean Circulation Model". In: *Engineering Simulations* 22.2, pp. 8–24. URL: https://hal.archives-ouvertes.fr/hal-00003946.

Blayo, Eric and Laurent Debreu (1999). "Adaptive mesh refinement for finite-difference ocean models: First experiments". In: *Journal of Physical Oceanography* 29.6, pp. 1239–1250. URL: https://hal.archives-ouvertes.fr/hal-01096127.

Debreu, Laurent and Eric Blayo (1998). "On the Schwarz alternating method for ocean models on parallel computers." In: *Journal of Computational Physics* 141.2, pp. 93–111. DOI: 10.1006/jcph.1998.5898. URL: https://hal.inria.fr/inria-00592597.

Book chapters

Debreu, Laurent, Emilie Neveu, François-Xavier Le Dimet, and Ehouarn Simon (2014). "Multigrid algorithms and local mesh refinement methods in the context of variational data assimilation". In: *Lecture notes of Les Houches summer school 2012*. Ed. by Eric Blayo, Marc Bocquet, Emmanuel Cosme, and F. Cugliandolo Leticia. Oxford University Press, p. 576. URL: https://hal.inria.fr/hal-01095939.

Lemarié, Florian, Laurent Debreu, and Eric Blayo (2013a). "Optimal control of the convergence rate of Global-in-time Schwarz algorithms". In: *Domain Decomposition Methods in Science and Engineering XX*. Ed. by R. Bank, M. Holst, O. Widlund, and J. Xu. volume 91 of Lecture Notes in Computational Science and Engineering. Springer-Verlag Berlin Heidelberg, pp. 599–606. DOI: 10.1007/978-3-642-35275-1_71. URL: https://hal.archives-ouvertes.fr/hal-00661979.

Blayo, Eric and Laurent Debreu (2006). "Nesting ocean models". In: *An Integrated View of Oceanography: Ocean Weather Forecasting in the 21st Century*. Ed. by Eric Chassignet and Jacques Verron. Kluwer. URL: https://hal.inria.fr/inria-00187576.

Debreu, Laurent, Eric Blayo, and Bernard Barnier (2005). "A general adaptive multi-resolution approach to ocean modelling: experiments in a primitive equation model of the North Atlantic, Adaptive Mesh Refinement - Theory and Applications". In: *Computational Science and Engineering*. Vol. 41, ISBN 978-3-540-21147-1. Springer, pp. 303–313. URL: https://hal.archives-ouvertes.fr/hal-00184033.

Part II

Introduction

Introduction to numerical ocean modelling

In this introduction, I summarise what I consider as the salient points underlying the building of a numerical ocean model.

Continuous formulation

An ocean model is composed of a system of equations and initial and boundary conditions.

System of equations

The equations system is associated with a number of physical assumptions (e.g. Boussinesq, hydrostaticity) according to some characteristic scales. Several equivalent formulations of the same equation system may exist (e.g. flux/vector invariant forms) and naturally flavour the conservation of specific quantities.

Subgrid-scale modelling

Knowing that the system is going to be discretised in a finite dimensional space, the numerical model seeks for a filtered (in some sense) solution and subgrid-scale (SGS) models may be derived at the continuous level. Conservation properties apply to the unfiltered solution and this has to taken into account in the derivation of the SGS models (Eden, Czeschel, and Olbers 2014).

Initial and boundary conditions

Given the turbulent nature of geophysical fluids, sensitivity to initial conditions may be large. Data assimilation techniques (see 4) are important tools to improve the model predictability. Closed and open boundaries require the specification of boundary conditions and possibly the coupling with other components (see 2.3).

When possible, the relevancy of the chosen equations set augmented by the SGS model and the boundary conditions should be mathematically analysed (Lions, Temam, and Wang 1992; Bennis et al. 2008).

Numerical modelling

Conservation properties and numerical accuracy

The discretisation step should aim at maintaining the conservation properties, accordingly to the chosen continuous formulation and the SGS models. The objective is also to be as accurate as possible in order to prevent dispersion errors to induce spurious energy transfer across scales . For consistency, the truncation errors of the discrete schemes should be smaller than the SGS models.

Dissipation at small scales

One of the objective of the subgrid-scale models is to dissipate energy at small scales and to damp noise associated with numerical dispersion errors. The dissipation process should however not alter the effective resolution of the resulting schemes. Subgrid scale models can be based on explicit scale selective dissipation or being built in the numerical schemes (e.g. advection schemes (Implicit Large Eddy Simulation (ILES), (Kent, Thuburn, and Wood 2012)). In this last case, a precise control of dissipation mechanisms (both in amplitude and orientation) may be difficult to obtain (see 3.1.1).
For near 2D (quasi-geostrophic) turbulence, whatever the original formulation is chosen (e.g. flux/vector invariant forms) and whatever how the dissipation mechanism is introduced (explicitly or implicitly), part of the upscaling of energy from small to large scales is altered by the dissipation processes. Thus it may be needed to introduce energy backscattering. This may be achieved using some form of well chosen antidissipation (Thuburn, Kent, and Wood 2014). The other possibility is to move to probabilistic modelling based either on stochastic parameterisations (Mémin 2014) or by using numerical schemes with built-in statistical properties (Harten and Lax 1981).

Numerical methods

Discretisation errors are functions of several choices among them vertical and horizontal grids, momentum and tracers advection . . . (see 3). In general, there is also a need to try to maintain coherency between discretization choices and physical assumptions at the continuous level (e.g. Shchepetkin and McWilliams 2011). The numerical schemes should not try to compensate from missing physics in the continuous formulation.
Multiscale/multiresolution methods (see 2.2, 5) are an effective way of reducing discretisation error and of lowering the impact of the choice of the SGS models.

High Performance Computing

The emergence of new computing architectures will probably lead to a complete revisit of traditionally used algorithms. New directions of parallelisation have to be sought and the main advances will probably be achieved at the mathematical/algorithmic level. Time parallelisation, task parallelism, highly adaptive methods have to be considered. The new computing architectures flavour the use of ensemble simulations. How to take benefit from these ensemble simulations for the improvement of the numerical model itself (e.g. SGS models) is an open question.

Part III

Past research activities: Numerical modelling and data assimilation for the ocean circulation

Chapter 1

Summary of main contributions

My past research activities focused on the development on numerical modelling and data assimilation methods for ocean circulation models. The scales under consideration go from global to regional and coastal configurations.

1.1 Historical perspective

It can be accepted that the lack of computational power and the associated lack of horizontal and vertical grid resolution is one of the main sources of numerical modelling errors. It indeed leads to large truncation errors, to an important role of subgrid-scale parameterizations, to an approximate representation of domain geometry ... During my PhD (1997-2000), I was first interested in local mesh refinement methods. After having initially worked on adaptive mesh refinement and associated refinement criteria, I focused on the derivation of efficient grid interactions for static local mesh refinement. Adaptive mesh refinement (AMR) requires the root grid to be at least eddy permitting and this was not the case at that time. In a near future, the interest for AMR in ocean modelling should probably increase.

Research on local mesh refinement techniques raises the problem of boundary conditions specifications and I was then naturally interested in the design of boundary conditions in a more general framework including open boundary conditions and coupling problems (PhD of Florian Lemarié, Lemarié 2008).

Local mesh refinement methods and the choice of boundary conditions obviously have strong interactions with the numerical kernel of the model itself. I eventually realized that, in order to these methods to be applied efficiently in realistic configurations, work on numerical methods was also required. At that time, I already had integrated mesh refinement methods in several ocean models (including NEMO, ROMS, MARS3D, HYCOM) and had acquired a good knowledge of the main differences between these state of the art ocean models. That was the starting point of my work on numerical ocean modelling (PhD of Jérémie Demange (Demange 2014), COMODO (French numerical ocean modelling community) ANR projects).

During all this time, I was also interested in optimal control and data assimilation techniques. The ultimate aim of this work resides in a better understanding of the numerical model and the identification of the sources of error, in particular a good knowledge of its sensitivity to different parameters. Thus I first worked on variational data assimilation methods for embedded models (including a control of boundary conditions) (PhD of Ehouarn Simon, Simon 2007). With Emilie Neveu (Neveu 2011), we then successfully applied multigrid techniques for the solution of the variational data assimilation (ANR MSDAG (Multiscale Data

Assimilation in Geophysics)). Even if in this study the control is the initial condition, the objective is really to allow a control of the whole model trajectory as it will be presented in my research project in relation with subgrid-scale parameterizations.

1.2   Local mesh refinement for structured meshes

At the global and regional scales, most of the current ocean models are discretised on structured grids. Given the computational cost related to the numerical simulation of the ocean, the spatial resolution is one of the key points of the quality of the results. So I was interested in locally refined structured grids. Most of the work is linked to the design of efficient interactions between the grids of different resolutions. This includes the interpolation and restriction schemes and their links with conservation properties at interfaces. These have been extended to higher orders than in the existing literature in Debreu and Blayo 2008. The interface conditions themselves can rely on absorbing boundary conditions techniques as we have studied in Blayo and Debreu 2005. Some of my work is also specific to the modelling of the ocean as the management of nontrivial temporal refinement in models that use time splitting techniques Debreu, Marchesiello, et al. 2012. With Eric Blayo, I also worked on adaptive mesh refinement that allows an evolution of grid hierarchy according to some refinement criteria (Blayo and Debreu 1999).

A large number of realistic ocean models (HYCOM, MARS3D, NEMO, ROMS) uses the results of this research and the main impact is that two-way local mesh refinement methods are now widely used by the ocean modeling community.

1.3   Model coupling methods

Coupling methods cover a more general framework of interactions between two models of potentially different physics. Particular interest has been focused on the coupling between ocean and atmosphere models where we looked at the use of global in time domain decomposition methods (a.k.a. Schwarz waveform relaxation method). The PhD of Florian Lemarié has led to progress on issues both at the theoretical and applied levels. At the theoretical level, the coupling between the ocean and the atmosphere can be schematised on the model problem of two diffusion equations. For this type of coupling, new results on optimised boundary conditions of order 1 (Fourier) were obtained initially in the case of constant but discontinuous coefficients on each domain (Lemarié, Debreu, and Blayo 2013b) and these results were extended to the case of spatially variable coefficients in Lemarié, Debreu, and Blayo 2013c. Algorithms commonly used in forecasting centres correspond to a single iteration of this Schwarz iterative algorithm and thus can be proved to be unstable. Realistic applications using domain decomposition methods in time were made by coupling a realistic model of ocean (ROMS) to a realistic atmosphere model (WRF). This application has shown that the implementation of the iterative Schwarz method significantly reduces forecast uncertainty when we vary some of the model parameters (here coupling frequency and initial conditions) (Lemarié, Marchesiello, et al. 2014).

The work on the coupling algorithms and conditions of interfaces enabled to highlight some of the major shortcomings of current models used for climate simulations. Several projects

including applied mathematicians, oceanographers and meteorologists are now underway to properly formulate the coupling by working both on interfaces conditions (this being also related to boundary layers parameterisations) and coupling algorithms.

1.4 Variational data assimilation and multiresolution approaches

Having worked on methods of local mesh refinement, I have been naturally interested in the application of variational data assimilation techniques within this framework. This was the topic of the PhD Ehouarn Simon. The objective was to formulate the problem of variational data assimilation problem (here optimal control of initial conditions) in the case of models using local mesh refinement, this both in passive interaction (ie without feedback from the high resolution grid to low resolution grid) and in active interaction (with feedback). We also studied the possibility of an additional control of intergrid transfers (correction term added to interactions) (Simon, Debreu, and Blayo 2011). During Emilie Neveu PhD, we used (possibly nonlinear) multigrid methods to accelerate the minimization of the objective function. A detailed study of the convergence of the multigrid methods (ellipticity, approximation property) has been done both on linear and more complex nonlinear cases (Neveu, Debreu, and Le Dimet 2011). More recently I showed how to hybridize a traditional preconditioner (based on the background error covariance matrix) and a multigrid preconditioner within a Krylov method (Debreu, Neveu, Simon, et al. 2015).

The results are very promising and should also help to develop some of the points highlighted in my research program, such as control of the model error and treatment of strongly nonlinear case by continuation method.

1.5 Numerical methods

My first subject of interest was the control of the orientation of numerical diffusion (Marchesiello, Debreu, and Couvelard 2009; Lemarié, Debreu, Shchepetkin, et al. 2012). The strong stratification of the ocean imposes privileged directions in the water masses mixing. When the vertical coordinate system is not aligned with the constant density surfaces (isopycnal surfaces), numerical mixing, either explicit through a diffusion term or implicit to upwind biased advection schemes, leads to unacceptable results. Therefore my work, mainly in collaboration with P. Marchesiello and F. Lemarié, consisted in the proposal of an implementation of a diffusion tensor rotated along isopycnal surfaces. At the numerical level, this corresponds to the derivation of a stable discretization of a fourth order mixed derivatives problem.

During Jéremie Demange PhD, we used the technique of projection onto normal modes (in the vertical direction) to explore several important issues. The first of them is a better understanding of fast (barotropic)/slow(baroclinic) modes splitting techniques that are used in ocean modelling. We first showed that the assumption currently used in the mode splitting technique (rigid lid assumption) was an important source of instability (Demange, Debreu, et al. 2014b). We also studied the propagation of internal waves. In most current models, this propagation is treated in a basic way (second order centered discretization). In addition

to propose the implementation of higher order schemes (horizontal pressure gradient and horizontal divergence), we proposed a computation of diffusive terms based on a decomposition in normal modes. The impact of the vertical discretization (grid staggering and numerical schemes) has also been analized.

The developments on the rotation of diffusion tensor have been implemented in several ocean realistic models, they help to limit some important problems in current ocean models and allows a lesser sensitivity of the induced numerical mixing to the choice of the vertical coordinate system.

Chapter 2

Local mesh refinement and model coupling

At the global and regional scales, most of the current ocean models are discretised on structured grids. Given the computational cost related to the numerical simulation of the ocean, the spatial resolution is one of the key points of the quality of the results. So I was interested in locally refined structured grids. Most of the work is linked to the design of efficient interactions between grids of different resolutions. This includes the interpolation and restriction operators and their links with conservation properties at interfaces. These have been extended to higher orders than in the existing literature in Debreu and Blayo 2008. The interface conditions themselves can rely on absorbing boundary conditions techniques as we have studied in Blayo and Debreu 2005. Some of my work is also specific to the modelling of the ocean as the management of nontrivial temporal refinement in models that use time splitting techniques (Debreu, Marchesiello, et al. 2012). With Eric Blayo, I also worked on adaptive mesh refinement that allows an evolution of the grid hierarchy according to some refinement criteria (Blayo and Debreu 1999; Debreu, Blayo, and Barnier 2005).

Coupling methods cover a more general framework of interactions between two models of potentially different physics. Particular interest has been focused on the coupling between ocean and atmosphere models where we looked at the use of global in time domain decomposition methods (a.k.a. Schwarz waveform relaxation method). The PhD of Florian Lemarié has led to progress on issues both at the theoretical and applied levels. At the theoretical level, the coupling between the ocean and the atmosphere can be schematised on the model problem of two diffusion equations. For this type of coupling, new results on optimised boundary conditions of order 1 (Fourier) were obtained initially in the case of constant but discontinuous coefficients on each domain (Lemarié, Debreu, and Blayo 2013b) and these results were extended to the case of spatially variable coefficients in Lemarié, Debreu, and Blayo 2013c. Algorithms commonly used in forecasting centres correspond to a single iteration of this Schwarz iterative algorithm and thus can be proved to be unstable. Realistic applications using domain decomposition methods in time were made by coupling a realistic model of ocean (ROMS) to a realistic atmosphere model (WRF). This application has shown that the implementation of the iterative Schwarz method significantly reduces forecast uncertainty when we vary some of the model parameters (here coupling frequency and initial conditions) (Lemarié, Marchesiello, et al. 2014).

2.1   Introduction

As explained in the introductory part, the cost of the integration of numerical ocean/atmospheric models is huge. As a consequence, a potentially large part of the spectral range of both the dynamic and the topography scales is not resolved by the computational grid. Local mesh refinement methods aim at putting the computational effort where (and possibly when) it is the most useful. The idea is thus to increase the mesh resolution based on a static or dynamic criterion. Static refinements are most of the time linked to a specific area of interest or are linked to a particular topographic feature. Adaptive refinements can be used to adapt the grid resolution to the dynamical features of the flow. The grid resolution is increased spatially and a corresponding time refinement is usually applied in order to satisfy a stability criterion.

The unstructured grid approach provides a natural solution for mesh refinement owing to its straightforward refinement process, assuming that an efficient meshing tool is available. A new development phase of unstructured grid models has emerged in recent years with several improvements regarding long-standing issues: preservation of geostrophic balance (Maddison et al. 2011); and local/global conservation properties (Hanert et al. 2004; Levin, Iskandarani, and Haidgovel 2006). The reader is referred to Ham et al. 2009; Deleersnijder, Legat, and Lermusiaux 2010; Maddison et al. 2011; Sidorenko et al. 2011; Danilov 2013 for an overview of recent achievements. However, the additional numerical cost of unstructured grid modelling and the ratio of computational cost over accuracy remains to be objectively evaluated and compared to the traditional structured grid approach.

At the beginning of this work and at the scales of interest (global/regional), most of the realistic ocean models were written on structured grids and it is still the case. We thus investigated the application of local mesh refinement methods on structured grids.

We were also interested in coupling algorithms where here also the mathematical problem can be view as interactions at the domain boundaries (which in this case do not overlap). For these two problems, the following framework can be used:

$$
\begin{aligned}
&\frac{\partial u_1}{\partial t} + \mathcal{L}_1(u_1) = 0 &&\text{for } x \in \Omega_1 &\qquad& \frac{\partial u_2}{\partial t} + \mathcal{L}_2(u_2) = 0 &&\text{for } x \in \Omega_2 \\
&\mathcal{B}_1 u_1 = \mathcal{B}_1 u_2 &&\text{for } x \in \partial\Omega_1 &\qquad& \mathcal{B}_2 u_2 = \mathcal{B}_2 u_1 &&\text{for } x \in \partial\Omega_2 \qquad (2.1)\\
&u_1(x, t = 0) = u_0(x) &&&& u_2(x, t = 0) = u_0(x)
\end{aligned}
$$

The following cases can occur:

1. The domain Ω_2 is included in Ω_1 and the domain Ω_2 is discretized at higher resolution: *local mesh refinement*. Physical parameterizations and numerical schemes can be adapted to the grid resolutions of each domain.

2. The domains Ω_1 and Ω_2 are disjoints and have a common boundary. The solution u_2 is given: *open boundary problem*

3. The domains Ω_1 and Ω_2 are disjoints and have a common boundary: *model coupling*

In all these cases, the general question is to how to adequately choose the exchange operators $\mathcal{B}$? Both the continuous and the discrete forms of these operators will impact the solutions.

2.2   Local mesh refinement

2.2.1   Formulation

As shown on figure (2.1), we here consider the case of a high (or fine) resolution model, covering the local domain ω, embedded in a coarser resolution model covering the larger domain Ω. With obvious notations, the local fine resolution grid and the global coarse resolution grid are denoted respectively ω_f and Ω_c. The corresponding state vectors are denoted respectively $\mathbf{X}_f$ and $\mathbf{X}_c$. We also denote ω_c the part of the grid Ω_c corresponding to the local domain ω.
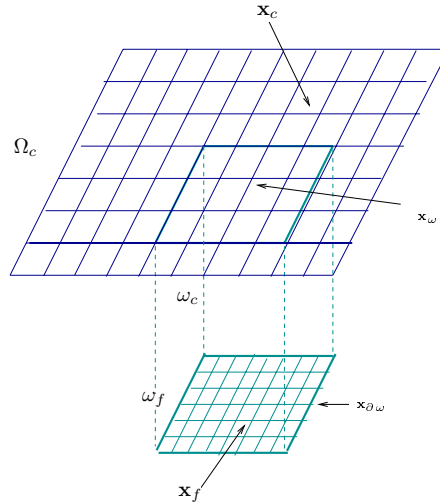

Figure 2.1: Notations used in the definition of the nested models

In the case of **one-way interaction**, the coarse grid model provides boundary conditions to the high resolution model using an interpolation operator I_c^f. In the case of **two-way interaction**, a feedback term from the fine grid onto the coarse grid is added. The coarse solution is updated locally (in $\mathring{\omega}_c$, the interior of ω_c) by the high resolution solution using a restriction operator I_f^c. Semi-discretized equations of the nested system can be written as follows:

Domain Ω_c   **Domain ω_f**

$$
\begin{cases}
\dfrac{\partial \mathbf{X}_c}{\partial t} = F(\mathbf{X}_c, \mathbf{X}_\omega) & \text{on} \quad \Omega_c \times [0, T] \\
\mathbf{X}_c(t = 0) = \mathbf{x}_c \\
\mathbf{X}_\omega = I_f^c(\mathbf{X}_f) & \text{on} \quad \mathring{\omega}_c \times [0, T]
\end{cases}
\qquad
\begin{cases}
\dfrac{\partial \mathbf{X}_f}{\partial t} = F(\mathbf{X}_f, \mathbf{X}_{\partial\omega}) & \text{on} \quad \omega_f \times [0, T] \\
\mathbf{X}_f(t = 0) = \mathbf{x}_f \\
\mathbf{X}_{\partial\omega} = I_c^f(\mathbf{X}_c) & \text{on} \quad \partial\omega_f \times [0, T]
\end{cases}
$$

$$(2.2)$$

where $\mathbf{X}_{\partial\omega}$ represents the information coming from the coarse grid onto $\partial\omega_f$, the boundary of the fine grid and $\mathbf{X}_\omega$ represents the information coming from the fine grid onto the coarse grid in $\mathring{\omega}_c$. For stability reason, a time refinement is also applied. After discretization, the problems have to be integrated in a specific order. The model is first integrated on the coarse grid Ω_c then on the high resolution grid ω_f with boundary conditions coming from a spatio-temporal interpolation of the coarse grid solution. Then an update step occurs in case of two-way interaction. An example of this integration with a time refinement of 2 is
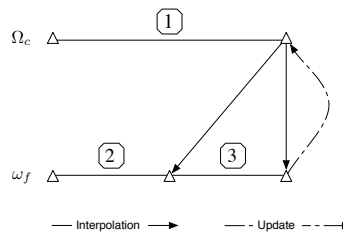
shown on figure (2.2).

Figure 2.2: Integration des deux grilles basse et haute rsolution au cours d'un pas de temps basse rsolution pour un raffinement temporel de 2

Local mesh refinement for structured grids have existed for a while. They have in particular been strongly developed in the context of structured adaptive refinement methods (AMR, Baden et al. 2000). They have been mainly applied to hyperbolic systems, using a finite volume discretization method on collocated variables.

At the beginning of our work in 1995, applications of local mesh refinement methods in oceanography and meteorology, were mainly restricted to static one-way interactions. A review of local mesh refinement (or embedding) techniques in the context of ocean modelling can be found in Debreu and Blayo 2008.

2.2.2 Contributions

My main contributions have been to work on several aspects of two-way nesting methods in order to be able to use them routinely as it is done today. In the context of ocean modeling, in comparison with the previously mentioned hyperbolic / finite volume techniques, many additional problems arise: bathymetry (i.e. complex geometry) treatment, grid staggering and complex temporal integration schemes (including slow/fast modes splitting).

High order restriction schemes, conservation properties and impact on numerical stability Debreu, Marchesiello, et al. 2012[1]

In Debreu, Marchesiello, et al. 2012, we showed how to derive a conservative multiresolution scheme using high order restriction schemes (i.e. higher order than the classical average operators). This is achieved using a refluxing procedure as in the original algorithm of Berger and Rigoutsos, but by extending the expression of the fluxes to the higher order update formula. In addition, we show, using a modified equation approach, that depending on the underlying discretization schemes additional viscosity may have to be added in order to get a stable and conservative scheme. In practice, the use of high order restriction operators has a strong impact on the solutions by preventing a too strong aliasing between small scales of the fine grid resolution and large scales of the coarse grid solution.

---

[1]See 6

Local mesh refinement for split-explicit free surface models (Debreu, March-esiello, et al. 2012)[2]

As previously mentioned, to be efficient, a temporal refinement strategy has to be added to the spatial refinement in order for the whole grid hierarchy not to be constraint by the smallest grid size. Local time refinement is not obvious in ocean models due to the stiffness of these systems that, in practice, leads to a fast/slow (barotropic/baroclinic) modes separation. In particular, the external/barotropic mode associated with the movement of the free surface is integrated forward with smaller time steps than the internal/baroclinic modes. This time scale separation complicates the management of local time refinement, especially when the fast mode is time filtered before being combined with the slow modes. Debreu, Marchesiello, et al. 2012 provides one solution to this problem and leads to the first algorithm where two-way nesting and local time refinement are applied with a coupling between grids occurring at the frequency of the small (external) time steps.

Criteria for adaptive mesh refinement and grid initialization (Blayo and Debreu 1999; Debreu, Blayo, and Barnier 2005)

Adaptive mesh refinement (AMR) (e.g. Berger and Oliger 1984) methods allow the grid hierarchy to evolve in time. In comparison with static refinements, two new issues arise: the choice of the refinement criterion and of the initialization procedure when new grids are created. First experiments on oceanic applications have been presented in Blayo and Debreu 1999 on a barotropic quasi-geostrophic (QG) model and then on a multilayer QG model. These were the first applications of structured adaptive mesh refinement in ocean models. Realistic applications (using the OPA model) are summarized in Debreu, Blayo, and Barnier 2005. In this paper, we compare several refinement criteria based either on the velocity norm, the relative vorticity or the Hunt criterion (a measure of the balance between vorticity and shearing (Hunt, Wray, and Moin 1998; Delcayre 1999)). The question of grid initialization of the (moving) high resolution grids was also discussed in Debreu, Blayo, and Barnier 2005. The OPA model used in this application was a rigid lid ocean model: the depth integrated horizontal velocities are non divergent and so derived from a barotropic streamfunction. When a new grid is initialized, the velocity fields and the barotropic streamfunction have to satisfy this constraint. The easiest way to proceed is in correcting the velocity fields in agreement with the interpolated streamfunction. It however leads to strong corrections (in particular in areas where coarse and fine bathymetries strongly differs) and, in Debreu, Blayo, and Barnier 2005, we introduced another solution where both the interpolated velocity fields and streamfunction are corrected and where the additional constraint of conservation of barotropic vorticity is applied.

Open boundary conditions

Main differences with two-way local mesh refinement

Even it can be written under the same abstract formulation, there are some important differences between two-way local mesh refinement and open boundary conditions or model coupling.

In the design of grid interactions (i.e. choice of $\mathcal{B}_1$ and $\mathcal{B}_2$) for local mesh refinement, we

---

[2]See 6

always have one criterion in mind: when the refinement factors in space and time equal one, the multigrid numerical solution should match the one obtained without any refinement. This criterion is mainly required when going to trully multigrid approaches with a large number of high resolution grids where we also want that when two high resolution grids are neighbors the solution through the interface is the same as if only one grid was present. This criterion strongly restricts the choice of operators $\mathcal{B}_1$ and $\mathcal{B}_2$ and grid interactions only occur via a ghost cell approach.

One of the objectives of the choice of the operator $\mathcal{B}_1$ in case of an open boundary problem is to allow the outgoing information to leave the computational domain. In two-way mesh refinement, this characteristic is inherent to the method through the update of the coarse grid solution and thus does not require specific boundary condition on the fine grid.

The open boundary conditions case corresponds to a given solution u_2 for example coming from a coarser resolution run or from a climatology. In Blayo and Debreu 2005, the main boundary conditions have been revisited under the point of view of characteristic variables. The work has been primarily done on shallow water models. The main idea is here to use the characteristic variables to be able to specify either incoming information (specified by external data u_2) and outgoing information that has to be given by internal solution (most of the time requiring extrapolation at boundaries). For the following linearized shallow water model (written here in 1D) :

$$\frac{\partial \eta}{\partial t} + u_0 \frac{\partial \eta}{\partial x} + H \frac{\partial u}{\partial x} = 0$$
$$\frac{\partial u}{\partial t} + u_0 \frac{\partial u}{\partial x} + g \frac{\partial \eta}{\partial x} = 0$$

the characteristic variables are given by $w_\pm = u \pm \sqrt{\frac{g}{H}}\eta$ and propagates at speeds $\lambda_\pm = u_0 \pm \sqrt{gH}$. For a left (resp. right) boundary, w_+ (resp. w_-) is the incoming characteristic variable and should be prescibed by external data while w_- (resp. w_+) is the outgoing characteristic variable and should be computed from internal values. An efficient implementation of the use of characteristic variables for boundary conditions on a Arakawa C grid has been designed by Alexander Shchepetkin and is described in Mason et al. 2010.

In Blayo and Debreu 2005, the procedure is then extended to a linearized, flat bottom, primitive equation models using a vertical mode decomposition approach which allows to rewrite the original problem into a series of shallow water models corresponding to the barotropic and the baroclinic modes.

2.2.3   Some applications

The grid interactions techniques previously summarized have been integrated in several realistic ocean models. The computational aspects are managed using the AGRIF software described in chapter (5). Local mesh refinement with two-way interactions is now a mature technique and a lot of applications have been performed. Figure (2.3) illustrates the use of mesh refinement for downscaling and process studies using the ROMS-AGRIF model (Marchesiello, Capet, et al. 2011) and the use of mesh refinement for upscaling purposes using the NEMO-AGRIF model (Biastoch, Boning, and Lutjeharms 2008).
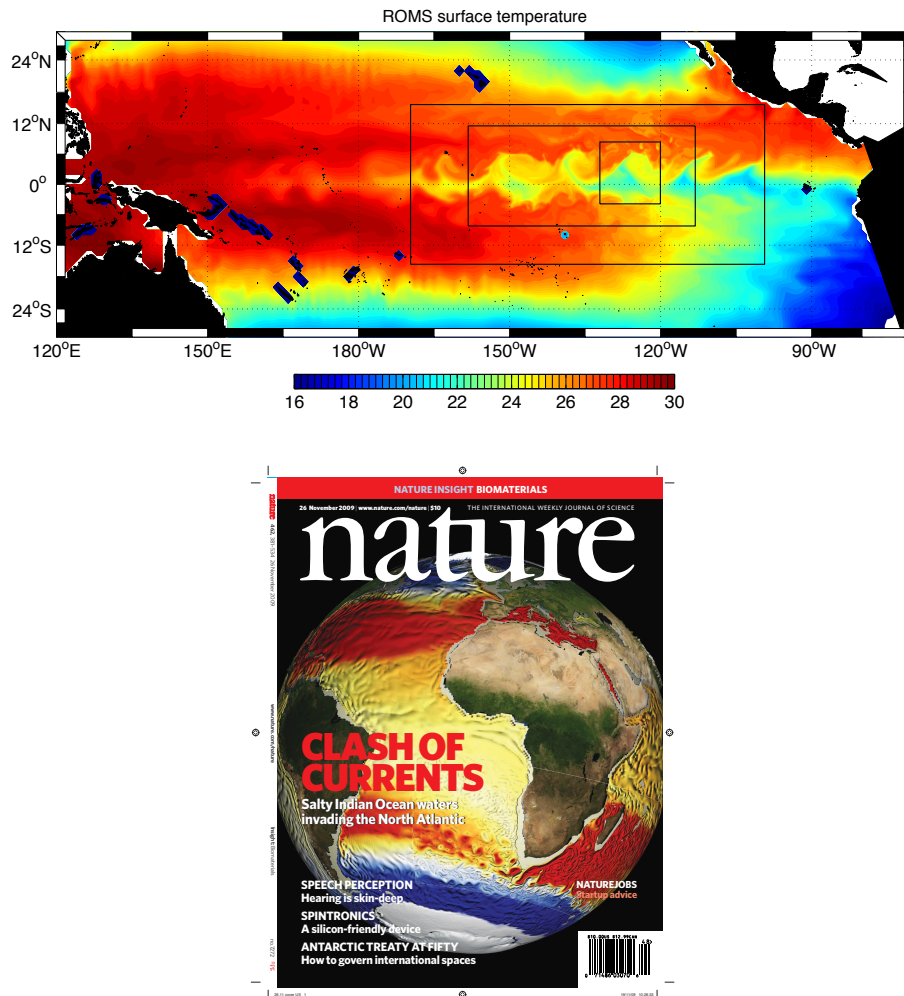
Figure 2.3: Two applications of local mesh refinement with two-way interaction. Top: study of tropical wave instabilities (Marchesiello, Capet, et al. 2011). Bottom: zoom in the Agulhas current and study of the upscaling impact on the global circulation (Biastoch, Boning, and Lutjeharms 2008)

2.2.4 Comments and perspectives

- *On the use of adaptive mesh refinement*:
  Our realistic adaptive mesh refinement applications were done at relatively coarse resolution (1/3°). At these non eddy permitting resolutions, the location of refinement areas is mainly dictated either by topographic features or by very strong currents (e.g. Gulf Stream). Thus the added value of grid adaptivity is small in comparison with static grid refinements. Today, oceanic simulations, in particular with regional models, are performed at much higher, eddy resolving, resolutions and there is a clear regain of interest for the application of adaptive mesh refinement.

- *On the combination of solutions at different resolutions*:
  Local mesh refinement for structured grids naturally leads to the computation of model solutions at different grid resolutions. In my past research, I did not explore how these

solutions can be interpreted in term of subgrid scales parameterizations. Superparameterization is now an active area of research (e.g. Majda and Grooms 2014) and, based on my experience with local mesh refinement, I am now indeed interested in the design of multiresolution subgrid sacles models (Sagaut, Deck, and Terracol 2006).

- *On the link between mesh refinement methods and underlying discretization schemes:* The behavior of mesh refinement methods is obviously related to grid interactions schemes. However, it is also strongly linked with internal underlying discretization schemes. For example, use of advanced grid interactions in a numerical model which does not properly take into account directions of information propagation will probably not be successful, trying to enforce conservation (using refluxing techniques) in a numerical model which uses a time stepping algorithm that cannot be written under flux form (e.g. LeapFrog with Asselin filter) is also useless. This strong link between local mesh refinement (or more generally boundary conditions) and internal numerical schemes was the first reason for me to be interested in numerical methods.

2.3   Model coupling

We now consider the case of model coupling.

2.3.1   Problem formulation

$$\frac{\partial u_1}{\partial t} + \mathcal{L}_1(u_1) = 0 \qquad \text{for } x \in \Omega_1 \qquad \qquad \frac{\partial u_2}{\partial t} + \mathcal{L}_2(u_2) = 0 \qquad \text{for } x \in \Omega_2$$
$$\mathcal{B}_1 u_1 = \mathcal{B}_1 u_2 \qquad \qquad \text{for } x \in \partial\Omega \qquad \mathcal{B}_2 u_2 = \mathcal{B}_2 u_1 \qquad \qquad \text{for } x \in \partial\Omega \qquad (2.3)$$
$$u_1(x, t = 0) = u_0(x) \qquad \qquad \qquad u_2(x, t = 0) = u_0(x)$$

The first problem is in the definition of the interface operators $\mathcal{B}_1$ and $\mathcal{B}_2$ in order to the problem to be well-posed. Additionally, as will be explained in the next section, it is sometimes necessary to use iterative algorithms to solve (2.3). In that case, we are looking for boundary operators $\mathcal{B}_1$ and $\mathcal{B}_2$ that lead to a fast convergence of the iterative process.

Model coupling and optimized Schwarz waveform relaxation methods

During the PhD of Florian Lemarié, we begun our work on ocean atmosphere coupling. The mathematical aspects have been focused on the coupling of two diffusion equations representatives to the coupling of oceanic and atmospheric boundary layers as illustrated on Fig. (2.4).
In current ocean atmosphere coupled applications (e.g. seasonal forecasts, climate studies), the coupling is applied at the level of successive time windows $[t_i, t_i + T]$ and can be formulated as follows:

$$\Omega_1, t \in [t_i, t_i + T] \qquad \qquad \qquad \Omega_2, t \in [t_i, t_i + T]$$
$$\frac{\partial u_1}{\partial t} + \mathcal{L}_1(u_1) = 0 \qquad \qquad \qquad \frac{\partial u_2}{\partial t} + \mathcal{L}_2(u_2) = 0$$
$$\mathcal{B}_1 u_1(t) = \mathcal{B}_1 u_2(t_i) \qquad \qquad \qquad \mathcal{B}_2 u_2(t) = \mathcal{B}_2 u_1(t)$$

The domain Ω_1 and associated $\mathcal{L}_1$ operator correspond to the atmosphere while $\Omega_2, \mathcal{L}_2$ correspond to the ocean. The atmospheric model is integrated during the whole time windows
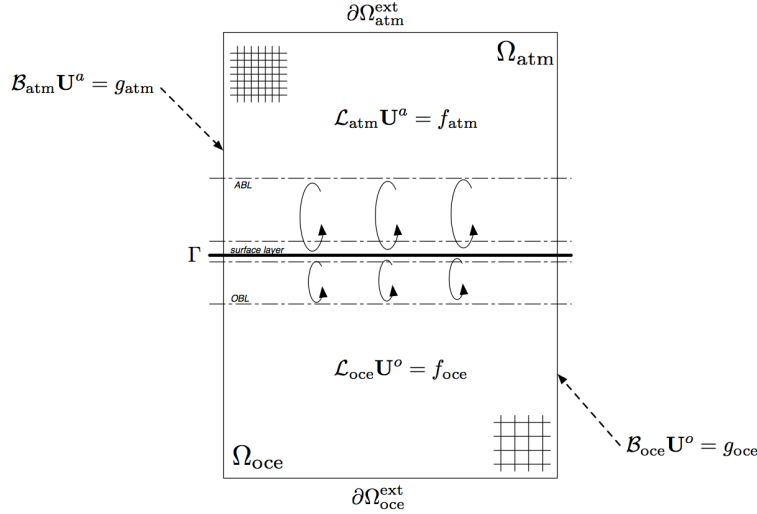
Figure 2.4: Coupling between atmospheric and oceanic models

using oceanic data (e.g. sea surface temperature) at the beginning of the time windows (t_i). The oceanic model is then integrated computing surface fluxes using atmospheric variables. It can be easily proved (e.g. on diffusion equations, see Lemarié, Blayo, and Debreu 2015) that this asynchronous algorithm can be unstable and indeed is just one iteration of an iterative coupling algorithm written under the following global in time Schwarz framework (written here under multiplicative form):

$$\Omega_1, t \in [t_i, t_i + T] \qquad\qquad \Omega_2, t \in [t_i, t_i + T]$$

$$\frac{\partial u_1^k}{\partial t} + \mathcal{L}_1 u_1^k = 0 \qquad\qquad \frac{\partial u_2^k}{\partial t} + \mathcal{L}_2 u_2^k = 0$$

$$\mathcal{B}_1 u_1^k(t) = \mathcal{B}_1 u_2^{k-1}(t) \qquad\qquad \mathcal{B}_2 u_2^k(t) = \mathcal{B}_2 u_1^{k-1}(t)$$

The objective is then to derive boundary operators $\mathcal{B}_1$ and $\mathcal{B}_2$ is order to get the correct solution (e.g. consistency of solution and its derivatives at interfaces) at convergence of the iterative process, a convergence that we want to be as fast as possible. For this, we derived optimised Schwarz waveform relaxation methods (Gander and Halpern 2007).
As previously mentioned, we study their derivations on the coupling of two diffusion equations:

$$\frac{\partial u_1^k}{\partial t} - \mu_1 \frac{\partial^2 u_1^k}{\partial x^2} = 0 \quad \text{for } x \in \Omega_1 \qquad \frac{\partial u_2^k}{\partial t} - \mu_2 \frac{\partial^2 u_2^k}{\partial x^2} = 0 \qquad \text{for } x \in \Omega_2$$

$$\frac{\partial u_1^k}{\partial x} + p_1 u_1^k = \frac{\partial u_2^{k-1}}{\partial x} + p_1 u_2^{k-1} \quad \text{for } x \in \partial\Omega_1 \qquad \frac{\partial u_2^k}{\partial x} + p_2 u_2^k = \frac{\partial u_1^{k-1}}{\partial x} + p_2 u_1^{k-1} \quad \text{for } x \in \partial\Omega_2$$

$$u_1^k(x, t = 0) = u_0(x) \qquad\qquad u_2^k(x, t = 0) = u_0(x)$$

$$(2.4)$$

where we have here assumed an approximation of optimal boundary operators (known as absorbing boundary conditions) in the form of two-sided ($p_2 \neq p_1$) Robin transmission conditions. The convergence study is done by rewriting system (2.4) in term of evolution of errors and by applying a temporal Fourier transform to the resulting system. The convergence rate

for a Fourier mode of frequency ω can then be written as:

$$\rho(p_1, p_2, \boldsymbol{\zeta}) = \sqrt{\frac{\left((p_1 - \boldsymbol{\zeta})^2 + \boldsymbol{\zeta}^2\right)\left((p_2 - \gamma\boldsymbol{\zeta})^2 + \gamma^2\boldsymbol{\zeta}^2\right)}{\left((p_1 + \gamma\boldsymbol{\zeta})^2 + \gamma^2\boldsymbol{\zeta}^2\right)\left((p_2 + \boldsymbol{\zeta})^2 + \boldsymbol{\zeta}^2\right)}} \tag{2.5}$$

where $\gamma = \sqrt{\frac{\mu_1}{\mu_2}}$ et $\boldsymbol{\zeta} = \zeta/\sqrt{\zeta_{\min}\zeta_{\max}}$, $\zeta = \sqrt{|\omega|\mu_1}$. ω is in the range $\omega_{\min} = \frac{\pi}{T}$ et $\omega_{\max} = \frac{\pi}{\Delta t}$ where T is the size of the temporal window and Δt is the model time step. The optimal parameters $p_1^\star, p_2^\star$ are the solutions of the optimisation problem:

$$\min_{p_1, p_2 > 0} \left(\max_{\zeta \in [\mu^{-1}, \mu]} \rho(p_1, p_2, \zeta) \right), \qquad \mu = \sqrt{\zeta_{\max}/\zeta_{\min}} \tag{2.6}$$

In Lemarié, Debreu, and Blayo 2013b, the solution of the minmax problem (2.6) is solved in the case of constant (but distinct) diffusion coefficients μ_1, μ_2. The analytical values of p_1, p_2 are found for the first time in the case of a two-sided optimisation (i.e. $p_1 \neq p_2$). The performance of the resulting algorithm on a discrete problem is illustrated on figure (2.5) for different values of γ and μ. On this figure, the boundary condition is denoted by DN (Dirichlet-Neumann), NR* (optimised Neumann-Robin), RR* (optimized Robin-Robin) and RR$^{(as)}$ (asymptotically optimised Robin-Robin). This last boundary condition is obtained by minimising the Taylor development of the convergence rate (2.5) around small frequencies ω.
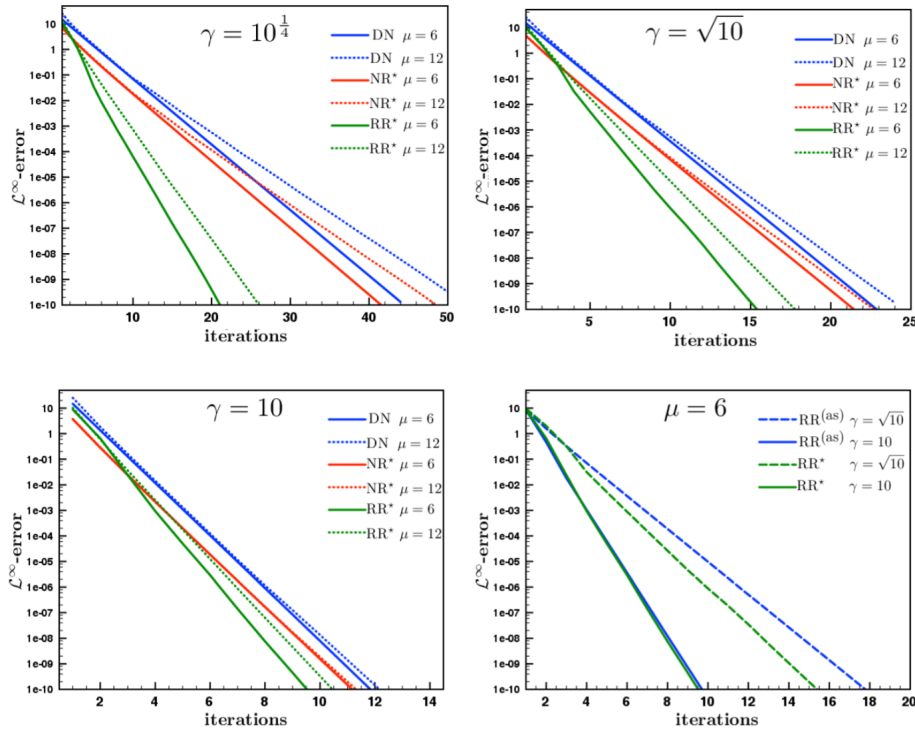

Figure 2.5: Convergence for $\gamma = 10^{\frac{1}{4}}$ (top, left), $\gamma = \sqrt{10}$ (top, right) and $\gamma = 10$ (bottom, left) for $\mu = 6$ and $\mu = 12$ in the DN, RR*, and NR* cases. Comparison between RR* and RR$^{(as)}$ (bottom, right)

The extension to spatially variable diffusion coefficients is studied in Lemarié, Debreu, and

Blayo 2013c using a projection of the solution on a basis of eigenvectors of a Sturm-Liouville problem.

The optimisation problem has also been solved in Lemarié, Debreu, and Blayo 2013a at the discrete level using discrete optimal control techniques where p_1 and p_2 are the control parameters. This allows to take into account the discretisation schemes of both the model operator (here the diffusion equation) and of the Robin boundary conditions.

2.3.2 Some applications

Ocean atmosphere problem

The global in time Schwarz algorithm has been applied to realistic ocean atmosphere coupling simulations using the models ROMS and WRF to simulate the genesis and propagation of tropical cyclone Erica (Lemarié, Marchesiello, et al. 2014) (see figure (2.6)).
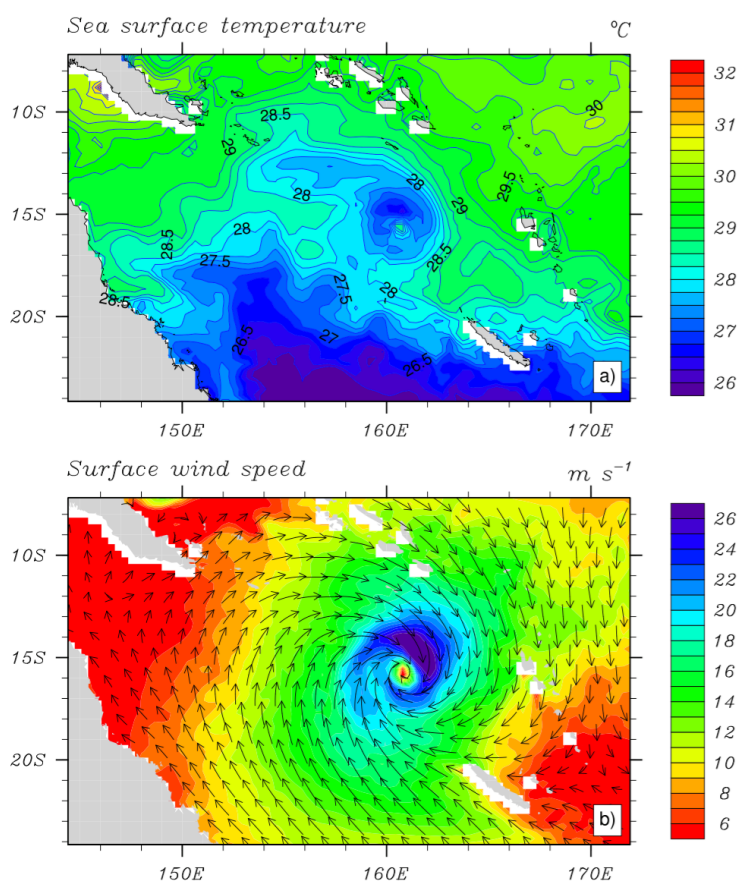
Figure 2.6: Snapshots (March 12, 2003 at 8 p.m. GMT) of (a) ROMS sea surface temperature (b) WRF 10 meter winds during a coupled simulation.

Ensemble simulations have been designed by perturbations of the coupling frequency and the initial conditions. One ensemble has been integrated using the Global-in-Time Schwarz Method and an other using the traditional asynchronous method. The results, illustrated on figure (2.7), show significant differences in terms of ensemble spread (with respect to the cyclone trajectory and intensity), the Schwarz iterative coupling method leading to a reduced spread. This suggests that part of the model sensitivity to perturbed parameters can be

attributed to inaccuracies in the coupling method. Specifically, coupling inconsistencies can spuriously increase the physical stochasticity of simulated atmospheric and oceanic events (materialised here by the ensemble spread). For our particular case, three iterations of the Schwarz method are sufficient to improve the coupled solutions with respect to the ensemble spread. In this paper, usual (non optimised) Dirichlet - Neumann boundary conditions has been used due to the complexity of the physical parameterisations inside the boundary layers.
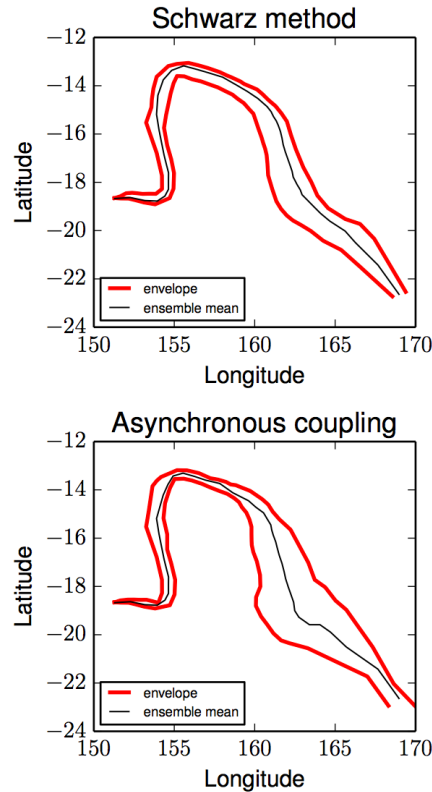
Figure 2.7:   Ensemble envelopes (thick grey lines) and means (thin black lines) for the cyclone track obtained with Schwarz method (top) and the asynchronous method (bottom) using minimum pressure for the tracking

Parallel computing on heterogenous platforms

Schwarz methods has been recognised for a while as a way of performing parallel computing and limiting the frequency of data exchanges (at the price of the iterative process). This was actually the subject my first research work for the solution of elliptic equations on parallel computers (Debreu and Blayo 1998). Global in time Schwarz methods, described in the previous section, also allow to limit the number of synchronisations in the model integrations since the communications occur only at the level of the time window. Like traditional (space) Schwarz methods, they have a number of advantages:

- to adapt the numerical/physical schemes to the different domains

- to adapt the grid resolution (both in space and time) to the different domains

But there are also a number of additional advantages for the computation on heterogenous platform:

- to deal with fault tolerance : when a computing core or node is faulty, only the corresponding subdomain has to be rerun (and this only on the current time window)

- to deal with load balancing : the most powerful computers treat a larger number of subdomains.

I have made simple application of SWR method for the solution of 2D advection problem on parallel computers. A realistic application of SWR have also been investigated using the WRF model. These two practical applications however raised a number of new questions that can probably be theoretically tackled:

- How to optimise the size of the time windows and the size of the overlap region (in case of overlapping Schwarz methods) taking into account both the convergence rate but also the cost of data exchanges between computers ?

- What is the impact of the necessary sampling of boundary data on the convergence rate and on the accuracy of the solution ? Indeed in practical simulations, the boundary data cannot be stored without being sampled in order to avoid two much data exchanges

2.3.3 Comments and perspectives

- *On the cost of the Schwarz algorithm:*
  The obvious problem of iterative Schwarz algorithm is its computational cost. An open question is if simplified/reduced models can be used to perform the first iterations of the algorithm.
  The cost of the Schwarz algorithm can also be alleviated if used in conjunction with another iterative method. This is typically the case when variational data assimilation methods, leading to the minimisation of an objective function, are applied.
  Joint use of global in time Schwarz algorithms and parallel in time algorithms (e.g. parareal Lions, Maday, and Turinici 2001) is also an interesting subject for high performance computing on next generation platforms.

- *Schwarz methods and boundary layer parameterisations:*
  The realistic experiments presented in paragraph (2.3.2) have been done with non optimised boundary conditions due to the complexity (and potentially non differentiability) of the boundary layer parameterisations (bulk formulae). Looking at the formulation of these parameterisations in term of the convergence of the Schwarz algorithm is a subject currently addressed in the PhD of Charles Emmanuel Pelletier (supervised by Eric Blayo and Florian Lemarié).

Chapter 3

Numerical methods for ocean modelling

My first subject of interest was the control of the orientation of numerical diffusion (Marchesiello, Debreu, and Couvelard 2009; Lemarié, Debreu, Shchepetkin, et al. 2012). The strong stratification of the ocean imposes privileged directions in the water masses mixing. When the vertical coordinate system is not aligned with the constant density surfaces (isopycnal surfaces), numerical mixing, either explicit through a diffusion term or implicit to upwind biased advection schemes, leads to unacceptable results. Therefore my work, mainly in collaboration with P. Marchesiello and F. Lemarié, consisted in the proposal of an implementation of a diffusion tensor rotated along isopycnal surfaces. At the numerical level, this corresponds to the derivation of a stable discretization of a fourth order mixed derivatives problem.

During Jéremie Demange PhD, we used the technique of projection onto normal modes (in the vertical direction) to explore several important issues. The first of them is a better understanding of fast (barotropic)/slow(baroclinic) modes splitting techniques that are used in ocean modelling. We first showed that the assumption currently used in the mode splitting technique (rigid lid assumption) was an important source of instability (Demange, Debreu, et al. 2014b). We also studied the propagation of internal waves. In most current models, this propagation is treated in a basic way (second order centered discretization). In addition to propose the implementation of higher order schemes (horizontal pressure gradient and horizontal divergence), we proposed a computation of diffusive terms based on a decomposition in normal modes. The impact of the vertical discretization (grid staggering and numerical schemes) has also been analized.

3.1   Isopycnal diffusion and rotation of diffusion tensors

Most ocean numerical models employ isoneutral mixing operators either to parameterize the effect of unresolved mesoscale eddies (Gent and Mcwilliams 1990; Smith and Gent 2004), or more basically to control dispersive errors Lemarié, Kurian, et al. 2012. It is thus very common for non-isopycnic models to implement a rotation of the diffusion tensor in a direction non-aligned with the computational grid. The benefits of a rotated mixing operator in simulating large scale flows are undeniable (e.g. Danabasoglu, McWilliams, and Gent 1994;

Lengaigne et al. 2003). Much of the improvements brought by the Gent and Mcwilliams 1990 parameterization of mesoscale eddies in coarse resolution models are also generally attributed to the orientation of lateral diffusive transport to be along isoneutral directions (Gent 2011). Redi 1982 provided the continuous form of the rotation tensor; however additional efforts were required to proceed to the actual implementation at the discrete level. Several works (Cox 1987; Danabasoglu and Mc Williams 1995; Griffies et al. 1998; Mathieu, Deleersnijder, and Beckers 1999; Beckers, Burchard, Campin, et al. 1998; Beckers, Burchard, Deleersnijder, et al. 2000) tackled this problem that turned out to be more tedious than expected. The discretization in space raises difficulties to properly conserve the monotonicity (Mathieu and Deleersnijder 1998; Beckers, Burchard, Deleersnijder, et al. 2000) and global tracer variance dissipation properties (Griffies et al. 1998) of the continuous operator once the problem is discretized. Moreover, due to the small vertical, relative to horizontal, grid distance typically used in numerical models the vertical and cross terms of the tensor can impose a severe restriction on the time step when explicit-in-time methods are used to advance the rotated operator. This stability problem is alleviated by the use of a standard backward Euler scheme for the vertical component of the tensor (Cox 1987), at the expense of splitting errors and associated errors in the balance between the active tracer isoneutral diffusive fluxes (Griffies 2004, Chap. 16). This approach is used in all the state-of-the-art ocean climate models. The existing work on the isoneutral diffusion has been essentially carried out on the second-order (Laplacian) operator and under the small slope approximation (Cox 1987; Gent and Mcwilliams 1990).

3.1.1   Contributions[1]

Second order diffusion

The rotation of the diffusion along a target coordinate $s^\star$ starting from a vertical coordinate s is written as follows (in a 2D x-z configuration):

$$\frac{\partial T}{\partial t} + \frac{\partial uT}{\partial x}\bigg|_s + \frac{\partial wT}{\partial s} = \mu \, \frac{\partial^2 T}{\partial x^2}\bigg|_{s^\star=cste}$$

The rotated diffusive term can be written:

$$\mu \, \frac{\partial^2 T}{\partial x^2}\bigg|_{s^\star=cste} = \mu \nabla \cdot \begin{pmatrix} 1 & \alpha_x \\ \alpha_x & \alpha_x^2 \end{pmatrix} \nabla T, \qquad \nabla = \begin{pmatrix} \dfrac{\partial}{\partial x}\bigg|_s \\ \dfrac{\partial}{\partial s} \end{pmatrix} \tag{3.1}$$

where α_x is the slope between iso-s and iso-$s^\star$ curves:

$$\alpha_x = -\frac{\partial s^\star}{\partial x}\bigg|_s \bigg/ \frac{\partial s^\star}{\partial s}$$

The rotation leads to an important numerical issue: part of the diffusion is orientated vertically which leads, due to the small grid size in that direction, to a strong stability constraint on the time step. When a second order diffusion is applied, this problem is usually solved by using a time implicit scheme for the vertical component. In practice, this fully implicit treatment may not be required and in Lemarié, Debreu, Shchepetkin, et al. 2012 we flawoured to

---

[1]See 7

use the stabilized correction technique as introduced in Houwen and Verwer 1979.
The rotation (3.1) can be written under the sum of second order derivatives along x and s and one mixed derivative:

$$\frac{T^{n+1} - T^n}{\Delta t} = D^{xx,xs}(T) + D^{ss}(T)$$

where

$$D^{xx,xs}(T) = \mu \left[\frac{\partial^2 T}{\partial x^2} + 2\alpha_x \frac{\partial^2 T}{\partial x \partial s} \right], \quad D^{ss}(T) = \mu \alpha_x^2 \frac{\partial^2 T}{\partial s^2}$$

The stabilized correction technique can be written as a predictor-corrector step:

$$\frac{T^{n+1,\star} - T^n}{\Delta t} = D^{xx,xs}(T^n) + D^{ss}(T^n)$$

$$\frac{T^{n+1} - T^{n+1,\star}}{\Delta t} = \theta \left[D^{ss}(T^{n+1}) - D^{ss}(T^n) \right]$$

Let σ is the parabolic Courant number along x

$$\sigma = \mu \frac{\Delta t}{\Delta x^2}$$

If a fully explicit scheme was used (i.e. $\theta = 0$) then the stability constraint would be $\sigma(1 + S_x^2) \leq \frac{1}{2}$, where $S_x = \alpha_x \frac{\Delta x}{\Delta z}$.
It is shown in Lemarié, Debreu, Shchepetkin, et al. 2012 that, in order to get the same stability constraint than the unrotated operator ($\sigma \leq \frac{1}{2}$), the parameter θ has to be chosen according to[2]:

$$S_x^2 \sigma \theta = \frac{1}{2} \max\{-1 + 2\sigma(1 + S_x^2), 0\}$$

The value of θ ranges from $\theta = 0$ when the explicit scheme is stable ($-1 + 2\sigma(1 + S_x^2) \leq 0$) to $\theta = 1$ when $\sigma = 1/2$. The amount of implicit diffusion is thus always smaller compared with the fully implicit scheme. In practice it leads to a more accurate approximation of the vertical diffusion.

Fourth order diffusion

Spurious diapycnal diffusion (artificial numerical mixing across isopycnal surfaces) can also come from the diffusive part of upwind biased advection schemes. This has been illustrated in Marchesiello, Debreu, and Couvelard 2009 where the use of a third order upwind advection scheme is shown to fundamentally change water masses after only a small period of integration as shown on figure (3.1).
The third order advection scheme can be split into a fourth order (non dissipative) advection and a corresponding fourth order diffusion term. The idea is then to rotate the diffusion term. In this case, the stability constraint, linked with the discretisation of vertical and mixed terms, is even stronger. This is illustrated on figure 3.2 where the ratio of unrotated diffusion maximum time step over rotated diffusion maximum time step is plotted.
In Marchesiello, Debreu, and Couvelard 2009, using the topography following coordinate

---

[2]the exact expression depends on the spatial discrete formulation of the rotated tensor (see Lemarié, Debreu, Shchepetkin, et al. 2012)
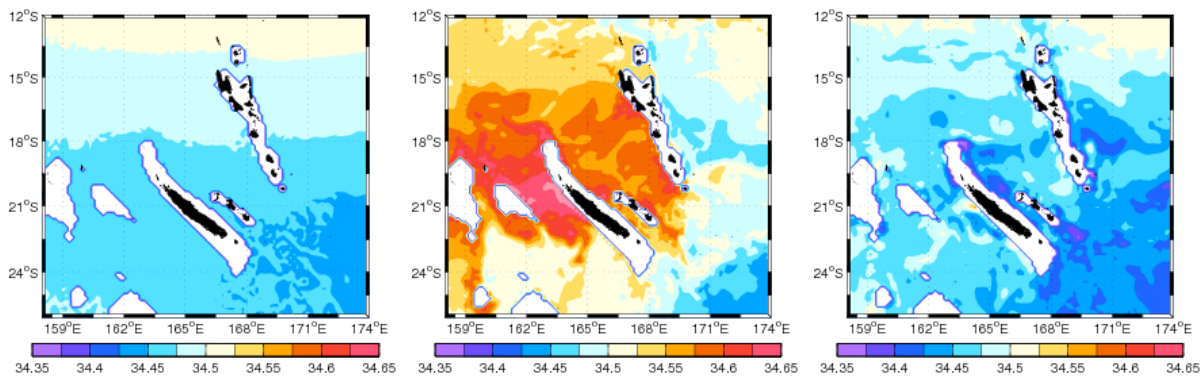
Figure 3.1:   Salinity at 1000m depth around New Caledonia. Climatology (left), results after six months of simulation with a third order upwind tracer advection scheme (middle) and with fourth order rotated diffusion (right).

ROMS model, this problem is solved by choosing $s^\star = z$ instead of $s^\star = \rho$ (which is generally less constraining) and also by limiting the diffusion coefficients (clipping) as a function of the stability constraint, which in practice corresponds to deviate from the desired diffusion direction. However, in Lemarié, Debreu, Shchepetkin, et al. 2012, we were able to extend the preceding stabilised correction technique to a fourth order diffusion operator with mixed derivatives. As for the second order case, the stabilisation requires only one solution of a tridiagonal solver (the stabilising implicit diffusion is still laplacian).

In Lemarié, Debreu, Shchepetkin, et al. 2012, we were also interested in the spatial discretisation of the rotated operators. Indeed, the spatial discretisation of the isopycnal mixing operators is a difficult problem that has been thoroughly tackled by Beckers, Burchard, Campin, et al. 1998; Beckers, Burchard, Deleersnijder, et al. 2000; Griffies et al. 1998.

Finally the impact of isopycnal diffusion is also clearly visible on the kinetic energy spectra. This has been reported in a paper submitted to ocean modelling (**Soufflet2015**). Limiting diapycnal diffusion results in sharper fronts and more intense surface currents. Indeed the supply of available potential energy needed to sustain frontal processes can be rapidly drained by diapycnal diffusion.

Comments and perspectives

Our developments on rotation of diffusion tensors allow the model to be less sensitive to the choice of the vertical coordinate. It however raises several questions.

- *On the monotony of the rotated operators:*
  The linear rotated diffusion operators are not monotonic. The derivation of monotonic diffusion operators is possible (see Beckers, Burchard, Deleersnijder, et al. 2000) but it relies on rather complex and costly schemes. One can imagine that the monotony of the full scheme (i.e. diffusion plus advection) could be maintained using approaches like flux corrected transport (FCT) schemes. However, it will push the problem on the control of the orientation of diffusion in non linear schemes like FCT (or any other extrema preserving scheme).
  This point shows that, even if the rotation of diffusion tensors has enable strong improvements in realistic simulations, the choice of the vertical coordinate system remains the key point.
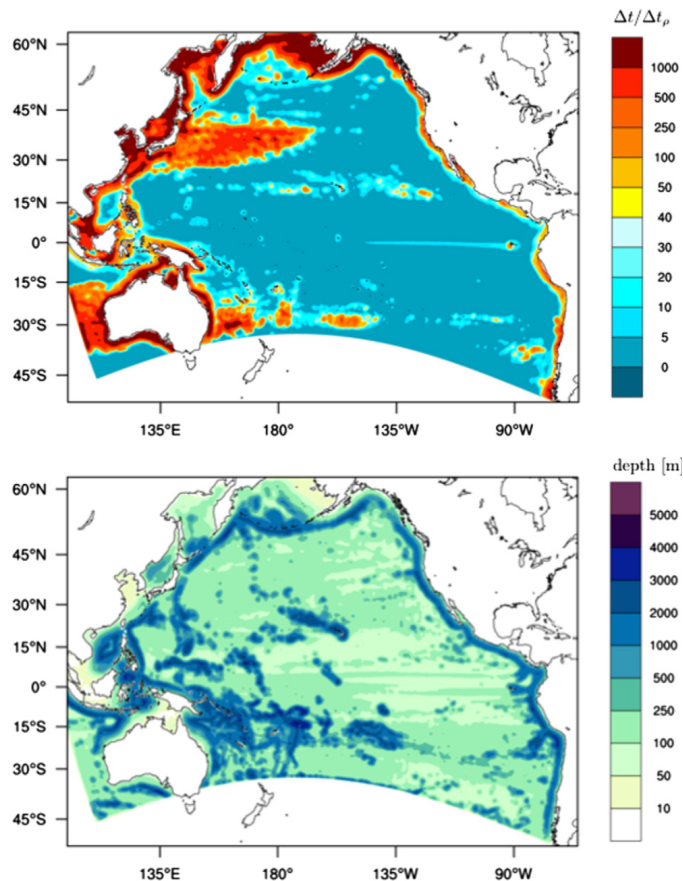
Figure 3.2: Annual mean of the maximum value of the ratio $\Delta t/\Delta t_\rho$ for each water column (top), with Δt the time-step of the ROMS model using the method of stabilized corrections scheme to advance the rotated biharmonic operator and Δt_ρ the time-step which would be needed to advance the same operator but with a explicit scheme. Depth of the maximum (bottom). $\Delta t/\Delta t_\rho$ is first computed using seasonal averages and is then averaged to get the annual mean.

- *On the regularity of velocity fields:*
  Spurious diapycnal diffusion is also strongly linked with the regularity of the velocity fields. This has been clearly illustrated in Illicak et al. 2012 where experiments at different Reynolds numbers are produced. Therefore it is an open question if the current ocean models have enough dissipation mechanisms in processes affecting the velocity fields. In particular, monotonic momentum advection schemes are rarely used and internal gravity waves resulting from the coupling between velocity and density are usually discretised with basic, strongly dispersive, schemes.

3.2 External/Internal gravity waves

During the PhD of Jérémie Demange, we studied the propagation of external and internal gravity waves using a normal mode decomposition approach. In this section, I summarise salient points regarding the normal mode decomposition of the 2D (x-z) linearised (around $u = u_0$) flat bottom inviscid primitive equations (i.e. under the hydrostatic and Boussinesq

assumptions). For more details about the vertical mode decomposition, see Kundu and Cohen 2002; Blayo and Debreu 2005; Demange, Debreu, et al. 2014a. In the following, $u(x, z, t)$ and $w(x, z, t)$ denote the perturbation components of fluid velocities, $p(x, z, t)$ and $\rho(x, z, t)$ denote pressure and density perturbations around a state $(\bar{p}(z), \bar{\rho}(z))$ satisfying the hydrostatic balance $\dfrac{d\bar{p}(z)}{dz} = -\bar{\rho}(z)g$ where $\overline{\rho}(z)$ is a reference density profile. Using those notations, the system of interest reads

$$\frac{\partial u}{\partial t} + u_0 \frac{\partial u}{\partial x} + \frac{1}{\rho_0} \frac{\partial p}{\partial x} = 0, \qquad \text{Momentum conservation,} \qquad (3.2)$$

$$\frac{\partial p}{\partial z} = -g\rho, \qquad \text{Hydrostatic equilibrium,} \qquad (3.3)$$

$$\frac{\partial u}{\partial x} + \frac{\partial w}{\partial z} = 0, \qquad \text{Continuity / Incompressibility,} \qquad (3.4)$$

$$\frac{\partial \rho}{\partial t} + u_0 \frac{\partial \rho}{\partial x} + w \frac{d\overline{\rho}}{dz} = 0, \qquad \text{Energy conservation.} \qquad (3.5)$$

In the vertical direction the model extends from the flat bottom $z = -H$ to the free surface $z = \eta(x, t)$. The surface and bottom boundary conditions read

$$\frac{\partial \eta}{\partial t} = w(0), \qquad (3.6)$$

$$w(z = -H) = 0. \qquad (3.7)$$

On a discrete grid, with n vertical levels, the solutions of (3.2-3.5) can be decomposed using vertical modes $M_q(z)$:

$$\begin{cases} u(x, z, t) = \displaystyle\sum_{q=0}^{n-1} u_q(x, t) M_q(z), \\ p(x, z, t) = \rho_0 g \displaystyle\sum_{q=0}^{n-1} h_q(x, t) M_q(z), \\ \rho(x, z, t) = -\rho_0 \displaystyle\sum_{q=0}^{n-1} h_q(x, t) \frac{dM_q(z)}{dz}, \end{cases} \qquad (3.8)$$

where the modes $M_q(z)$ are the eigenvectors of the following Sturm-Liouville problem

$$\begin{cases} \Lambda M_q = \lambda_q M_q, \\ \dfrac{dM_q}{dz}\bigg|_{z=0} = -\dfrac{N^2(0)}{g} M_q(0), \\ \dfrac{dM_q}{dz}\bigg|_{z=-H} = 0, \end{cases} \qquad (3.9)$$

where $\Lambda = -\dfrac{d}{dz}\left(N^{-2}\dfrac{d}{dz}\right)$, with $N^2(z) = -\dfrac{g}{\rho_0}\dfrac{d\overline{\rho}}{dz}$ the Brunt-Väisälä frequency assumed to be positive. Each mode $M_q(z)$ is associated to a positive eigenvalue $\lambda_q = c_q^{-2}$ (sorted in

increasing order). The vertical modes are orthonormal with respect to the dot product

$$\langle f, g \rangle = \frac{1}{H} \int_{-H}^{0} f(z)g(z)dz \tag{3.10}$$

The first mode ($q = 0$) is called the barotropic mode and is almost depth-independent (i.e. $\lambda_0 \approx 0, M_q(0) \approx 1$) (it is exactly depth-independent when the rigid lid assumption is assumed (i.e. $\left.\dfrac{dM_q}{dz}\right|_{z=0} = 0$ in 3.9)).

For constant N, an analytical expression of the modes and their associated eigenvalues can easily be found (Cushman-Roisin and Beckers 2011)

$$M_q(z) = \sqrt{2} \cos \left(\frac{q\pi}{H} z \right), \qquad c_q = \frac{NH}{q\pi}, \qquad q \geq 1. \tag{3.11}$$

Fig. 3.3 shows the first four baroclinic modes for $H = 4000$m and $N = 2.10^{-3}\text{s}^{-1}$.
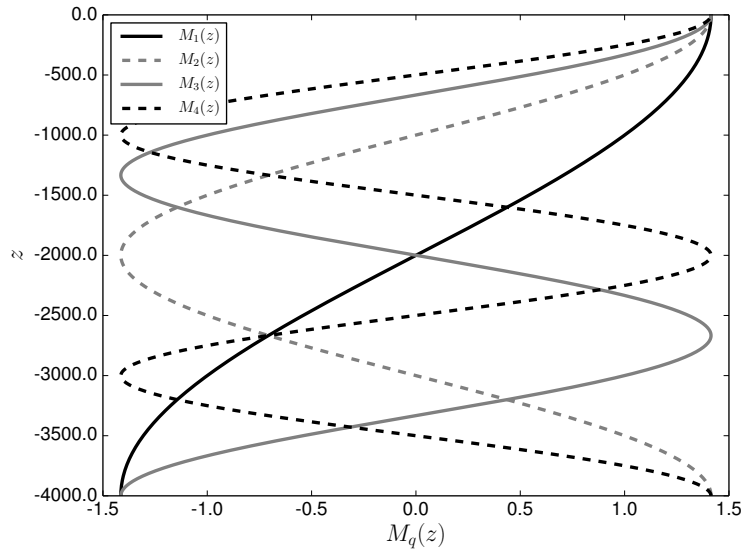
Figure 3.3: Baroclinic modes $M_q(z)$ (defined in (3.11)) for $1 \leq q \leq 4$ with respect to the depth z.

Projection of equations (3.2-3.5) onto the vertical modes M_q leads to the following system:

$$\partial_t u_q + u_0 \frac{\partial u_q}{\partial x} + g\partial_x h_q = 0, \tag{3.12}$$

$$\partial_t h_q + u_0 \frac{\partial h_q}{\partial x} + \frac{c_q^2}{g}\partial_x u_q = 0. \tag{3.13}$$

- The evolution of u_q is obtained by taking the dot product of the momentum equation 3.2 by the mode M_q[3]

$$\frac{\partial u_q}{\partial t} + g\frac{\partial h_q}{\partial x} = 0 \tag{3.14}$$

---

[3]In the following, we assume $u_0 = 0$

- The evolution of h_q is more complex to obtained:

$h_q = \dfrac{1}{\rho_0 g H} \displaystyle\int_{-H}^{0} p M_q$ can be expressed as a fonction of ρ as

$$h_q = \frac{1}{\rho_0 g H} \int_{-H}^{0} p M_q = -\frac{1}{\rho_0 g H} \int_{-H}^{0} \frac{\mathrm{d}p}{\mathrm{d}z} \int_{-H}^{z} M_q = \frac{1}{\rho_0 H} \int_{-H}^{0} \rho \int_{-H}^{z} M_q = -\frac{1}{\rho_0 H \lambda_q} \int_{-H}^{0} \rho N^{-2} \frac{\mathrm{d}M}{\mathrm{d}z}$$

So that the time evolution of h_q is given by:

$$
\begin{aligned}
\frac{\partial h_q}{\partial t} &= -\frac{1}{\rho_0 H \lambda_q} \int_{-H}^{0} \frac{\partial \rho}{\partial t} N^{-2} \frac{\mathrm{d}M_q}{\mathrm{d}z} \\
&= \frac{1}{\rho_0 H \lambda_q} \int_{-H}^{0} \omega \frac{\mathrm{d}\bar{\rho}}{\mathrm{d}z} N^{-2} \frac{\mathrm{d}M_q}{\mathrm{d}z} \\
&= -\frac{1}{g \lambda_q H} \int_{-H}^{0} \omega \frac{\mathrm{d}M_q}{\mathrm{d}z} \\
&= \frac{1}{g \lambda_q H} \int_{-H}^{0} \frac{\partial \omega}{\partial z} M_q \\
&= -\frac{1}{g \lambda_q H} \int_{-H}^{0} \frac{\partial u}{\partial x} M_q \\
&= -\frac{1}{g \lambda_q H} \frac{\partial u_q}{\partial x}
\end{aligned}
$$

which leads to (3.13).

Thus the important relations that have been used are:

$$\frac{1}{\rho_0 g H} \int_{-H}^{0} p M_q = -\frac{1}{\rho_0 H \lambda_q} \int_{-H}^{0} \rho N^{-2} \frac{\mathrm{d}M}{\mathrm{d}z} \tag{3.15}$$

and

$$\int_{-H}^{0} \omega \frac{\mathrm{d}M_q}{\mathrm{d}z} = -\int_{-H}^{0} \frac{\partial u}{\partial x} M_q \tag{3.16}$$

At this point, let us draw two important remarks

- The order of accuracy for the discretisation of $\partial_x h_q$ is thus directly linked to the order of accuracy of the pressure gradient discretisation.

- The order of accuracy for the discretisation of the term $\partial_x u_q$ is linked to the order of approximation of the horizontal divergence in the continuity equation.

In (3.12, 3.13), each modal projection leads to a shallow water system which can also be expressed in terms of characteristic variables. The corresponding characteristic variables y_q are

$$y_q^{\pm} = u_q \pm \frac{g}{c_q} h_q,$$

which propagate at speed $\pm c_q$, they indeed satisfy the transport equation

$$\frac{\partial y_q^{\pm}}{\partial t} \pm c_q \frac{\partial y_q^{\pm}}{\partial x} = 0. \tag{3.17}$$

The main objective of our research was to look at the numerical accuracy of the discrete propagation of these internal waves in an ocean model.

3.2.1 Contributions

Numerical representation of internal waves

<u>Horizontal discretisation:</u>
As mentioned earlier, the pressure gradient term and the horizontal divergence in the continuity equation are generally discretised using low (second) order approximations. Even if the use of a staggered grid (Arakawa C grid) eliminates the $2\Delta x$ computational mode, there is still a lot of improvement that can be achieved using fourth order approximations as shown on figure (3.4).
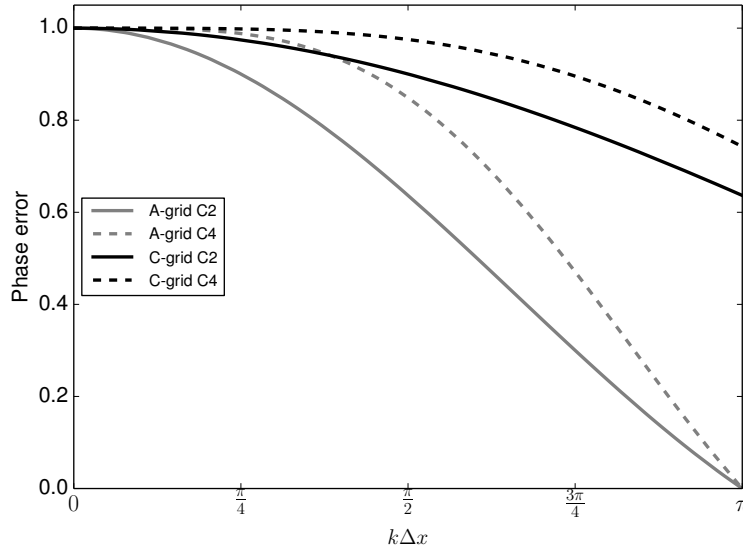

Figure 3.4: Phase error with respect to the normalized wavenumber $\theta_x = k\Delta x$ for non-staggered (gray lines) and staggered (black lines) grids for second (solid lines) and fourth-order (dashed lines) approximations.

<u>Vertical discretisation:</u>
The most influential factor of the discrete waves propagation speed is the choice of the vertical grid and the staggering of density and momentum. Two grid staggerings are known in the literature: Lorenz and Charney-Phillips vertical grids (Arakawa and Moorthi 1988; Leslie and Purser 1992; Cullen et al. 1997; Thuburn 2006). They are depicted on figure (3.5), the main difference being the density being at the centre of the cells on the Lorenz grid and at the cell interfaces on the Charney-Phillips grid.

The continuous dispersion relation related to system (3.2, 3.3, 3.4, 3.5) is given by $\omega = \dfrac{k_x}{k_z}N$ where k_x and k_z are the horizontal and vertical wavenumbers. If the Brunt Vaisala frequency N and the vertical grid step Δz are assumed to be constant, it is possible to study impact of the vertical grid staggering by computing the corresponding discrete dispersion relation (see Thuburn 2006). In the general case of non constant N and non constant vertical grid step, it is interesting to derive the discrete Sturm-Liouville problems in order to deduce the discrete wave propagation speeds and the vertical structure of the normal modes. The resulting discrete system[4] depends both on the vertical grid staggering (Lorenz or Charney-Phillips),

---

[4]The discrete system is obtained by studying the discrete equivalents of relations 3.15, 3.16
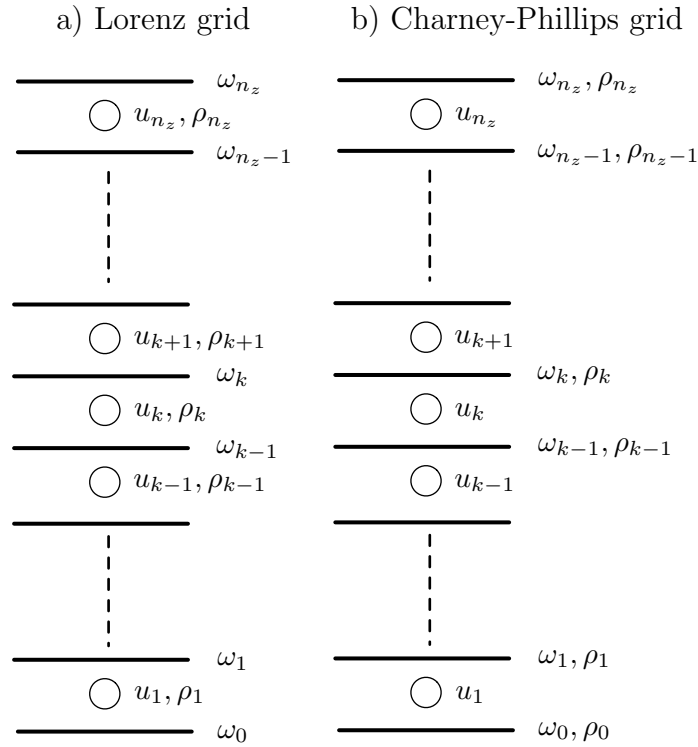
a) Lorenz grid   b) Charney-Phillips grid

Figure 3.5: Vertical location of state variables on the Lorenz and Charney-Phillips grids

the numerical approximation of $w\dfrac{\mathrm{d}\overline{\rho}}{\mathrm{d}z}$ and the numerical approximation of the hydrostatic equilibrium 3.3 (including boundary conditions for high order schemes). It can then be show that, in case of second order approximations, the corresponding discrete Sturm-Liouville problems are given by :

$$-\frac{1}{\lambda}\left(N_{k+1}^{-2}\frac{M_{k+1}-M_k}{\Delta z_{k+1}} - N_k^{-2}\frac{M_k-M_{k-1}}{\Delta z_k}\right) = \frac{1}{4}\left[(M_{k-1}+M_k)\,\Delta z_k + (M_k+M_{k+1})\,\Delta z_{k+1}\right], \text{ for } 1 \leq k \leq n_z - 1$$

$$-\frac{1}{\lambda}N_1^{-2}\frac{M_1-M_0}{\Delta z_1} = \frac{1}{4}(M_0+M_1)\Delta z_1$$

$$\frac{1}{\lambda}N_{n_z}^{-2}\frac{M_{n_z}-M_{n_z-1}}{\Delta z_{n_z}} = \frac{1}{4}(M_{n_z-1}+M_{n_z})\Delta z_{n_z}$$

$$(3.18)$$

on a Lorenz grid and by

$$-\frac{1}{\lambda}\left(N_{k+1}^{-2}\frac{M_{k+1}-M_k}{\Delta z_k^w} - N_k^{-2}\frac{M_k-M_{k-1}}{\Delta z_{k-1}^w}\right) = M_k\Delta z_k \qquad (3.19)$$

on a Charney-Phillips grid.

Note that on a Lorenz grid the modes M_q are located at layers interfaces while on a Charney-Phillips grid normal modes are associated with cell centres. Both systems (3.18, 3.19) can be written under the form $AM = \lambda BM$ which defines a generalised eigenvalue problem. In the Lorenz grid case, the matrix B is semi-definite and a computational mode exists. However in both cases, the pencil $\{A, B\}$ is Hermitian definite and so a set of orthogonal eigenvectors with respect to the matrix B can be found. The matrix B defines the discrete (potentially semi-) inner product corresponding to (3.10).

Figures (3.6) (resp. (3.7)) show the associated phase errors in the case of a constant (resp. non constant) Brunt-Vaisala frequency. It is interesting to note that the behaviour of the Charney-Phillips grid is quite different with a constant or a non constant Brunt-Vaisala frequency. On these figures, results obtained on a Lorenz grid with a fourth order discretisation of the hydrostatic equilibrium are also indicated.
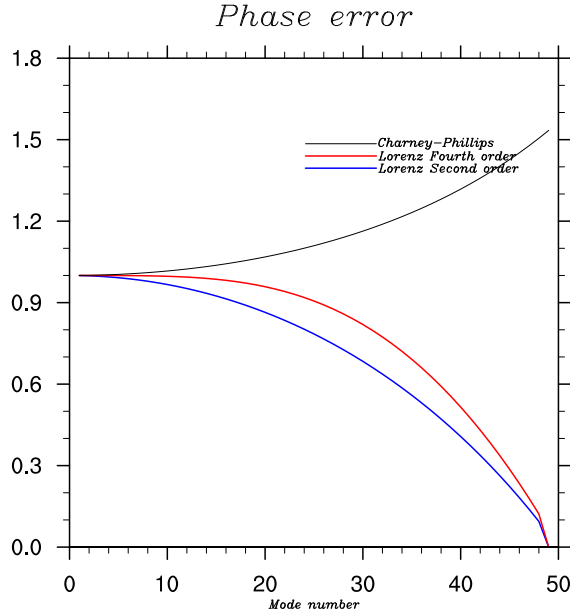

Figure 3.6: Phase error c_q/c_q^{exact} for constant Brunt-Vaisala frequency

Numerical diffusion and internal waves

Internal waves propagates in the ocean and the atmosphere and as mentioned above are discretised through centered schemes which may lead to dispersion errors and aliasing through nonlinearities. The continuous increase of resolution and the addition of more physics (e.g. tides for the ocean) will make the representation of internal waves and their potential breaking more and more important in the coming years. Knowing how to dissipate these waves seems to be an important issue.

During the PhD of Jérémie Demange, the normal mode decomposition was used to compute internal wave speed dependent diffusion. The state variables are projected onto the vertical modes and a velocity dependent diffusion is computed for each internal modes, the resulting diffusion is then projected back onto the original space. The velocity dependent diffusion has been computed using either a first order upwind scheme (leading to a second order diffusion term), a Total Variation Diminishing (TVD) scheme or a Monotonicity Preserving (MP) scheme. This approach is probably the most efficient when all the assumptions leading to the normal mode decomposition are valid (in particular, linearisation around a vertically constant background velocity u_0 and flat bottom). Its extension to more general case is an open question. Note that it also requires a non staggered grid to be able to collocate the Riemann invariants.

A much simple variant of this approach is traditionally used in three dimensional Discontinuous Galerkin (DG) models. Here a Lax Friedrichs approach is applied to smooth the
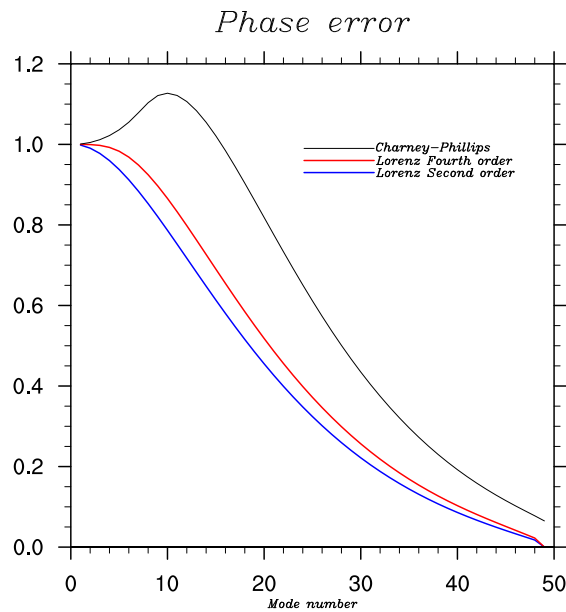
Figure 3.7: Phase error c_q/c_q^{exact} for non constant Brunt-Vaisala frequency

jumps at interfaces and the diffusion coefficient of the Lax Friedrich method is based on an estimate of the sum of the phase speed of the first baroclinic mode and the maximum advection velocity. This approach obviously leads to too much dissipation of the higher baroclinic modes.

Stability of the external/internal mode coupling

In the normal mode decomposition, the fastest mode corresponds to the barotropic mode with a propagation speed equal to $c_0 \approx \sqrt{gH}$. To face the stability limit associated with the barotropic mode, ocean models rely on barotropic/baroclinic mode splitting. The barotropic mode is integrated separately from the baroclinic modes using either an implicit time stepping algorithm or using time splitting techniques. The later are often preferred due to smaller dispersion errors. The barotropic mode is thus integrated using a smaller time step. Since the barotropic mode is almost depth-independent, this assumption is taken in ocean models and thus the barotropic component correspond to the depth averaged quantities.

To prevent instabilities associated to these splitting errors, a time filtering of the barotropic variables has to be applied. This can be achieved either by using a diffusive time stepping algorithm in the barotropic integration itself (Killworth et al. 1991) or in the baroclinic integration (Hallberg 1997). But in practice, most ocean models perform this time-filtering using explicit averaging filters (Nadiga et al. 1997; Shchepetkin and McWilliams 2009) involving the sub-time steps instantaneous barotropic solutions, before reconciliation with the 3D parts. In addition to the inexact splitting above, several other reasons motivate the need for some form of time filtering (Shchepetkin and McWilliams 2005; Shchepetkin and McWilliams 2009). Aliasing errors due to nonlinearities are obviously an additional source of instability controlled by time averaging. The benefit effect of recomputing at least the fast barotropic part of this term has been studied in Morel, Baraille, and Pichon 2008. Barotropic/baroclinic mode splitting for free surface ocean models remains an issue to con-

sider since it can require a large amount of unphysical diffusion to achieve a stable integration of the mode-split equations. This has been studied in several papers (e.g. Hallberg 1997; Higdon and Szoeke 1997; Kamenkovich and Nechaev 2009). However in Demange, Debreu, et al. 2014b, we introduce a new framework for the stability analysis of the splitting technique. The analysis is based on a decomposition that uses the true (depth-dependent) barotropic mode and the associated baroclinic modes. Our study reveals that the amount of diffusion induced by classical averaging filters is much larger than needed to compensante the inexact mode splitting (i.e. under the depth-independent assumption). We thus favor the use of slightly dissipative 2D time stepping algorithms. The numerical experiments were done here in a very simplified model where all the assumptions of the normal mode decomposition are valid. We have however also run several realistic experiments using the ROMS model. Adding to the 2D barotropic time stepping algorithm an amount of laplacian diffusion corresponding to the theoretical study presented in this paper (and removing the existing averaging filter) has led to long terms stable runs and seems to be enough to prevent aliasing errors. It however remains to be validated on a full set of realistic experiments.

Using 2D dissipative time stepping algorithms has several additional advantages over the averaging filters. First the barotropic integration stops at time $n + 1$ and does not require additional time steps like in averaging filters. This lowers the computational cost, especially on parallel computers where the barotropic 2D integration is the less scalable part of the numerical model. It also allows to obtain a continuous free surface temporal elevation (no restart at each baroclinic time step). Finally it strongly simplifies the implementation of grid nesting with coupling at the barotropic level Debreu, Marchesiello, et al. 2012.

3.2.2 Comments and perspectives

- *On the numerical discretisation of internal waves*:
  High order discretisation of the horizontal pressure gradient and the horizontal divergence could lead to less dispersive discretizations. To our knowledge, none ocean models are using high order discretisation of the horizontal divergence and so it has to be experimented. Note that in non hydrostatic simulations, it would however lead to the solution of a Poisson system with a large matrix stencil. It can however be overcome using a pseudo-compressible approach which precludes the use of the solution of a Poisson system.
  The derivation of the discrete Sturm-Liouville problem allows the study the impact of vertical grid staggering and vertical discretizations. Done here in the case of a z coordinate model, it would be interesting to extend this study to other vertical coordinate systems.

- *On internal waves and dissipation mechanisms*:
  Fourth order horizontal discretisation, as described below, allow to achieve relatively low dispersion error (on a Arakawa C grid). However vertical discretisation introduces itself large dispersion error. It is always true for the Lorenz grid, with an inherent computational mode, but it is also true for the Charney-Phillips grid with variable Brunt-Vaisala frequency or variable vertical grid step. It is thus important to study how to dissipate the associated small scales without using two large diffusion coefficients (e.g. in a Lax Friedrichs approach). Adding diffusion through the time stepping algorithm has also to be studied.

Chapter 4

Data assimilation

Having worked on local mesh refinement methods, I have been naturally interested in the application of variational data assimilation techniques within this framework. This was the topic of the PhD of Ehouarn Simon (Simon 2007). The objective was to formulate the problem of variational data assimilation problem in the case of models using local mesh refinement, this both in passive interaction (ie without feedback from the high resolution grid to low resolution grid) and in active interaction (with feedback). We also studied the possibility of an additional control of intergrid transfers (correction term added to interactions) (Simon, Debreu, and Blayo 2011). During Emilie Neveu PhD (Neveu 2011), we applied (possibly nonlinear) multigrid methods to accelerate the minimization of the objective function. A study of the convergence of the multigrid methods (ellipticity, approximation property) has been done both on linear and more complex nonlinear cases Neveu, Debreu, and Le Dimet 2011. More recently I showed how to hybridize a traditional preconditioner (based on the background error covariance matrix) and a multigrid preconditioner within a Krylov method (Debreu, Neveu, Simon, et al. 2015).

4.1 Variational data assimilation

We consider the time evolution of a system governed by the following equation:

$$
\begin{aligned}
\frac{\mathrm{d}X}{\mathrm{d}t} &= F(X) \\
X(t = t_0) &= \mathbf{x}
\end{aligned}
\tag{4.1}
$$

$\mathbf{x}$ is the initial condition at time $t = t_0$ and is our control parameter. The variational data assimilation problem consists in finding the minimum of a cost function $J(\mathbf{x})$ that measures the distance from the numerical model to the observations and includes a regularization term associated to background $\mathbf{x}_b$.

$$
J(\mathbf{x}) = \frac{1}{2} (\mathbf{x} - \mathbf{x}_b)^T \mathbf{B}^{-1} (\mathbf{x} - \mathbf{x}_b) + \frac{1}{2} (H(X(\mathbf{x}, t)) - \mathbf{y})^T \mathbf{R}^{-1} (H(X(\mathbf{x}, t)) - \mathbf{y})
\tag{4.2}
$$

Here $\mathbf{y}$ are the observations. H is the observation operator from model space to observation space, $\mathbf{R}$ and $\mathbf{B}$ are respectively the observations and background error covariances matrices. When observations are available at a number N_{obs} of different times t_i, the cost function can be more precisely written as:

$$J(\mathbf{x}) = \frac{1}{2}\|\mathbf{x} - \mathbf{x}_b\|^2_{\mathbf{B}^{-1}}$$

$$+ \frac{1}{2}\sum_{i=0}^{N_{\text{obs}}-1} \left(H_i\left(X(\mathbf{x}, t_i)\right) - \mathbf{y}_i\right)^T \mathbf{R}_i^{-1}\left(H_i\left(X(\mathbf{x}, t_i)\right) - \mathbf{y}_i\right) \quad (4.3)$$

At a minimum $\mathbf{x}^\star$ of J, the gradient is zero

$$\nabla_{\mathbf{x}}J(\mathbf{x}^\star) = 0 \quad (4.4)$$

When the model F and the observations operator H are linear, the cost function is quadratic and the solution of (4.4) is equivalent to the solution of

$$\mathbf{A}\mathbf{x}^\star = \mathbf{b} \quad (4.5)$$

where $\mathbf{A}$ is the Hessian of the cost function:

$$\mathbf{A} = \mathbf{B}^{-1} + \mathbf{G}^T\mathbf{R}^{-1}\mathbf{G}$$

where $\mathbf{G}$ is a compact representation that includes both the model and the observation operators and the right hand side b is given by

$$\mathbf{b} = \mathbf{B}^{-1}\mathbf{x}_b + \mathbf{G}^T\mathbf{R}^{-1}\mathbf{y}$$

In practice, the direct model can make use of local mesh refinement and thus the question is how to accordingly modify the data assimilation algorithm.

In addition, the huge computational costs of the direct and adjoint models bring us to study the application of mulitigrid methods in order to lower the cost of the data assimilation procedure.

4.2 Data assimilation and local mesh refinement

Local mesh refinement has been introduced in chapter 2. As previously mentioned, when the direct model is using local mesh refinement, the data assimilation method has to be adapted. Obviously, the idea can also be to locally increase the mesh refinement in order to take benefit from a dense observation network and thus lowering representativeness errors.

Concerning sequential data assimilation, previous work has been done, using the notion of "multigrid state vector", in Barth et al. 2007a for the application of a SEEK (Singular Evolutive Extended Kalman) filter in a two-way nested model of the Ligurian Sea. Similar ideas have been used in Melet, Verron, and Brankart 2012; Djath et al. 2014).

One way to deal with local mesh refinement and data assimilation in a weaker sense is to take the high resolution solution as observations for the coarse solution. The smooth semi-prognostic method adapted to local mesh refinement in Sheng et al. 2005 enters in this category of weakly coupled models.

Here we focus on variational data assimilation for strongly coupled models.

4.2.1 Formulation of the variational problem

In order to obtain a formulation of variational data assimilation in the specific context of a two-grid system, we have first to re-define several notions.

State vector

The state vector $\mathbf{X}$ of the two-grid model is composed of the state vectors of both grids:

$$\mathbf{X} = \begin{bmatrix} \mathbf{X}_c \\ \mathbf{X}_f \end{bmatrix}$$

It corresponds to the "multigrid state vector" proposed in Barth et al. 2007b. Therefore the initial condition $\mathbf{x}$, which will be the control variable for the minimization problem, and its background value $\mathbf{x}^b$ read with obvious notations:

$$\mathbf{x} = \begin{bmatrix} \mathbf{x}_c \\ \mathbf{x}_f \end{bmatrix} \qquad \mathbf{x}^b = \begin{bmatrix} \mathbf{x}_c^b \\ \mathbf{x}_f^b \end{bmatrix}$$

Cost function

The cost function is defined as the sum of the misfit to the first guess and the misfits to the observations on both grids:

$$
\begin{aligned}
J(\mathbf{x}) \;=\;& J^b(\mathbf{x}) + J_c^{obs}(\mathbf{x}) + J_f^{obs}(\mathbf{x}) \\
=\;& \frac{1}{2}(\mathbf{x} - \mathbf{x}^b)^T \mathbf{B}^{-1}(\mathbf{x} - \mathbf{x}^b) \\
& + \frac{1}{2}\sum_{i=0}^{N}[H_c^i(\mathbf{X}_c^i(\mathbf{x})) - \mathbf{y}_c^i]^T \mathbf{R}_c^{i\,-1}[H_c^i(\mathbf{X}_c^i(\mathbf{x})) - \mathbf{y}_c^i] \\
& + \frac{1}{2}\sum_{i=0}^{N}[H_f^i(\mathbf{X}_f^i(\mathbf{x})) - \mathbf{y}_f^i]^T \mathbf{R}_f^{i\,-1}[H_f^i(\mathbf{X}_f^i(\mathbf{x})) - \mathbf{y}_f^i]
\end{aligned}
$$

where $\mathbf{B}$ is now a two-grid error covariance matrix. The preceding cost function is well adapted to one-way simulations. In case of two-way simulations, it can be modified by not taking into account the coarse grid solution inside the fine grid domain.

4.2.2 Contributions: The two-grid optimality systems

The gradient of the background term J^b reads $\nabla J^b(\mathbf{x}) = \mathbf{B}^{-1}(\mathbf{x} - \mathbf{x}^b)$. The gradients of the observation terms J_c^{obs} and J_f^{obs} can be obtained using the adjoint method (e.g. Le Dimet and Talagrand 1986) applied to the nested system. We note $\mathbf{P}$ the coarse resolution component of the adjoint vector ($\mathbf{P}$ is the adjoint variable of $\mathbf{X}_c$) and $\mathbf{Q}$ the high resolution one ($\mathbf{Q}$ is the adjoint variable of $\mathbf{X}_f$). In the case of two-way interaction, the adjoint system reads:

<div style="border:1px solid">

Two-way optimality system

Domain Ω_c

$$\left\{ \begin{array}{l} \left\{ \begin{array}{l} \dfrac{\partial \mathbf{X}_c}{\partial t} = F(\mathbf{X}_c, \mathbf{X}_\omega) \quad \text{on} \quad \Omega_c \times [0,T] \\[2mm] \mathbf{X}_c(x,0) = \mathbf{x}_c \\[2mm] \mathbf{X}_\omega = I_f^c(\mathbf{X}_f) \quad \text{on} \quad \mathring{\omega}_f \times [0,T] \end{array} \right. \\[10mm] \left\{ \begin{array}{l} \dfrac{\partial \mathbf{P}}{\partial t} + \left[\dfrac{\partial F}{\partial \mathbf{X}_c} \right]^* . \mathbf{P} + \mathbf{I}_f^c \left[\dfrac{\partial F}{\partial \mathbf{X}_{\partial \omega}} \right]^* . \mathbf{Q} = \mathbf{H}_c^* \mathbf{R}_c^{-1}(\mathbf{H}_c \mathbf{X}_c(t) - \mathbf{y}_c(t)) \\[3mm] \mathbf{P}(T) = 0 \end{array} \right. \\[8mm] \nabla_{\mathbf{x}_c} J^{obs} = -\mathbf{P}(0) \end{array} \right.$$

Domain ω_f

$$\left\{ \begin{array}{l} \left\{ \begin{array}{l} \dfrac{\partial \mathbf{X}_f}{\partial t} = F(\mathbf{X}_f, \mathbf{X}_{\partial\omega}) \quad \text{on} \quad \omega_f \times [0,T] \\[2mm] \mathbf{X}_f(x,0) = \mathbf{x}_f \\[2mm] \mathbf{X}_{\partial\omega} = I_c^f(\mathbf{X}_c) \quad \text{on} \quad \partial\omega_f \times [0,T] \end{array} \right. \\[10mm] \left\{ \begin{array}{l} \dfrac{\partial \mathbf{Q}}{\partial t} + \left[\dfrac{\partial F}{\partial \mathbf{X}_f} \right]^* . \mathbf{Q} + \mathbf{I}_c^f \left[\dfrac{\partial F}{\partial \mathbf{X}_\omega} \right]^* . \mathbf{P} = \mathbf{H}_f^* \mathbf{R}_f^{-1}(\mathbf{H}_f \mathbf{X}_f(t) - \mathbf{y}_f(t)) \\[3mm] \mathbf{Q}(T) = 0 \end{array} \right. \\[8mm] \nabla_{\mathbf{x}_f} J^{obs} = -\mathbf{Q}(0) \end{array} \right.$$

</div>

where the operator $\mathbf{I}_c^f = \mathbf{I}_c^f(\mathbf{X}_c)$ is the linearization of I_c^f in $\mathbf{X}_c$ and the operator $\mathbf{I}_f^c$ is the adjoint of $\mathbf{I}_c^f$ and where the operator $\mathbf{I}_f^c = \mathbf{I}_f^c(\mathbf{X}_f)$ is the linearization of I_f^c in $\mathbf{X}_f$ and the operator $\mathbf{I}_c^f$ is the adjoint of $\mathbf{I}_f^c$. We observe a feedback from the high resolution adjoint model onto the coarse resolution one, in the opposite direction of the interactions existing in the direct formulation. In two way, the addition of a feedback from the high resolution solution to the coarse resolution one leads to an interaction in the adjoint model from the coarse resolution adjoint solution to the high resolution one. Like for the direct system, the two grids must be integrated simultaneously in this adjoint system.

In Simon, Debreu, and Blayo 2011, the importance of the design of the background error covariance matrices have been addressed. The B matrix is modeled by

$$B = \left(\begin{array}{c|c} B_{cc} & B_{cf} \\ \hline B_{fc} & B_{ff} \end{array} \right)$$

where the B_{cc}, B_{ff} matrices are traditional background error covariance matrices where Gaussian correlations are approximated using a Laplacian diffusion operator and computed independently on each grid. The cross terms B_{cf}, B_{fc} are there to include constrains on the coarse and fine analysis increments using the grid interactions operators. Figure (4.1) shows the increments obtained for mono observations experiments using a shallow water model and with different formulations of the two-grid background error covariance matrix. The B_{multi} formulation includes the cross terms while the B_{indep} formulation does not.

The structures of the coarse grid increments are fundamentally different between the two formulation both in magnitude and geometry. In particular, as expected, the increments obtained on the coarse grid using the B_{multi} formulation matches very well the ones computed
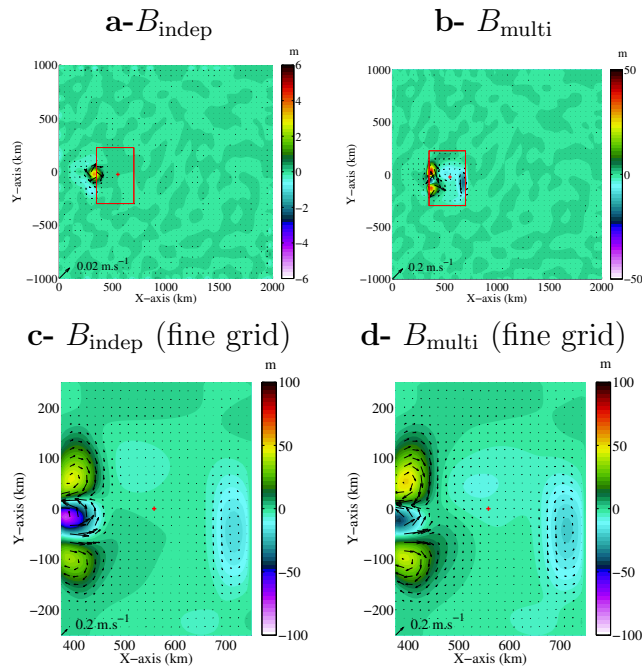
Figure 4.1: Single observation experiments: map of the coarse (reps. fine) resolution analysis increment for the case of : the matrix B_{indep} (a- (resp. c-)), the matrix B_{multi} (b- (resp. d-)). The high resolution grid is localized by the red box. The observation is localized by a red cross in the centre of fine grid.

on the fine grid.

Finally, in Simon, Debreu, and Blayo 2011, we also look at the effect of adding a control on the grid interactions thus allowing a weaker coupling between grids. However the chosen numerical experiments were not fully satisfactory. Indeed, in addition to difficulties in the specification of the additional error covariance matrices, the observations were only present on the high resolution domain and thus a large part of the control was done by the control of the boundary conditions of the fine grid leading to a degradation of the coarse grid results. Experiments with observations both on coarse and fine domains produce better results..

4.2.3   Comments and perspectives

- *On the multigrid background error covariance matrix:*
  When using a Gaussian correlation operator approximated by a diffusion operator Weaver and Courtier 2001, a fully two-grid B covariance matrix can also be obtained by applying the laplacian diffusion in a two-grid context (i.e. with coarse-fine grid interactions at the level of each step of the diffusion operator). Preliminary experiments in the 3DVAR version of the NEMO ocean model support the superiority of this approach.

4.3   Multigrid methods for variational data assimilation

The idea is here to apply multigrid methods for the solution of 4.5. In the optimal control framework, several attempts have been made to apply multigrid methods, either for linear or non linear optimization (see Borzì and Schulz 2009 for a review). Lewis and Nash 2005 focus on the control of the initial condition for a linear advection equation with a specific cost function and discretization scheme that renders the problem fully elliptic (i.e. large scale components of the error are more efficiently reduced on a coarser grid) and thus well suited for multigrid methods. In Neveu, Debreu, and Le Dimet 2011; Debreu, Neveu, Simon, et al. 2015, multigrid methods are applied to a simple 2D (1D in space, 1D in time) variational assimilation problem using a cost function $J(\mathbf{x})$ that mimics those used in more realistic applications in the context of geophysical fluids.

4.3.1   Multigrid methods: algorithm

The general idea of multigrid methods is to begin by reducing the small scale components of the error on the current (high resolution) grid Ω_f. This is called the pre-smoothing step and should be achieved in a few iterations according to the ellipticity of the system (large eigenvalues at small scales). The error is then smooth and can be appropriately computed on a coarse resolution grid Ω_c during the coarse grid correction step. The correction is then interpolated back to the fine grid. Since the interpolation operator can in turn produce small scale error components, a post-smoothing step is finally applied.

The basic algorithm with two grid levels can be written: MULTIGRID(ν_1,ν_2,Ω_f,$\mathbf{x}_f$,b_f)

1. Pre-smoothing: Apply ν_1 steps of an iterative method $\mathbf{S}_1$ on a fine grid for the solution of $\mathbf{A}_f\mathbf{x}_f = \mathbf{b}_f$. During pre-smoothing, the error $\mathbf{e}_f = \mathbf{x}_f - \mathbf{x}^*$ evolves as:

$$\mathbf{e}_f \leftarrow \mathbf{S}_1^{\nu_1}\mathbf{e}_f.$$

2. Coarse grid correction

   • Transfer the residual onto a coarser grid

   $$\mathbf{r}_c = \mathbf{I}_f^c(\mathbf{b}_f - \mathbf{A}_f\mathbf{x}_f), \quad I_f^c : \text{ restriction operator}$$

   • Solve the problem on the coarse grid

   $$\mathbf{A}_c\delta\mathbf{x}_c = \mathbf{r}_c. \tag{4.6}$$

   • Transfer the correction onto the fine grid

   $$\mathbf{x}_f = \mathbf{x}_f + \mathbf{I}_c^f\delta\mathbf{x}_c, \quad \mathbf{I}_c^f : \text{ interpolation operator}$$

3. Post-smoothing: Apply ν_2 steps of an iterative method $\mathbf{S}_2$ (most of the time identical to $\mathbf{S}_1$) onto a fine grid for the solution of $\mathbf{A}_f\mathbf{x}_f = \mathbf{b}_f$. During post-smoothing, the error $\mathbf{e}_f = \mathbf{x}_f - \mathbf{x}^*$ evolves as:

   $$\mathbf{e}_f \leftarrow \mathbf{S}_2^{\nu_2}\mathbf{e}_f.$$

The extension of this two grid algorithm to a multi grid algorithm is done recursively by solving eq. 4.6 by a multigrid algorithm. Eq. 4.6 is replaced by

$$\text{For } n = 1 \ldots \gamma, MULTIGRID(\nu_1, \nu_2, \Omega_c, \delta\mathbf{x}_c, \mathbf{r}_c)$$

The number γ of recursive calls determines the kind of multigrid algorithms: the best known being the V-cycle ($\gamma = 1$) and W-cycle ($\gamma = 2$) and are depicted in figure (4.2).
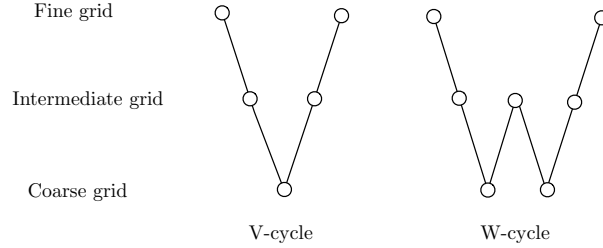

Figure 4.2: V-cycle and W-cycle algorithms in the case of three grid levels

Full Approximation Scheme variant

In the multigrid algorithm introduced above, the coarse grid correction seeks a solution for the error $\delta\mathbf{x}_c$ (eq. 4.6). It is possible to rewrite the algorithm in an equivalent form where a coarse solution is searched for instead. This is the Full Approximation Scheme (FAS) (Brandt 1982) which has a natural extension to non linear operators. The coarse grid correction step is obtained by expressing the coarse grid correction $\delta\mathbf{x}_c$ as $\mathbf{x}_c - I_f^c\mathbf{x}_f$ and the problem is solved for the full approximation $\mathbf{x}_c$ instead of the correction $\delta\mathbf{x}_c$:

- Solve the problem on the coarse grid

$$\mathbf{A}_c\mathbf{x}_c = \mathbf{b}_c \tag{4.7}$$

  where

$$\mathbf{b}_c = \mathbf{r}_c + \mathbf{A}_c\mathbf{I}_f^c\mathbf{x}_f = \mathbf{I}_f^c\mathbf{b}_f + \left(\mathbf{A}_c\mathbf{I}_f^c - \mathbf{I}_f^c\mathbf{A}_f\right)\mathbf{x}_f.$$

- Transfer the correction onto the fine grid

$$\mathbf{x}_f = \mathbf{x}_f + \mathbf{I}_c^f\left(\mathbf{x}_c - \mathbf{I}_f^c\mathbf{x}_f\right).$$

Ingredients of convergence: the smoothing and approximation properties

We refer to Hackbusch 2003 for a detailed explanation of the different ingredients of the convergence proof.
The relation between the error $\mathbf{e}_f = \mathbf{x}_f - \mathbf{x}^*$ before ($\mathbf{e}_f^{\text{before}_{cc}}$) and after ($\mathbf{e}_f^{\text{after}_{cc}}$) the coarse grid correction step is given by:

$$\mathbf{e}_f^{\text{after}_{cc}} = \left(\mathbf{I} - \mathbf{I}_c^f\mathbf{A}_c^{-1}\mathbf{I}_f^c\mathbf{A}_f\right)\mathbf{e}_f^{\text{before}_{cc}}.$$

Including the smoothing steps (and assuming only pre-smoothing is applied ($\nu_1 = \nu, \nu_2 = 0$),

$$\mathbf{e}_f^{k+1} = \left(\mathbf{I} - \mathbf{I}_c^f\mathbf{A}_c^{-1}\mathbf{I}_f^c\mathbf{A}_f\right)\mathbf{S}^\nu\mathbf{e}_f^k.$$

The smoothing steps $\mathbf{S}^\nu$ should remove most of the error at small scales while the coarse grid correction step should remove the large scale error. This property, along with the approximation property which states the coarse grid matrix $\mathbf{A}_c$ is close to the fine grid matrix $\mathbf{A}_f$, enable to show that the spectral radius of the multigrid iteration matrix $\mathbf{\Phi} = \left(\mathbf{I} - \mathbf{I}_c^f \mathbf{A}_c^{-1} \mathbf{I}_f^c \mathbf{A}_f \right) \mathbf{S}^\nu$ can be made less than one if a sufficient number of smoothing steps ν are applied.

4.3.2   Contributions[1]

Ellipticity and approximation properties

For the case of a simple linear advection equation, a detailed study of the ellipticity and approximation properties has been done in Neveu, Debreu, and Le Dimet 2011; Debreu, Neveu, Simon, et al. 2015. Using a cost function with characteristics similar to the ones typically used in geophysical applications, we showed the important role played by the background error covariance matrix and preconditioning on the ellipticity. Then, for the model problem of a transport equation, the quality of approximation of the fine grid system by one with a coarser resolution has been investigated. Numerical errors, in particular those of dissipative nature, alter the quality of this approximation. As an example, figure (4.3) from Debreu, Neveu, Simon, et al. 2015 shows the divergence of the multigrid solution after a few cycles.
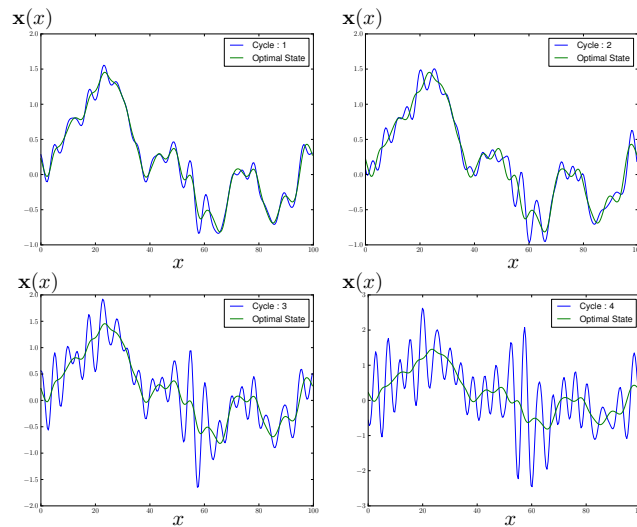

Figure 4.3: Evolution of the multigrid solution during the four first cycles and comparison with the true solution of the optimal control problem.

Robustness and efficiency have been achieved by using multigrid iterations inside the preconditioning step of a conjugate gradient algorithm as described in the next paragraph.

Multigrid methods as preconditioner

In Debreu, Neveu, Simon, et al. 2015, we look at the multigrid method as a preconditioner for a Krylov method. We introduced an hybrid preconditioner using a combination of the multigrid method and the usual preconditioning using the B matrix (or its square root).

---

[1]See paper ZZZ

This renders the resulting algorithm much more robust and less sensitive to the quality of the approximation property. If we note $\mathbf{K}$ the left preconditioner:

$$\mathbf{K}^{-1}\mathbf{A}\mathbf{x} = \mathbf{K}^{-1}b$$

The hybrid preconditioner is defined by :

$$\mathbf{K}^{-1} = I_c^f \mathbf{A}_c^{-1} I_f^c + (I - I_c^f I_f^c)^T \mathbf{B}_f (I - I_c^f I_f^c) \tag{4.8}$$

where I_f^c et I_c^f are restriction and prolongation operators. This preconditioner is thus a sum of a coarse resolution inversion and the traditional B-preconditioning. The combination is done using the restriction/prolongation operators : large scales are solved using the multigrid method while small scales are preconditioned by $\mathcal{B}$. The performance are illustrated on figure (4.4) in term of number of (high resolution) model integrations and of total computational time (that includes the time spent on the coarse grids). This figure compares the unigrid solution (with or without preconditioning by the square root of B) with the Krylov multigrid preconditioned algorithms applied to either an original non preconditioned system $(\mathbf{K}_{BMGNP}^{-1})$ or to an original $\mathbf{B}^{1/2}$ preconditioned system $(\mathbf{K}_{BMGNP}^{-1})$. The refinement factor is equal to 3 both in space and time.
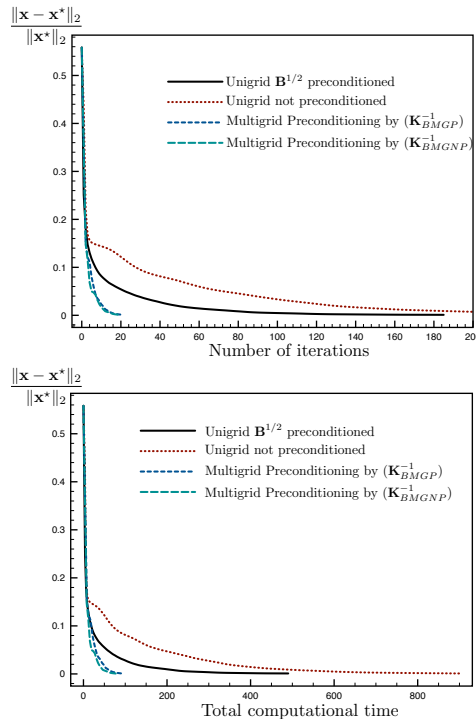
Figure 4.4: Refinement factor $\rho = 3$. Evolution of the error $\left(\dfrac{\|\mathbf{x} - \mathbf{x}^\star\|_2}{\|\mathbf{x}^\star\|_2}\right)$ as a function of the number of fine grid iterations (top) and of the total computational time in seconds (bottom) for $L_{\text{corr}}/\Delta x = 10$ and with three grid levels.

4.3.3   Comments and perspectives

- *On the improvement of the optimization:*
  In Debreu, Neveu, Simon, et al. 2015, the successive minimizations on the coarse grid

levels are done independently. There is thus a strong area of improvement than can potentially be achieved by learning from the preceding minimizations (e.g. Gratton, Sartenaer, and Tshimanga 2011).

- *On the non linear algorithms*:
  For nonlinear data assimilation problems (non linear model or non linear observation operators), the Full Approximation Scheme can be applied. Most of the time however, a line search algorithm has to be added to the coarse grid correction (Neveu 2011) and this has to be investigated. The use of a Full Multigrid algorithm, where the minimization starts at the coarsest level, helps to reduce the impact of the accuracy of the line search algorithm.
  It remains to study if the hybrid B-multigrid preconditioner can be used in the context of a nonlinear conjugate gradient algorithm (where the line search is done by the conjugate gradient itself). Other multilevel optimization algorithms could also be applied (e.g. Gratton, Malmedy, and Toint 2012) and compared.
  It is interesting to note than instead of being applied to the Euler equation 4.5, it is also possible to apply the Full Approximation Scheme to the complete optimality system. In the non-linear case, this naturally leads to correction terms in the coarse grid model equations. In addition, it enables a natural extension to local multigrid approaches where the coarse grid model equations are locally corrected by a defect between coarse and fine solutions. At the convergence of the iterative process, the global solution corresponds to the one of a two-way nesting algorithm: the coarse grid solution is the restriction of the fine grid solution (see Debreu, Neveu, Le Dimet, et al. 2014).

Chapter 5

The AGRIF software: Adaptive Grid Refinement In Fortran

AGRIF (Adaptive Grid Refinement In Fortran) is a local mesh refinement software which can be used in any model discretized on a structured mesh and written in Fortran. The software has now more than 15 years of existence and its development began during my PhD on adaptive mesh refinement. Its development has been financially supported by Inria, Mercator-Ocean, SHOM and IFREMER.

5.1 Main characteristics

The software is divided in two parts. A library composed of the main functions for grid hierarchy management (potentially adaptively) and for grid interactions The other part of the software deals with source to source code translation and allows an automatic extension of a unigrid grid code. This last part is using Fortran lexical and syntaxic analysis (implemented using the Flex and Yacc software packages). AGRIF is mainly designed for existing large codes. It is then used to minimize the required changes and to allow a simple integration of local mesh refinement features.
The library is composed of 16000 lines of Fortran 90 code and the source to source translator is composed of 17000 lines of Yacc, Flex and C code.
AGRIF deals with 1, 2 or 3D mesh refinement of structured (staggered or collocated) grids, allows static and/or dynamic grid refinement and is fully parallelized.

5.2 Similar software packages

The functionalities implemented in the model independent part (library) can be found in several other software packages. The most well known being SAMRAI (https ://computation-rnd.llnl.gov/SAMRAI/) and CHOMBO (http ://commons.lbl.gov/display/chombo). These are two C++ libraries that includes all the necessary functionalities for (adaptive) mesh refinement in 1, 2 or 3D.

This is mainly the code conversion part that brings to the AGRIF software its originality. The main advantage is that model developers do not have to worry about the computational complexities of mesh refinement. This is especially true for the very large numerical code like the atmosphere and ocean models for which a complete rewrite is not affordable. So

that at this time, the main targets of the AGRIF software are very large codes written in Fortran.

The Fortran library of AGRIF is also developed in a different way that the ones of SAMRAI and CHOMBO. These last two are indeed specialized for the solution of hyperbolic problems and are very performant in this case. For other kind of applications, they can however look too constraining. More generally I think that the AGRIF software allows a larger flexibility in the kind of grid interactions scheme that can be used. The AGRIF software also deals with mesh coarsening allowing to reduce the grid resolution for particular applications (e.g. advection of passive tracers at coarser resolution than the dynamical fields). Finally as the AGRIF library is used in several operational codes that are run on supercomputers, all the parts of library (in particular interpolation/restrictions procedures) have been highly optimized on scalar as well as vectorial architectures.

5.3   Current use of the AGRIF software

AGRIF is currently integrated in the following models:

- HYCOM (HYbrid Coordinate Ocean Model)

- NEMO (Nucleus for European Modelling of the Ocean)

- MARS3D (Model for Applications at Regional Scale)

- MESO-NH (Mesoscale non-hydrostatic model)

- ROMS (Regional Oceanic Modelling System)

- MSFF (MultiScale Flow in Fortran)

More than 200 publications relate the use of the AGRIF software. Three of them are illustrated on figure (5.3).

Contributions

I was originally the main developer of the software. I am still the manager of the software development and has supervised several engineers working on its development. I also contribute to expertise for private compagnies.

Comments and perspectives

- *Towards truly multiresolution ocean models*:
  There is still a lot of debate between unstructured and structured grid ocean modelling. Both approaches have drawbacks and advantages. From my point of view, the potential of structured mesh refinement is far from having fully exploited. Research on static mesh refinement was a first step necessary to get an understanding of the underlying problems. This work is now quite mature and going to truly multiresolution ocean models is the next step. This will require some developments in the AGRIF library, in particular in term of load balancing on parallel computers. This work is already funded by several projects.

Zoom sur le courant des Aiguilles, Biastoch et al, Nature, 2009
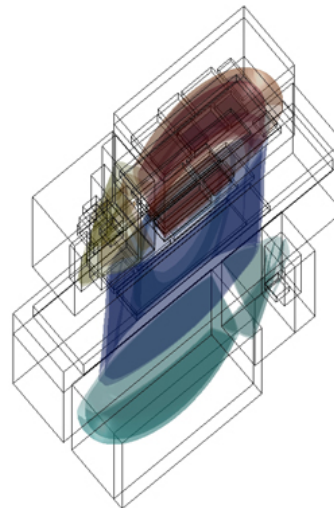
Dynamique d'un vortex, Ossmani et al, Mutiscale Model. Simul, 2010
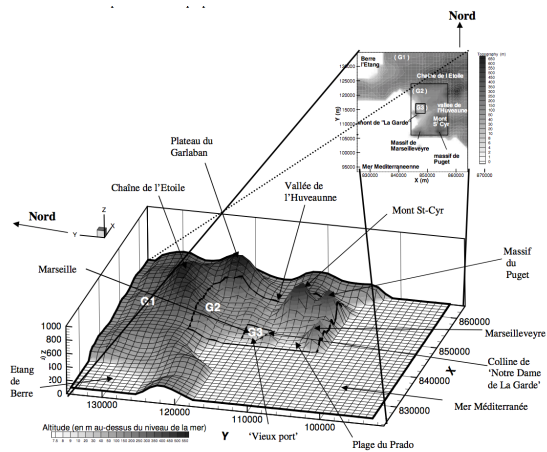
Simulation numérique de l'atmosphère urbaine, MESONH (MeteoFrance)

Part IV

Research project: Dissipation mechanisms, multiresolution/multiscale algorithms and optimisation methods, high performance computing

I first summarize the main comment and perspectives that have been drawn though this manuscript:

- *On the use of adaptive mesh refinement*:
  Our realistic adaptive mesh refinement applications were done at relatively coarse resolution (1/3°). At these non eddy permitting resolutions, the location of refinement areas is mainly dictated either by topographic features or by very strong currents (e.g. Gulf Stream). Thus the added value of grid adaptivity is small in comparison with static grid refinements. Today, oceanic simulations, in particular with regional models, are performed at much higher, eddy resolving, resolutions and there is a clear regain of interest for the application of adaptive mesh refinement.

- *On the combination of solutions at different resolutions*:
  Local mesh refinement for structured grids naturally leads to the computation of model solutions at different grid resolutions. In my past research, I did not explore how these solutions can be interpreted in term of subgrid scales parameterizations. Superparameterization is now an active area of research (e.g. Majda and Grooms 2014) and, based on my experience with local mesh refinement, I am now indeed interested in the design of multiscale turbulence models (Sagaut, Deck, and Terracol 2006).

- *On the link between mesh refinement methods and underlying discretisation schemes:*
  The behavior of mesh refinement methods is obviously related to grid interactions schemes. However, it is also strongly linked with internal underlying discretization schemes. For example, use of advanced grid interactions in a numerical model which does not properly take into account directions of information propagation will probably not be successful, trying to enforce conservation (using refluxing techniques) in a numerical model which uses a time stepping algorithm that cannot be written under flux form (e.g. LeapFrog with Asselin filter) is also useless. This strong link between local mesh refinement (or more generally boundary conditions) and internal numerical schemes was the first reason for me to be interested in numerical methods.

- *On the cost of the Schwarz algorithm:*
  The obvious problem is the cost related to this Schwarz iterative algorithm. An open question is if simplified/reduced models can be used to perform the first iterations of the algorithm.
  The cost of the Schwarz algorithm can also be alleviated if used in conjunction with another iterative method. This is typically the case when variational data assimilation methods, leading to the minimization of an objective function, are applied.
  Joint use of global in time Schwarz algorithms and parallel in time algorithms (i.e. parareal) is also an interesting subject for high performance computing on next generation platforms.

- *Schwarz methods and boundary layer parameterisations:*
  The realistic experiments presented in paragraph (2.3.2) have been done with non optimised boundary conditions due to the complexity (and potentially non differentiability) of the boundary layer parameterizations (bulk formulae). Looking at the formulation of these parameterisations in term of the convergence of the Schwarz algorithm is a question addressed in the PhD of Charles Emmanuel Pelletier (supervised by Eric Blayo and Florian Lemarié).

- *On the monotony of the rotated operators:*
  The linear rotated diffusion operators are not monotonic. The derivation of monotonic diffusion operators is possible (see Beckers, Burchard, Deleersnijder, et al. 2000) but it relies on rather complex and costly schemes. One can imagine that the monotony of the full scheme (i.e. diffusion plus advection) can be maintained using approaches like flux corrected transport (FCT) schemes. However, it will push the problem on the control of the orientation of diffusion in non linear schemes like FCT (or any other extrema preserving scheme).
  This point shows that, even if the rotation of diffusion tensors has enable strong improvements in realistic simulations, the choice of the vertical coordinate system remains the key point.

- *On the regularity of velocity fields:*
  Spurious diapycnal diffusion is also strongly linked with the regularity of the velocity fields. This has been clearly illustrated in Illicak et al. 2012 where experiments at different Reynolds numbers are produced. Therefore it is an open question if the current ocean models have enough dissipation mechanisms in processes affecting the velocity fields. In particular, monotonic momentum advection schemes are rarely used and internal gravity waves resulting from the coupling between velocity and density are usually discretized with basic, strongly dispersive, schemes.

- *On the numerical discretization of internal waves*:
  High order discretization of the horizontal pressure gradient and the horizontal divergence may lead to less dispersive discretizations. To our knowledge, none ocean models are using high order discretization of the horizontal divergence and so it has to be experimented. Note that in non hydrostatic simulations, it would however lead to the solution of a Poisson system with a large stencil matrix. It can however be overcome using a pseudo-compressible approach which precludes the use of the solution of a Poisson system. The derivation of the discrete Sturm-Liouville problem allows the study the impact of vertical grid staggering and vertical discretizations. Done here in the case of a z coordinate model, it would be interesting to extend this study to other vertical coordinate systems.

- *On internal waves and dissipation mechanisms*:
  Fourth order horizontal discretization, as described below, allow to achieve relatively low dispersion error (on a Arakawa C grid). However vertical discretization introduces itself large dispersion error. It is always true for the Lorenz grid, with an inherent computational mode, but it is also true for the Charney-Phillips grid with variable Brunt-Vaisala frequency or variable vertical grid step. It is thus important to study how to dissipate the associated small scales without using two large diffusion coefficients (e.g. in a Lax Friedrichs approach). In realistic simulations, one may hope to be able to get an estimate of the internal wave propagation speeds along with an estimate of vertical eigenmodes which allows to put a a more selective diffusion term. Potential diffusion through the time stepping algorithm has obviously also to be studied.

- *On the multigrid background error covariance matrix:*
  When using a correlation operator based on a diffusion operator, a fully two-grid B covariance matrix can also be obtained by applying the laplacian diffusion in a two-grid

context (i.e. with coarse-fine grid interactions at the level of each step of the diffusion operator). Preliminary experiments in the 3DVAR version of the NEMO ocean model support the superiority of this approach.

- *On the improvement of the optimization*:
  In Debreu, Neveu, Simon, et al. 2015, the successive minimizations on the coarse grid levels are done independently. There is thus a strong area of improvement than can potentially be achieved by learning from the preceding minimizations (e.g. Gratton, Sartenaer, and Tshimanga 2011).

- *On the non linear algorithms*:
  For non linear data assimilation problems (non linear model or non linear observation operators), the Full Approximation Scheme can be applied. Most of the time however, a line search algorithm has to be added to the coarse grid correction (Neveu 2011) and this has to be investigated. The use of a Full Multigrid algorithm, where the minimization starts at the coarsest level, helps to reduce the impact of the accuracy of the line search algorithm. It remains to study if the hybrid B-multigrid preconditioner can be used in the context of a nonlinear conjugate gradient algorithm (where the line search is done by the conjugate gradient itself). Other multilevel optimization algorithms could also be applied (e.g. Gratton, Malmedy, and Toint 2012) and compared.
  It is also interesting to note than instead of being applied to the Euler equation 4.5, it is also possible to apply the Full Approximation Scheme to the complete optimality system. In the non-linear case, this naturally leads to correction terms in the coarse grid model equations. It also allows a natural extension to local multigrid approaches where the coarse grid model equations are locally corrected by a defect between coarse and fine solutions. At the convergence of the iterative process, the global solution corresponds to the one of a two-way nesting algorithm: the coarse grid solution is the restriction of the fine grid solution (see Debreu, Neveu, Le Dimet, et al. 2014).

- *Towards truly multiresolution ocean models*:
  There is still a lot of debate between unstructured and structured grid ocean modelling. Both approaches have drawbacks and advantages. From my point of view, the potential of structured mesh refinement is far from having fully exploited. Research on static mesh refinement was a first step necessary to get an understanding of the underlying problems. This work is now quite mature and going to truly multiresolution ocean models is the next step. This will require some developments in the AGRIF library, in particular in term of load balancing on parallel computers. This work is already funded by several projects.

In the light of these perspectives, I would like to conduct a research project based on three main axes: *physical and numerical dissipation mechanisms, multiresolution/multiscale algorithms and optimisation methods, high performance computing.*

Dissipation mechanisms, multiresolution/multiscale algorithms and optimisation methods, high performance computing

Physical and numerical dissipation mechanisms

The mathematical/numerical analysis of the continuous/discrete systems, even difficult to perform, should probably be more often investigated. This is a special concern for the regularity of the continuous and discrete solutions according to the physical and/or numerical dissipation mechanisms (Rebollo and Lewandowski 2014). This can be done for the derivation of subgrid-scale models, as an example for vertical mixing schemes (e.g. Deleersnijder, Hanert, et al. 2008; Bennis et al. 2008). Internal waves propagation is also one of the most relevant questions. Parameterisation of their nonlinear interactions is obviously an important matter. Work done on the regularity of shallow water solutions (on a staggered C grid and without Riemann solvers) (e.g. Doyen and Gunawan 2014)) is also a way to look at the problem in the spirit of (monotone) implicit large eddy simulation (ILES) and monotone integrated large eddy simulation (MILES) methods. It would be interesting to see if it can be extended to internal waves.

Lowering the dispersion error, while maintaining an acceptable (or a minimum) level of dissipation should be an objective. It remains to see if (M)ILES can be applied to ocean/atmosphere modelling without damaging important physical properties through their implicit diffusion.

Multiresolution/multiscale algorithms and optimisation methods

Multiresolution methods allows to gain in efficiency (accuracy / computational cost) by lowering the impact of subgrid-scale models and/or truncation errors. They can also be used to derive multiresolution subgrid-scale models that take benefit of the solutions at different grid resolutions (Sagaut, Deck, and Terracol 2006).

Parameters estimation (for example to calibrate a subgrid-scale model) can be difficult to applied without a multiresolution approach due to the large dimensionality of the problem. Decomposing the scales of control parameters according to the grid resolutions leads to multiscale optimisation methods.

Finally, multilevel techniques can also help to solve highly non linear optimisation problems. The underlying idea is here to start from a coarse resolution grid where the optimisation problem is smoother and then to progressively increase the model resolution. This however requires a good consistency between subgrid-scale models at the different grid resolutions and the Full Approximation Scheme may be the right mathematical tool to maintain such consistency.

High performance computing

An efficient use of the new and future computers architecture necessary require a rethinking of traditional numerical algorithms. The search for an increase degree of parallelism will probably rely on the parallelisation of the temporal dimension. Use of iterative algorithms like parareal (Lions, Maday, and Turinici 2001) and their joint use with global in time domain decomposition (Schwarz waveform relaxation method) is a potential key of success.

Numerous works are currently done for the application of these techniques on hyperbolic systems with different variants of the parareal scheme (PFASST, PITA ...). In the field of geophysical fluids, work has also begun on shallow water equations (Haut and Wingate 2014).

Parallel in time methods can then be used both for the integration of the direct model but also combined with other iterative algorithms like optimal control techniques (Maday, Riahi, and Salomon 2013).

Context

I am the coordinator of the COMODO project, funded by the French National Research Agency (ANR), a project which brings together the whole French community in ocean modelling. Besides its scope on research on numerical methods for ocean models, over the years, the project has lead to more collaborations among ocean modellers but also between ocean modellers and applied mathematicians. This project will end in 2016 and the hope is that the scientific animation part of the project will be sustainably funded.

From its beginning in 2011, one of the objective of the COMODO project is also to build a suite of idealised benchmarks for numerical ocean models. In addition to model evaluation, this suite greatly contributes to the increase of the number of applied mathematicians that contributes to the improvements to numerical ocean models. This is an essential tool, currently maintained by the French community and we are now trying to promote this tool at the international level. Similar projects exist in atmospheric modelling (Dynamical Core Model Intercomparison Project, (DCMIP)) and in data assimilation (SANGOMA).

This research project will be done in the context of the AIRSEA Inria and Jean Kuntzmann laboratory team, a research team in applied mathematics for oceanic and atmospheric flows. The team has four main research axes: advanced numerical methods for oceanic and atmospheric models, dealing with uncertainties, model reduction and high performance computing. The research project of the team has a strong focus on the study of subgrid-scale modelling using either deterministic and statistical approaches.

Part V

Tirés à part

The first paper entitled "Two-way nesting in split-explicit ocean models: Algorithms, implementation and validation" details the grid interactions implemented in the ROMS-AGRIF model. It deals with restriction operators, conservation via refluxing schemes and coupling at the fast (barotropic) level.

The second paper "On the stability and accuracy of the harmonic and biharmonic isoneutral mixing operators in ocean models" describes temporal and spatial discretisations of second and fourth order rotated diffusion operators. The main result is the derivation of a spatial and temporal discretisation of a fourth order rotated operator that allows to maintain the same stability condition as the non rotated operator.

In the third paper "Multigrid solvers and multigrid preconditioners for the solution of variational data assimilation problems", we investigate the use of multigrid methods for the solution of data assimilation problems. Smoothing and approximation properties are studied. Lack of robustness of the multigrid solver is explained and illustrated and an hybrid preconditioner is proposed.

Chapter 6

Two-way nesting in split-explicit ocean models: Algorithms, implementation and validation, *Ocean Modelling (2012)*
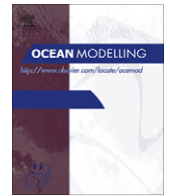
Two-way nesting in split-explicit ocean models: Algorithms, implementation and validation

Laurent Debreu [a,*], Patrick Marchesiello [b], Pierrick Penven [c,d], Gildas Cambon [b]

[a] INRIA, MOISE Project-Team and Laboratoire Jean Kuntzmann, 51 rue des Mathématiques, 38400 Saint Martin d'Hères, France
[b] LEGOS (UMR 5566: CNES, CNRS, IRD, UPS), Toulouse, France
[c] LPO (UMR 6523: CNRS, IFREMER, IRD, UBO), Plouzané, France
[d] LMI ICEMASA, Department of Oceanography, University of Cape Town, Rondebosch, South Africa

ARTICLE INFO

ABSTRACT

A full two-way nesting approach for split-explicit, free surface ocean models is presented. It is novel in three main respects: the treatment of grid refinement at the fast mode (barotropic) level; the use of scale selective update schemes; the conservation of both volume and tracer contents via refluxing. An idealized application to vortex propagation on a β plane shows agreement between nested and high resolution solutions. A realistic application to the California Current System then confirm these results in a complex configuration. The selected algorithm is now part of ROMS_AGRIF. It is fully consistent with ROMS parallel capabilities on both shared and distributed memory architectures. The nesting implementation authorizes several nesting levels and several grids at any particular level. This operational capability, combined with the inner qualities of our two-way nesting algorithm and generally high-order accuracy of ROMS numerics, allow for realistic simulation of coastal and ocean dynamics at multiple, interacting scales.

© 2012 Elsevier Ltd. All rights reserved.

1. Introduction

Despite a tremendous increase in available computing power, the computational cost of numerical ocean models remains challenging, especially as submesoscale dynamics are now being investigated. The use of high spatial and temporal resolutions reduces local truncation errors of discrete numerical schemes and allows for a better representation of small dynamical scales and topographic features. Mesh refinement allows access to higher resolution in areas of interest at a limited computational cost. This paper focuses on improvement to existing mesh refinement methods for structured meshes.

The unstructured grid approach provides a natural solution for mesh refinement owing to its straightforward refinement process, assuming that an efficient meshing tool is available. A new development phase of unstructured grid models has emerged in recent years with several improvements regarding long-standing issues: preservation of geostrophic balance (Maddison et al., 2011); and local/global conservation properties (Hanert et al., 2004; Levin et al., 2006). The reader is referred to Ham et al. (2009), Deleersnijder et al. (2010), and Sidorenko et al. (2011) for an overview of recent achievements. However, the additional numerical cost of unstructured grid modeling and the ratio of computational cost

over accuracy remains to be objectively evaluated and compared to the traditional structured grid approach. In addition, an important challenge for unstructured mesh models is the implementation of local time-stepping algorithms with better numerical properties. To our knowledge, no real progress on this issue has been reported, at least regarding ocean modeling. We expect that our treatment of time refinement in the present study will be profitable to both structured and unstructured grid methods.

Nesting (or embedding) techniques for structured meshes generally consists of a local high resolution grid (HR or child grid) embedded in a coarse resolution grid (CR or parent grid) that provides the boundary conditions. If this is the only transfer of information between the two grids, the model is said to be in *one-way interaction*. If there is also a transfer of information from the child back to the parent grid (update), the model is in *two-way interaction*. The development of two-way methods have been favored by ocean modelers as they present, in principle, a more continuous interfacial behavior. The various two-way interaction schemes mainly differ by the type of interpolation, location of dynamical interface (the grid points where update is set to occur), conservation properties and type of update (full update or weaker interaction). A recent review of two-way embedding algorithms can be found in Debreu and Blayo (2008), along with recent applications focusing on upscaling impact (Biastoch et al., 2008); fine-scale dynamics (Marchesiello et al., 2011); and topographic refinement (Sannino et al., 2009). The definition of grid refinement in the

* Corresponding author. Tel.: +33 4 76 51 48 60; fax: +33 4 76 63 12 63.
   E-mail address: Laurent.Debreu@imag.fr (L. Debreu).

embedding approach generally requires coarse and fine grids to fully overlap. In case of complex geometry (i.e., with rivers and estuaries), this can be a drawback since the coarse grid domain may have to be unnecessarily large. In this case, a more powerful alternative is the composite grid formulation where grids only overlap in connecting areas (Warner et al., 2010). This formulation is not explicitly addressed here but our treatment of mesh refinement is relevant to both embedded and composite grid methods.

In this paper, we present and evaluate a set of choices made in an implementation of two-way nesting methods allowing simultaneous spatial and temporal refinement in a split-explicit, free surface ocean model. In split-explicit time-stepping, fast barotropic quantities are integrated forward in time at a smaller time step than required by the 3D equations. One important question is: how can parent and child grids be coupled at the barotropic level? To our knowledge, this question has not been raised in the literature; reported methods propose that coupling be done at the baroclinic level or that time refinement be avoided altogether (which considerably simplifies the problem). This point is discussed in Section 2.2 after a brief reminder of grid nesting basics (Section 2.1). Section 2.3 focuses on update schemes. In the past, interpolation schemes have received much more attention than update schemes, which often consist of a simple area-weighted average operator chosen for its conservation properties. Here, we propose a scale selective approach to construct the update operator. The respect of conservation properties is another important issue for long term integration. Here, conservation is achieved by flux correction, a classic approach in adaptive mesh refinement for structured grids (Berger and Oliger, 1984; Berger and Colella, 1989). This is presented in Section 2.4 along with its impact on stability and error properties of the resulting scheme. The different methods are evaluated in the idealized case of a baroclinic vortex propagating on a β plane (Section 3). A realistic application to the California Current System is also presented; its results are discussed in light of theoretical arguments and idealized experiments.

2. Two-way nesting algorithms

2.1. General algorithm

For a general review of two-way nesting algorithms, the reader is referred to Debreu and Blayo (2008). Here, the basic algorithm is briefly described while improvements for various parts of the problem are proposed in the following sections. For simplicity, we consider a single child grid covering a subdomain ω of the parent domain Ω, as illustrated in Fig. 1. The boundary of the child grid is delimited by the interface Γ.

The coarse resolution grid has a mesh size given by Δx_H, while the fine resolution grid has a mesh size $\Delta x_h = \Delta x_H / \rho$ where ρ is the spatial mesh refinement ratio (an integer). The partial differential equations solved by the model are written in the following form:

$$\frac{\partial q}{\partial t} = L(q)$$

along with an initial condition and lateral boundary conditions at the limits of Ω. These equations are discretized on the coarse and fine grid domains by:

$$\frac{\partial q_H}{\partial t} = L_H(q_H), \quad \frac{\partial q_h}{\partial t} = L_h(q_h) \tag{1}$$

Thus L_H and L_h are discretizations of the same continuous operator L at different resolutions.[1] The child grid needs lateral boundary con-
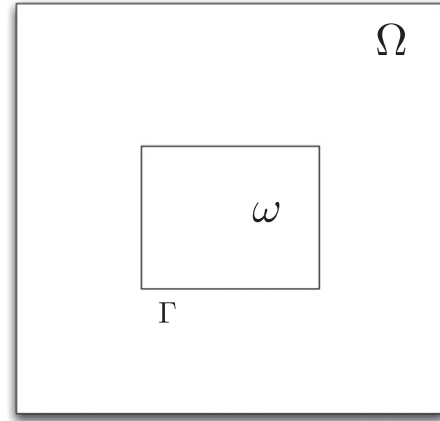
---

[1] Note that, in principle, a different choice of numerical schemes and parameterizations may be adopted in the refined grid. However, this would complicate the issue of interface continuity already posed by grid refinement itself.

Fig. 1. Local refinement. Ω is the domain covered by the coarse resolution grid while ω is covered by the high resolution grid. Γ is the boundary of the high resolution domain ω.

ditions at the interface Γ and, in two-way mode, the coarse solution is updated using the fine solution. This is modeled by two different operators: an interpolator (P) and a restriction operator (R). In practice, adequate choices of P and R depend on the operator L and the numerical schemes used for its discretizations L_H and L_h. One useful constraint is that these choices do not affect the model solution if the refinement coefficient is 1 (i.e., in this special case: $L_h = L_H$ and q_H takes exactly the same values whether nesting is used or not). This constraint ensures consistency of methodology; we thus checked that it is satisfied in all developments presented in the following, i.e., barotropic/baroclinic coupling Section 2.2, conservation Section 2.4, sponge layers Section 2.5.

Assuming that the model is fully explicit, the algorithm can be written in the following simplified form:

1. $q_H^{n+1} = L_H(q_H^n)$
2. For $m = 1 \ldots \rho_t$ do

$$q_h^{n+\frac{m}{\rho_t}} = L_h\left(q_h^{n+\frac{(m-1)}{\rho_t}}\right)$$

$$q_h^{n+\frac{m}{\rho_t}}\Big|_\Gamma = P(q_H^n, q_H^{n+1})$$

3. $q_H^{n+1}\big|_\omega = R(q_h^{n+1})$

Here, ρ_t is the time refinement factor $\left(\rho_t = \frac{\Delta t_H}{\Delta t_h}\right)$ and equals the space refinement factor ρ if the model is restricted to a CFL (Courant Friedrichs Levy) stability condition. Step (1) corresponds to the integration of the coarse grid model for one time step Δt_H on Ω, while step (2) corresponds to the integration of the fine grid model for ρ_t time steps. The interpolator P makes use of q_H^n and q_H^{n+1} to produce space and time interpolations on the interface Γ. In attempting to apply this algorithm to realistic ocean models, several key issues are raised. When the time evolution of state variables is decomposed into two parts (barotropic and baroclinic), the management of grid interaction becomes complex. This is the subject of the next section.

2.2. Coupling at the barotropic level

The most restrictive constraint on the time step of a primitive equations ocean model is dictated by the speed of external gravity waves. Several methods could be applied to filter out the fast mode associated with external gravity waves, thus relaxing this constraint. A first choice is to completely remove these waves by applying a rigid lid approximation (Bryan, 1969), leading to the

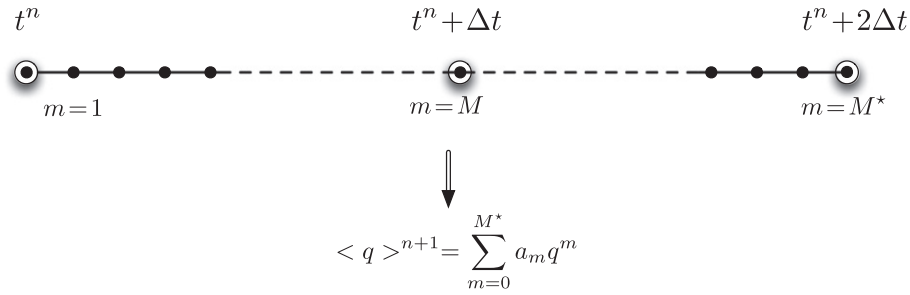$$< q >^{n+1} = \sum_{m=0}^{M^\star} a_m q^m$$

Fig. 2. Time filtering for a uniformly weighted filter $\left(a_m = \frac{1}{M^\star+1}\right)$.

resolution of a barotropic vorticity equation. An alternative approach is an implicit time-stepping method that filters external gravity waves, thereby allowing integration of the free surface equations at the slow mode time step (Dukowicz and Smith, 1994). For such models, the treatment of the fast mode in nested grids has already been tackled in the literature. Laugier et al. (1996) applied local defect correction methods for a rigid lid ocean model, while more recently Haley and Lermusiaux (2010) introduced strongly coupled embedding schemes for free-surface, split-implicit ocean models.

Another widely used method is the split-explicit time integration method of Blumberg and Mellor (1987) and Killworth et al. (1991). In this case, the barotropic time step is a ratio of the baroclinic time step and the barotropic mode is integrated separately. A reported advantage of the split-explicit method is that there is no need to solve a computationally expensive (at high resolution) elliptic system, as opposed to the rigid lid and implicit methods (Killworth et al., 1991). Perharps more importantly, on numerical grounds, split-explicit methods also provide a better representation of Rossby waves speed than implicit methods that produce large dispersion error. Therefore, new generation oceanic models have generally adopted the split-explicit method, even though it comes with additional complexity at an algorithmic level. Our study proposes solutions to circumvent the difficulties associated with the increased complexity of time splitting in the case of grid nesting.

An important aspect of the split-explicit method is that once the barotropic mode has been integrated, a filtering pass is required in order to remove scales not resolved by the 3D solution (see Shchepetkin and McWilliams, 2005, for a review of these filters), although this may be avoided if the 2D time stepping algorithm is dissipative enough. In order to compute a filtered value of fast quantities (barotropic velocities and free surface) at time $t_{n+1} = t_n + \Delta t$, where Δt is the 3D time step increment, the period of integration has to exceed time t_{n+1}. In the case of grid nesting, this leads to several difficulties that are described in the next paragraph. It should be noted that most existing nesting methods avoid these difficulties by coupling parent and child grids at the baroclinic level only. However, this simpler approach does not provide some of the desired properties of a full coupling between the grids. In particular, it violates the previously mentioned constraint that the model solution be unaffected by nesting in case where the refinement coefficient is one.

2.2.1. Problem definition

Let M be the ratio of the baroclinic and barotropic time steps ($\Delta t' = \frac{\Delta t}{M}$) and $M^\star$ be the number of time steps done in the barotropic mode. $M^\star$ is dependent on the time filter applied for the fast mode. As an example, Fig. 2 presents a uniformly weighted filter over time interval $[t^n, t^n + 2\Delta t]$ (in this case $M^\star = 2M$).

The filtered variables are computed using the following formula:

$$< q>^{n+1} = \sum_{m=1}^{M^\star} a_m q^m \qquad (2)$$

where q^m denotes an instantaneous barotropic variable (free surface or vertically integrated transport) and where it is required that the weights a_m be normalized and that the result of (2) be centered at time $t_n + \Delta t$, which is equivalent to

$$\sum_{m=0}^{M^\star} a_m = 1, \quad \sum_{m=0}^{M^\star} a_m m = M$$

Let us now consider the time integration of the embedded model assuming a time refinement factor of 2. Fig. 3 represents the successive steps of time refinement at the baroclinic level while Fig. 4 details the barotropic integration.

From Fig. 4, it appears that the interaction scheme between barotropic quantities at coarse and high resolution can not simply be based on instantaneous values. The coarse grid values are computed at a time ($t_n + 2\Delta t$) greater than their high resolution equivalent ($t_n + 3\Delta t/2$), making it impossible to update the parent from the child grid values. To solve this problem, we propose a method based on interactions between *intermediate* averaged values of fast quantities.

2.2.2. Coupling between filtered variables

Let us define the intermediate filtered variables at the barotropic time step α by the following expression

$$< q>_\alpha = \sum_{m=0}^{\alpha} a_{m,\alpha} q^m, \quad 0 \leqslant \alpha \leqslant M^\star \qquad (3)$$

where $a_{m,\alpha}$ are a new family of weights and where $< q >_\alpha$ is required to be centered at time $t^n + \frac{\alpha}{M^\star}\Delta t \in [t^n; t^n + \Delta t]$. It is now possible to exchange all required information between parent and child grid solutions through these new variables. During the first child grid time step (step 2 in Fig. 5), the connection between parent
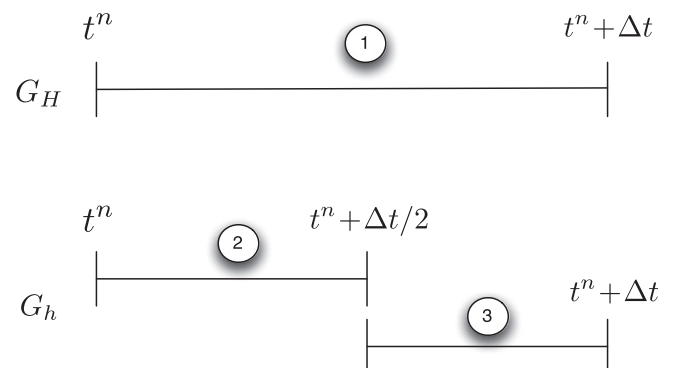
Fig. 3. Time integration at the baroclinic level. Top: parent grid. Bottom: child grid.
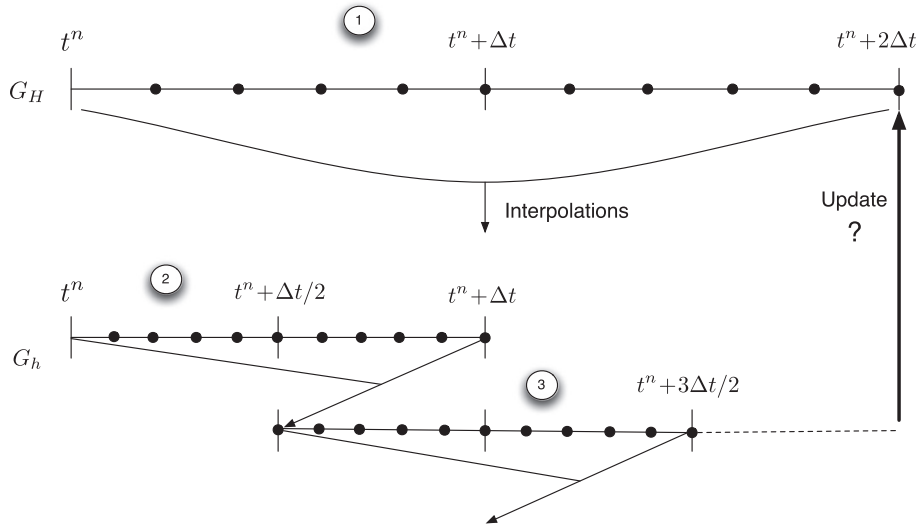
Fig. 4. Time integration at the barotropic level. The figure represents the position in time of the instantaneous barotropic quantities. The barotropic subcycles are restarted from the previously computed filtered values. Top: parent grid. Bottom: child grid.

and child grid variables, q_H and q_h, is done through the requirement that

$$<q_h>_\alpha =<q_H>_{\alpha/\rho_t} \iff \sum_{m=0}^{\alpha} a_{m,\alpha}q_h^m = \sum_{m=0}^{\alpha/\rho_t} a_{m,\alpha/\rho_t}q_H^m \qquad (4)$$

α is assumed here to be a multiple of ρ_t but linear interpolation in time is applied when this is not the case. Eq. (4) is consistent since $<q_h>_\alpha$ is centered at time $t^n + \frac{\alpha}{M^\star}\Delta t_h$ while $<q_H>_{\alpha/\rho_t}$ is centered at time $t^n + \frac{\alpha/\rho_t}{M^\star}\Delta t_H = t^n + \frac{\alpha}{M^\star}\Delta t_h$. In step 3 of Fig. 5, this equation is modified to give:

$$<q_h>_\alpha =<q_H>_{M^\star/\rho_t+\alpha/\rho_t} \qquad (5)$$

From (4) (or from (5)), we deduce the value of the fine grid variables as a function of the coarse grid variables:

$$q_h^\alpha = \frac{1}{a_{\alpha,\alpha}} \left(\sum_{m=0}^{\alpha/\rho_t} a_{m,\alpha/\rho_t}q_H^m - \sum_{m=0}^{\alpha-1} a_{m,\alpha}q_h^m \right) \qquad (6)$$

and a similar (reversed) relation is used in the update step. Additionally, we require that the definition of $<q>_\alpha$ is continuous over the barotropic fine grid steps. Since in step 3, the instantaneous variables are restarted (see Fig. 2) from a previous average value

equal to $<q>^{n+1}$, we have to enforce $<q>_{M^\star} =<q>^{n+1}$ which is equivalent to

$$a_{m,M^\star} = a_m$$

Given $a_m, 0 \leqslant m \leqslant M^\star$, the weights of the original time filter, we finally obtain that the coefficients $a_{m,\alpha}$ of the intermediate filters should satisfy the following relations

$$\begin{cases} \sum_{m=0}^{\alpha} a_{m,\alpha} = 1, & \sum_{m=0}^{\alpha} a_{m,\alpha}m = \frac{\alpha}{M^\star}M, \quad \forall\, 0 \leqslant \alpha \leqslant M^\star \\ a_{m,M^\star} = a_m, & 0 \leqslant m \leqslant M^\star \end{cases} \qquad (7)$$

The way these coefficients are computed in practice is described in the appendix. Fig. 6 shows intermediate weights at barotropic time steps $M^\star/4$, $M^\star/2$ and $M^\star$, for several typical filters. Here M is taken to be 48 and the different filters are: (a) flat weights over [0:2M], (b) flat weights over [M/2:3M/2], (c) cosine shape filter and (d) power law shape filter (see Shchepetkin and McWilliams, 2005).

2.2.3. Computational advantage

Improvement of the physical solution expected by the treatment of nesting at the barotropic level is paid for by added algorithmic complexity. Nevertheless, it also has a computational
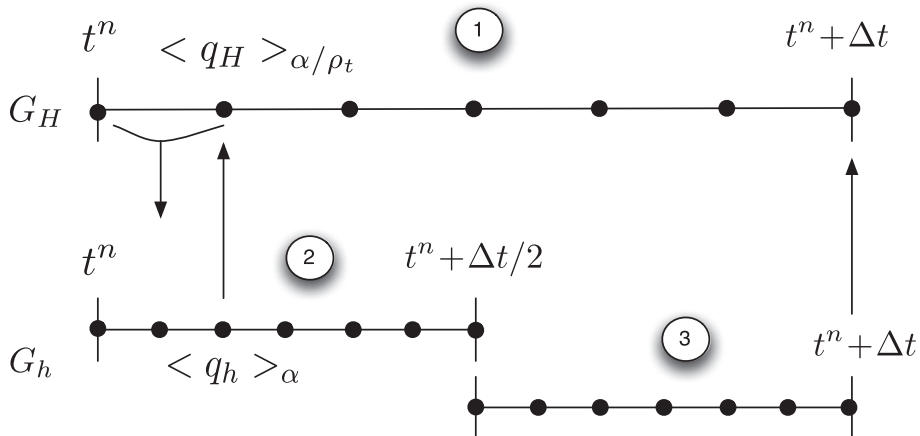

Fig. 5. Time integration at the barotropic level. The figure represents the position in time of the intermediate filtered barotropic quantities. Top: parent grid. Bottom: child grid.
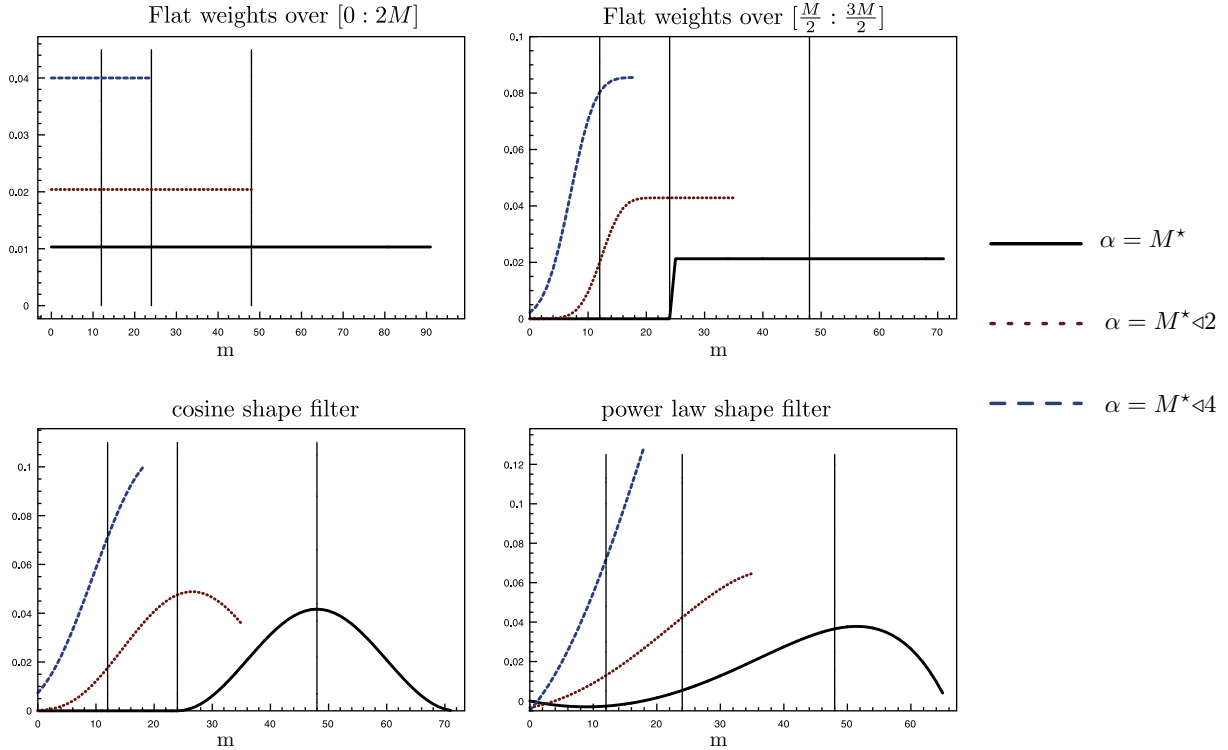
Flat weights over $[0:2M]$

Flat weights over $[\frac{M}{2}:\frac{3M}{2}]$

$\alpha = M^{\star}$

$\alpha = M^{\star} \triangleleft 2$

$\alpha = M^{\star} \triangleleft 4$

cosine shape filter

power law shape filter

Fig. 6. The intermediate weights $a_{m,\alpha}$ for barotropic time step $\alpha = M^{\star}/4$, $\alpha = M^{\star}/2$, $\alpha = M^{\star}$ and for different filtering algorithms. $M = 48$. The vertical lines indicate the desired average values. Flat weights over [0:2 M] (top left), flat weights over [M/2:3 M/2] (top right), cosine shape filter (bottom left) and power law shape filter (bottom right).

advantage. Nested grids only interact within an interface area whose size is given by the coarse grid operators stencil. The coarse grid solution in the fine grid domain affects neither the fine grid solution nor the coarse grid solution outside the fine grid domain. Therefore, the restriction steps of two-way nesting algorithms need only be applied for coarse grid points located in this interface area. On distributed-memory parallel computers, this significantly reduces the amount of data that needs to be exchanged and the computational gain can be important.

2.3. Update schemes

This section is devoted to the study of update (or restriction) operators. For reasons explained in Section 2.4, we do not limit ourselves to what is sometimes referred to as conservative update schemes, i.e. area-weighted averages of the fine grid values. The general design of an update operator should be based on the following two criteria:

- Transfer maximum information to the coarse grid for well-resolved scales on this grid
- Filter scales not resolved on the coarse grid

We study three different update schemes in light of their Fourier symbols: Average; Shapiro Filter; and Full-Weighting. We present these schemes in the one-dimensional case for a mesh refinement ratio of 3; the index i refers to the index of the child grid point that coincides with the parent grid point:

- Average: The restriction operator is given by

$$\frac{1}{3}(u_{i-1} + u_i + u_{i+1})$$

with Fourier symbol : $A(\theta) = \frac{1}{3}(1 + 2\cos\theta)$

where $\theta = k\Delta x \in [0:\pi]$, k being the wavenumber.

- Shapiro filter: The restriction operator is given by

$$\frac{1}{4}(u_{i-1} + 2u_i + u_{i+1})$$

with Fourier symbol : $A(\theta) = \frac{1}{2}(1 + \cos\theta)$

- Full-Weighting operator: The restriction operator is given by

$$\frac{1}{9}(u_{i-2} + 2u_{i-1} + 3u_i + 2u_{i+1} + u_{i+2})$$

with Fourier symbol : $A(\theta) = \frac{1}{9}(3 + 4\cos\theta + 2\cos 2\theta)$

The derivation of the full-weighting operator is linked to the definition of so-called first and second orders of a restriction operator as defined by Hemker (2001) in the context of multigrid methods and briefly summarized here:

- A discrete restriction operator with Fourier symbol $A(\theta)$ is of first order (or low frequency order) m if m is the largest integer such that

$$A(\theta) = 1 + O(|\theta|^m), \quad \text{for } |\theta| \to 0$$

- A discrete restriction operator with Fourier symbol $A(\theta)$ is of second order (or high frequency order) m if m is the largest integer such that

$$A(\theta + 2\pi p/\rho) = O(|\theta|^m), \quad \text{for } |\theta| \to 0, \quad \forall p \in]0, \rho[$$

Using these definitions, high order restriction operators can be built for other mesh refinement ratios. It can be shown that the full-weighting operator is second order accurate both at low and high frequencies $(A(\theta) = 1 + O(|\theta|^2)$ and $A(\theta + 2\pi/3) = O(|\theta|^2))$, that the average operator is of first order 2 and second order 1 and that
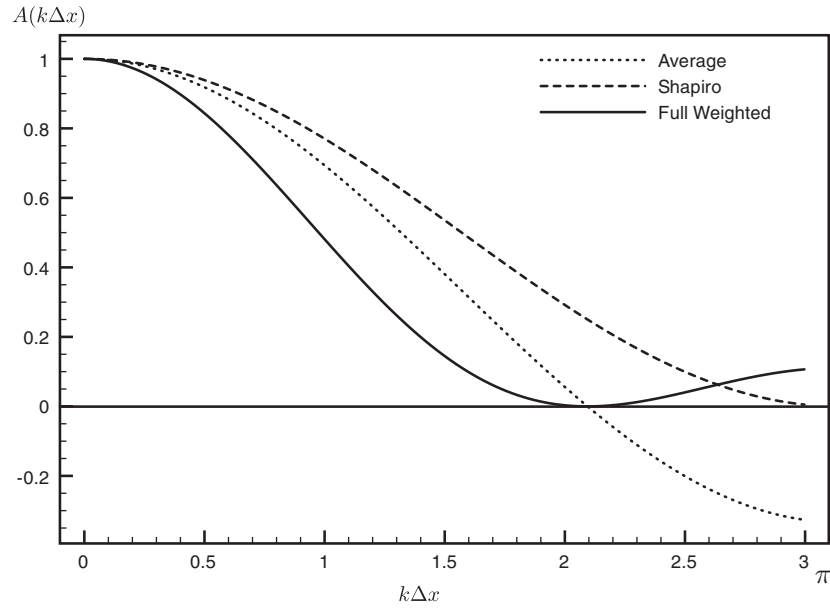
Fig. 7. Amplification factor for typical restriction operators (and for a mesh refinement factor of 3).
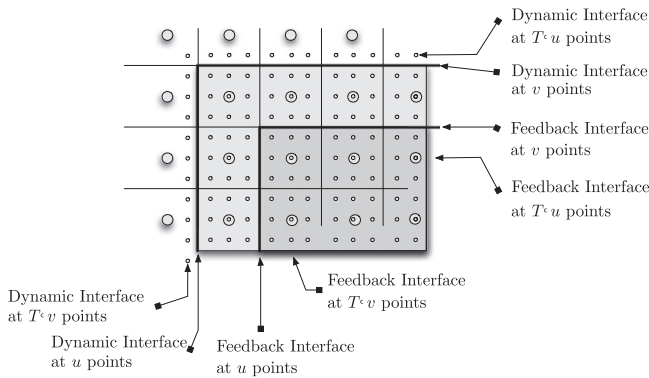

Fig. 8. Separation of dynamic and feedback interfaces on a Arakawa *C*-grid for a mesh refinement factor of 3. Update occurs in the dark grey area; without interface separation, tracer values and tangential velocities would also be updated in the light grey area.

the Shapiro filter is of first order 2 and second order 0. The symbols are all real, so that there is no dispersion error. The curves of the amplification factors are represented in Fig. 7. What is clearly visible, and will be emphasized by the numerical experiments, is that usual restriction operators apart from the the full-weighting operator are not designed to properly damp subgrid scale features. In practice, this defect has to be corrected by artificially increasing diffusion near the parent/child interface (sponge layers).

2.3.1. Separation of dynamic and feedback interfaces

The so-called dynamic and feedback interfaces are sketched in Fig. 8. The dynamic interface denotes the fine grid boundary where the fine solution is forced by the coarse solution; the feedback interface is the outer limit of the area where the coarse solution is updated by the fine solution. There are several reasons for separating dynamic and feedback interfaces (see Debreu and Blayo, 2008) that will be evaluated in the following idealized experiments. One reason comes from the evidence that if noise is produced it will concentrate near the dynamic interface and thus those interface values should not be used to update the parent grid.

2.3.2. Free surface, tracer and velocity updates

In a free surface ocean model, for conservation reasons, the discrete time evolution of the free surface elevation can be written in terms of the divergence of a barotropic transport (volumetric fluxes):

$$\eta_{i,j}^{n+1} = \eta_{i,j}^{n} - \frac{\Delta t}{\Delta x \Delta y}\left[U_{i+\frac{1}{2}j} - U_{i-\frac{1}{2}j} + V_{i,j+\frac{1}{2}} - V_{i,j-\frac{1}{2}}\right] \tag{8}$$

where η is the free surface elevation, U and V are barotropic transports in the x and y directions and i and j are the horizontal grid indices. A consistent update scheme for free surface and barotropic transport can be obtained by applying the restriction operator to the right hand side of this equation. Let's consider the situation represented in Fig. 9 where the mesh refinement factor is equal to 3.

If the free surface restriction operator is a simple average of the nine fine grid cells (and assuming no time refinement), the time evolution of the updated free surface is given by:

$$\eta_{i_c j_c}^{n+1} = \eta_{i_c j_c}^{n} - \frac{\Delta t}{9\Delta x_f \Delta y_f}\left[\left(U_{i_f+\frac{3}{2}j_f-1} + U_{i_f+\frac{3}{2}j_f} + U_{i_f+\frac{3}{2}j_f+1}\right)\right.$$
$$- \left(U_{i_f-\frac{3}{2}j_f-1} + U_{i_f-\frac{3}{2}j_f} + U_{i_f-\frac{3}{2}j_f+1}\right)$$
$$+ \left(V_{i_f-1j_f+\frac{3}{2}} + V_{i_f j_f+\frac{3}{2}} + V_{i_f+1j_f+\frac{3}{2}}\right)$$
$$\left. - \left(V_{i_f-1j_f-\frac{3}{2}} + V_{i_f j_f-\frac{3}{2}} + V_{i_f+1j_f-\frac{3}{2}}\right)\right]$$
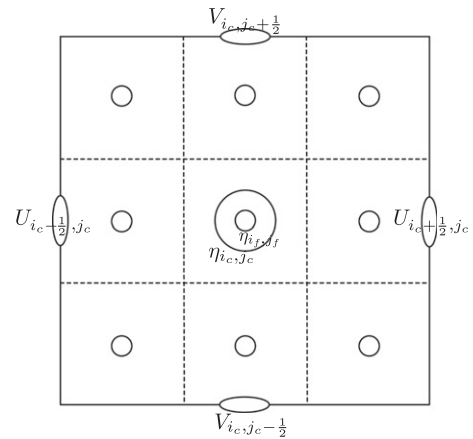

Fig. 9. A coarse grid cell divided in nine fine grid cells on a *C*-grid.

where i_c and j_c are the indices in the coarse grid and i_f and j_f in the fine grid (see Fig. 9). In consistence with the average restriction operator for free surface, the coarse grid barotropic transports can be updated by the relations:

$$U_{i_c+\frac{1}{2}j_c} = U_{i_f+\frac{3}{2}j_f-1} + U_{i_f+\frac{3}{2}j_f} + U_{i_f+\frac{3}{2}j_f+1}$$
$$V_{i_c j_c+\frac{1}{2}} = V_{i_f-1 j_f+\frac{3}{2}} + V_{i_f j_f+\frac{3}{2}} + V_{i_f+1 j_f+\frac{3}{2}}$$

This corresponds for U to an injection in the x-direction and an average in the y-direction and reciprocally for V. This couple of restriction operators (average for free surface, injection/average for velocities) will be denoted in the following by *update_mix_low*. The corresponding high order update schemes will be denoted by *update_mix_high* and is the full-weighting operator on free surface, which can be shown to lead for transport variables to a couple of average/full-weighting restriction operators.

For constancy preservation, tracer values should also be updated with the same update operator as the free surface and the three-dimensional velocities (or more precisely volumetric fluxes) should be updated with the same update operator as barotropic velocities. Table 1 summarizes the different restriction operators that will be evaluated.

2.4. Conservation properties by refluxing

On a uniform model grid, conservation is guaranteed when numerical schemes are written in flux form. In two-way nesting procedures, this property is generally lost at the grids interface. Enforced conservation has several computational issues and imposes strong requirements on the intergrid transfer operators that may in turn lead to a loss of accuracy, as will be shown. However, this constraint is recommended for long term integrations. Therefore, after reviewing the basic requirements for conservation on a nested grid, we propose a flux correction algorithm that answers these requirements and present a study of its numerical properties.

2.4.1. Definition and discretization

Let us consider a two dimensional domain and q the solution of the following equation written in conservative form

$$\frac{\partial q}{\partial t} + \frac{\partial f}{\partial x} + \frac{\partial g}{\partial y} = 0$$

where f and g may contain both advective and diffusive fluxes. Then, assuming that the integral of fluxes f and g cancels along the boundaries of Ω, Q_Ω, integral of q over the domain Ω, is constant in time (at the continuous level):

$$Q_\Omega(t) = \int_\Omega q(x,y,t)\,dx\,dy \quad \Rightarrow \quad \frac{dQ_\Omega(t)}{dt} = \int_{\partial\Omega} f\,ds + \int_{\partial\Omega} g\,ds = 0$$

In the nested grid system, the quantity Q_Ω is defined by the summation over the high resolution domain ω and its complement in Ω:
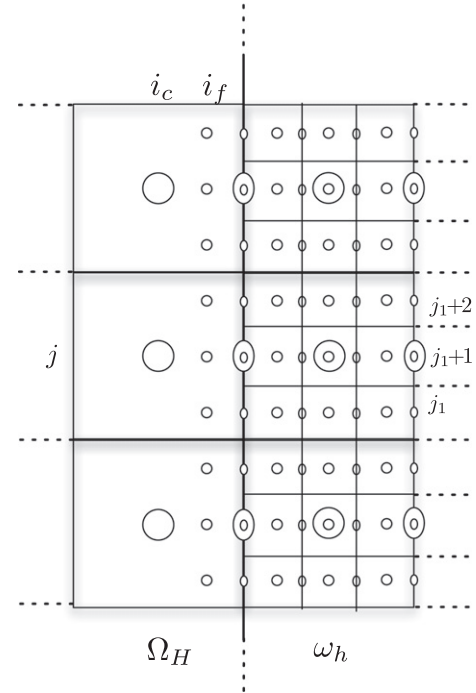
$$Q_\Omega = Q_\omega + Q_{\Omega\setminus\omega}$$

Fig. 10. The coarse resolution domain Ω on the left and the high resolution domain ω on the right for a C-grid with a mesh refinement factor of 3.

Let us now make the following assumptions for simplicity:

- As illustrated in Fig. 10, we consider a two dimensional domain infinite in both x and y directions. The left (resp. right) part of the domain is at coarse (resp. high) resolution. Note that the black thick line in Fig. 10 refers here to the feedback interface which is the relevant interface for conservation issues in two-way nesting.
- The variable $q_{i,j}^n$ is cell centered
- The time stepping scheme is an explicit Euler scheme

$$q_{i,j}^{n+1} = q_{i,j}^n - \frac{\Delta t}{\Delta x \Delta y}(F_{i+\frac{1}{2}j} - F_{i-\frac{1}{2}j}) - \frac{\Delta t}{\Delta x \Delta y}(G_{i,j+\frac{1}{2}} - G_{i,j-\frac{1}{2}}) \quad (9)$$

where $F_{i+\frac{1}{2}j}, G_{i,j+\frac{1}{2}}$ are volumetric fluxes: $F_{i+\frac{1}{2}j} = f_{i+\frac{1}{2}j}\Delta y, G_{i,j+\frac{1}{2}} = g_{i,j+\frac{1}{2}}\Delta x$. In a finite volume framework, the definition of $Q_{\Omega\setminus\omega}$ at discrete level is unambiguously given by

$$Q_{\Omega\setminus\omega}^n = \sum_{i\leqslant i_c,j} \Delta x_c \Delta y_c \ q_{i,j}^{c,n}$$

while on the high resolution domain ω, Q_ω^n can be defined either using fine grid point values:

$$Q_\omega^{F,n} = \sum_{i\geqslant i_f,j} \Delta x_f \Delta y_f \ q_{i,j}^{f,n} \quad (10)$$

Table 1
Four choices of restriction operators for free surface (η), tracers (q) and velocities (u,v) on an Arakawa C-grid.

Operator	Direction	(η,q)	(u,U)	(v,V)
Average	x	average	average	average
	y	average	average	average
Full-Weighting	x	full-weighting	full-weighting	full-weighting
	y	full-weighting	full-weighting	full-weighting
update_mix_low	x	average	copy	average
	y	average	average	copy
update_mix_high	x	full-weighting	average	full-weighting
	y	full-weighting	full-weighting	average

or using coarse grid point values:

$$Q_\omega^{C,n} = \sum_{i>i_c,j} \Delta x_c \Delta y_c \; q_{i,j}^{c,n} \tag{11}$$

In two-way applications, these two expressions are not independent since, inside ω, $q_{i,j}^{c,n}$ is a function of $\left(q_{i,j}^{f,n}\right)_{i,j}$ given by the update operator. Note also that these two expressions are strictly identical only when the restriction operator is a simple area weighted average of the fine grid values.

Let's for the moment assume that the first definition of Q_ω^n, $Q_\omega^{F,n}$, is taken. At discrete level, Q_Ω at time $t = t^n$ is then given by

$$Q_\Omega^n = \sum_{i \leqslant i_c,j} \Delta x_c \Delta y_c \; q_{i,j}^{c,n} + \sum_{i \geqslant i_f,j} \Delta x_f \Delta y_f \; q_{i,j}^{f,n} \tag{12}$$

where, as shown in Fig. 10, i_c and i_f denote the nearest coarse and fine grid indices to the left of the interface. Then after one time step, according to Eq. (9) we obtain:

$$Q_\Omega^{n+1} = Q_\Omega^n - \Delta t_c \sum_j F_{i_c+\frac{1}{2}j}^{c,n} + \Delta t_f \sum_{p=0}^{\rho_t-1} \sum_{j_1} \sum_{j_f=j_1}^{j_1+\rho-1} F_{i_f+\frac{1}{2}j_f}^{f,n+p/\rho_t}$$
$$= Q_\Omega^n - \Delta t_c \sum_j \left(F_{i_c+\frac{1}{2}j}^{c,n} - \mathcal{F}_{i_c+\frac{1}{2}j}^{f,n} \right) \tag{13}$$

where

$$\mathcal{F}_{i_c+\frac{1}{2}j}^{f,n} = \frac{1}{\rho_t} \sum_{p=0}^{\rho_t-1} \sum_{j_f=j_1}^{j_1+\rho-1} F_{i_f+\frac{1}{2}j_f}^{f,n+p/\rho_t} \tag{14}$$

In general, there will be a misfit between the coarse and fine grid fluxes so that the flux differences on the right hand side do not cancel and conservation is artificially lost: $Q_\Omega^{n+1} \neq Q_\Omega^n$.

If, instead of $Q_\omega^{F,n}$, Q_ω^n is defined by $Q_\omega^{C,n}$ then the discrete integral of Q is simply given by its summation over the entire coarse grid domain:

$$Q_\Omega^n = \sum_{i,j} \Delta x_c \Delta y_c \; q_{i,j}^{c,n} \tag{15}$$

In this case, an expression similar to Eq. (13) can be obtained, but this time with a definition of $\mathcal{F}_{i_c+\frac{1}{2}j}^{f,n}$ that is a function of the restriction operator used for the quantity $q_{i,j}^c$. If the average restriction operator is chosen, we recover expression (14) which spatially corresponds for the fluxes to the *update_mix_low* operator described in paragraph Section 2.3.2 (copy in the x-direction and average in the y-direction). If the full-weighting restriction operator is chosen, it can be shown that $\mathcal{F}_{i_c+\frac{1}{2}j}^{f,n}$ should be computed from the fine grid fluxes using the *update_mix_high* restriction operator (average in the x-direction, full-weighting in the y-direction).

2.4.2. Flux correction algorithm

In some cases, the flux difference appearing in Eq. (13) can be easily cancelled by applying conservative interpolation. For example, from the time evolution of free surface elevation (Eq. (8)) with no time refinement, it appears that a conservative interpolation of the barotropic transport at the interface must lead to global volume conservation. An example of such second order conservative interpolation for the barotropic transport can be found in Barth et al. (2005). Additional difficulties arise when time refinement is applied and when tracer conservation is desired. To overcome those, we propose a flux correction algorithm inherited from the adaptive mesh refinement community. It follows from the algorithm of Berger and Oliger (1984) and Berger and Colella (1989). The idea is to apply a modification of the coarse grid variables that takes into account the misfit between coarse and fine grid fluxes. Starting from Eq. (13), a correction is applied to the coarse grid variable at time $n + 1$ near the boundary as follows:

$$q_{i_c j}^{n+1,*} = q_{i_c j}^{n+1} + \frac{\Delta t_c}{\Delta x_c \Delta y_c} \left(F_{i_c+\frac{1}{2}j}^{c,n} - \mathcal{F}_{i_c+\frac{1}{2}j}^{f,n} \right) \tag{16}$$

This equation implies that the coarse grid variable at index j has been integrated using, on the right interface, fluxes computed from the fine grid solution:

$$q_{i_c j}^{n+1,\star} = q_{i_c j}^n - \frac{\Delta t_c}{\Delta x_c \Delta y_c} \left(\mathcal{F}_{i_c+\frac{1}{2}j}^{f,n} - F_{i_c-\frac{1}{2}j}^{c,n} \right) \tag{17}$$

The algorithm is easy to implement assuming that the time evolution of q can be written in terms of flux divergences, as was indeed the case for the Euler time scheme. The program stores the fine grid fluxes at the boundary and makes a summation in time and space over the fine grid cells. Using this procedure, the overall scheme can be made conservative *whatever the update scheme is*. It implies that the update scheme does not have to be "conservative" (area-weighted average of the fine grid values in a coarse grid cell) and can be constructed entirely with regards to its filtering properties (see Section 2.3).

2.4.3. Choice of Q_ω formulation

As presented in the previous paragraph, the choice of the discrete value of Q_ω impacts the computation of the equivalent fine grid flux $\mathcal{F}_{i_c+\frac{1}{2}j}^{f,n}$ and so the flux correction algorithm. The choice between formulations (10) and (11) can be based on the assumption that, as explained in paragraph Section 2.3.2, consistent restriction operators are used for free surface, tracers and velocities (e.g. average/*update_mix_low* or full-weighting/*update_mix_high*). Then, definition (11) naturally leads to the same restriction operators for the computation of the equivalent fine grid flux. More importantly, the use of the same restriction operators for velocities and fluxes $\mathcal{F}_{i_c+\frac{1}{2}j}^{f,n}$ is needed to maintain the property of constancy preservation after the flux correction procedure. This formulation will thus be preferred.

2.4.4. Analysis

It is worth analyzing the conservation scheme because, as will be seen, it can be a source of instability. In order to perform a numerical analysis, the problem is reduced to the one dimensional advection equation modified by the flux correction term in Eq. (16). Time refinement is omitted here for simplicity. In this particular case, Eq. (16) can be rewritten

$$q_{i_c}^{n+1,*} = q_{i_c}^{n+1} + \frac{\Delta t_c}{\Delta x_c} \left(F_{i_c+\frac{1}{2}}^n - F_{i_f+\frac{1}{2}}^n \right) \quad \text{since } \mathcal{F}_{i_c+\frac{1}{2}j}^{f,n} = F_{i_f+\frac{1}{2}}^n \tag{18}$$

where we have assumed that an average restriction operator is used for q_i^c so that both definitions (10) and (11) leads to Eq. (18).

Let us assume that the interpolation at mid-points of the original advection scheme is an approximation of order p_1:

$$q_{i_f+\frac{1}{2}}^\star = g(\ldots, q_{i_f}, q_{i_f+1}, \ldots) = q_{i_f+1/2} + \alpha \frac{\partial^{p_1} q}{\partial x^{p_1}} (\Delta x_f)^{p_1} + \text{HOT} \tag{19}$$

HOT stands for High Order Terms. Then the numerical flux is a consistent approximation of the continuous flux at order p_1, written (assuming a linear flux function f):

$$F_{i_f+\frac{1}{2}}^n = f\left(q_{i_f+\frac{1}{2}}^\star\right) = f(q_{i_f+\frac{1}{2}}) + f\left(\alpha \frac{\partial^{p_1} q}{\partial x^{p_1}} (\Delta x_f)^{p_1}\right) + \text{HOT}$$

Doing the same for the coarse grid flux leads to

$$F_{i_c+\frac{1}{2}}^n = f(q_{i_f+\frac{1}{2}}) + f\left(\alpha \frac{\partial^{p_1} q}{\partial x^{p_1}} (\Delta x_c)^{p_1}\right) + \text{HOT}$$

Let us further assume that the advection velocity u_0 is constant so that f is given by $f(q) = u_0 q$. Expression (18) becomes:

$$q_{i_c}^{n+1,*} - q_{i_c}^{n+1} = u_0 \frac{\Delta t_c}{\Delta x_c} \left[\alpha \frac{\partial^{p_1} q}{\partial x^{p_1}} ((\Delta x_c)^{p_1} - (\Delta x_f)^{p_1}) \right]$$
$$= u_0 \Delta t_c \left[\alpha \frac{\partial^{p_1} q}{\partial x^{p_1}} (\Delta x_c)^{p_1-1} (1 - 1/\rho^{p_1}) \right] \tag{20}$$
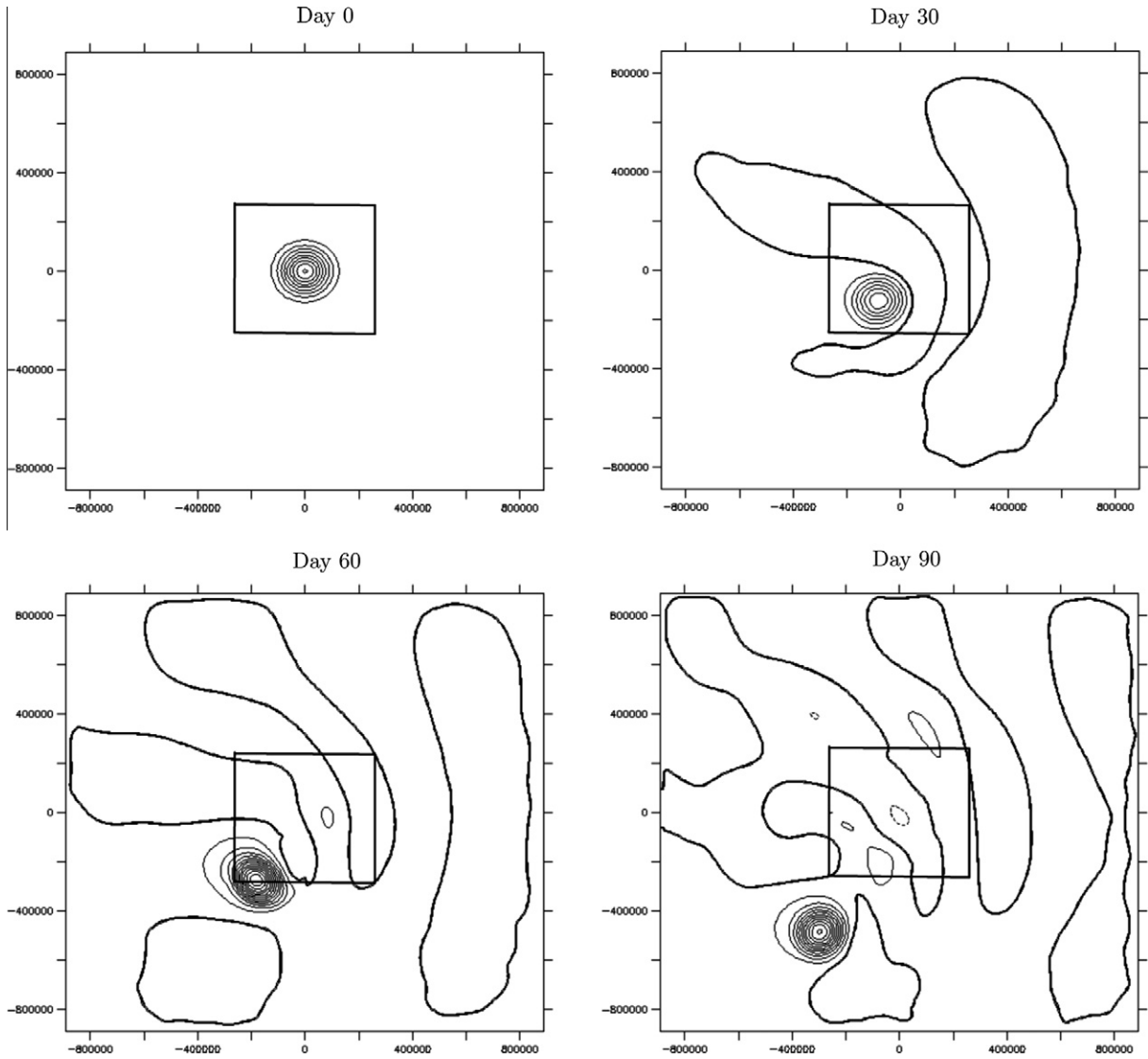
Fig. 11. Evolution of surface elevation in the reference, non-nested, high resolution solution. The contour interval is 10 cm. The location of high resolution domain used in nesting experiments is indicated.

It follows from Eq. (20) that the order of approximation near the interface is decreased to $p_1 - 1$ by the flux correction algorithm. Additionally, if the original advection scheme uses even-order mid-point interpolation, it may affect stability because then (20) may represent anti-diffusion. Moreover, as can be guessed, instabilities are amplified when the mesh refinement ratio ρ is large.

2.5. The sponge layer

Inevitably, small scales produced on the fine grid need to be filtered near the interface to improve continuity between coarse and fine solutions. This is usually done through a so-called sponge layer. In its design, we require that the filter only acts on the scales that are unresolved by the coarse grid. One approach is to damp the difference between coarse and fine grid values near the boundary. In practice, it can be written using a Laplacian diffusion as follows:

$$\frac{\partial q_h}{\partial t} = G_h + \nabla \cdot \mu \nabla \left(q_h - q_h^C \right)$$

where here q_h denotes any quantities to be filtered (tracers and dynamics) and q_h^C its equivalent on the coarse grid. To be consistent,

q_h^C must be defined using the restriction operator (used in the update procedure). This can be written as

$$q_h^C = \left(I_H^h I_h^H \right) q_h$$

where I_H^h is an interpolation operator. In two-way nesting, $I_h^H q_h$ corresponds to q_H the coarse grid values. The sponge layer is then written as:

$$\frac{\partial q_h}{\partial t} = G_h + \nabla \cdot \left(\mu \nabla \left(q_h - I_H^h q_H \right) \right)$$

where μ is a coefficient ranging from its maximal value μ_0 at the interface to 0 a few grid points away from it (usually at a distance of 3 coarse grid cells). This sponge layer is applied both on momentum and tracers. When applied on tracers, the diffusive fluxes are stored and added to the advective fluxes for later use in the refluxing algorithm Section 2.4.2.

3. A ROMS test case: baroclinic vortex

The algorithms presented in this paper were implemented in the Regional Oceanic Modeling System (ROMS; Shchepetkin and
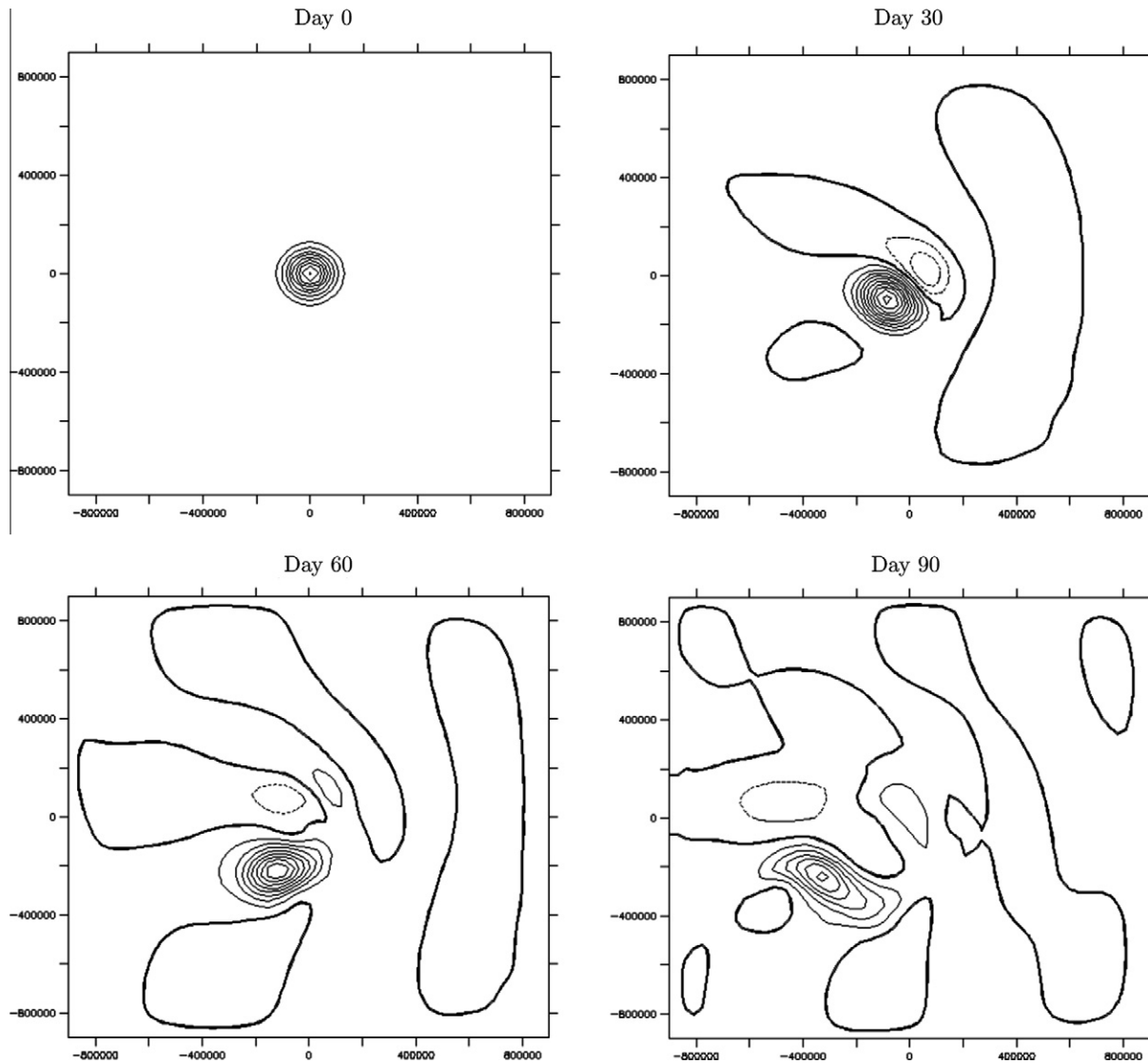
Fig. 12. Evolution of surface elevation in the coarse, non-nested, solution. The contour interval is 10 cm.

McWilliams, 2005) and are here evaluated using the baroclinic vortex test case. The idealized experiment of a baroclinic and initially axisymmetric vortex propagating on a β-plane has been described by McWilliams and Flierl (1979). It has been used to evaluate nesting performances by Spall and Holland (1991) in the case of a rigid-lid model. Its use has been extended by Penven et al. (2006) to free surface models and ROMS one-way nesting. In these applications, as in the present one, performance evaluation is based on the comparison between the nested solution and a reference solution, which is computed on a fine grid over the whole domain.

3.1. Model configuration and simulations

A full description of initial conditions and model configuration can be found in Penven et al. (2006) and are only summarized here. The vortex is initialized as a Gaussian surface pressure distribution with a maximum surface geostrophic velocity of 1 m.s^{-1} and a horizontal e-folding scale of 60 km. We consider a baroclinic vortex in the presence of a continuous background stratification, with no motion below 2500 m. The initial horizontal velocities are in geostrophic equilibrium with the initial pressure field.

The grids are square, on a flat bottom (H_0 = 5000 m), using a β-plane approximation centered around 38.5° N. The parent grid domain is 1800 km × 1800 km, while the child grid domain is approximately 580 km × 580 km. We use 10 evenly spaced vertical levels, no explicit horizontal viscosity unless specified in sponge areas (there is implicit dissipation in the upstream biased advection scheme), no vertical viscosity, and no bottom friction. The Brünt–Vaissala frequency is fixed at N = 0.003 s^{-1}. The horizontal resolution of the coarse grid is 30 km and the mesh refinement ratio is set to 3, leading to a resolution of 10 km for the child grid. The parent domain is assumed unbounded, which requires open boundary conditions on each side, as described by Marchesiello et al. (2001). The evaluation of the nested solution is made against a reference solution computed with high resolution (10 km) on the whole parent grid domain. In all experiments, we use the power law shape function to compute intermediate filtered variables at the barotropic level since it is already used in ROMS to filter external gravity waves in the barotropic/baroclinic coupling.

The vortex evolution in the reference solution is depicted in Fig. 11 for the free surface elevation. Due to β, the anticyclonic vortex, initially axisymmetric, propagates south-westward and
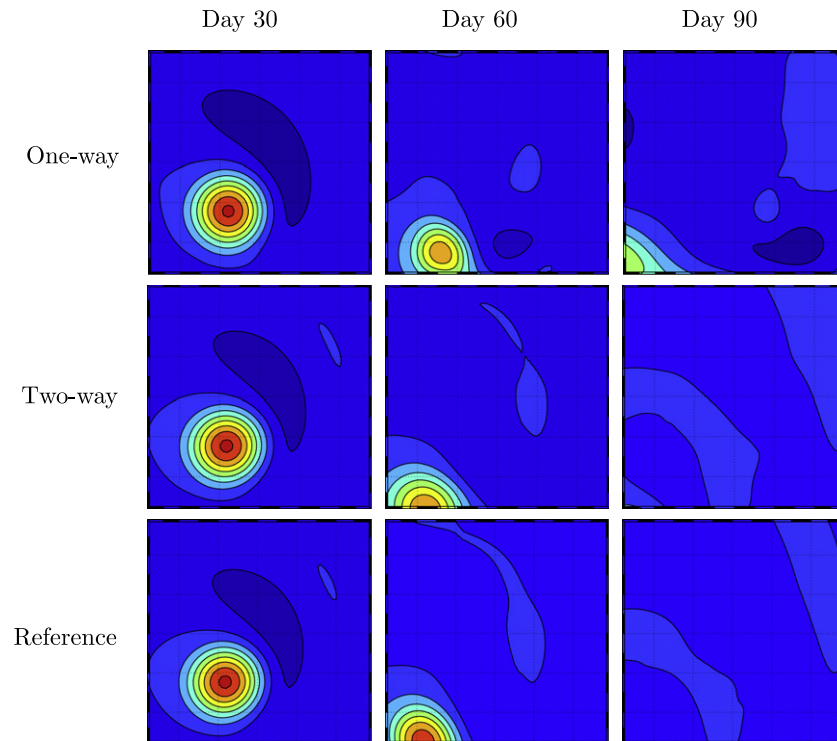
Fig. 13. Evolution of surface elevation in the child grid domain for one-way (top), two-way (middle) and reference solutions (bottom). The two-way solution is obtained with *update_mix_high* restriction, separate interfaces and sponge layer. The contour interval is 10 cm.
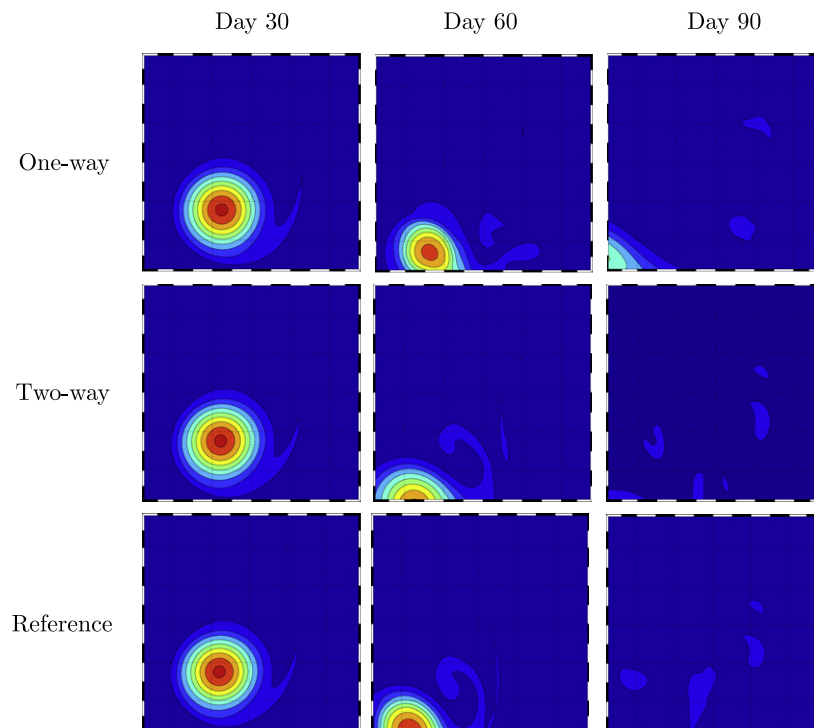
Fig. 14. Evolution of temperature [°C] in the child grid domain for one-way (top), two-way (middle) and reference solutions (bottom). The two-way solution is obtained with *update_mix_high* retriction, separate interfaces and sponge layer. The contour interval is 0.2 °C.

changes its shape by Rossby-wave dispersion. The vortex retains part of its axisymmetric shape, but weakens as it emits a train of weak-amplitude Rossby-waves mostly in its wake. As explained by McWilliams and Flierl (1979), advective effects compensate the β-related leakage, preserving the vortex pattern. In the coarse resolution case, the advective axisymmetrisation effects are reduced and the vortex experiences strong dispersion, resulting in loss of integrity (Fig. 12). When grid refinement is applied (Figs.
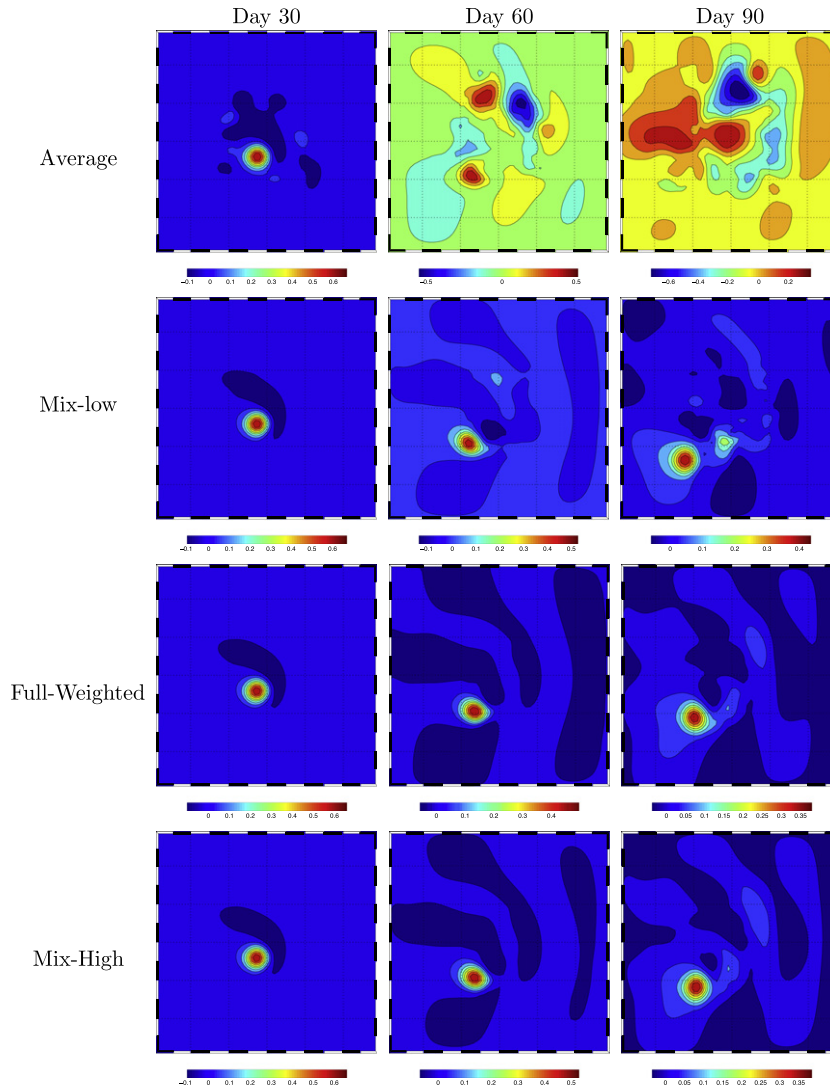
Fig. 15. Free surface elevation (on the coarse grid domain) after day 30, 60 and 90 (from left to right) for different update schemes (without sponge layer and without interfaces separation).

Fig. 16. Normalized RMS error [%] in the vortex test case for free surface elevation (left) and temperature (right). In the nesting procedure, neither sponge layer nor interface separation are applied.

13 and 14) in either one-way or two-way mode, most of the high resolution properties are recovered. However, two-way nesting is clearly an improvement over one-way nesting, depending though on the nesting algorithm, as will be shown.

3.2. Update schemes

In a first series of experiments, the performance of update schemes presented in Section 2.3 are investigated. All the simula-

Fig. 17. Normalized RMS error [%] in the vortex test case for free surface elevation (left) and temperature (right). In the nesting procedure, interface separation is applied without sponge layer.

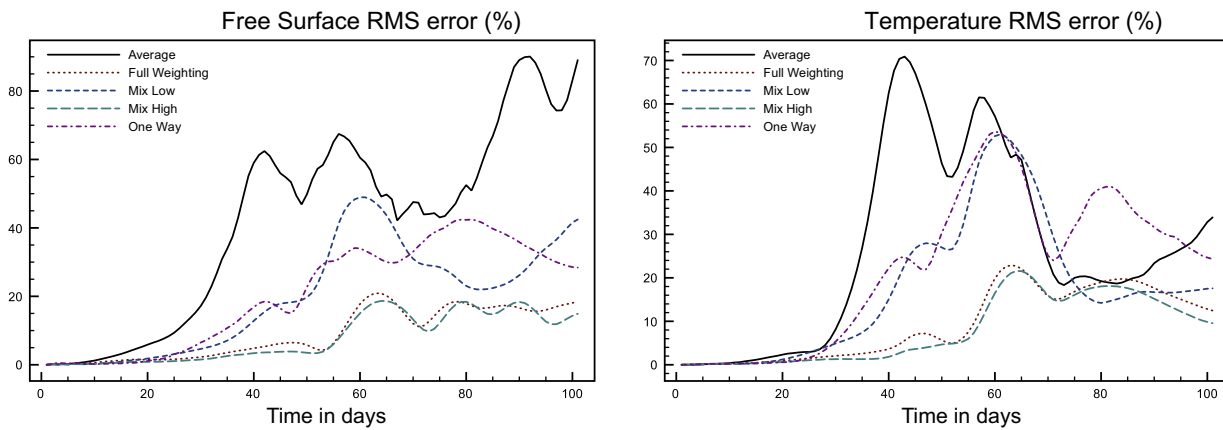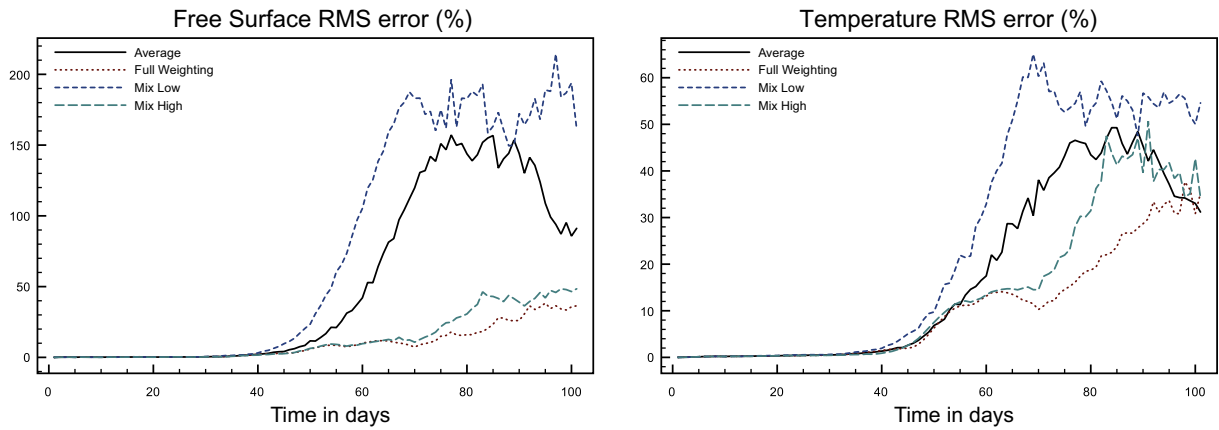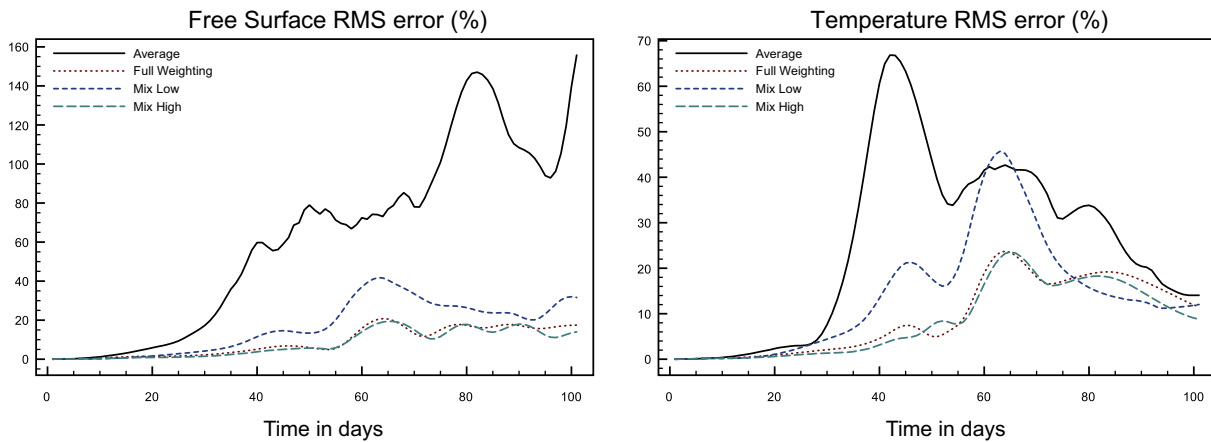**Fig. 18.** Normalized RMS error [%] in the vortex test case for free surface elevation (left) and temperature (right). In the nesting procedure, a sponge layer is applied but not interface separation.

tions are made without sponge layers and without separated dynamic and feedback interfaces. Fig. 15 shows the solutions obtained using four different update schemes: average, full-weighting, *update_mix_low* and *update_mix_high*. Note that additional experiments using either a direct-injection update scheme (copy of child values at corresponding locations of the parent grid with no spatial filtering) or the Shapiro update scheme are not shown since they both lead to unstable solutions (the simulation 'blows up" at day 3 for direct-injection and at day 7 for Shapiro).

The simulations based on the average and *update_mix_low* operators lead to noisy solutions where the coarse solution is contaminated by fine scale structures (Fig. 15). Normalized RMS errors are given in Fig. 16; for comparison, it also includes the results from the one-way simulation presented by Penven et al. (2006). This analysis shows that usual updating procedures can be detrimental to the physical solution and cause a degradation of the one-way procedure (for example, Average update in Fig. 16). However, a more sophisticated update scheme, such as the full-weighting, can yield a 50% improvement over the one-way solution by enhancing continuity at the grids interface. As stated earlier, the average operator is unable to damp the small scale modes approaching the interface, which leads to the degradation of the solution. In the one-way and full-weighting two-way solutions, the largest errors occur as the vortex crosses the interface (around day 50) while using the average operator they occur much earlier, when the first dispersed Rossby waves have reached the interface.

In the absence of additional diffusion, low order restriction operators (average, *update_mix_low*) are thus very sensitive to small perturbations.

3.3. Sponge layer and separation of dynamical/feedback interfaces

Separation of dynamical and feedback interfaces requires the application of a sponge layer to prevent the drift of the fine solution in the zone between dynamical and feedback interfaces. Interfaces separation alone does not improve and even increases RMS errors (Fig. 17). In this case again, high order restriction operators present lower RMS error than their low order equivalent. A sponge layer alone (using maximum diffusivity $\mu_0 = 500$ m^2.s^{-1} for both tracers and momentum) is not much better at reducing the noise associated with low order restriction operators (Fig. 18). The combination of both methods results in a clear improvement (by about 30%) for all simulations (Fig. 19). The normalized RMS error on free surface does not exceed 12% (compared to 40% in one-way simulations). This improvement results from the suppression of the feedback of the largest errors from the fine solution (generally located at the closest point from the interface) into the coarse solution. The fact that the solution is now much less sensitive to the choice of restriction operator is the result of (1) not updating errors created near the interface and (2) damping small scales by the sponge layer, thus in effect replacing the inner-filtering of high order restriction operators. Therefore, weaknesses of low order restric-
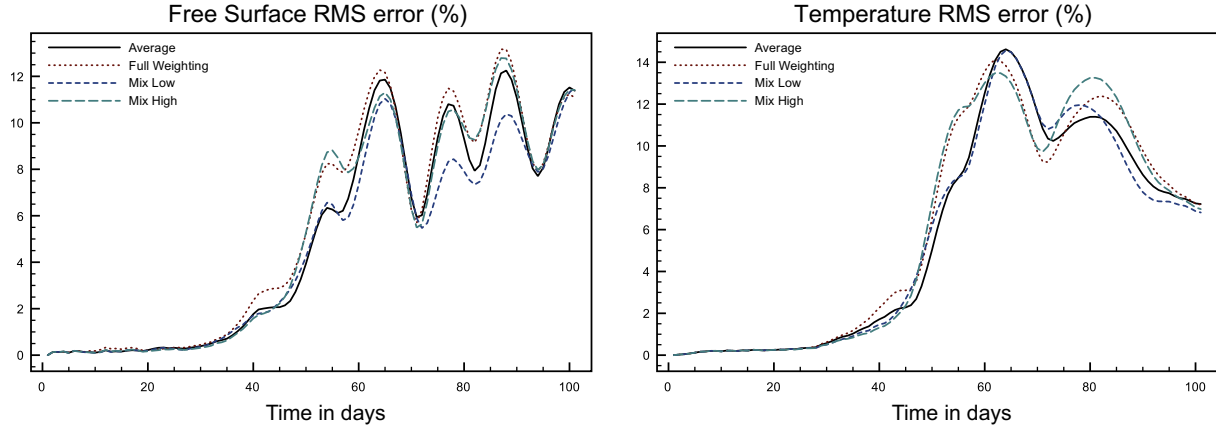
Fig. 19. Normalized RMS error [%] in the vortex test case for free surface elevation [m] (left) and temperature (right). In the nesting procedure, both sponge layer and interface separation are applied.
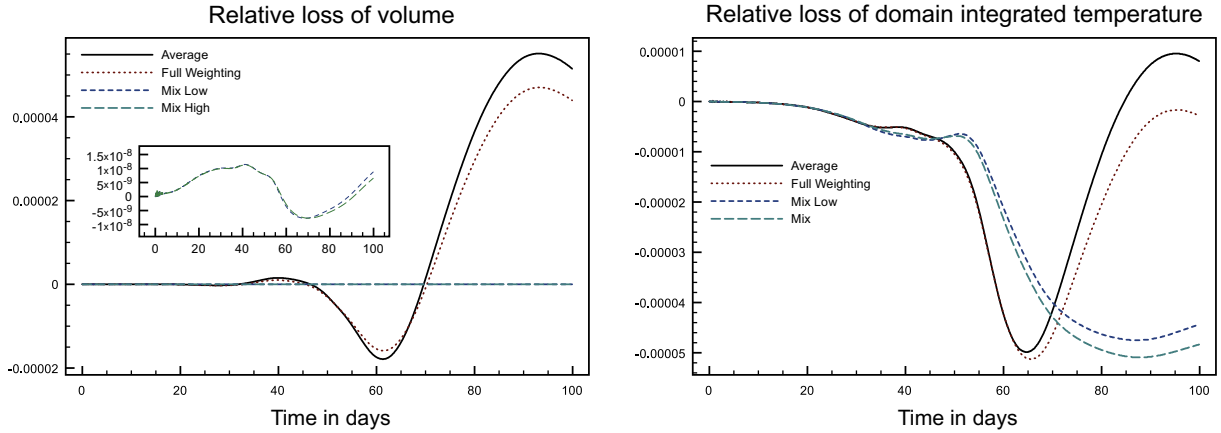

Fig. 20. Time evolution of relative loss of volume (left) and temperature (right) resulting from not enforcing conservation in the two-way coupling. The subview inside the left panel shows the small residual volume loss of Mix Low and Mix High schemes.

tion operators can be partially overcome by additional techniques. Yet, they remain sensitive to the choice of these techniques, in particular to diffusivity values as illustrated in the sponge-free case (Fig. 17), and we expect that they perform differently on various model applications. The robustness of high order operators will indeed be fully revealed in the realistic experiments of Section 4.

3.4. Conservation

We now analyze the effects of maintaining conservation using the refluxing algorithm described in Section 2.4. As a first step, the computation of the fluxes misfit between high and coarse resolution, as given by Eq. (13), are implemented as a diagnostic tool. Fig. 20 shows the results of accumulated fluxes misfit for volume (free surface) and temperature. Plotted quantities correspond to

$$\delta\eta = \frac{Q_\eta^n - Q_\eta^0}{Q_\eta^0}, \ Q_\eta^n = \int_S (H_0 + \eta^n)\mathrm{d}x,$$

$$\delta T = \frac{Q_T^n - Q_T^0}{Q_T^0}, \ Q_T^n = \int_\Omega T^n \mathrm{d}x$$

where the discrete expressions of Q_η^n and Q_T^n are computed according to Eq. (15). Note that the subscripts in Q now design the variables η and T, and Q is integrated over the domain Ω. As explained in paragraph Section 2.4.2, *update_mix_low* and *update_mix_high* operators are intrinsically more conservative. In particular,

they lead to a nearly exact conservation of volume. However, they cannot prevent a heat loss.

Heat and mass loss can be exactly corrected by the refluxing procedure. To assess whether this correction affects the other properties of the nesting schemes, the normalized RMS errors for both free surface and temperature are presented in Fig. 21 (where the solutions with and without conservation are compared). Note that this is done only for the *update_mix_low* and *update_mix_high* operators since the other restriction operators do not preserve constancy when the refluxing procedure is applied. In addition, the sponge layer diffusion coefficient μ_0 was increased to a high value of $1000 \ \mathrm{m^2.s^{-1}}$ in order to maintain stability in the simulations. This is in agreement with the analysis of paragraph Section 2.4.4, which predicts instability for the second-order mid-point interpolation used in ROMS advection scheme (that globally produces a third order accurate scheme in a finite difference sense). Other experiments (not shown here) confirm that this increase of viscosity does not affect the conclusion of our sensitivity study on conservation. This analysis shows that enforcement of conservation leads to a small increase in RMS error, which is not in contradiction with the analysis of Section 2.4.4.

3.5. Coarse grid improvement

Finally, we analyze the vortex solution in the parent domain (outside the refinement area) starting from the time when it begins
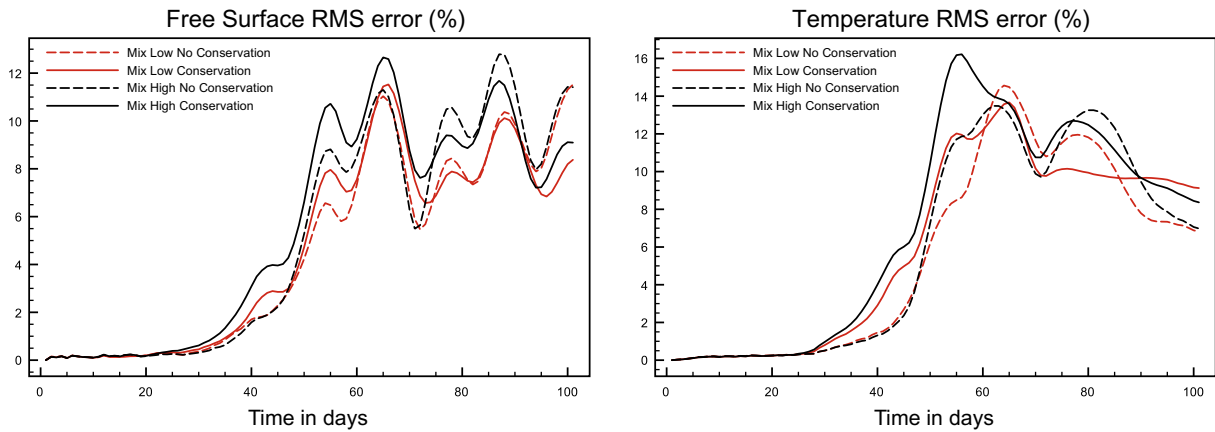
Fig. 21. Normalized RMS error [%] for free surface and temperature with and without conservation.
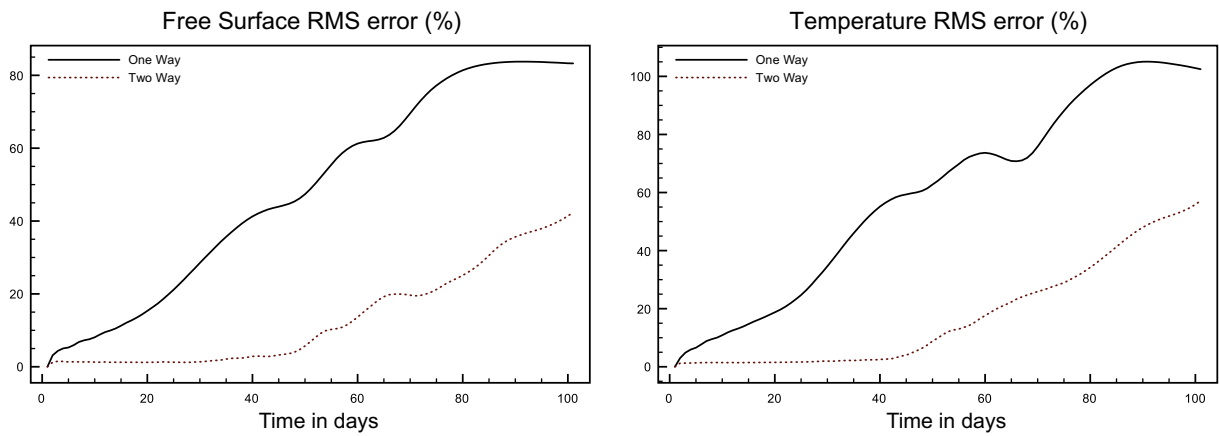

Fig. 22. Normalized RMS error [%] on the coarse grid domain for free surface (left) and temperature (right) and for the one-way solution (the error is in this case the same as in the uniformly coarse resolution case) and two-way solution.

to cross the interface. Normalized RMS errors are indicated in Fig. 22. When the vortex is located inside the refinement area, the coarse solution error in two-way nesting is close to the fine solution error which is very small. In one-way nesting, degradation due to the dominance of wave dispersion over advective axisymmetrization effects is rapidly apparent as the coarse solution gets no feedback from the fine grid (Fig. 12). As the vortex crosses the interface (around day 50), the two-way solution starts to degrade as well. However, the error remains much smaller than in the one-way experiment. This experiment illustrates the lasting benefit of two-way coupling beyond the refinement area, a capability that is of particular interest in the context of upscaling and teleconnection processes.

4. Two-way nesting for the California Current System

The two-way nesting algorithm selected from the previous analysis is now tested in a realistic configuration that covers the full spectrum of dynamical scales and large topographic variations (this is the same procedure as presented by Penven et al. (2006) for the one-way algorithm).

The reference experiment (REF) is an equilibrium solution of the California Current System (CCS) at 5 km resolution (Marchesiello et al., 2003). It is compared with an equivalent simulation at 15 km resolution (LOW) and 2 experiments based on a 5 km coastal grid nested in this larger scale model. A first simulation is made

using only one-way nesting (1-WAY), the other is based on the two-way methodology described above (2-WAY). Because ROMS numerical schemes have evolved since its first applications in the CCS (essentially the pressure gradient algorithm, equation of state, barotropic time stepping and barotropic/baroclinic coupling algorithm; see Shchepetkin and McWilliams, 2009, for a review), these new solutions are similar but not identical to the results obtained previously (Marchesiello et al., 2003; Penven et al., 2006). There are also several differences in the configuration parameters. First, the topography (based on GEBCO, http://www.gebco.net/) is regridded to ensure volume equality between the nested grid and REF. Second, the western boundary of the nested grid is pushed 100 km further offshore to encompass the main coastal transition zone. Third, initial and large scale boundary conditions are derived, using ROMSTOOLS (Penven et al., 2008), from the World Ocean Atlas 2005 (Conkright et al., 2002). Note that, as described by Penven et al. (2006), a smooth transition between coarse and fine gridded topography is provided within 5 coarse-grid points of the interface (the topographies on the first two grid points are identical).

Algorithmic choices for two-way nesting in the CCS simulations were made on the basis of both theoretical arguments and results of the ideal test case presented earlier. These choices are: (1) nesting at the barotropic level; (2) either "low" (*Mix Low*) or "high" (*Mix High*) order update schemes; (3) dynamical and feedback interfaces separation (4) sponge layer acting on the difference between fine and coarse solutions (with maximum diffusivity $\mu_0 = 250 \text{ m}^2.\text{s}^{-1}$ for tracers and $\mu_0 = 125 \text{ m}^2.\text{s}^{-1}$ for momentum).
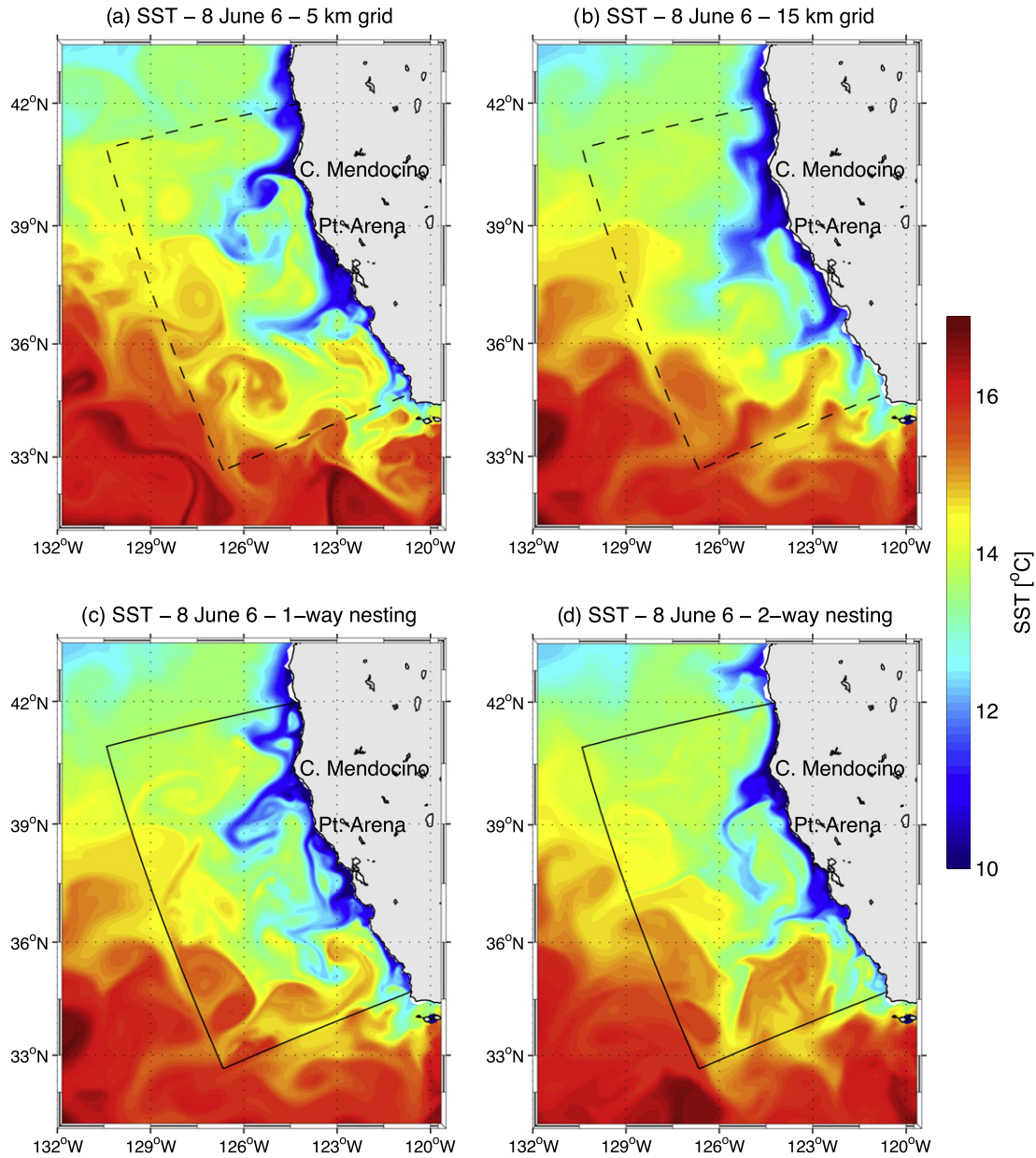
Fig. 23. Sea surface temperature [°C] for 8 June of model year 6. a: REF. b: LOW. c: 1-WAY. d: 2-WAY.

Volume conservation is also constrained. However, tracer flux correction was not fully satisfying, with stability problems arising in the course of the long-term simulation. We believe this to be a result of two main problems. In Subsections 2.4.4 and 3.4, we noted a potential instability associated with the flux correction algorithm when even order midpoint-interpolation are used, as is the case in ROMS. But maybe more importantly, the connection area for realistic simulations with complex topography needs particular attention, especially when flux correction is applied. The latter requires additional constraints on the discrete form of the topography along the interface.[2] Nevertheless, the absence of tracer

conservation enforcement in the following experiments did not lead to any significant drift of the solutions.

All experiments are integrated for 10 years. Analyses are performed from years 4 to 10. Fig. 23 represents sea surface temperature (SST) on June 8 of year 6 (same dates as in Penven et al., 2006) for the 4 experiments. Typical summer SST patterns in REF (Fig. 23(a)) represent upwelled coastal waters, upwelling fronts and filaments extending from the major capes. These intra-seasonal features are of chaotic nature (Marchesiello et al., 2003), i.e., they cannot be compared individually at any particular time but only in a statistical way. We will thus focus on patterns and their potential alteration by the nested interface. Next, mean and variance fields will be analysed, keeping in mind that 7 years of sampling is too short to properly reduce the standard error of estimators. Only large regional features will thus be compared as opposed to small-scale details.

In LOW (Fig. 23(b)), the fronts are more diffuse and the overall pattern is smoother. Coastal upwelling is also less intense. As de-

---

[2] We are currently investing this issue. One possible solution could be an extension of an algorithm proposed by Haley and Lermusiaux (2010, see their Appendix C.1.1): topography smoothing, constrained by the slope parameter for reducing pressure gradient errors, must be also made consistent with restriction operators in the connection area and, in our case, with the flux correction procedure.
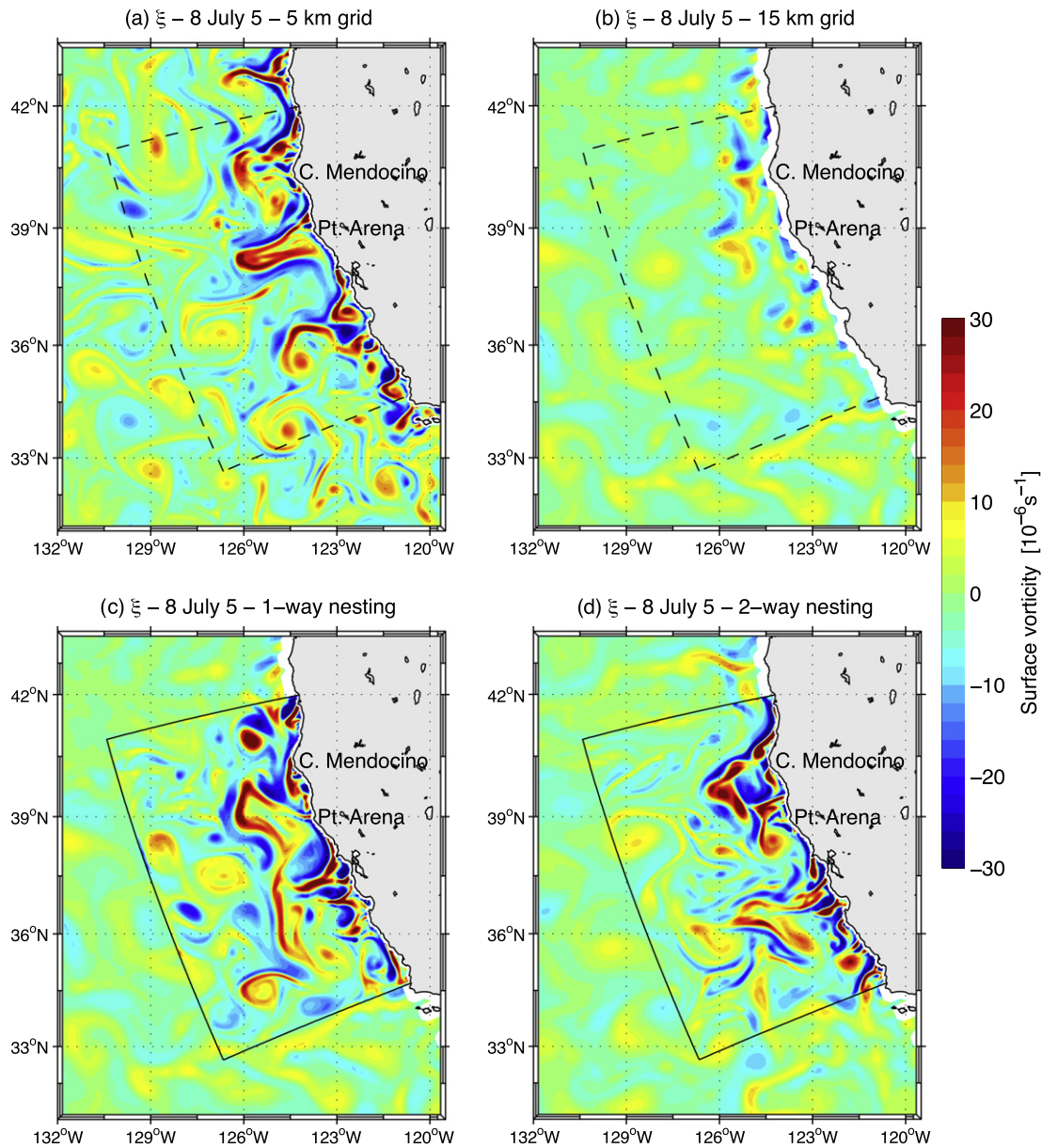
Fig. 24. Sea surface vorticity [$10^6\,s^{-1}$] for 8 July of model year 5. a: REF. b: LOW. c: 1-WAY. d: 2-WAY.

scribed by Penven et al. (2006), 1-WAY is able to recover the general SST patterns observed in REF: upwelling fronts and filaments (Fig. 23(c)). However, discontinuities are apparent at the parent–child interface, while they never occur in the simulation with two-way nesting (Fig. 23(d)).

Surface vorticity can be used as an indicator of flow discontinuities at the interface. It is displayed in Fig. 24 for July 8 of year 5. In REF (Fig. 24(a)), we recognize the strong negative/positive values associated with coastal jets, upwelling filaments streaming offshore, and a collection of offshore cyclonic and anticyclonic eddies. These structures almost disappear in LOW (Fig. 24(b)). In 1-WAY, there is no major discernible discontinuity at the boundaries (Fig. 24(c)), but there are meaningful differences with REF: eddies tend to concentrate near the western interface, probably affecting the offshore extension and propagation of coastal features. This accumulation of eddy energy seems absent in 2-WAY (Fig. 24(d); note the offshore eddy at [128°W, 38°N] which evolves around the interface), resulting in turbulent patterns resembling those of REF.

The mean sea surface height (SSH) in REF (Fig. 25(a)) exhibits the 3 large meanders of the CCS described by Marchesiello et al. (2003). In this new simulation, they appear slightly less prominent but they are similarly located: off Cape Mendocino, Monterey Bay and Point Conception. They are also present in LOW (Fig. 25-b) but the detachment of the flow at Cape Mendocino is delayed, resulting in a southward shift of the general pattern. In 1-WAY and 2-WAY (Fig. 25(c) and (d)), the detachment at Cape Mendocino is similar to REF, as well as the re-attachment of the flow along the coast off Point Arena, and the detachment north of Monterey Bay. 1-WAY amplifies the meanders near the southern boundary of the child domain and underestimates the northern meander. Overall, 2-WAY is a closer solution to REF, albeit with some discrepancies (stronger currents near the northern child boundary). This suggests that the northern interface between coarse and fine grids is situated at a critical point with respect to the dynamics of the CCS, as discussed by Penven et al. (2006).

The following comparisons illustrate the performance of nesting in maintaining the mean statistical characteristics of mesoscale
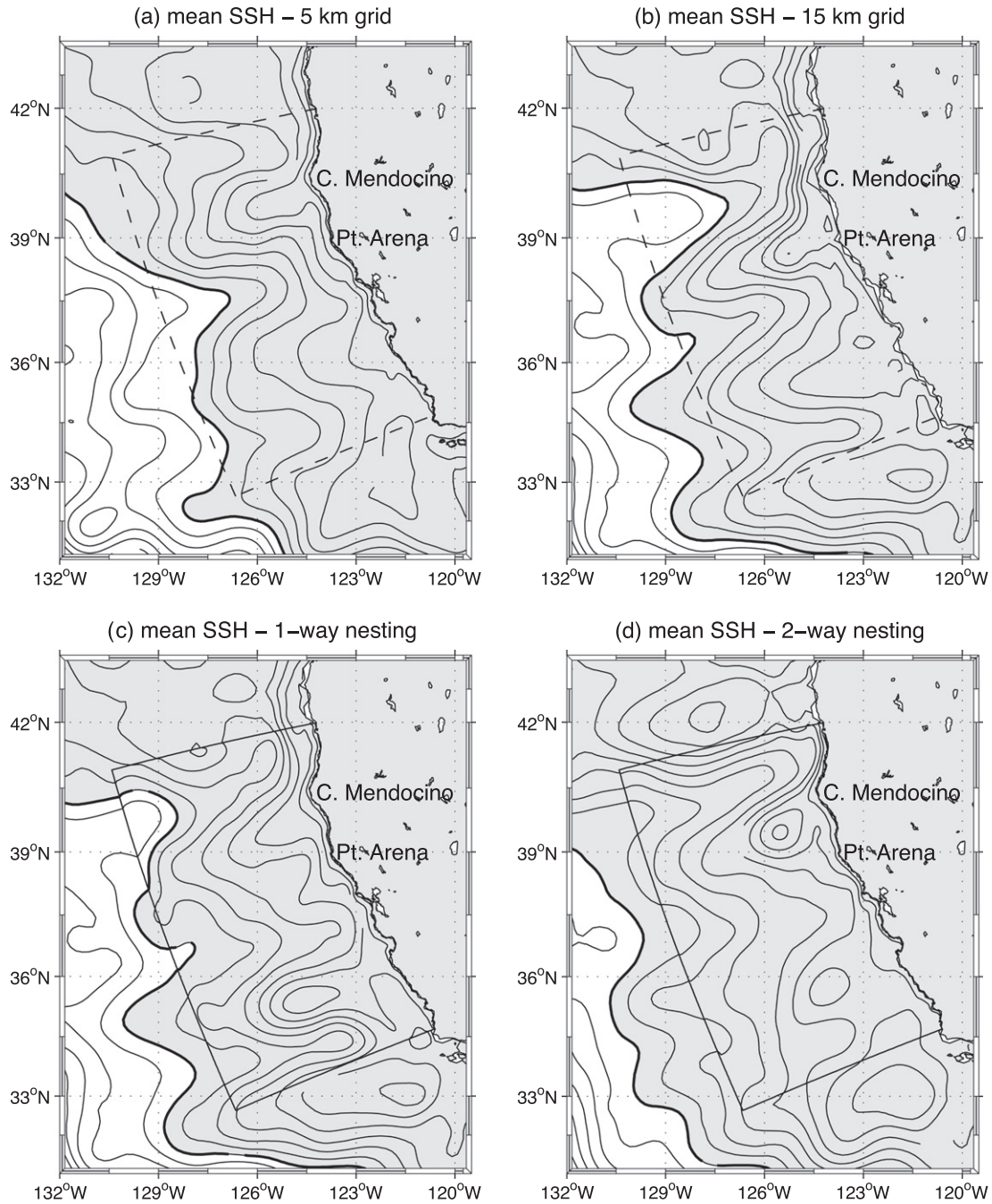
Fig. 25. Mean sea surface height (SSH) [cm]. a: REF. b: LOW. c: 1-WAY. d: 2-WAY.

variability. The SSH standard deviation (or root mean square: RMS SSH) is a measure of CCS variability. In REF, maximum values of 6 to 8 cm are produced offshore in the core of the CCS (Fig. 26(a)); a maximum of 8 cm is located off Cape Mendocino. RMS SSH is at least 30% lower in LOW (Fig. 26(b)); 1-WAY and 2-WAY recover most of the patterns observed in REF, but 1-WAY shows excessive variability along the western interface (Fig. 26(c)), which is absent from 2-WAY (Fig. 26(d)). Interestingly, some mesoscale variability is preserved outside the refinement area in the two-way nested solution, which emphasizes the improvement that refinement may provide to connected areas.

A final experiment shows that 2-WAY is sensitive to the update procedure, consistently with the baroclinic vortex test case: using *update_mix_low* in place of *update_mix_high*, the solution appears

degraded (compare Fig. 27 with Figs. 25 and 26). This is particularly true in the southern part of the child domain, around 35°N, where excessive variability is generated close to the boundary by *update_mix_low* in comparison with the reference solution and the solution produced by *update_mix_high* (Fig. 27b and Fig. 26). This result again illustrates the inability of low order update schemes to filter unresolved scales, and the limited usefulness of sponge layers.

These experiments provide a demonstration that the selected two-way nested algorithm is stable and accurate for long-term integrations of regional oceanic configurations. It also confirms that two-way is an improvement to one-way nesting in various ways: continuity of fine and coarse solutions at the grids interface; dynamical integrity of the solutions in the refinement area (as a re-
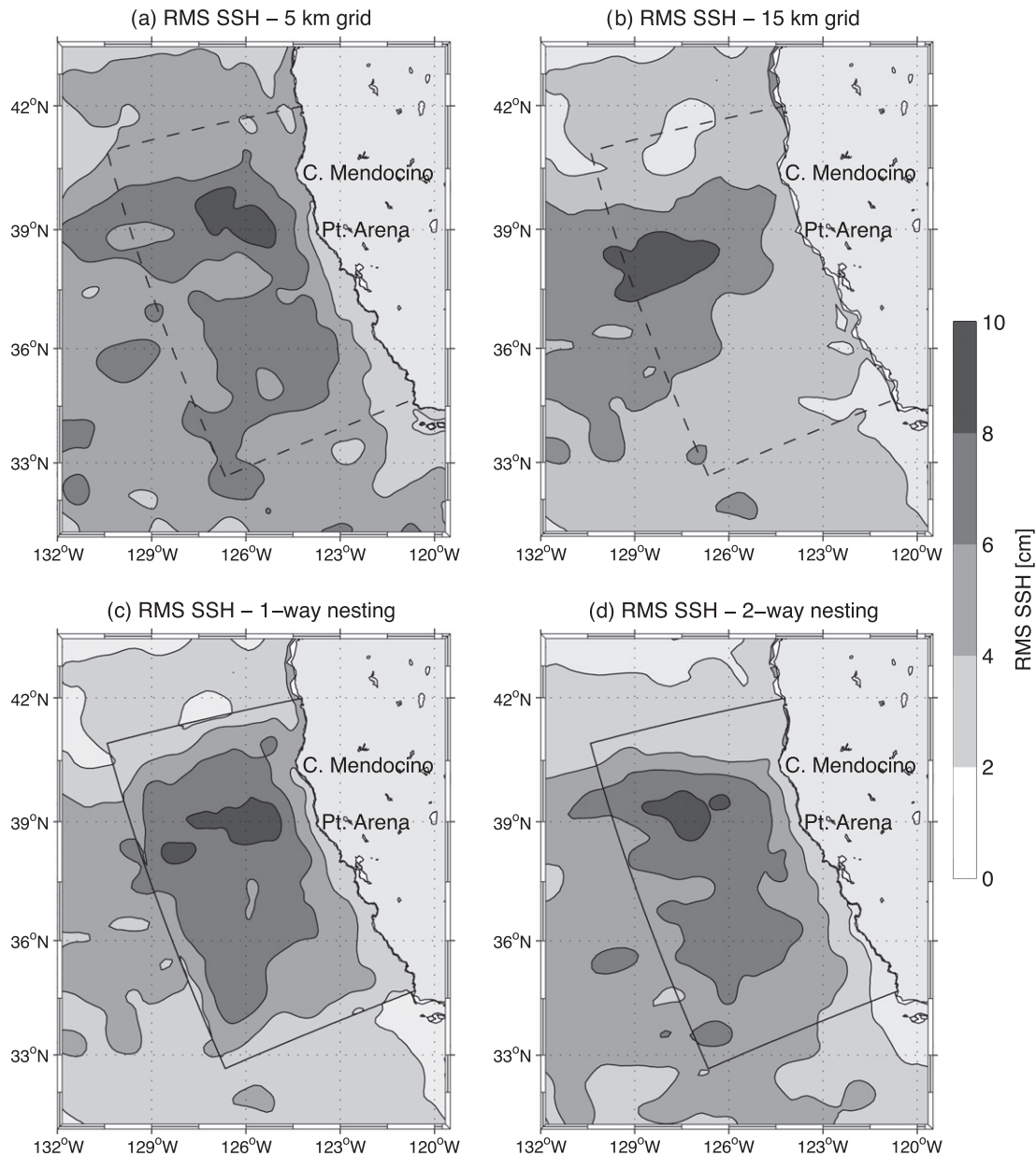
Fig. 26. Root mean square of sea surface height (RMS SSH) [cm]. a: REF. b: LOW. c: 1-WAY. d: 2-WAY.

sult of better interface transparency); and improvements outside the refinement area.

5. Conclusion

Algorithms for the implementation of two-way interactions in a split-explicit free surface ocean model were described. A new solution was proposed for the coupling between coarse and fine grid solutions at the barotropic level based on the introduction of intermediate averaged values. Solutions to the conservation problem using a flux correction algorithm was proposed and its stability was analyzed. The key role of the update scheme is also emphasized and the use of a full-weighting operator is proposed for its excellent properties regarding the filtering of small scale features.

These developments were implemented in ROMS and tested in the idealized framework of a baroclinic vortex. A comparison with a reference solution computed at high resolution shows agreement

in the refinement area and improvements in the coarse grid area as well. Normalized RMS errors do not exceed 12% for free surface elevation and 14% for temperature after 100 days of integration. They are small in comparison with one-way simulations and previous two-way implementations tested with the same idealized case.

The selected nesting algorithm is part of ROMS_AGRIF (a nested version of ROMS) and is freely available under CeCILL-C license at the ROMS_AGRIF website (http://roms.mpl.ird.fr/). It is fully compatible with ROMS parallel capabilities on both shared and distributed memory architectures (OPEN_MP or Message Passive Interface protocols). It has been successfully tested in a realistic simulation of the California Current System and clearly improves over one-way nested algorithms on interface continuity and dynamical integrity of the fine and coarse solutions. The nesting implementation of ROMS_AGRIF allows several levels of embedding and several grids at one particular level. These capabilities, combined with the inner qualities of our two-way nesting algo-

Fig. 27. Mean and RMS SSH [cm] in the 2-WAY experiment with *update_mix_low*.

rithm and generally high-order accuracy of ROMS numerics, allow for realistic simulations of coastal and ocean dynamics at multiple scales, and of upscaling and teleconnection problems.

Appendix A. Weights computation
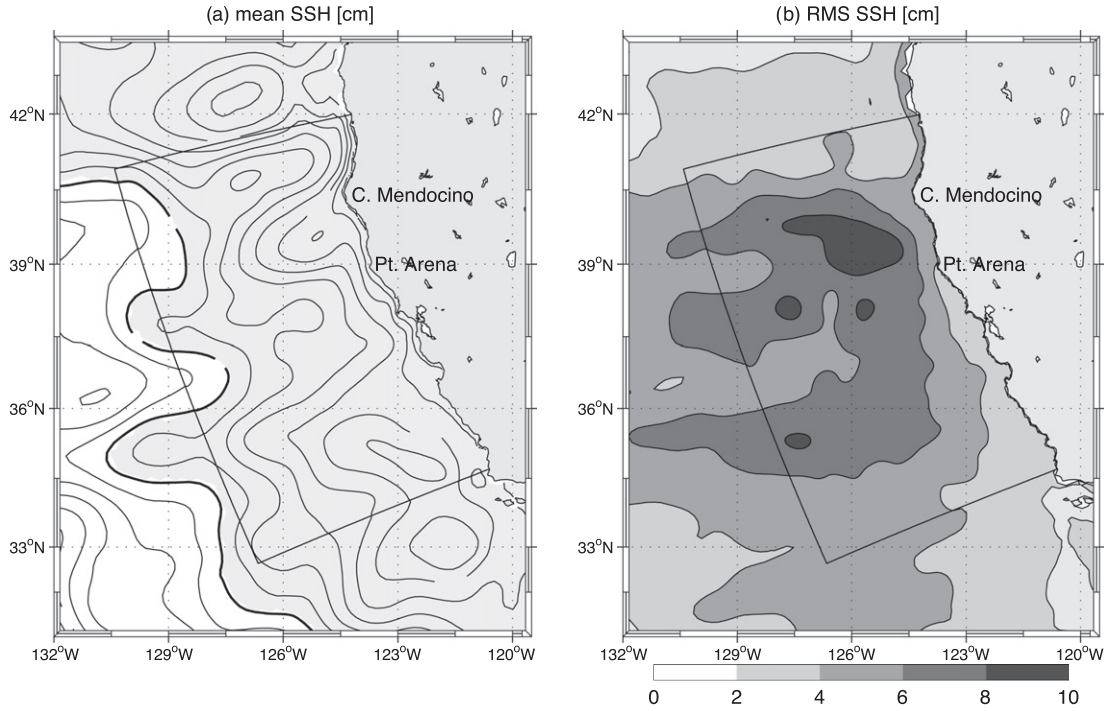
To obtain intermediate averaged values, there are several ways to compute weights satisfying (7). Here, a simple method is described. Weights for $\alpha = M^\star$ are fixed by the second condition in (7). The other weights are defined by a reccurence formula backward in time. If we suppose that $a_{m,\alpha}$ are normalized and centered at time $t = t^n + \frac{\alpha}{M^\star}\Delta t$ then we search for weights $a_{m,\alpha-1}$ normalized and centered at time $t = t^n + \frac{(\alpha-1)}{M^\star}\Delta t$ with a simple combination:

$$a_{m,\alpha-1} = \mu\ a_{m,\alpha} + \nu\ a_{m+1,\alpha} \tag{A.1}$$

It can be shown that normalization and centering respectively imply the two following relations to be satisfied by μ and ν

$$\mu\ (1 - a_{\alpha,\alpha}) + \nu\ (1 - a_{0,\alpha}) = 1 \tag{A.2}$$

$$\mu\ \left(\frac{\alpha}{M'}M - a_{\alpha,\alpha}\alpha\right) + \nu\ \left(\frac{\alpha}{M'}M - 1 + a_{0,\alpha}\right) = \frac{\alpha-1}{M'}M \tag{A.3}$$

Eqs. (A.2) and (A.3) are solved for (μ, ν). The discriminant of the system is given by

$$\Delta = \frac{\alpha}{M'}M(a_{0,\alpha} - a_{\alpha,\alpha}) + [1 - a_{0,\alpha}][(\alpha+1)a_{\alpha,\alpha} - 1]$$

There is one particular case for which the discriminant vanishes: the case of flat weights over $[1:M^\star]$ for which $M^\star = 2M, a_{m,M^\star} = \frac{1}{M^\star+1}, \forall m$. The discriminant vanishes but the system is compatible since both Eqs. (A.2), (A.3) can be rewritten as

$$\mu + \nu = \frac{M^\star + 1}{M^\star}$$

From (A.1) $a_{m,M^\star-1} = \frac{1}{M^\star}$ and by recurrence

$$a_{m,\alpha} = \frac{1}{\alpha+1}, \quad \forall\alpha, \forall m$$

The intermediate coefficients are simply rescaled from the original ones. In more general cases, it seems difficult to find conditions on a_m so that the discriminant never vanishes. For all typical tested filters, it does not.

References

Barth, A., Alvera-Azcárate, A., Rixen, M., Beckers, J.-M., 2005. Two-way nested model of mesoscale circulation features in the ligurian sea. Prog. Oceanogr. 66, 171–189.

Berger, M.J., Colella, P., 1989. Local adaptive mesh refinement for shock hydrodynamics. J. Comput. Phys. 82, 64–84.

Berger, M.J., Oliger, J., 1984. Adaptive mesh refinement for hyperbolic partial differential equation. J. Comput. Phys. 53, 484–512.

Biastoch, A., Böning, C.W., Lutjeharms, J.R.E., 2008. Agulhas leakage dynamics affects decadal variability in atlantic overturning circulation. Nature 456, 489–492.

Blumberg, A.F., Mellor, G.L., 1987. A description of a three-dimensional coastal ocean circulation model. In: Heaps, N. (Ed.), Three-Dimensional Coastal Ocean Models, vol. 4. American Geophysical Union, p. 208.

Bryan, F., 1969. A numerical method for the study of the circulation of the world ocean. J. Comput. Phys. 4, 347–376.

Conkright, M.E., Locarnini, R.A., Garcia, H.E., O'Brien, T.D., Boyer, T.P., Stephens, C., Antonov, J.I., 2002. World Ocean Atlas 2001: Objective Analyses, Data Statistics, and Figures, CD-ROM Documentation. Technical report, National Oceanographic Data Center, Silver Spring, MD.

Debreu, L., Blayo, E., 2008. Two-way embedding algorithms: a review. Ocean Dyn. 58, 415–428.

Deleersnijder, E., Legat, V., Lermusiaux, P.F.J., 2010. Mutil-scale modelling of coastal, shelf and global ocean dynamics. Ocean Dyn. 60, 1357–1359.

Dukowicz, J.K., Smith, R.D., 1994. Implicit free-surface method for the Bryan–Cox–Semtner ocean model. J. Geophys. Res. 99, 7991–8014.

Haley, P.J., Lermusiaux, P.F.J., 2010. Multiscale two-way embedding schemes for free-surface primitive-equations in the multidisciplinary simulation, estimation and assimilation system. Ocean Dyn. 60, 1497–1537.

Ham, D.A., Pain, C.C., Hanert, E., Pietrzak, J., Schröter, J., 2009. Special issue: the sixth international workshop on unstructured mesh numerical modelling of coastal, shelf and ocean flows. Imperial College London, september 1921, 2007. Ocean Model. 28, 1.

Hanert, E., Roux, D.Y.L., Legat, V., Deleersnijder, E., 2004. Advection schemes for unstructured grid ocean modelling. Ocean Model. 7, 39–58.

Hemker, P.W., 2001. On the order of prolongations and restrictions in multigrid procedures. J. Comput. Appl. Math. 32, 423–429.

Killworth, P.D., Stainforth, D., Webb, D.J., Paterson, S.M., 1991. The development of a free-surface Bryan–Cox–Semtner ocean model. J. Phys. Oceanogr. 21, 1333–1348.

Laugier, M., Angot, P., Mortier, L., 1996. Nested grid methods for an ocean model: a comparative study. Int. J. Numer. Methods Fluids 23, 1163–1195.

Levin, C., Iskandarani, M., Haidgovel, D., 2006. To continue or discontinue: comparisons of continuous and discontinuous Galerkin formulations in a spectral element ocean model. Ocean Model. 15, 56–70.

Maddison, J.R., Marshall, D.P., Pain, C.C., Piggott, M.D., 2011. Accurate representation of geostrophic and hydrostatic balance in unstructured mesh finite element ocean modelling. Ocean Model. 39, 248–261.

Marchesiello, P., McWilliams, J.C., Shchepetkin, A., 2001. Open boundary condition for long-term integration of regional oceanic models. Ocean Model. 3, 1–21.

Marchesiello, P., McWilliams, J.C., Shchepetkin, A., 2003. Equilibrium structure and dynamics of the California Current System. J. Phys. Oceanogr. 33, 753–783.

Marchesiello, P., Capet, X., Menkes, C., Kennan, S.C., 2011. Submesoscale dynamics in tropical instability waves. Ocean Model. 39, 31–46.

McWilliams, J.C., Flierl, G.R., 1979. On the evolution of isolated nonlinear vortices. J. Phys. Oceanogr. 9, 1155–1182.

Penven, P., Debreu, L., Marchesiello, P., McWilliams, J.C., 2006. Application of the ROMS embedding procedure for the central California upwelling system. Ocean Model. 12, 157–187.

Penven, P., Marchesiello, P., Debreu, L., Lefèvre, J., 2008. Software tools for pre- and post-processing of oceanic regional simulations. Environ. Model. Soft. 23, 660–662. http://dx.doi.org/10.1016/j.envsoft.2007.07.004.

Sannino, G., Herrmann, M., Carillo, A., Rupolo, V., Ruggiero, V., Artale, V., Heimbach, P., 2009. An eddy-permitting model of the mediterranean sea with a two-way grid refinement at the strait of gibraltar. Ocean Model. 30 (1), 56–72.

Shchepetkin, A.F., McWilliams, J.C., 2005. The regional oceanic modeling system (ROMS): a split-explicit, free-surface, topography-following-coordinate oceanic model. Ocean Model. 9, 347–404.

Shchepetkin, A.F., McWilliams, J.C., 2009. Correction and commentary for Ocean forecasting in terrain-following coordinates: Formulation and skill assessment of the regional ocean modeling system by Haidvogel et al. J. Comput. Phys. 227, 3595–3624.

Sidorenko, D., Wang, Q., Danilov, S., Schröter, J., 2011. Fesom under coordinated ocean-ice reference experiment forcing. Ocean Dyn. 61, 881–890.

Spall, M.A., Holland, W.R., 1991. A nested primitive equation model for oceanic applications. J. Phys. Oceanogr. 21, 205–220.

Warner, J.C., Geyer, W.R., Arango, H.G., 2010. Using a composite grid approach in a complex coastal domain to estimate estuarine residence time. Comput. Geosci. 36, 921–935.

Chapter 7

On the stability and accuracy of the harmonic and biharmonic isoneutral mixing operators in ocean models,
Ocean Modelling (2012)

On the stability and accuracy of the harmonic and biharmonic isoneutral mixing operators in ocean models

F. Lemarié [a,*], L. Debreu [b], A.F. Shchepetkin [a], J.C. McWilliams [a]

[a] Institute of Geophysics and Planetary Physics, University of California, 405 Hilgard Avenue, Los Angeles, CA 90095-1567, United States
[b] INRIA, MOISE Project-Team and Laboratoire Jean Kuntzmann, 51 rue des Mathématiques, 38041 Grenoble Cedex 9, France

ARTICLE INFO

ABSTRACT

Ocean models usually rely on a tracer mixing operator which diffuses along isoneutral directions. This requirement is imposed by the highly adiabatic nature of the oceanic interior, and a numerical simulation needs to respect these small levels of dianeutral mixing to maintain physically realistic results. For non-isopycnic models this is however non-trivial due to the non-alignment of the vertical coordinate isosurfaces with local isoneutral directions, rotated mixing operators must therefore be used. This paper considers the numerical solution of initial boundary value problems for the harmonic (Laplacian) and biharmonic rotated diffusion operators. We provide stability criteria associated with the conventional space–time discretizations of the isoneutral Laplacian operator currently in use in general circulation models. Furthermore, we propose and study possible alternatives to those schemes. A new way to handle the temporal discretization of the rotated biharmonic operator is also introduced. This scheme requires only the resolution of a simple one-dimensional tridiagonal system in the vertical direction to provide the same stability limit of the non-rotated operator. The performance of the various schemes in terms of stability and accuracy is illustrated by idealized numerical experiments of the diffusion of a passive tracer along isoneutral directions.

1. Introduction

Most ocean numerical models employ isoneutral[1] mixing operators either to parameterize the effect of unresolved mesoscale eddies (Gent and McWilliams, 1990; Smith and Gent, 2004), or more basically to control dispersive errors (Lemarié et al., 2012). It is thus very common for non-isopycnic models to implement a rotation of the diffusion tensor in a direction non-aligned with the computational grid. The benefits of a rotated mixing operator in simulating large scale flows are undeniable (e.g., Danabasoglu et al. (1994), Lengaigne et al. (2003)). Much of the improvements brought by the Gent and McWilliams (1990) parameterization of mesoscale eddies in coarse resolution models are also generally attributed to the orientation of lateral diffusive transport to be along isoneutral directions (Gent, 2011).

Redi (1982) provided the continuous form of the rotation tensor; however additional efforts were required to proceed to the actual implementation at the discrete level. Several works (Cox,

1987; Danabasoglu and McWilliams, 1995; Griffies et al., 1998; Mathieu et al., 1999; Beckers et al., 1998, 2000) tackled this problem that turned out to be more tedious than expected. The discretization in space raises difficulties to properly conserve the monotonicity (Mathieu and Deleersnijder, 1998; Beckers et al., 2000) and global tracer variance dissipation (Griffies et al., 1998) properties of the continuous operator once the problem is discretized. Moreover, due to the small vertical, relative to horizontal, grid distance typically used in numerical models the vertical and cross terms of the tensor can impose a severe restriction on the time step when explicit-in-time methods are used to advance the rotated operator. This stability problem is alleviated by the use of a standard backward Euler scheme for the vertical component of the tensor (Cox, 1987), at the expense of splitting errors[2] and associated errors in the balance between the active tracer isoneutral diffusive fluxes (Griffies, 2004, Chap. 16). This approach is used in all the state-of-the-art ocean climate models. The existing work on the isoneutral diffusion has been essentially carried out on the second-order (Laplacian) operator and under the small slope approximation (Cox, 1987; Gent and McWilliams, 1990).

---

* Corresponding author. Tel.: +1 310 825 5402; fax: +1 310 206 3051.
  E-mail address: florian@atmos.ucla.edu (F. Lemarié).

[1] Throughout the paper we use the terminology "isoneutral direction" (sometimes referred to as "epineutral direction" or simply "neutral direction" in the literature) which is tangent to the locally-referenced potential density surface and whose definition is purely local (McDougall, 1987), rather than "isopycnal direction" which more generally refers to the direction tangent to a potential density surface referenced to an arbitrary fixed pressure.

[2] In the context of this paper, splitting errors are associated with the splitting of the isoneutral Laplacian operator into a time-explicit part (the horizontal components and cross-derivative terms) and a time-implicit part (the vertical component).

Although very few studied so far, a rotated biharmonic operator may be of interest for high resolution simulations due to its known property of scale selectivity. A biharmonic operator non-aligned with the direction of the computational grid is used in Marchesiello et al. (2009) and Lemarié et al. (2012), and discussed in Griffies (2004) (Chap. 14). Because global climate models are now targeting increasingly higher horizontal resolution, the question of the viability of such an operator is not only relevant for the regional modeling community but also for the ocean climate community. As an illustration, Hecht (2010) shows that for a 0.1^0 resolution global model the use of a Lax–Wendroff scheme with an intrinsic numerically-induced diffusion aligned with the horizontal direction leads to too much of a spurious dianeutral mixing in the Equatorial Pacific. This result suggests that even for eddy-resolving simulations an isoneutral mixing operator could be required. This motivates the design of a scale-selective (high-order) rotated operator. This is however not straightforward to maintain the stability of such an operator which can produce undesirable effects like overshooting/undershooting (Delhez and Deleersnijder, 2007) and spurious cabelling processes (Griffies, 2004, Chap. 14). To our knowledge, the current implementations of rotated biharmonic operators are based on an explicit Euler scheme in time with ad hoc tapering or clipping of the neutral slopes to maintain good stability properties (Marchesiello et al., 2009). This approach has however the undesirable effect to allow spurious dianeutral mixing even at places where the slopes are modest and satisfy the small slope approximation.

The aim of this paper is to study a set of space–time discretizations of the rotated harmonic and biharmonic mixing, and to assess them in terms of accuracy, stability and monotonicity violations. One additional constraint we impose to ourselves is accuracy relative to large grid slope ratios (defined as the ratio between the neutral slope and the aspect ratio of the computational grid) in order to make the scheme adequate for use in a terrain-following σ-coordinate model. Indeed, problems with σ models are generally more pernicious than with z-level models because it is not unusual that the slope between the computational grid and the isoneutral direction steepens to be greater than the grid aspect ratio. The paper is organized as follows. In Section 2 we introduce the formulation of the isoneutral mixing problem as well as three different ways to discretize the problem in space. Then Sections 3 and 4 are respectively dedicated to the temporal discretization of the rotated Laplacian and biharmonic operators. Section 5 provides the useful details to proceed to the actual implementation of the different schemes in ocean models. Finally, numerical experiments are designed to illustrate the properties of various space–time discretizations in Section 6. For clarity, the important notations used throughout the paper are given in Table 1.

An alternative approach to the use of isoneutral mixing operators is the design of a vertical coordinate system following the isopycnals (e.g., Hallberg and Adcroft, 2009; Hofmeister et al., 2010; Leclair and Madec, 2011). The present paper is a complementary effort in exploring the merits of different approaches to representing the nearly adiabatic flow in the oceanic interior.

2. Isoneutral mixing problem formulation

2.1. Continuous formulation

This section briefly introduces the continuous form of the problem under investigation throughout the paper. The three spatial directions are labeled x_1, x_2 for the horizontal coordinates, and x_3 for the vertical coordinate. We note q the tracer of interest, ∇

Table 1
Important notations for the three-dimensional analysis of the isoneutral mixing operators, where $m = 1,2,3$ denotes the three spatial direction.

State variables	
q	Three dimensional tracer (can be temperature or salinity)
ρ	Three dimensional density field
Coordinates and spatial operators	
x_1, x_2	Horizontal coordinates
x_3	Vertical coordinate, pointing upward.
Δx_m	Measure of the grid-box interface in the x_m direction
Δt	Time-step for the temporal discretization
$\partial_m = \partial_{x_m}$	Partial derivative in the x_m direction
$\mathscr{D}_2$	Isoneutral Laplacian operator, defined in (2.1)
$\mathscr{D}_4$	Isoneutral biharmonic operator, defined in (2.8)
$\mathbf{F} = (F^{(1)}, F^{(2)}, F^{(3)})$	Diffusive flux, defined in (2.7) at a continuous level and in (2.13), (2.14), and (2.19) at a discrete level
$\mathscr{J}_m(q, \rho)$	Jacobian determinant, defined as $\partial_m q \partial_3 \rho - \partial_m \rho \partial_3 q$
$\delta_m q$	Discrete differentiation in the x_m direction, defined in (2.12) (for $\delta_m \rho$ a particular instance of differentiation to allow computation of isoneutral directions is presented in Section 5.6)
Parameters	
κ_m	Diffusivity in the x_m direction
B_m	Hyperdiffusivity in the x_m direction
$\boldsymbol{\alpha} = (\alpha_1, \alpha_2, 0)$	Neutral slope vector, defined in (2.5)
s_m	grid slope ratio, defined in (2.22)
β_m	Parameter controlling the stencil of the spatial discretization of isoneutral mixing operators, defined in (2.21)
$w^{\pm}$	Switches to select the computational stencil depending on the orientation of neutral slopes, defined in (2.15)
θ	Stabilizing parameter for the Method of Stabilizing Corrections, defined in (3.3)
$\bar{\kappa}$	Stabilizing diffusivity for the Method of Stabilizing Corrections, defined in (4.1)
σ_m	Parabolic Courant number in the x_m direction, defined in (3.4)
$\sigma_m^{(4)}$	Square root of the biharmonic Courant number in the x_m direction, defined in (4.2)
z_{mn}	Discrete Fourier modes multiplied by Δt, defined in (3.14)
ϕ_m	Normalized Fourier frequency ($|\phi_m| \leqslant \pi$) in the x_m direction
λ	Exact amplification factor of the isoneutral Laplacian (Section 3) and biharmonic (Section 4) operators
$\tilde{\lambda}$	Approximate amplification factor obtained after space–time discretization of the isoneutral Laplacian (Section 3) and biharmonic (Section 4) operators
μ_2	Ratio between the maximum time-steps allowed for stability of the horizontal and the isoneutral Laplacian operators discretized using a forward Euler scheme, defined in (3.33)
μ_4	Same as μ_2 for the biharmonic operator, defined in (4.14)

the three-dimensional gradient operator and $\partial_m = \partial_{x_m}(m = 1, 3)$. Following Redi (1982) a mixing operator $\mathscr{D}_2$ leading to diffusion along isoneutral directions with a diffusivity κ can be defined as

$$\mathscr{D}_2 = \mathbf{V} \cdot (\mathbf{R}\nabla q) = \sum_{m=1}^{3} \partial_m \left(\sum_{n=1}^{3} r_{mn} \partial_n q \right), \quad \mathbf{R} = [r_{mn}]_{1 \leqslant m,n \leqslant 3}, \quad (2.1)$$

with $\mathbf{R}$ the following rotation tensor

$$r_{mn} = \kappa \left(\delta_{mn} - \frac{(\partial_m \rho)(\partial_n \rho)}{\|\nabla \rho\|^2} \right), \quad (2.2)$$

where δ_{mn} is the conventional Kronecker delta and ρ is the locally referenced potential density. This form of the tensor shows that the matrix $\mathbf{R}$ is symmetric positive semi-definite ($r_{mm} \geqslant 0$ and $|r_{mn}| \leqslant \sqrt{r_{mm}r_{nn}}$) and thus defines a diffusion tensor. Moreover, by construction, the diffusive flux which takes the form $\mathbf{F} = (F^{(1)}, F^{(2)}, F^{(3)})$ with $F^{(m)} = -\sum_{n=1}^{3} r_{mn} \partial_n q$ satisfies the orthogonality condition $\mathbf{F} \cdot \boldsymbol{\rho}_\perp = 0$, with $\boldsymbol{\rho}_\perp$ the unit vector in the dianeutral direction. In the limit that horizontal density gradients are much more smaller than vertical gradients (i.e., $\sqrt{(\partial_1 \rho)^2 + (\partial_2 \rho)^2}/\partial_3 \rho \ll 1$), a simpler form of the tensor, preserving the isoneutral form of mixing, can be devised (Cox, 1987; Gent and McWilliams, 1990). This assumption corresponds to the so-called small slope approximation, and reduces the tensor (2.2) to

$$\begin{cases} r_{mn} = \kappa \delta_{mn}, & (1 \leqslant m, n \leqslant 2), \\ r_{m3} = r_{3m} = -\kappa \partial_m \rho/\partial_3 \rho, & (1 \leqslant m \leqslant 2), \\ r_{33} = \kappa((\partial_1 \rho)^2 + (\partial_2 \rho)^2)/(\partial_3 \rho)^2. \end{cases} \quad (2.3)$$

This formulation of the rotated diffusion under the small slope approximation had also been derived early by Solomon (1971) in a two-dimensional (x_1, x_3) case. Throughout this paper we consider the small slope approximation and we allow an anisotropy in the diffusivities (i.e., $\kappa_1 \neq \kappa_2$), the corresponding matrix form of the tensor is

$$\mathbf{R} = \begin{pmatrix} \kappa_1 & 0 & \kappa_1 \alpha_1 \\ 0 & \kappa_2 & \kappa_2 \alpha_2 \\ \kappa_1 \alpha_1 & \kappa_2 \alpha_2 & \kappa_1 \alpha_1^2 + \kappa_2 \alpha_2^2 \end{pmatrix}, \quad (2.4)$$

with

$$\boldsymbol{\alpha} = (\alpha_1, \alpha_2, 0) = -\frac{(\partial_1 \rho, \partial_2 \rho, 0)}{\partial_3 \rho}, \quad (2.5)$$

the neutral slope vector. It is straightforward to check that this form of the tensor preserves the symmetry as well as the semi-positive definiteness of the full tensor (2.2). For a Laplacian diffusion of a tracer field q in an unbounded domain $\Omega = \mathbb{R}^3$, we can cast the corresponding evolution problem over a time interval $[0,T]$ under a conservative form

$$\begin{cases} \partial_t q = \mathscr{D}_2(q) = \mathbf{V} \cdot (\mathbf{R}\nabla q) = -\mathbf{V} \cdot \mathbf{F} & \text{in } \Omega \times [0,T], \\ q|_{t=0} = q_0(x_1, x_2, x_3) & \text{in } \Omega, \end{cases} \quad (2.6)$$

with q_0 a given initial condition, and

$$-\mathbf{F} = \begin{pmatrix} -F^{(1)} \\ -F^{(2)} \\ -F^{(3)} \end{pmatrix} = \begin{pmatrix} \kappa_1(\partial_1 q + \alpha_1 \partial_3 q) \\ \kappa_2(\partial_2 q + \alpha_2 \partial_3 q) \\ -\alpha_1 F^{(1)} - \alpha_2 F^{(2)} \end{pmatrix}. \quad (2.7)$$

This problem is here temporarily defined on an unbounded spatial domain in order to facilitate the theoretical study in Sections 3 and 4. For bounded domains, we provide the necessary boundary conditions in Section 5. Using the notations previously defined, the problem for the rotated biharmonic operator reads

$$\begin{cases} \partial_t q = \mathscr{D}_4(q) = -\mathscr{D}_2(\Phi), & \text{with } \Phi = \mathscr{D}_2(q), & \text{in } \Omega \times [0,T], \\ q|_{t=0} = q_0(x_1, x_2, x_3) & \text{in } \Omega, \end{cases} \quad (2.8)$$

For the biharmonic case, the diffusivities κ_1 and κ_2 in (2.4) must be replaced by $\sqrt{B_1}$ and $\sqrt{B_2}$ with B_1 and B_2 the hyper-diffusivities. Following Griffies (2004) (Chap. 14), we formulate the biharmonic operator as the composition of two rotated Laplacian operators with coefficients $\sqrt{B_m}$ $(m = 1, 2)$ because this form ensures that, at the continuous level, the variance of q is strictly dissipated. In the remainder of the paper we focus on the initial value problems (2.6) and (2.8) with the tensor of rotation defined in (2.4).

Unless explicitly said differently, we will use throughout the paper the subscript m to denote the horizontal directions, $m = (1, 2)$.

2.2. Spatial discretization of the isoneutral diffusion operator

2.2.1. Semi-discrete considerations

The spatial discretization of the isoneutral diffusion operator is a difficult problem which have been thoroughly tackled by Cox (1987), Beckers et al. (1998, 2000), Griffies et al. (1998). We, first, briefly introduce the delicacies associated with the implementation of the operator $\mathscr{D}_2$. Because the x_1 and x_2 directions are independent when adopting the small slope approximation, we consider only the problem defined in the (x_1, x_3) plane. As derived in Beckers et al. (2000), the continuous formulation of the rotated Laplacian operator can be formulated as

$$\mathscr{D}_2(q) = \partial_1 \left(\kappa_1 \frac{\mathscr{I}_1(q, \rho)}{\partial_3 \rho} \right) - \partial_3 \left(\kappa_1 \frac{\partial_1 \rho}{\partial_3 \rho} \frac{\mathscr{I}_1(q, \rho)}{\partial_3 \rho} \right)$$

where $\mathscr{I}_1(q, \rho) = \partial_1 q \partial_3 \rho - \partial_1 \rho \partial_3 q$ is a Jacobian determinant. The main difficulty resides in the evaluation of the $\mathscr{I}_1(q, \rho)/\partial_3 \rho$ term on a staggered grid. This term has to be evaluated at the cell interfaces referred to as u-points and w-points in Fig. 1. Note that, usually, the neutral slope $\partial_1 \rho/\partial_3 \rho$ used in practice is not the result of a discretization scheme only, but additional ad hoc constraints taking the form of a smoothing, tapering, or clipping procedure are applied; more details concerning this point are given in Section 5. Defining the arithmetic average operators $\overline{\cdot}^{(1)}$ in the horizontal and $\overline{\cdot}^{(3)}$ in the vertical, and noting that the natural position of the $\partial_1 q$ and $\partial_1 \rho$ (resp. $\partial_3 q$ and $\partial_3 \rho$) terms is at u-points (resp. w-points), several linear discretizations of the Jacobian determinant can be proposed using a semi-discrete view of the problem:

- A simple discrete analog of the Jacobian $\mathscr{I}_1$ has been implemented in the early versions of the MOM-GFDL[3] model (Cox, 1987; Danabasoglu and McWilliams, 1995), at u-points and w-points the discretization reads

$$\begin{cases} \mathscr{I}_1^u(q, \rho) = \partial_3 \rho \left(\partial_1 q - \partial_1 \rho \frac{\overline{\partial_3 q}^{(3,1)}}{\overline{\partial_3 \rho}^{(3,1)}} \right) \\ \mathscr{I}_1^w(q, \rho) = \partial_3 \rho \left(\partial_1 \overline{q}^{(3,1)} - \partial_1 \overline{\rho}^{(3,1)} \frac{\partial_3 q}{\partial_3 \rho} \right) \end{cases} \quad (2.9)$$

where q and ρ are subject to a double averaging in the x_3 and x_1 directions before differencing, which makes this approach prone to a computational mode (Griffies et al., 1998). Note that the $\partial_3 \rho$ in front of the parenthesis has a passive role here because this is formally $\mathscr{I}_1(q, \rho)/\partial_3 \rho$ that we aim at discretizing.
- An other way to compute the Jacobian is by differencing before averaging, as proposed in Griffies et al. (1998). In this case we have

---

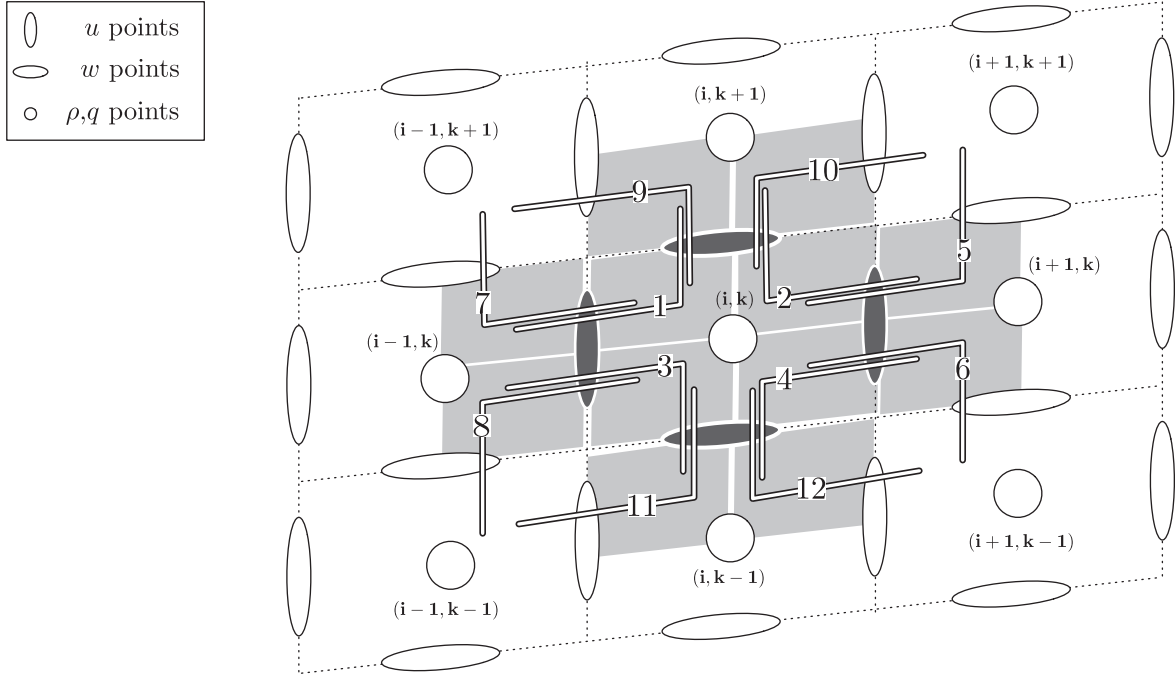[3] Geophysical Fluid Dynamics Laboratory.

Fig. 1. Grid stencil, constructed upon 12 triads, involved in the computation of the rotated Laplacian operator in the (x_1, x_3) plane. Each triad has an associated quarter cell (gray shaded areas). The zonal $F^{(1)}$ and vertical $F^{(3)}$ components of the isoneutral diffusive flux are computed at the cell interfaces surrounding the (i, k) location (dark grey shaded points). The numbering of the triads is meant to be consistent with the one used in Griffies (2004) (Chap. 16).

$$
\begin{cases}
\mathscr{I}_1^u(q, \rho) = \partial_3 \rho \left(\partial_1 q - \partial_1 \rho \, \overline{\overline{\left[\frac{\partial_3 q}{\partial_3 \rho}\right]}}^{(1,3)} \right) \\
\mathscr{I}_1^w(q, \rho) = \partial_3 \rho \left(\overline{\overline{\partial_1 q}}^{(1,3)} - \overline{\overline{\partial_1 \rho}}^{(1,3)} \left[\frac{\partial_3 q}{\partial_3 \rho}\right] \right),
\end{cases}
\tag{2.10}
$$

where the term in brackets could be simply replaced by $\partial q / \partial \rho$, however we keep $\partial_3 \rho$ explicitly to clearly identify the neutral slopes.

- To obtain more symmetry between the u and w points we can define the following quantity at the corners of the grid cells (sometimes referred as to Ψ-points)

$$
\mathscr{I}_1^\Psi(q, \rho) = \partial_3 \rho \left(\overline{\partial_1 q}^{(3)} - \overline{\partial_1 \rho}^{(3)} \overline{\left[\frac{\partial_3 q}{\partial_3 \rho}\right]}^{(1)} \right)
$$

which gives

$$
\mathscr{I}_1^u(q, \rho) = \overline{\mathscr{I}_1^\Psi(q, \rho)}^{(3)}, \quad \text{and} \quad \mathscr{I}_1^w(q, \rho) = \overline{\mathscr{I}_1^\Psi(q, \rho)}^{(1)}.
$$

This discretization has the interesting property to define the neutral slopes at Ψ-points only, which makes it more convenient to handle the tapering, clipping, or smoothing procedure. Indeed, for the schemes (2.9) and (2.10) this procedure has to be done twice, at u and w points. However this discretization has the major drawback not to reduce to the classical $(1, -2, 1)$ stencil when the neutral slopes vanish, which disqualifies it.

- We can suggest a last approach which would consist in providing more flexibility to the discretization by introducing two sets of weights v_n^u and v_n^w in the problem. We define the operator $\overline{\cdot}^{(v^u)}$ as the weighted average of the four w-points surrounding a u-point, and $\overline{\cdot}^{(v^w)}$ as the weighted average of the four u-points surrounding a w-point. A generalization of scheme (2.10) is

$$
\begin{cases}
\mathscr{I}_1^u(q, \rho) = \partial_3 \rho \left(\partial_1 q - \partial_1 \rho \left\{ \overline{\left[\frac{\partial_3 q}{\partial_3 \rho}\right]}^{(v^u)} \right\} \right) \\
\mathscr{I}_1^w(q, \rho) = \partial_3 \rho \left(\overline{\partial_1 q}^{(v^w)} - \overline{\partial_1 \rho}^{(v^w)} \left[\frac{\partial_3 q}{\partial_3 \rho}\right] \right),
\end{cases}
\tag{2.11}
$$

The parameters v_n^u and v_n^w are set by requiring additional properties of the discretization scheme. An example is the LINEAR1 scheme of Beckers et al. (2000) which sets the v_n^u and v_n^w coefficients to get the most compact stencil in the dianeutral direction to reduce the amount of spurious dianeutral mixing. This scheme reduces to a $(1, -2, 1)$ stencil in the diagonal when the angle between the computational grid and the isoneutral direction is ±45 degrees; this property is not satisfied by (2.10).

To our knowledge, three different schemes are currently in use in ocean models. The Nucleus for European Modeling of the Ocean (NEMO, Madec (2008)) and Coupled Large-scale Ice Ocean (CLIO, Goosse et al. (2008), Mathieu et al. (1999)) models use the Cox (1987) discretization (2.9). In NEMO, an horizontal two-dimensional Laplacian operator acting to smooth the neutral slopes provides the extra diffusion needed to stabilize the scheme (Cox, 1987; Mathieu and Deleersnijder, 1998; Griffies et al., 1998). In the Modular Ocean Model (MOM, Griffies (2010)) and Parallel Ocean Program (POP, Smith et al. (2010)) the discretization (2.10) based on the tracer/density triad formalism (Fig. 1) is used. A triad is defined as an elementary computational stencil of the jacobian $\mathscr{I}_1(q, \rho)$, and therefore of the rotated operator (Griffies et al., 1998). In MOM, an extra vertical smoothing of the $\partial_3 \rho$ term is used (Griffies, 2010, Chap. 16). Finally, even if not explicitly documented, the scheme (2.11) is implemented in the σ-coordinate Regional Oceanic Modeling System (ROMS, Shchepetkin and McWilliams (2005)) and is routinely used so far to rotate along geopotentials the explicit diffusion in the sponge layers near the open boundaries. We describe below the procedure to compute the weighted averages, and we show that this scheme can also be expressed in a tracer triad formalism. In the present study, the MOM/POP discretization is referred to as TRIADS, the NEMO/CLIO discretization as COX, and the ROMS discretization as SW-TRIADS (SW stands for switching).

From our experience, besides the instability identified by Griffies et al. (1998), the TRIADS and COX schemes provide very similar

results. The differences are greater between the TRIADS and the SW-TRIADS schemes, we thus focus our study on those two schemes only.

2.2.2. Discrete fluxes

We define

$$\delta_1 q_{i+\frac{1}{2},j,k} = q_{i+1,j,k} - q_{i,k} \quad \text{and} \quad \delta_3 q_{i,j,k+\frac{1}{2}} = q_{i,j,k+1} - q_{i,j,k}. \qquad (2.12)$$

The metric terms $(\Delta x_2)_{i+\frac{1}{2}j}$ and $(\Delta x_3)_{i+\frac{1}{2}j,k}$ are the horizontal and vertical measures of the corresponding grid-box interfaces and $(\Delta x_1)_{i+\frac{1}{2}j}$ is the distance between $q_{i+1,j,k}$ and $q_{i,j,k}$. The vertical index k varies from $k = 1$ for the first grid cell next to the ocean floor to $k = N$ at the surface, N corresponds to the number of vertical levels of the discretization. The methodology to compute the $\delta_m\rho$ terms to obtain the isoneutral directions is given explicitly later in Section 5.6 and differs from the formula (2.12).

The interfacial $F^{(1)}$ flux discretized using the TRIADS scheme reads

$$-F^{(1,\text{triads})}_{i+\frac{1}{2},j,k} = \kappa_1 (\Delta x_2)_{i+\frac{1}{2}j} (\Delta x_3)_{i+\frac{1}{2}j,k} \left[\frac{\delta_1 q_{i+\frac{1}{2},j,k}}{(\Delta x_1)_{i+\frac{1}{2}j}} - \frac{\delta_1 \rho_{i+\frac{1}{2},j,k}}{(\Delta x_1)_{i+\frac{1}{2}j}} \cdot \frac{1}{4} \left\{ \frac{\delta_3 q_{i,j,k-\frac{1}{2}}}{\delta_3 \rho_{i,j,k-\frac{1}{2}}} \right. \right.$$
$$\left. \left. + \frac{\delta_3 q_{i+1,j,k+\frac{1}{2}}}{\delta_3 \rho_{i+1,j,k+\frac{1}{2}}} + \frac{\delta_3 q_{i+1,j,k-\frac{1}{2}}}{\delta_3 \rho_{i+1,j,k-\frac{1}{2}}} + \frac{\delta_3 q_{i,j,k+\frac{1}{2}}}{\delta_3 \rho_{i,j,k+\frac{1}{2}}} \right\} \right]. \qquad (2.13)$$

Using the notations introduced in Fig. 1, we see that the TRIADS scheme uses the four triads labelled 2, 4, 5, and 6 with the same weight $w = 1/4$. The derivatives in the x_1-direction are computed along the horizontal segment of a triad while the derivatives in the x_3-direction are computed along the vertical segment. Alternatively, the spirit of the LINEAR1 scheme introduced in Beckers et al. (2000) is to weight those triads depending on the orientation of the slope by keeping only two of them. The LINEAR1 scheme was originally derived for a constant slope, we extend this scheme to the case with spatially variable neutral slopes to obtain the more general SW-TRIADS scheme. If we assume a stable stratification (i.e., $\delta_3 \rho_{i,j,k+\frac{1}{2}} < 0, \ \forall k$), this scheme reads

$$-F^{(1,\text{sw-triads})}_{i+\frac{1}{2},j,k} = \kappa_1 (\Delta x_2)_{i+\frac{1}{2}j} (\Delta x_3)_{i+\frac{1}{2}j,k} \left[\frac{\delta_1 q_{i+\frac{1}{2},j,k}}{(\Delta x_1)_{i+\frac{1}{2}j}} - \frac{1}{2} \left\{ \frac{w^+_{i+\frac{1}{2},j,k}}{(\Delta x_1)_{i+\frac{1}{2}j}} \left(\frac{\delta_3 q_{i,j,k-\frac{1}{2}}}{\delta_3 \rho_{i,j,k-\frac{1}{2}}} \right. \right. \right.$$
$$\left. \left. \left. + \frac{\delta_3 q_{i+1,j,k+\frac{1}{2}}}{\delta_3 \rho_{i+1,j,k+\frac{1}{2}}} \right) + \frac{w^-_{i+\frac{1}{2},j,k}}{(\Delta x_1)_{i+\frac{1}{2}j}} \left(\frac{\delta_3 q_{i,j,k+\frac{1}{2}}}{\delta_3 \rho_{i,j,k+\frac{1}{2}}} + \frac{\delta_3 q_{i+1,j,k-\frac{1}{2}}}{\delta_3 \rho_{i+1,j,k-\frac{1}{2}}} \right) \right\} \right]. \qquad (2.14)$$

with

$$w^+_{i+\frac{1}{2},j,k} = \max\left(\delta_1 \rho_{i+\frac{1}{2},j,k}, 0\right), \qquad w^-_{i+\frac{1}{2},j,k} = \min\left(\delta_1 \rho_{i+\frac{1}{2},j,k}, 0\right). \qquad (2.15)$$

Depending on the orientation of the slope, either triads 4 and 5 are selected, or triads 2 and 6. This results in a compact four point stencil for the discretization of the $F^{(1,\text{sw-triads})}_{i+\frac{1}{2},j,k}$ interfacial flux. The cancellation of the contribution of cross-isoneutral points with the SW-TRIADS scheme tends to reduce the amount of spurious dianeutral mixing associated with discretization errors. This point will be exemplified in Section 6. The discretization of the vertical flux $F^{(3)}$ does not raise any additional difficulty for the TRIADS scheme and can be found in Griffies et al. (1998). We show in the next subsection a way to construct the vertical flux $F^{(3,\text{sw-triads})}_{i,j,k+\frac{1}{2}}$ so that the SW-TRIADS scheme satisfies a globally diminishing tracer variance.

2.3. Global tracer variance dissipation

As shown in Griffies et al. (1998), the TRIADS scheme has been constructed to ensure that the discretized operator globally satisfies the tracer variance dissipation property of the continuous

operator. This scheme is designed on the basis of the variational principle. A weak form of the problem under investigation can be defined through

$$\mathscr{G}[q] = -\frac{1}{2} \int_\Omega \nabla q \cdot (\mathbf{R}\nabla q) \, d\Omega \qquad (2.16)$$

where $\mathscr{G}[q]$ is a functional whose Frèchet derivative $\delta\mathscr{G}[q]/\delta q$ gives the diffusion operator. Due to the symmetric positive semi-definite property of the diffusion tensor $\mathbf{R}$, $\mathscr{G}$ is negative semi-definite. This property implies that the corresponding operator acts to decrease the total tracer variance, indeed Griffies et al. (1998) showed that $\partial_t \int_\Omega q^2 \, d\Omega = 4\mathscr{G}[q]$. Unlike the COX scheme, the TRIADS scheme provides a negative semi-definite functional at the discrete level, thus ensuring that the corresponding discretized operator is globally strictly dissipative (Griffies et al., 1998; Smith and Gent, 2004; Griffies, 2004). The reader is referred to Griffies (2004) (Chap. 16) for more details about the foundations for the dissipation functional and its discretization.

Consistent with the notations introduced in Griffies (2004) (Chap. 16) the discretization of the functional $\mathscr{G}$, in the (x_1, x_3) plane, is given by

$$\mathscr{G}^{(x_1-x_3)}[q] = -\frac{1}{2} \sum_{i,k} \sum_{n=1}^{12} A(n) V(n) \left[\frac{\delta_1 q(n)}{\Delta x_1(n)} + \alpha_1(n) \frac{\delta_3 q(n)}{\Delta x_3(n)} \right]^2 \equiv \sum_{i,k} \left(\sum_{n=1}^{12} L^{(n)}_{i,k} \right), \qquad (2.17)$$

where the subscripts (i,k) run over all the cells of the computational domain. In (2.17), $A(n)$ is the diffusivity associated with triad n, $V(n)$ is the volume of quarter-cell n, $\Delta x_1(n)$ and $\Delta x_3(n)$ are respectively the length of the horizontal and vertical segments of triad n. For a given cell (i,k), the contribution to the discrete functional is given by $\sum_{n=1}^{12} L^{(n)}_{i,k}$ which corresponds to 12 nonpositive components associated with 12 quarter cells, built in such a way that there is a unique volume $V(n)$ and diffusivity $A(n)$ for each quarter-cell (represented as light gray shaded areas in Fig. 1). This procedure ensures that $\mathscr{G}^{(x_1-x_3)}[q]$ is negative semi-definite. For example, the contribution of triad 1 to the discretized diffusion operator is given by

$$\frac{\delta L^{(1)}_{i,k}}{\delta q_{i,k}} = -A(1)V(1) \left(\frac{\delta_1 q(1)}{\Delta x_1(1)} + \alpha_1(1) \frac{\delta_3 q(1)}{\Delta x_3(1)} \right) \left(\underbrace{\frac{1}{\Delta x_1(1)}}_{\text{contribution to } F^{(1)}} - \underbrace{\frac{\alpha_1(1)}{\Delta x_3(1)}}_{\text{contribution to } F^{(3)}} \right) \qquad (2.18)$$

which shows that when a triad is used to compute $F^{(1)}$, the same triad is used to compute $F^{(3)}$. The only difference between the TRIADS and the SW-TRIADS schemes is in the weighting of the 12 triads, the SW-TRIADS scheme simply cancels the contribution of certain triads depending on the orientation of the neutral slope α_1, which is equivalent to set $A(n)$ to zero for those triads. This means that once a triad n is rejected during the computation of $F^{(1,\text{sw-triads})}$ it cannot be used again to compute $F^{(3,\text{sw-triads})}$ because the diffusivity $A(n)$ associated with this triad is zero. If we follow this simple rule, we find that there is a unique way to define the vertical interfacial flux $F^{(3,\text{sw-triads})}_{i,j,k+\frac{1}{2}}$:

$$-F^{(3,\text{sw-triads})}_{i,j,k+\frac{1}{2}} = \kappa_1 \frac{(\Delta x_3)_{i,j,k+\frac{1}{2}}}{\delta_3 \rho_{i,j,k+\frac{1}{2}}} \left[\frac{w^+_{i-\frac{1}{2},j,k}}{(\Delta x_1)_{i-\frac{1}{2}j}} \left(\frac{\delta_1 \rho_{i-\frac{1}{2},j,k}}{(\Delta x_1)_{i-\frac{1}{2}j}} \cdot \frac{\delta_3 q_{i,j,k+\frac{1}{2}}}{\delta_3 \rho_{i,j,k+\frac{1}{2}}} - \frac{\delta_1 q_{i-\frac{1}{2},j,k}}{(\Delta x_1)_{i-\frac{1}{2}j}} \right) \right.$$
$$+ \frac{w^+_{i+\frac{1}{2},j,k+1}}{(\Delta x_1)_{i+\frac{1}{2}j}} \left(\frac{\delta_1 \rho_{i+\frac{1}{2},j,k+1}}{(\Delta x_1)_{i+\frac{1}{2}j}} \cdot \frac{\delta_3 q_{i,j,k+\frac{1}{2}}}{\delta_3 \rho_{i,j,k+\frac{1}{2}}} - \frac{\delta_1 q_{i+\frac{1}{2},j,k+1}}{(\Delta x_1)_{i+\frac{1}{2}j}} \right)$$
$$+ \frac{w^-_{i-\frac{1}{2},j,k+1}}{(\Delta x_1)_{i-\frac{1}{2}j}} \left(\frac{\delta_1 \rho_{i-\frac{1}{2},j,k+1}}{(\Delta x_1)_{i-\frac{1}{2}j}} \cdot \frac{\delta_3 q_{i,j,k+\frac{1}{2}}}{\delta_3 \rho_{i,j,k+\frac{1}{2}}} - \frac{\delta_1 q_{i-\frac{1}{2},j,k+1}}{(\Delta x_1)_{i-\frac{1}{2}j}} \right)$$
$$\left. + \frac{w^-_{i+\frac{1}{2},j,k}}{(\Delta x_1)_{i+\frac{1}{2}j}} \left(\frac{\delta_1 \rho_{i+\frac{1}{2},j,k}}{(\Delta x_1)_{i+\frac{1}{2}j}} \cdot \frac{\delta_3 q_{i,j,k+\frac{1}{2}}}{\delta_3 \rho_{i,j,k+\frac{1}{2}}} - \frac{\delta_1 q_{i+\frac{1}{2},j,k}}{(\Delta x_1)_{i+\frac{1}{2}j}} \right) \right] \times \frac{1}{W} \qquad (2.19)$$
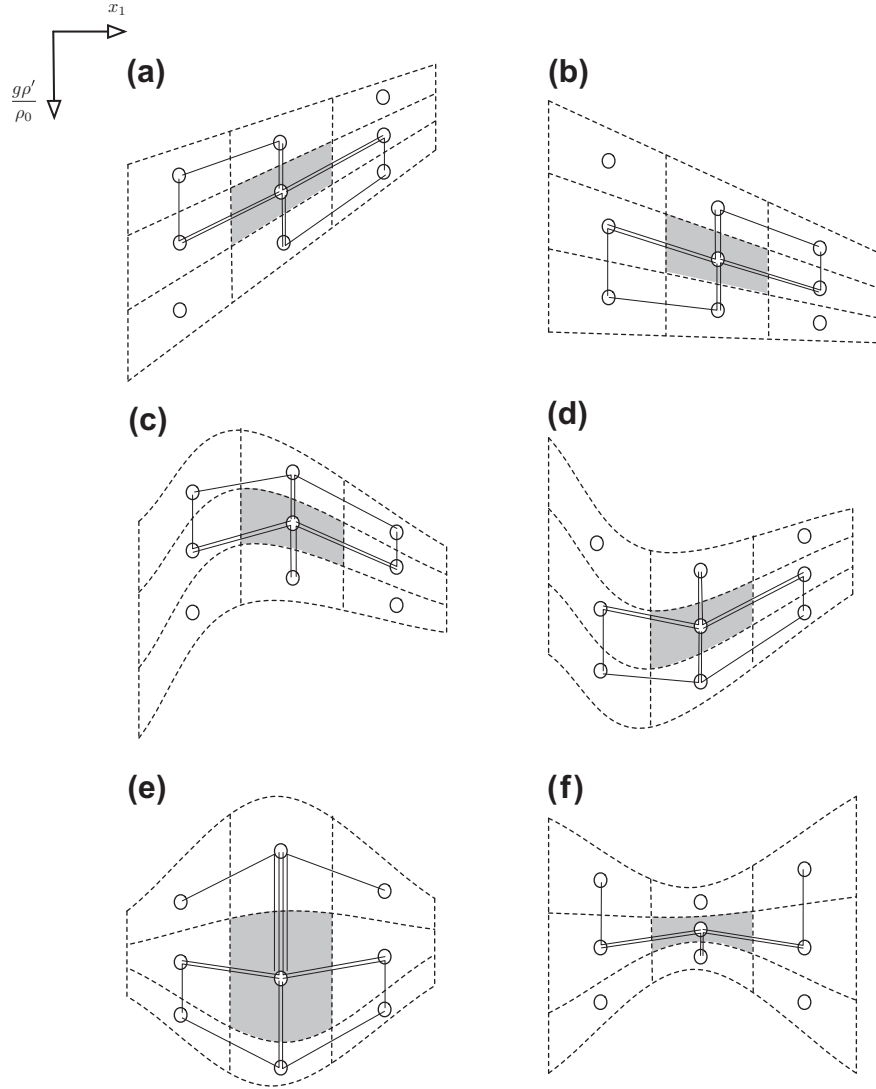
Fig. 2. Computational stencil, represented as triads (black lines), involved in the computation of the rotated Laplacian operator with the SW-TRIADS scheme for different orientations between the computational grid (dashed lines) and the isoneutral direction which corresponds to horizontal lines in the $(x_1, g\rho'/\rho_0)$ frame. In cases (a)–(d), six triads are selected while eight triads are selected in (e) and 4 in (f).

where W corresponds to the number of selected triads, i.e., the number of nonzero $w^\pm$ terms. For $W = 2$, it is easy to check that the rotated operator discretized with the SW-TRIADS scheme is based on exactly six triads and is consistent with the functional discretization (2.17) where the contribution of the six other triads is rejected by setting their associated diffusivities to zero. As illustrated in Fig. 2, we have $W = 2$ for the common situations encountered in ocean models. There are however some degenerated cases (Fig. 2(e) and (f)) for which $W \neq 2$. In those very specific cases, the scheme does not satisfy the functional discretization because some triads are used to compute $F^{(3)}$ with a different weight than it is used to compute $F^{(1)}$. We can show easily that when the stratification has a $2\Delta x_1$ mode, as studied in Griffies et al. (1998), the SW-TRIADS ensures a global tracer variance reduction.

The SW-TRIADS scheme is a special instance of the TRIADS scheme, it thus makes the implementation of this scheme as straightforward. When spatially variable diffusion coefficients are used, each triad must be weighted by the corresponding coefficient. Usually, those coefficients are computed at the horizontal interfacial u points. In this case, in (2.19) the constant diffusivity κ_1 should be dropped and each coefficient $w^\pm$ must be multiplied by the corresponding diffusivity. Because each triad crosses exactly

one u point (Fig. 1) there is a unique diffusivity associated with a given triad.

It is worth mentioning that the tracer variance diminishing property should not be confused with the total variation diminishing (TVD) property which is monotonicity preserving. As we show in Section 6, the rotated operators discretized with the TRIADS or the SW-TRIADS scheme do not preserve monotonicity (Mathieu and Deleersnijder, 1998; Beckers et al., 2000).

Because the rotated biharmonic operator corresponds to two successive rotated Laplacian operators, it does not raise any additional difficulties as long as the spatial discretization is concerned. In the two following sections we consider the time integration of the rotated operators, and we assume that the slope vector $\boldsymbol{\alpha}$ is spatially constant and that the grid is uniform to make the stability analysis tractable. For a constant slope, the discrete approximation $\widetilde{\mathscr{D}_2}$ of the rotated operator at the position (i,j,k) is given by

$$(\widetilde{\mathscr{D}_2})_{i,j,k} = -\left[\frac{F^{(1)}_{i+\frac{1}{2},j,k} - F^{(1)}_{i-\frac{1}{2},j,k}}{\Delta x_1 \Delta x_2 \Delta x_3} + \frac{F^{(2)}_{i,j+\frac{1}{2},k} - F^{(2)}_{i,j-\frac{1}{2},k}}{\Delta x_1 \Delta x_2 \Delta x_3} + \frac{F^{(3)}_{i,j,k+\frac{1}{2}} - F^{(3)}_{i,j,k-\frac{1}{2}}}{\Delta x_3}\right]$$

$$= \sum_{p=-1}^{1}\sum_{l=-1}^{1}\mu^{(1)}_{p,l}q_{i+p,j,k+l} + \sum_{p=-1}^{1}\sum_{l=-1}^{1}\mu^{(2)}_{p,l}q_{i,j+p,k+l}, \qquad (2.20)$$

with

$$\left[\mu_{p,l}^{(m)}\right]_{-1\leqslant p,l\leqslant 1}=\frac{\kappa_m}{\Delta x_m^2}\begin{pmatrix}(\beta_m-1)\frac{s_m}{2} & s_m(s_m-\beta_m) & (1+\beta_m)\frac{s_m}{2} \\ 1-s_m\beta_m & -2(1+s_m^2)+2s_m\beta_m & 1-s_m\beta_m \\ (1+\beta_m)\frac{s_m}{2} & s_m(s_m-\beta_m) & (\beta_m-1)\frac{s_m}{2}\end{pmatrix}$$

$$(2.21)$$

where

$$s_m=\frac{\Delta x_m}{\Delta x_3}\alpha_m \tag{2.22}$$

is the grid slope ratio, $\beta_m\equiv 0$ gives the TRIADS scheme and $\beta_m=1$ for $s_m\geqslant 0$ (resp. $\beta_m=-1$ for $s_m<0$) the SW-TRIADS scheme. The rotated Laplacian operator in the x_m-direction is thus discretized on a centered 9-point stencil if $\beta_m=0$ and on a more compact 7-point stencil if $|\beta_m|=1$. As far as the rotated biharmonic is concerned, the discretization is based on a 25-point stencil with the TRIADS and a 19-point stencil with the SW-TRIADS. We do not investigate this possibility in this study, but the parameter β_m could be used as a degree of freedom to derive alternative properties of the discretization.

The grid slope ratio s_m, introduced in (2.21), is a key dimensionless parameter that will be used throughout this paper. This parameter corresponds to the ratio between the neutral slope α_m and the aspect ratio $\Delta x_3/\Delta x_m$. We thus have $s_m=\pm 1$ for a ± 45 degrees slope. Values of $|s_m|$ greater than 1 generally lead to a degradation of the accuracy of the rotated diffusion due to the need for extrapolation to compute the isoneutral direction. For typical applications with a coarse resolution global climate model, $|s_m|$ can reach $\mathcal{O}(10)$ values (e.g., $s_m=10$ for $\alpha_m=5\times 10^{-3}$, $\Delta x_1=100$ km, and $\Delta x_3=50$ m). Note that the use of slope clipping or tapering sets an upper bound on s_m which can not be arbitrarily large in this case. Large grid slope ratios should not be confused with large neutral slopes, meaning that large values of s_m can exist even under the small slope approximation. In the context of a σ to geopotentials rotation, as in Marchesiello et al. (2009), s_m corresponds to the so-called hydrostatic inconsistency number.

3. Time discretization of the isoneutral Laplacian operator

3.1. Proposed schemes

The overall objective of this section is to derive a time-integration scheme whose stability limit is imposed by the horizontal components of the tensor. In this case the constraint on the time step Δt of the temporal discretization would be equivalent between the rotated and the non-rotated operators. Moreover, because we are considering a diffusive process, we do not feel necessary to strive to design a high-order scheme in time, the aim is to keep the study as simple as possible. The rotated Laplacian operator $\mathscr{D}_2$, with neutral slopes α_m and diffusivities κ_m, can be linearly decomposed into a sum of three functions $\mathscr{D}_2(q)=\sum_{m=1}^3 G_m(q)$, where

$$\begin{cases}G_m(q)=\partial_m(\kappa_m[\partial_m q+\alpha_m\partial_3 q])+\partial_3(\alpha_m\kappa_m\partial_m q) & (m=1,2),\\ G_3(q)=\partial_3\big(\big[\kappa_1\alpha_1^2+\kappa_2\alpha_2^2\big]\partial_3 q\big).\end{cases}$$

$$(3.1)$$

We consider that the piece $G_0(q)=G_1(q)+G_2(q)$ is always treated explicitly in time-integration schemes, whereas G_3 represent a stiff and unidirectional contribution that can be treated implicitly, if needed. The integration of the G_0 term in an implicit manner would require the solution of a complicated implicit system in the horizontal direction which would be laborious to implement in parallel and would significantly affect the performances of the numerical model. The common practice in climate models is to

use a standard backward Euler scheme to advance the vertical G_3 component of the tensor (Cox, 1987). Using the time step $\Delta t>0$, we note q^n the approximation $q^n\approx q(t_n)$, with $t_n=n\Delta t$. The semi-discretized version of the scheme introduced by Cox (1987) is

$$q^{n+1}=q^n+\Delta t\{G_0(q^n)+G_3(q^{n+1})\}. \tag{3.2}$$

In the following this scheme will be referred to as (IMP) scheme. Moreover, the fully explicit version, i.e., with $G_3(q^n)$ instead of $G_3(q^{n+1})$ in (3.2), will be denoted by (EXP).

Following the work of Douglas (1962), Andreev (1967) or Craig and Sneyd (1988) (see also in 't Hout and Welfert (2009) for a review), split schemes such as alternating direction implicit (ADI) have proved valuable in the approximation of the solutions of multi-dimensional parabolic problems with mixed derivatives. This type of scheme is usually implemented with unidirectional implicit corrector steps in each spatial direction to pursue an unconditional stability. Alternatives to this scheme allowing one or more spatial directions to be treated explicitly can be found in Douglas and Gunn (1964), van der Houwen and Verwer (1979) or Hundsdorfer (2002). Those authors propose a multi-stage method: at the first stage, a consistent (explicit) approximation of the operator is evaluated, while all succeeding stages serve to improve the stability. This scheme has been called Method of Stabilizing Corrections (referred to as (MSC) hereafter) in van der Houwen and Verwer (1979) and seems particularly well suited for our problem because it provides a consistent, efficient, and easy-to-implement scheme with degrees of freedom to ensure good stability properties. Moreover, we see in Section 4 that this approach can be extended to the time-integration of the rotated biharmonic operator. For the diffusion problem (2.6), the (MSC) scheme reads

$$\begin{cases}q^\star=q^n+\Delta t\{G_0(q^n)+G_3(q^n)\},\\ q^{n+1}=q^\star+\theta\Delta t\{G_3(q^{n+1})-G_3(q^n)\},\end{cases}$$

$$(3.3)$$

where $\theta\geqslant 0$ is a real parameter. Note that for our purpose we only allow a stabilizing correction in the vertical direction. In (3.3), $\theta=0$ gives the (EXP) scheme and $\theta=1$ the (IMP) scheme. For $\theta=1/2$, we retrieve the Crank–Nicolson scheme, however we will see later that this scheme is not particularly well-suited in the context of the isoneutral Laplacian operator because it does not stabilize the cross-derivative terms as effectively as the (IMP) scheme. In the next section we study the stability range of the (EXP), (IMP) and (MSC) methods subject to the TRIADS or SW-TRIADS discretizations in space.

3.2. Important results

We give here the important results of our study on the Laplacian operator, the associated proof is provided in Section 3.3. Those results are given in terms of the parabolic Courant number

$$\sigma_m=\kappa_m\frac{\Delta t}{\Delta x_m^2}. \tag{3.4}$$

3.2.1. Horizontal Laplacian operator
When using an Euler forward scheme, the stability limit of the two-dimensional horizontal Laplacian operator, discretized on a five-point stencil,[4] is

$$\sigma_1+\sigma_2\leqslant\frac{1}{2}. \tag{3.5}$$

---

[4] A nine-point discrete Laplacian operator would provide a stability criterion which is somewhat less restrictive than for the usual five-point one.

3.2.2 Isoneutral Laplacian operator

- **TRIADS discretization**
  - The (EXP) scheme is stable for

$$\sigma_1(1 + s_1^2) + \sigma_2(1 + s_2^2) \leqslant \frac{1}{2} \qquad (3.6)$$

which is always more restrictive than (3.5).

  - The stability limit of the (IMP) scheme is given by (3.5).
  - The same stability constraint (3.5) is obtained for the (MSC) scheme when θ is chosen such that

$$(s_1^2\sigma_1 + s_2^2\sigma_2)\theta = \frac{1}{2}\max\{-1 + 2[\sigma_1(1+s_1^2) + \sigma_2(1+s_2^2)], 0\}. \qquad (3.7)$$

The value of θ ranges from $\theta = 0$ when the (EXP) scheme is stable to $\theta = 1$ when $\sigma_1 + \sigma_2 = 1/2$. The amount of implicit diffusion is thus always smaller with the (MSC) scheme compared with the (IMP) scheme.

- **SW-TRIADS discretization**
  - The (EXP) scheme is stable for

$$\sigma_1 \max\{s_1^2, 1\} + \sigma_2 \max\{s_2^2, 1\} \leqslant \frac{1}{2} \qquad (3.8)$$

which shows that for $s_1^2 \leqslant 1$ and $s_2^2 \leqslant 1$ the stability constraint is the same as the non-rotated operator.

  - As for the TRIADS case, the (IMP) scheme is stable if condition (3.5) is satisfied.
  - The stability condition (3.5) applies to the (MSC) scheme for

$$\theta = \max\left\{\frac{|s_1| - 1}{|s_1|}, \frac{|s_2| - 1}{|s_2|}, 0\right\} \qquad (3.9)$$

Before demonstrating those results, we draw a few remarks:

- As shown in Section 3.2.1, the values of θ given in (3.7) and (3.9) are sufficient conditions for stability. Some conservative choices have been made during the analysis to simplify the results.
- The value of θ in (3.7) is equal to 1 when $\sigma_1 + \sigma_2 = 1/2$. Consequently, if the diffusivities κ_m are constant everywhere and such that $\sigma_1 + \sigma_2 = 1/2$, the (MSC) scheme is equivalent to the (IMP) scheme. The (MSC) scheme can, however, be particularly interesting when flow-dependent diffusion coefficients are used because it minimizes the amount of implicit vertical diffusion required for stability.
- The Crank–Nicolson scheme (i.e., $\theta = 1/2$) does not provide a sufficient condition ensuring that the isoneutral Laplacian operator can be advanced with the same time step as the horizontal diffusion operator. Indeed, we show in (3.7) that values of θ larger than 1/2 are required, especially when $\sigma_1 + \sigma_2 = 1/2$.

We now provide the methodology to derive the stability conditions.

3.3. Proof through linear stability analysis

We first assume that the tracer q can be Fourier decomposed as

$$q(x_1, x_2, x_3, t) = \sum_{\mathbf{k}} A_{\mathbf{k}}(t) \exp\left(i\sum_{m=1}^{3} k_m x_m\right), \quad i = \sqrt{-1} \qquad (3.10)$$

with $\mathbf{k} = (k_1, k_2, k_3)$ the three-dimensional wave-vector. Substitution in (2.6) leads to the linear damping equation

$$\frac{dq}{dt} = -\eta q, \quad \text{with } \eta = \sum_{m=1}^{2}\kappa_m(k_m + \alpha_m k_3)^2, \qquad (3.11)$$

and subsequently

$$q(t_{n+1} = t_n + \Delta t) = \exp(-\eta\Delta t)q(t_n) = \lambda q(t_n). \qquad (3.12)$$

$\lambda = e^{-\eta\Delta t}$ provides the exact damping obtained with a "perfect" discretization. We can derive the approximate damping $\tilde{\lambda}$ provided by the space–time discretization

$$q(t_{n+1}) = \tilde{\lambda}(z_{11}, z_{22}, z_{33}, z_{31}, z_{13}, z_{32}, z_{23})q(t_n), \qquad (3.13)$$

where the z_{mn} terms are all real and obtained by substitution of discrete Fourier modes in (2.20) and multiplication by Δt:

$$z_{mm} = -2\sigma_m(1 - \cos\phi_m) \qquad\qquad m = 1, 2$$
$$z_{33} = -2(s_1^2\sigma_1 + s_2^2\sigma_2)(1 - \cos\phi_3)$$
$$z_{m3} = z_{3m} = -s_m\sigma_m[\sin\phi_m\sin\phi_3 - \beta_m(1 - \cos\phi_m)(1 - \cos\phi_3)] \quad m = 1, 2 \qquad (3.14)$$

with $\phi_m = k_m\Delta x_m$ ($|\phi_m| \leqslant \pi$) the normalized Fourier frequencies. Using those notations, we obtain $\eta\Delta t = \sum_{m=1}^{2}\sigma_m(\phi_m + s_m\phi_3)^2$ in (3.12).

The response function of the (MSC) time scheme (3.3) subject to the spatial discretization (2.20) and (2.21) is

$$\tilde{\lambda} = 1 + \frac{z_0 + z_{33}}{1 - \theta z_{33}}, \quad z_0 = \sum_{m=1}^{2}(z_{mm} + z_{m3} + z_{3m}). \qquad (3.15)$$

Stability of the scheme under investigation is obtained for $|\tilde{\lambda}| \leqslant 1$.

In the subsequent paragraphs we first show that the condition $\tilde{\lambda} \leqslant 1$ is satisfied whatever the value of θ, and whatever the spatial discretization. Then, we show that the TRIADS scheme always provides a more restrictive stability range than the SW-TRIADS scheme. Eventually, we derive the requirements to satisfy the constraint $\tilde{\lambda} \geqslant -1$ which ensures that the corresponding scheme is stable.

3.3.1. Upper bound on $\tilde{\lambda}$

To emphasize the fact that the z_{mm} terms are negative, we define $y_m = \sqrt{2\sigma_m(1 - \cos\phi_m)}$, and $y_3 = \sqrt{y_{31}^2 + y_{32}^2}$ (with $y_{3m} = \sqrt{2s_m^2\sigma_m(1 - \cos\phi_3)}$) so that $z_{mm} = -y_m^2$. Moreover, we introduce the vector $\boldsymbol{v}_m = (\sin\phi_m, \varsigma_m(1 - \cos\phi_m))$, with ς_m such that $\beta_m = -\varsigma_m\varsigma_3$ and $|\varsigma_m| \leqslant 1$. We can easily show that

$$z_{m3} = z_{3m} = -s_m\sigma_m(\boldsymbol{v}_m \cdot \boldsymbol{v}_3) \qquad (3.16)$$

and for $m = 1, 2$ (thanks to the condition $|\varsigma_m| \leqslant 1$)

$$\sigma_m\|\boldsymbol{v}_m\|^2 \leqslant \sigma_m\left\{\sin^2\phi_m + (1 - \cos\phi_m)^2\right\} = y_m^2, \qquad (3.17)$$

where $\|\bullet\|$ defines the ℓ_2-norm. Eqs. (3.16) and (3.17) imply that

$$-z_{33} - \sum_{m=1}^{2}(z_{mm} + z_{m3} + z_{3m}) = y_1^2 + y_2^2 + y_3^2 + 2s_1\sigma_1(\boldsymbol{v}_1$$
$$\cdot \boldsymbol{v}_3) + 2s_2\sigma_2(\boldsymbol{v}_2 \cdot \boldsymbol{v}_3)$$
$$\geqslant \sum_{m=1}^{2}\sigma_m\|\boldsymbol{v}_m\|^2 + s_m^2\sigma_m\|\boldsymbol{v}_3\|^2$$
$$+ 2s_m\sigma_m(\boldsymbol{v}_m \cdot \boldsymbol{v}_3)$$
$$= \sum_{m=1}^{2}\sigma_m\|\boldsymbol{v}_m + s_m\boldsymbol{v}_3\|^2 \geqslant 0. \qquad (3.18)$$

This result is sufficient to show that $\tilde{\lambda} \leqslant 1$, indeed thanks to (3.15) we have

$$\tilde{\lambda} = 1 - \left\{ \frac{-z_{33} - \sum_{m=1}^{2}(z_{mm} + z_{m3} + z_{3m})}{1 + \theta y_3^2} \right\} \leqslant 1, \tag{3.19}$$

because we showed that the term in curly brackets is positive. Note that this result is valid whatever $|\beta_m| \leqslant 1$ and hence whatever the spatial discretization. This result means that stability of the time discretization is obtained for $\tilde{\lambda} \geqslant -1$. In the following we first show that if this condition is satisfied by the TRIADS scheme the same applies to the SW-TRIADS scheme.

3.3.2. Effect of the cross-terms

As shown in (3.14), the difference between the two spatial discretizations under consideration appears only in the z_{3m} terms. The definition of the slope dependent parameter β_m for the SW-TRIADS scheme is such that for all s_m, $\beta_m s_m = |s_m|$. Substitution in (3.14) leads to

$$-z_{3m} = \sigma_m[s_m \sin \phi_m \sin \phi_3 - |s_m|(1 - \cos \phi_m)(1 - \cos \phi_3)]$$
$$\leqslant \sigma_m s_m \sin \phi_m \sin \phi_3. \tag{3.20}$$

This inequality shows that the cross-terms discretized using the SW-TRIADS scheme always provide a less restrictive stability constraint than when using the TRIADS scheme (which corresponds to $\beta_m = 0$ in (3.14)). It means that the condition $\tilde{\lambda} \geqslant -1$ is more difficult to satisfy with the TRIADS discretization. We thus consider in the remainder of this section the most restrictive case $\beta_m = 0$. We provide in Appendix B the results obtained for a non-zero value of β_m with the SW-TRIADS discretization.

3.3.3. Stability conditions

Starting from (3.15), stability is obtained for

$$\tilde{\lambda} \geqslant -1 \Longleftrightarrow \sum_{m=1}^{2} \varphi_m - 2(1 + \theta y_3^2) \leqslant 0, \quad \varphi_m = y_m^2 + y_{3m}^2 - z_{3m} - z_{m3}. \tag{3.21}$$

Taking $s_m = 0$ (i.e., $y_{3m} = z_{3m} = 0$) and $\theta = 0$ in (3.21) we find the stability constraint $y_1^2 + y_2^2 \leqslant 2$ which corresponds to the usual constraint (3.5) obtained when the horizontal Laplacian operator is integrated using an Euler explicit scheme. Ideally, this is the stability constraint we are targeting for the general case $s_m \neq 0$ so that the rotated Laplacian operator does not involve the use of a smaller time step than the non-rotated Laplacian operator. The stability condition (3.21) can be more conveniently written as

$$\varphi_1^\theta + \varphi_2^\theta \leqslant 2, \qquad \text{with } \varphi_m^\theta = \varphi_m - 2\theta y_{m3}^2. \tag{3.22}$$

The stability analysis therefore requires the derivation of a proper upper bound for the φ_m^θ functions. For clarity, we describe the computation of such an upper bound in Appendix A, and we recall here only the final result:

$$\varphi_1^\theta + \varphi_2^\theta \leqslant 2\sigma_1 \mathscr{M}(\theta, s_1) + 2\sigma_2 \mathscr{M}(\theta, s_2), \tag{3.23}$$

where

$$\mathscr{M}(\theta, s_m) = 1 + s_m^2(1 - 2\theta) + \sqrt{(1 + s_m^2)(1 + s_m^2(1 - 2\theta)^2)}. \tag{3.24}$$

Combining (3.22) and (3.23) we get the following criteria for stability,

$$2\sigma_1 \mathscr{M}(\theta, s_1) + 2\sigma_2 \mathscr{M}(\theta, s_2) \leqslant 2. \tag{3.25}$$

In the fully-explicit (EXP) case (i.e., $\theta = 0$) we get $\mathscr{M}(0, s_m) = 2(1 + s_m^2)$, the associated stability criteria reads

$$\sigma_1(1 + s_1^2) + \sigma_2(1 + s_2^2) \leqslant \frac{1}{2}. \tag{3.26}$$

This result leads to the stability condition (3.6) and is consistent with the result found in Mathieu et al. (1999) (Eq. (31)). Furthermore, for $\theta = 1$ (i.e., the (IMP) scheme), we get $\mathscr{M}(1, s_m) = 2$ and thus $\sigma_1 + \sigma_2 \leqslant 1/2$ which corresponds to the stability limit of the non-rotated operator. This result shows that by treating implicitly the vertical component of the tensor there is no additional constraint arising from the cross-terms. Finally, for the (MSC) scheme the optimal value of θ providing a minimum of implicit diffusion is solution of the equation $\sigma_1 \mathscr{M}(\theta, s_1) + \sigma_2 \mathscr{M}(\theta, s_2) = 1$. However, the analytical solution of this equation is extremely complex and would be impractical anyway for real applications. We, therefore, proceed in a more conservative way by noting that for $\theta \leqslant 1$

$$\mathscr{M}(\theta, s_m) \leqslant \mathscr{M}^\ddagger(\theta, s_m) = 2(1 + s_m^2) - 2\theta s_m^2. \tag{3.27}$$

It is now straightforward to determine the analytical solution $\theta^\star$ of the equation $\sigma_1 \mathscr{M}^\ddagger(\theta, s_1) + \sigma_2 \mathscr{M}^\ddagger(\theta, s_2) = 1$:

$$(s_1^2 \sigma_1 + s_2^2 \sigma_2)\theta^\star = \frac{1}{2}\max\{-1 + 2(1 + s_1^2)\sigma_1 + 2(1 + s_2^2)\sigma_2, 0\}. \tag{3.28}$$

We can check that $\theta^\star = 0$ if the (EXP) scheme is stable and $\theta^\star = 1$ for $\sigma_1 + \sigma_2 = 1/2$. In Fig. 3 we show the values of the stabilizing parameter $\theta^\star$ associated with the TRIADS scheme as well as the values of the stabilizing parameter obtained in Appendix B with the SW-TRIADS. We, first, want to emphasize the fact that those values of θ are sufficient conditions for stability but are not the optimal values, conservative choices have been made during our analysis. This remark explains why in Fig. 3 larger values of θ are shown for the SW-TRIADS, compared to the TRIADS (particularly for small values of σ_m), although we argue earlier that the TRIADS scheme always provide a more restrictive stability condition than the SW-TRIADS scheme. It can be shown that the value of θ given in (3.28) for the TRIADS scheme is also a sufficient condition for stability with the SW-TRIADS scheme.

In general, we see that the value of θ required to maintain stability of the scheme can be smaller than 1 in numerous cases and hence that splitting errors (as defined in footnote 2) associated with the (IMP) scheme can be further reduced. It, however, still needs to be checked that this reduction of splitting errors has a clear and meaningful impact on the physical solution of numerical models. This question is left for a future study.

3.4. Non-oscillatory scheme

Throughout the previous subsection we have considered the requirement $|\tilde{\lambda}| \leqslant 1$ which is a necessary condition for stability. However a more severe condition $0 \leqslant \tilde{\lambda} \leqslant 1$ may be required to ensure a non-oscillatory behavior of the temporal integration (Mathieu et al., 1999). This corresponds to the so-called "no flip-flop" condition, as opposed to the condition $|\tilde{\lambda}| \leqslant 1$ which allows a flip-flop behavior in time unlike the exact solution of the problem under investigation (Cushman-Roisin and Beckers, 2011, Chap. 5). Indeed, we see in (3.13) that negative values of $\tilde{\lambda}$ would allow the solution to oscillate at each time step because $\tilde{\lambda}, \tilde{\lambda}^2, \tilde{\lambda}^3, \ldots$ would change sign. It is straightforward to extend the results described in Section 3.3 to the "no flip-flop" case. In the non-rotated case, (3.5) reduces to

$$\sigma_1 + \sigma_2 \leqslant 1/4, \tag{3.29}$$

which means that the time step must be divided by two. In the rotated case, the (EXP) scheme satisfies the condition $\tilde{\lambda} \geqslant 0$ for

$$\sigma_1(1 + s_1^2) + \sigma_2(1 + s_2^2) \leqslant \frac{1}{4}. \tag{3.30}$$

For the (IMP) scheme, the absence of flip-flop requires

$$\sigma_1\left(1 + \sqrt{1 + s_1^2}\right) + \sigma_2\left(1 + \sqrt{1 + s_2^2}\right) \leqslant \frac{1}{2} \tag{3.31}$$
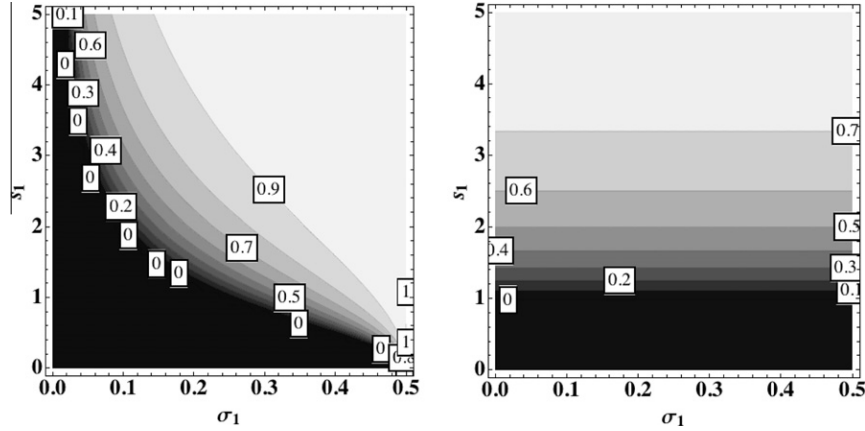
Fig. 3. Optimized values $\theta^\star$ (for $\sigma_2 = 0$) of the stabilizing parameter θ obtained with the TRIADS scheme (left) and the SW-TRIADS scheme (right) with respect to σ_1 and s_1.

which is the condition used in the CLIO model to set Δt (Mathieu et al., 1999). The inequality (3.31) shows that the no flip-flop condition is satisfied under a stability constraint more restrictive than (3.29). In the case of the (MSC) scheme, the no flip-flop condition is achieved if (3.29) is satisfied and if θ is chosen such that

$$(s_1^2\sigma_1 + s_2^2\sigma_2)\theta^\star = \frac{1}{2}\max\left\{-1 + 4(1 + s_1^2)\sigma_1 + 4(1 + s_2^2)\sigma_2, 0\right\}.$$
(3.32)

For this value of θ the scheme satisfies the "no flip-flop" condition if the horizontal terms do, which reduces to (3.29). In (3.32), the value of $\theta^\star$ varies from $\theta^\star = 0$ when (3.30) is satisfied to $\theta^\star = 2$ when $\sigma_1 + \sigma_2 = 1/4$. The aim here is not to claim that flip-flops should not be allowed. Indeed, the widely used horizontal Laplacian operator advanced with a forward Euler scheme allows flip-flops for $1/4 \leqslant \sigma_1 + \sigma_2 \leqslant 1/2$ and it did not turn out to be problematic in practice. This paragraph was meant to illustrate that, unlike the (IMP) scheme which is restricted by the cross-terms, the (MSC) scheme is general enough to ensure additional properties of the time discretization like the absence of flip-flops.

3.5. Comments

The literature on multi-dimensional parabolic problems with mixed derivatives has been focused on demonstrating the stability of the method of stabilizing corrections (and/or the ADI method). To our knowledge, there are no systematic studies on the impact of the stabilizing step on the accuracy of the solution. This point is discussed in this section and turns out to be very helpful to anticipate the behavior of the scheme in practical situations.

3.5.1. Spatial discretization

In Fig. 4 we show the amplification factor obtained when the (EXP) scheme is stable. Because in this case there are no splitting errors, this figure is indicative of the differences between the two spatial discretizations under consideration. To make the interpretation of the results easier, we consider the no flip-flop case. In the figure, we can not formally identify the direction of the computational grid because it represents a wavenumber space, but it is instructive to look at the amplification factor in several directions. Using (3.10), we find that ∇q and (k_1, k_3) are collinear. Moreover it is straightforward to see that the dianeutral direction and $\boldsymbol{\rho}_\perp = (-\alpha_1, 1)$ are collinear too, as well as the isoneutral direction and $\boldsymbol{\rho}_\parallel = (1, \alpha_1)$. We specifically look at two directions in the (ϕ_1, ϕ_3) plane corresponding to two different angles between ∇q and the isoneutral/dianeutral direction:

- $D_1 = \phi_1 + s_1\phi_3 = 0$ (i.e., $\nabla q \cdot \boldsymbol{\rho}_\parallel = 0$) corresponds to the direction along which ∇q is perpendicular to the isoneutral direction. In this case, q is constant in the isoneutral direction (because the iso-q lines are perpendicular to ∇q). Because an isoneutral mixing operator should not affect a tracer constant in the isoneutral direction, we expect the amplification factor λ to be equal to one along this line, otherwise it would indicate that the slope is computed in an inaccurate way and that dianeutral mixing occurs.
- A perpendicular to D_1 is $D_2 = \phi_3 - s_1\phi_1 = 0$ (i.e., $\nabla q \cdot \boldsymbol{\rho}_\perp = 0$) which corresponds to the direction along which ∇q is aligned with the isoneutral direction. In this case, we see from Fig. 4 (top panels) that the exact amplification factor is equivalent to the one of a one-dimensional Laplacian operator, indeed we would have $\eta\Delta t = \sigma_1(1 + s_1^2)^2\phi_1^2$.

Along the line $D_1 = 0$, the SW-TRIADS always provide a damping in better agreement with the exact one, compared to the TRIADS scheme, thus indicating a more accurate computation of the direction of diffusion for $s_1 = 1/2$ as well as $s_1 = 2$. We see that, for $\phi_3 = 0$, all the discretizations have the same behavior and that the mode $|\phi_1| = \pi$ is effectively damped. This was expected because the difference between the TRIADS and SW-TRIADS schemes is in the cross-terms which vanish for $\phi_3 = 0$. Unlike the SW-TRIADS, the TRIADS scheme has also the property to efficiently damp the checkerboard mode $(|\phi_1|, |\phi_3|) = (\pi, \pi)$, whatever the grid slope ratio (Fig. 4). The lack of damping associated with the SW-TRIADS is not problematic to solve the initial value problem (2.6) because we assume some regularity of the initial condition, and the checkerboard mode is not present in this case. However, when advective terms are considered they can allow the creation and accumulation of dispersive errors which are expected to be controlled by diffusive processes. We usually do not rely on the rotated operator to damp small scale noise in the vertical direction because the vertical mixing parameterization does it efficiently (otherwise grid-scale noise would arise when an horizontal Laplacian operator is used). In the horizontal direction, those operators are generally the only source of numerical filtering, and we thus expect them to control small-scale noise. For example, for $s_1 = 1/2$, the TRIADS scheme does it efficiently while the SW-TRIADS scheme damps the $2\Delta x_1$ mode $(|\phi_1| = \pi)$ only for well-resolved scales in the vertical $(|\phi_3| \leqslant \pi/2)$. Note that it is, however, expected that the $2\Delta x_3$ mode $(|\phi_3| = \pi)$ is already significantly damped by the vertical mixing scheme. The weak damping with the SW-TRIADS scheme can be seen also along the line $D_2 = 0$. In this direction, the exact amplification factor and the TRIADS scheme ensure a monotonic damping, indeed λ monotonically decreases when we go from well-resolved to
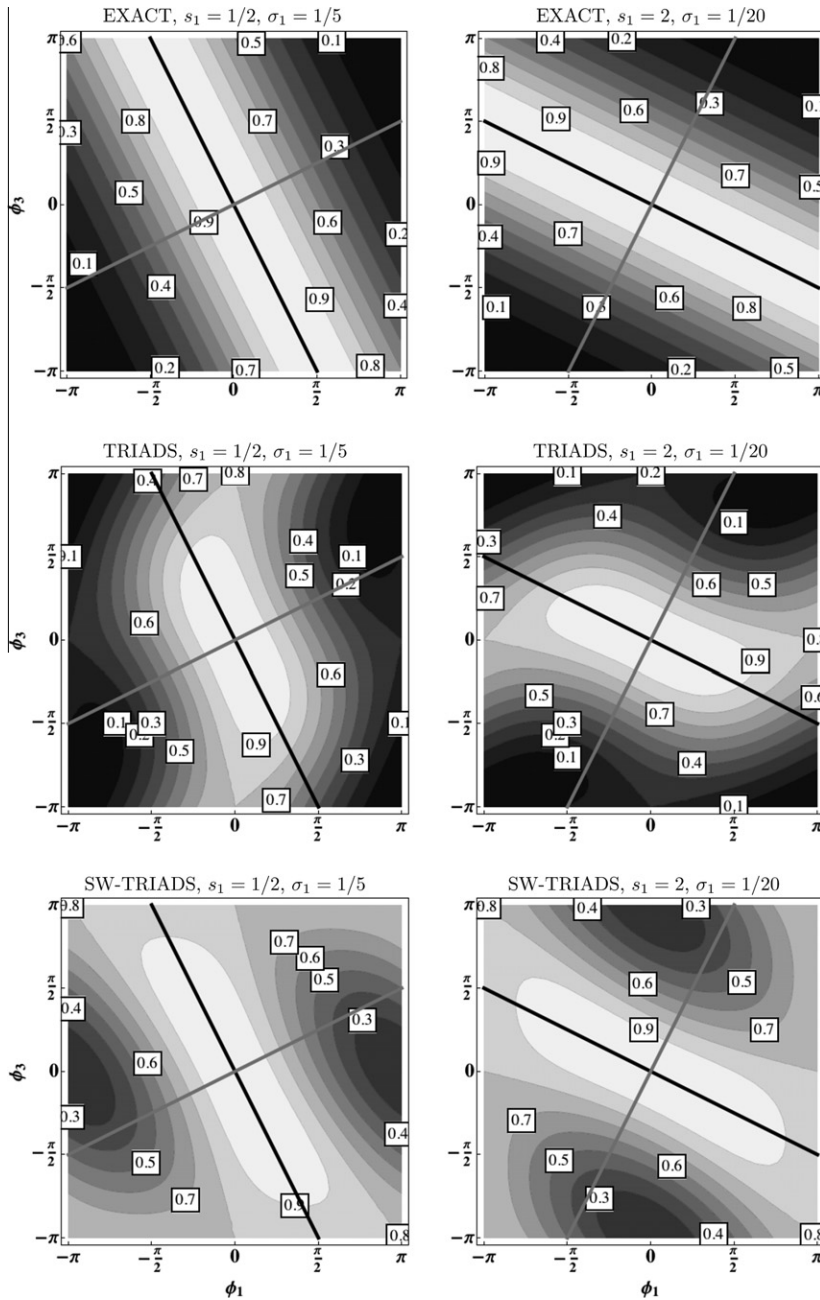
Fig. 4. Exact amplification factor in the (ϕ_1,ϕ_3) plane for $\sigma_1 = 1/4(1 + s_1^2)$ (i.e., when the (EXP) scheme is stable) with $s_1 = 1/2$ (top, left) and $s_1 = 2$ (top,right) in the two-dimensional (x_1,x_3) case (i.e., $\kappa_2 = 0$). Amplification factor for the (EXP) scheme with the TRIADS discretization (middle, left for $s_1 = 1/2$ and middle, right for $s_1 = 2$) and with the SW-TRIADS discretization (bottom, left for $s_1 = 1/2$ and bottom, right for $s_1 = 2$) for the same values of σ_1. The thick black line is $D_1 = 0$, the thick gray line is $D_2 = 0$.

poorly-resolved scales (i.e., when $|\phi_1|$ or $|\phi_3|$ increases). This property is not satisfied by the operator discretized with the SW-TRIADS. We thus expect the TRIADS to provide a better control of numerical noise and the SW-TRIADS to provide a more accurate computation of the direction of diffusion. Moreover, it is worth mentioning that numerical noise in the tracer fields can project into irreversible dianeutral mixing errors, especially when local Richardson number-dependent vertical mixing schemes are used in the oceanic interior.

3.5.2. Space–time discretization

We show in Fig. 5 the amplification factor for $s_1 = 1/2$ and $s_1 = 2$ when the (MSC) scheme is used with values of θ chosen such that there are no flip-flops in time. If we note Δt_ρ the time step of the

(EXP) scheme and Δt_0 the time step of the (MSC) scheme, we get the ratio μ_2 defined as

$$\mu_2 = \frac{\Delta t_0}{\Delta t_\rho} = 1 + s_1^2. \tag{3.33}$$

For $s_1 = 1/2$, we have $\mu_2 = 5/4$, and $\mu_2 = 5$ for $s_1 = 2$. When μ_2 is close to one, as for $s_1 = 1/2$, splitting errors are very small. We see that the left panels in Fig. 5 are very similar to the left panels in Fig. 4. For $\mu_2 = 5$, the damping along the line $D_1 = 0$ increases which indicates that the computation of the direction of diffusion become less and less accurate (Fig. 5, right panels). The space–time discretization is also relatively inaccurate along the line $D_2 = 0$ and the SW-TRIADS scheme suffers from non-monotonic damping. However, the
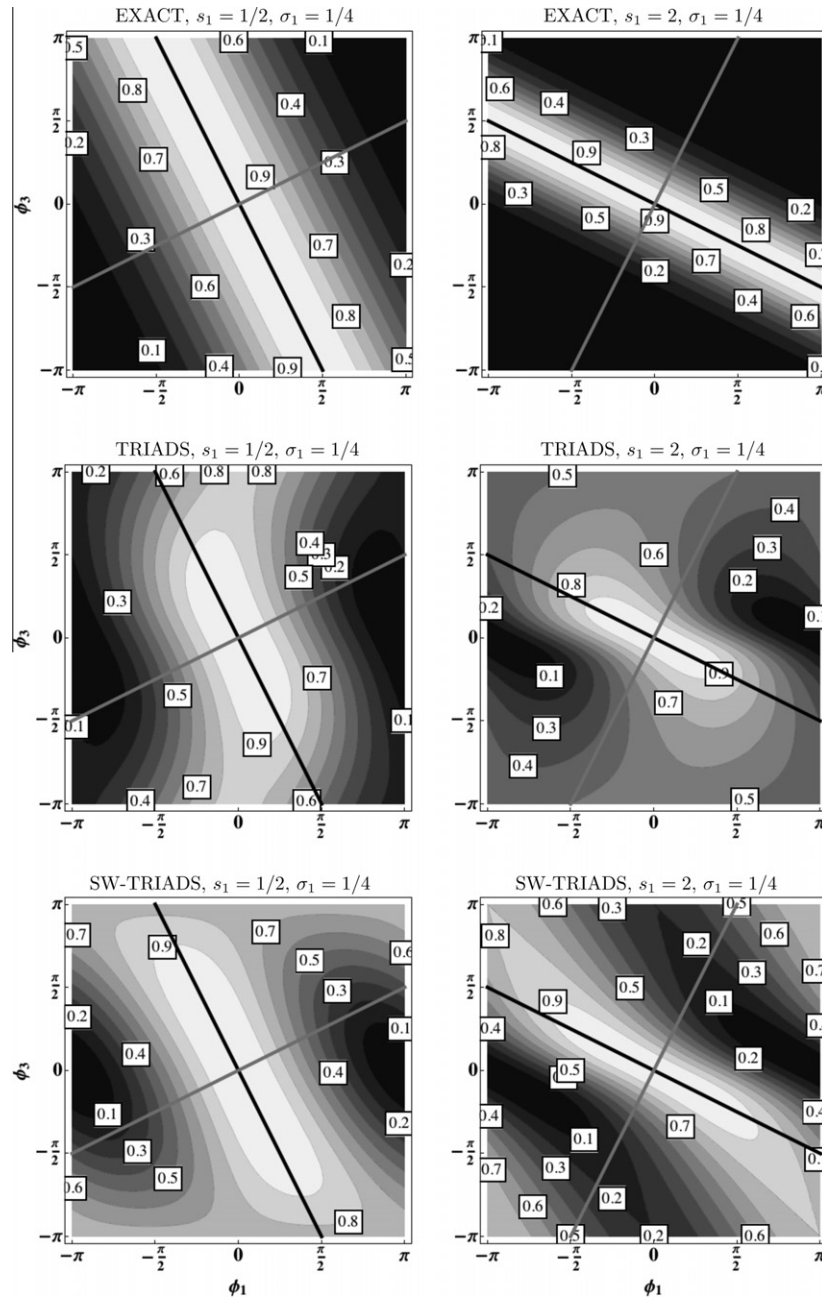
Fig. 5. Same as Fig. 4 for the (MSC) scheme with $\sigma_1 = 1/4$ (i.e., when the horizontal Laplacian advanced with the (EXP) scheme is stable and satisfies the no flip-flop condition).

schemes still perform well as long as the vertical scales are well-resolved (i.e., $|\phi_3| < \pi/2$).

4. Time discretization of the isoneutral biharmonic operator

4.1. Proposed scheme

As mentioned in the paper's introduction, the isoneutral biharmonic operator has never been thoroughly studied in the literature so far. One possible explanation is that people working on rotated operators were mainly interested in large-scale flows for which the scale-selectivity property is not a priority. Moreover, a very drastic reduction of the time step is required to maintain stability of such an operator. The aim of the present section is to tackle this last point by deriving a time integration scheme enabling an efficient and easy implementation of a rotated biharmonic operator. To our knowledge, no alternative to the usual explicit Euler scheme has been proposed. It is of course feasible to mimic the (IMP) scheme used for the rotated Laplacian operator but it would require the solution of a penta-diagonal system, and additional constraints would arise from the cross terms anyway. Indeed, an implicit vertical biharmonic operator can not stabilize the second order terms in x_3. Even if it is relatively counter-intuitive we show in the remainder of this section that it is possible to stabilize a biharmonic operator by means of a simple Laplacian operator. An alternative approach could be to use a combination of an implicit Laplacian operator and an implicit biharmonic operator in the vertical to stabilize separately the second-order and fourth-order terms, but it would increase substantially the complexity of the scheme.

In the same spirit as the method of stabilizing corrections introduced in Section 3.1, we thus propose to integrate the rotated biharmonic operator $\mathscr{D}_4$ in the following way:

$$\begin{cases} q^\star = q^n + \Delta t \mathscr{D}_4(q^n), \\ q^{n+1} = q^\star + \Delta t \partial_3 \{ \tilde{\kappa} \partial_3 q^{n+1} - \tilde{\kappa} \partial_3 q^n \}. \end{cases} \tag{4.1}$$

In (4.1), an explicit and consistent approximation of the operator is first computed, followed by a second stage aiming at improving the stability. For the aforementioned reasons, we decided to use a second-order diffusive operator for this second stage. Instead of the stabilizing parameter θ used in the previous section, we use here a stabilizing vertical diffusivity $\tilde{\kappa}$.

4.2. Important results

We first provide the results and prove them in Section 4.2.1. We keep the notations from the previous section but now with σ_m replaced by

$$\sigma_m^{(4)} = \frac{\sqrt{\Delta t B_m}}{\Delta x_m^2}, \tag{4.2}$$

where B_m is the hyperdiffusivity in the x_m direction.

4.2.1. Horizontal biharmonic operator

When using an Euler forward scheme, the stability limit of the two-dimensional horizontal biharmonic operator is

$$\left(\sigma_1^{(4)} + \sigma_2^{(4)} \right)^2 \leqslant \frac{1}{8}. \tag{4.3}$$

This result is also given in Griffies (2004) (Chap. 18).

4.2.2. Isoneutral biharmonic operator

- **TRIADS discretization**
  - The (EXP) scheme is stable for

$$\left(\sigma_1^{(4)}(1 + s_1^2) + \sigma_2^{(4)}(1 + s_2^2) \right)^2 \leqslant \frac{1}{8}. \tag{4.4}$$

  - The stability constraint of the (MSC) scheme is the same as the stability limit (4.3) for

$$\tilde{\kappa} = 8 \left(\frac{\Delta x_3^2}{\Delta t} \right) \left(\sigma_1^{(4)} s_1^2 + \sigma_2^{(4)} s_2^2 \right) \left((1 + s_1^2) \sigma_1^{(4)} + (1 + s_2^2) \sigma_2^{(4)} \right). \tag{4.5}$$

- **SW-TRIADS discretization**
  - The (EXP) scheme is stable for

$$\left(\sigma_1^{(4)} \max\{s_1^2, 1\} + \sigma_2^{(4)} \max\{s_2^2, 1\} \right)^2 \leqslant \frac{1}{8}. \tag{4.6}$$

  - The stability constraint of the (MSC) scheme is given by (4.3) for

$$\tilde{\kappa} = 8 \left(\frac{\Delta x_3^2}{\Delta t} \right) \left(S_1 \sigma_1^{(4)} + S_2 \sigma_2^{(4)} \right) \left((1 + S_1) \sigma_1^{(4)} + (1 + S_2) \sigma_2^{(4)} \right), \tag{4.7}$$

with $S_m = \max\{s_m^2 - |s_m|, 0\}$.

Note that, if we take $S_m = s_m^2$ in (4.7), we retrieve (4.5). Using the notations introduced in Section 2.2, we could write in a generic way $S_m = s_m(s_m - \beta_m)$, thus showing that S_m corresponds to the weight of the vertical points $(i,j,k+1)$ and $(i,j,k-1)$ in the stencil (2.21). We now give the proof of the stability results.

4.3. Linear stability analysis

We, first, define a vertical Courant number $\tilde{\sigma} = \tilde{\kappa} \Delta t / \Delta x_3^2$ associated with the stabilizing stage in (4.1), and we introduce $\tilde{y}_3 = \sqrt{2 \tilde{\sigma}(1 - \cos \phi_3)}$. The aim of this stability analysis is to determine a value of $\tilde{\sigma}$ (and hence $\tilde{\kappa}$) ensuring that the stability constraint of the rotated biharmonic operator is imposed by the horizontal components of the operator. Note that the exact amplification factor is now given by $\lambda = \exp(-\eta \Delta t)$ with $\eta = \sum_{m=1}^2 B_m (k_m + \alpha_m k_3)^4$, while the amplification factor after discretization is

$$\tilde{\lambda} = 1 - \frac{(y_1^2 + y_2^2 + y_3^2 - z_{13} - z_{31} - z_{23} - z_{32})^2}{1 + \tilde{y}_3^2} = 1 - \frac{(\varphi_1 + \varphi_2)^2}{1 + \tilde{y}_3^2}, \tag{4.8}$$

where φ_m is defined in (3.21). It is straightforward to check that $\tilde{\lambda} \leqslant 1$, stability is thus obtained for $\tilde{\lambda} \geqslant -1$; this condition is equivalent to

$$(\varphi_1 + \varphi_2)^2 - 2\tilde{y}_3^2 \leqslant 2. \tag{4.9}$$

We can first easily check that the stability limit of the horizontal biharmonic operator (i.e., with $s_m = 0$) is given by $(y_1^2 + y_2^2)^2 \leqslant 2$, leading to $\left(\sigma_1^{(4)} + \sigma_2^{(4)} \right)^2 \leqslant 1/8$. Furthermore, using the upper bound on φ_m found in Appendix A, we can derive the stability constraint for the forward Euler scheme (i.e., $\tilde{\kappa} = 0$),

$$(\varphi_1 + \varphi_2)^2 \leqslant 4 \left(\sigma_1^{(4)} \mathscr{M}(0, s_1) + \sigma_2^{(4)} \mathscr{M}(0, s_2) \right)^2$$
$$= 16 \left(\sigma_1^{(4)}(1 + s_1^2) + \sigma_2^{(4)}(1 + s_2^2) \right)^2 \leqslant 2, \tag{4.10}$$

where $\mathscr{M}$ is defined in (3.24), (4.10) leads to the expected result (4.4). As an illustration, this stability constraint implies that for $s_1 = s_2 = 2$, the time step used with the horizontal biharmonic operator should be reduced by a factor of 25 when using the rotated biharmonic operator.

In the general case $\tilde{\kappa} \neq 0$, we again use the upper bound on φ_m to get

$$(\varphi_1 + \varphi_2)^2 - 2\tilde{y}_3^2 \leqslant \mathscr{B}(\theta) = 4 \left(\sigma_1^{(4)} \mathscr{M}(\theta, s_1) + \theta y_{13}^2 + \sigma_2^{(4)} \mathscr{M}(\theta, s_2) + \theta y_{23}^2 \right)^2 - 2\tilde{y}_3^2, \tag{4.11}$$

stability is obtained for $\mathscr{B}(\theta) \leqslant 2$. For simplicity, we take $\theta = 1$ (i.e., $\mathscr{M} = 2$)

$$\mathscr{B}(\theta = 1) = 16 \left(\sigma_1^{(4)} + \sigma_2^{(4)} + (\sigma_1^{(4)} s_1^2 + \sigma_2^{(4)} s_2^2)(1 - \cos \phi_3) \right)^2$$
$$- 4\tilde{\sigma}(1 - \cos \phi_3) = 16 \left(\sigma_1^{(4)} + \sigma_2^{(4)} \right)^2$$
$$+ (1 - \cos \phi_3) \Big\{ 16 \left(\sigma_1^{(4)} s_1^2 + \sigma_2^{(4)} s_2^2 \right) \Big[2 \left(\sigma_1^{(4)} + \sigma_2^{(4)} \right)$$
$$+ (\sigma_1^{(4)} s_1^2 + \sigma_2^{(4)} s_2^2)(1 - \cos \phi_3) \Big] - 4\tilde{\sigma} \Big\}. \tag{4.12}$$

The stability constraint $\mathscr{B}(\theta = 1) \leqslant 2$ thus reduces to $\left(\sigma_1^{(4)} + \sigma_2^{(4)} \right)^2 \leqslant 1/8$ if the term in curly brackets in (4.12) is negative or zero. This requirement is satisfied for

$$\tilde{\sigma} \geqslant \sigma^\star = 8 \left(\sigma_1^{(4)} s_1^2 + \sigma_2^{(4)} s_2^2 \right) \left((1 + s_1^2) \sigma_1^{(4)} + (1 + s_2^2) \sigma_2^{(4)} \right), \tag{4.13}$$

which demonstrates (4.5). Less conservative values of $\tilde{\sigma}$ could be derived (like the one used in Lemarié et al. (2012)), however the algebra becomes very quickly complicated and tedious. The optimal
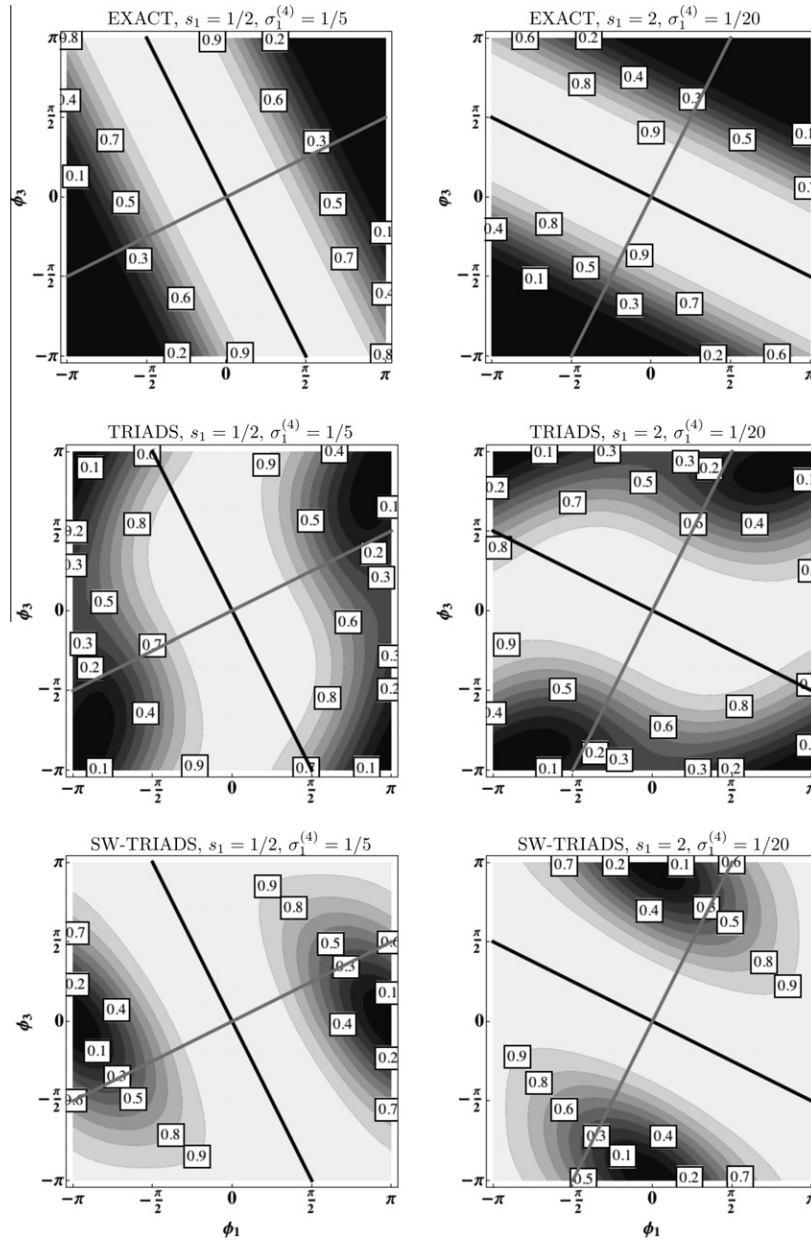
Fig. 6. Exact amplification factor in the (ϕ_1, ϕ_3) plane for $\sigma_1^{(4)} = \sqrt{1/16(1 + s_1^2)^2}$ (i.e., when the (EXP) scheme is stable) with $s_1 = 1/2$ (top, left) and $s_1 = 2$ (top, right) in the two-dimensional (x_1, x_3) case (i.e., $\kappa_2 = 0$). Amplification factor for the (EXP) scheme with the TRIADS discretization (middle, left for $s_1 = 1/2$ and middle, right for $s_1 = 2$) and with the SW-TRIADS discretization (bottom, left for $s_1 = 1/2$ and bottom, right for $s_1 = 2$) for the same values of σ_1. The thick black line is $D_1 = 0$, the thick gray line is $D_2 = 0$.

value (4.7) of the stabilizing parameter $\tilde{\sigma}$ obtained with the SW-TRIADS scheme is provided in Appendix B.

4.3.1. Non-oscillatory scheme

As for the Laplacian operator, we can derive the necessary constraints to satisfy $\tilde{\lambda} \geqslant 0$ instead of $\tilde{\lambda} \geqslant -1$. In this case, 1/8 should be replaced by 1/16 in (4.3), (4.4), and (4.6). Furthermore, if the stabilizing diffusivity (4.5) is multiplied by two, the (MSC) scheme satisfies the "no flip-flop" condition for $\left(\sigma_1^{(4)} + \sigma_2^{(4)}\right)^* \leqslant 1/16$.

4.4. Comments

We show in Figs. 6 and 7 the amplification factor obtained with a rotated biharmonic operator for $s_1 = 1/2$ and $s_1 = 2$ with the (EXP) and the (MSC) schemes in the no flip-flop case. We can draw the same remarks as for the Laplacian operator: the SW-TRIADS computes more accurately the direction of diffusion, however it suffers

from a lack of damping of the checkerboard mode. The ratio μ_4 between the time step of the (MSC) scheme and the one of the (EXP) scheme is given by

$$\mu_4 = \left(1 + s_1^2\right)^2. \tag{4.14}$$

For $s_1 = 1/2$, we get $\mu_4 \approx 1.56$. In this case, the results are very similar between the (MSC) and the (EXP) schemes. For $s_1 = 2$, the ratio becomes stiffer with $\mu_4 = 25$. However, the scheme behaves in a similar manner (Fig. 7, right panels) than the (EXP) scheme (Fig. 6, right panels).

4.5. Partial conclusion and limitations of our approach

We have shown so far that the Laplacian and biharmonic rotated operators can be made stable by combining an explicit-in-time evaluation with a semi-implicit stabilizing step. This
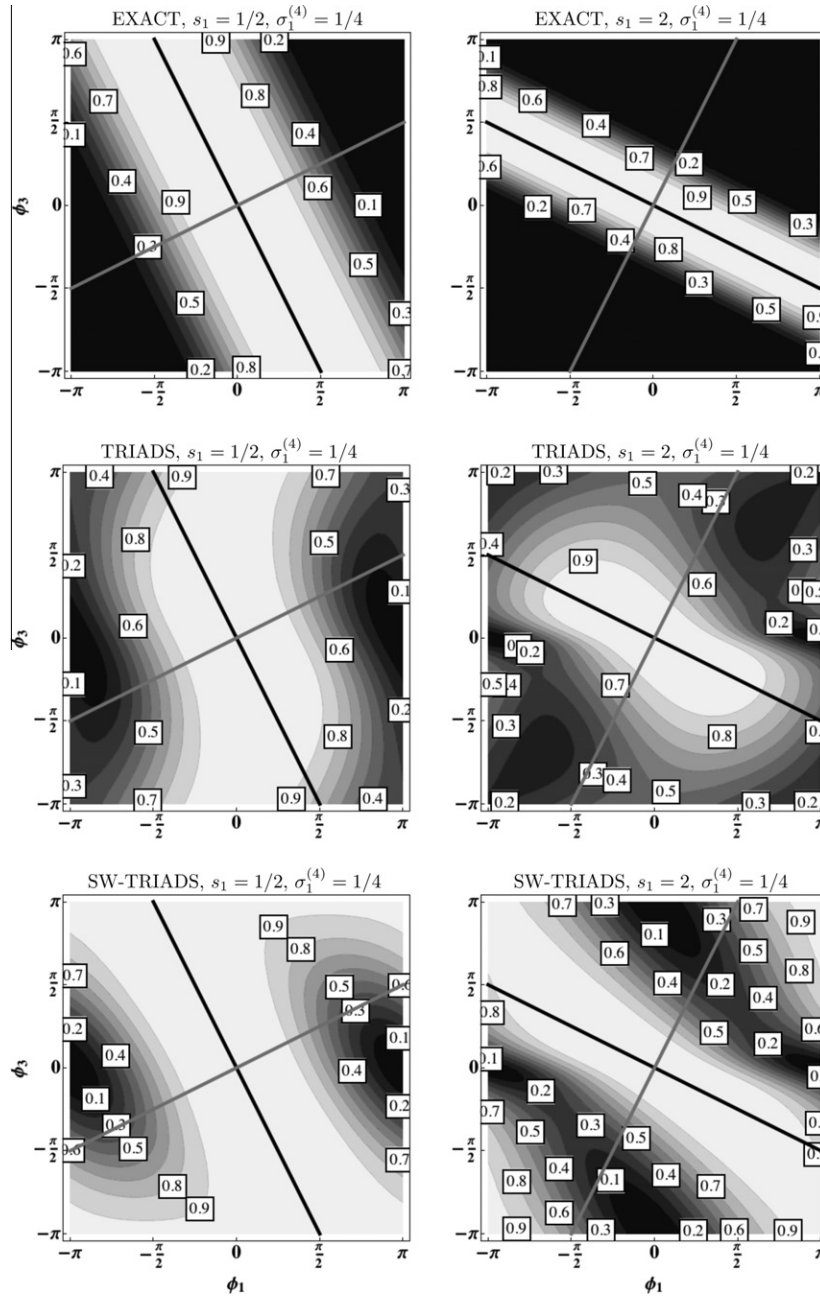
Fig. 7. Same as Fig. 6 for the (MSC) scheme with $\sigma_1^{(4)} = 1/4$ (i.e., when the horizontal biharmonic advanced with the (EXP) scheme is stable and satisfies the no flip-flop condition).

approach has the advantage to be extremely easy to implement because it requires only the inversion of a simple tridiagonal system in the vertical. For quite large grid slope ratios ($s_1 = 2$) the scheme performs relatively well but as the slope steepens to $s_1 = 10$ (Fig. 8) it can suffer from a lack of damping of the smallest resolved scales, especially for the rotated biharmonic operator. This behavior is reminiscent of the Crank–Nicolson scheme for which the small scale structures are not damped in the limit of large time-steps (Manfredi and Ottaviani, 1999). This problem thus arises when the time step used with the (MSC) scheme is significantly larger than the stability limit of the (EXP) scheme, i.e., when μ_4 or μ_2 are large (for $s_1 = 10$ we have $\mu_4 \approx 10,000$). This lack of damping affects only the vertical direction. The horizontal terms of the tensor, which are advanced explicitly, are still "active". Because the TRIADS scheme requires a larger value of $\tilde{\kappa}$

to stabilize the time-integration, this lack of damping is generally more pronounced with this scheme. This issue is also more obvious when we try to suppress the flip-flops in time by increasing the value of $\tilde{\kappa}$ (Fig. 8).

The fact that we restrict ourselves to implicit integrations only in the vertical direction reduces significantly the range of possible methods to try to mitigate this problem. If steep grid slope ratios are expected and accuracy matters, we could combine the (MSC) with a time-splitting approach, not to penalize the whole model. When using an Euler explicit scheme, if s_1 reaches $\mathcal{O}(10)$ values we should decrease the time step by a factor 10^4 compared to the time step of the horizontal biharmonic operator (indeed, $\mu_4 \approx 10,000$ for $s_1 = 10$). Several sub-steps of the (MSC) scheme to advance the rotated operator from time n to $n + 1$ would still be significantly more computationally efficient than using an explicit

Euler scheme. The use of a small number of sub-step clearly improves the damping properties of the rotated biharmonic operator which smoothes more efficiently the poorly resolved scales (Fig. 9). Based on the results shown in Fig. 9 we can recommend the use of 4 sub-steps to maintain a good accuracy of the rotated operator for steep grid slope ratios. We checked that for very large values of s_1 ($s_1 = 10^6$), 4 sub-steps are still sufficient to damp the smallest scales (not shown). Note that an even number of sub-steps ensures the absence of flip-flops.

5. Implementation of the proposed schemes in existing models

In this section, we provide additional information required for the implementation of the various schemes introduced in the previous sections.

5.1. Time-scheme for diffusive processes

As mentioned earlier, the majority of the global ocean climate models makes use of a rotated Laplacian operators advanced with the (IMP) scheme. For those models, the implementation of the (MSC) scheme is straightforward and does not require any additional global array for storage. In numerical models like ROMS or MitGCM[5] using a predictor–corrector scheme where provisional values $q^{n+\frac{1}{2}}$ are given by a predictor step (e.g., a Leapfrog-Adams–Moulton interpolation in ROMS or an Adams–Bashforth extrapolation in MitGCM), the (MSC) scheme and the implicit vertical diffusion can be combined with the corrector step in the following way:

$$\begin{cases} q^{n+1,\star} = q^n + \Delta t \ \mathrm{RHS}^{n+\frac{1}{2}} + \Delta t \ \mathscr{D}_4(q^n) - \Delta t \ \partial_3[\tilde{\kappa}\partial_3 q^n] \\ q^{n+1} = q^{n+1,\star} + \Delta t \ \partial_3[(K_3 + \tilde{\kappa})\partial_3 q^{n+1}], \end{cases} \tag{5.1}$$

where K_3 is the vertical eddy-diffusivity given by an appropriate parameterization of the sub-grid scale vertical mixing, and RHS contains all the terms other than diffusive terms. More generally, the explicit part of the stabilizing correction must be applied at the initial time of the tracer time step (i.e., at time n for ROMS/MitGCM, $n - 1/2$ for MOM4p1 (Griffies, 2010, Eq. (8.8)), or $n - 1$ for NEMO/POP), and the implicit part at the final time (i.e., at time $n + 1$ for ROMS/MitGCM/NEMO/POP, or $n + 1/2$ for MOM4p1). For models using a Leapfrog scheme, like NEMO or POP, Δt must be replaced by $2\Delta t$ (Madec, 2008; Smith et al., 2010).

5.2. Boundary conditions

We have considered so far a model problem defined on an unbounded domain. For realistic applications, the specification of boundary conditions is required and is based upon two requirements: the mixing operator conserves the tracer content and reduces the global tracer variance. Conservation of the tracer being diffused imposes $F^{(3)} = 0$ at $x_3 = \zeta$ (with ζ the free-surface) and $x_3 = -H$ (with H the depth of the water column). To ensure that the boundary conditions are consistent with the global tracer variance diminishing property it is convenient to use the tracer/density triads formalism defined in Section 2.3. Using the notations introduced in Fig. 1, we consider that the grid cell (i,k) is located at the ocean floor. The no-flux boundary condition requires $F^{(3)}_{i,k-\frac{1}{2}} = 0$ which involves that the triads 3,4,11 and 12 cancel. More generally, each time a given triad crosses the boundary the diffusivity $A(n)$ associated with this triad in the discrete functional (2.17) should be zero, and this triad can not participate in the computation of the $F^{(1)}$ interfacial fluxes in the grid-cell next to a boundary. At the bottom (i.e., for $k = 1$) we have

----
[5] Massachusetts Institute of Technology General Circulation Model, mitgcm.org

$$-F^{(1,\text{triads})}_{i+\frac{1}{2}j,1} = \frac{\kappa_1}{2}(\Delta x_2)_{i+\frac{1}{2}j}(\Delta x_3)_{i+\frac{1}{2}j,k} \cdot \frac{1}{2}\left(\frac{\delta_1 q_{i+\frac{1}{2}j,1}}{(\Delta x_1)_{i+\frac{1}{2}j}} - \frac{\delta_1 \rho_{i+\frac{1}{2}j,1}}{(\Delta x_1)_{i+\frac{1}{2}j}}\frac{\delta_3 q_{i+1j\frac{3}{2}}}{\delta_3 \rho_{i+1j\frac{3}{2}}}\right.$$
$$\left. + \frac{\delta_1 q_{i+\frac{1}{2}j,1}}{(\Delta x_1)_{i+\frac{1}{2}j}} - \frac{\delta_1 \rho_{i+\frac{1}{2}j,1}}{(\Delta x_1)_{i+\frac{1}{2}j}}\frac{\delta_3 q_{ij\frac{3}{2}}}{\delta_3 \rho_{ij\frac{3}{2}}}\right), \tag{5.2}$$

and

$$-F^{(1,\text{sw-triads})}_{i+\frac{1}{2}j,1} = \frac{\kappa_1}{2}(\Delta x_2)_{i+\frac{1}{2}j}(\Delta x_3)_{i+\frac{1}{2}j,k}\left(\frac{\delta_1 q_{i+\frac{1}{2}j,1}}{(\Delta x_1)_{i+\frac{1}{2}j}} - \frac{w^+_{i+\frac{1}{2}j,1}}{(\Delta x_1)_{i+\frac{1}{2}j}}\frac{\delta_3 q_{i+1j\frac{3}{2}}}{\delta_3 \rho_{i+1j\frac{3}{2}}}\right.$$
$$\left. - \frac{w^-_{i+\frac{1}{2}j,1}}{(\Delta x_1)_{i+\frac{1}{2}j}}\frac{\delta_3 q_{ij\frac{3}{2}}}{\delta_3 \rho_{ij\frac{3}{2}}}\right). \tag{5.3}$$

This approach can be seen as a diffusivity tapering because κ_1 is divided by two in the bottom most grid box. An other way to specify a boundary condition is to consider that $F^{(3)}_{i,j\frac{1}{2}} = 0$ because $(\delta_3 \rho_{i,j\frac{1}{2}})^{-1} = 0$ at the bottom. In this case we get

$$-F^{(1,\text{triads})}_{i+\frac{1}{2}j,1} = \kappa_1(\Delta x_2)_{i+\frac{1}{2}j}(\Delta x_3)_{i+\frac{1}{2}j,k}\left[\frac{\delta_1 q_{i+\frac{1}{2}j,1}}{(\Delta x_1)_{i+\frac{1}{2}j}} - \frac{\delta_1 \rho_{i+\frac{1}{2}j,1}}{(\Delta x_1)_{i+\frac{1}{2}j}}\cdot\frac{1}{4}\left\{\frac{\delta_3 q_{i+1j\frac{3}{2}}}{\delta_3 \rho_{i+1j\frac{3}{2}}} + \frac{\delta_3 q_{ij\frac{3}{2}}}{\delta_3 \rho_{ij\frac{3}{2}}}\right\}\right] \tag{5.4}$$

and

$$-F^{(1,\text{sw-triads})}_{i+\frac{1}{2}j,1} = \kappa_1(\Delta x_2)_{i+\frac{1}{2}j}(\Delta x_3)_{i+\frac{1}{2}j,k}\left(\frac{\delta_1 q_{i+\frac{1}{2}j,1}}{(\Delta x_1)_{i+\frac{1}{2}j}} - \frac{1}{2}\left\{\frac{w^+_{i+\frac{1}{2}j,1}}{(\Delta x_1)_{i+\frac{1}{2}j}}\frac{\delta_3 q_{i+1j\frac{3}{2}}}{\delta_3 \rho_{i+1j\frac{3}{2}}}\right.\right.$$
$$\left.\left. - \frac{w^-_{i+\frac{1}{2}j,1}}{(\Delta x_1)_{i+\frac{1}{2}j}}\frac{\delta_3 q_{ij\frac{3}{2}}}{\delta_3 \rho_{ij\frac{3}{2}}}\right\}\right). \tag{5.5}$$

This second approach is recommended only if a specific procedure is used to ensure that $(\partial_3 \rho)^{-1}$ goes smoothly to zero as a boundary is approached. The same remarks apply at the surface. For realistic applications, the direction of diffusion is generally progressively aligned with the horizontal direction when approaching the surface. This "boundary rotation" is generally done to avoid the rotated operator to interact with the parameterization of sub-grid scale vertical mixing and also to stay consistent with the small slope limit in the well mixed surface layer.

In the horizontal, homogeneous Neumann boundary conditions (i.e., $\partial_1 q = \partial_1 \rho = 0$) are imposed through masking at the coast. Again, because the biharmonic operator corresponds to two successive Laplacian operators, the specification of the boundary conditions does not imply additional difficulties, and the second boundary condition at the coast required for this operator is simply $\partial_1^3 q = \partial_1^3 \rho = 0$. It is straightforward to extend the results of this paragraph to the x_2-direction. The boundary condition for the stabilizing step in the (MSC) scheme is an homogeneous Neumann condition to ensure conservation of the tracer content.

A major difficulty when rotating the diffusion in the isoneutral direction is to maintain the numerical integrity of the scheme in poorly stratified regions, including boundary layers and convective regions. Here, the notion of numerical integrity encompasses several aspects: stay consistent with the small slope approximation, smoothly satisfy the boundary condition when conditions (5.4) and (5.5) are used, avoid any infinite slopes and associated infinite fluxes which would introduce numerical instabilities. In the next two subsections, we discuss more specifically those delicacies.

5.3. Boundary rotation

A specific procedure is required to safely consider that the neutral slope varies smoothly in the boundary layer and cancels at the surface. Several ways to handle the transition from isoneutral to horizontal mixing have been proposed in the literature (e.g., Treguier et al., 1997; Fox-Kemper et al., 2008; Ferrari et al., 2008; Ferrari et al., 2010, see also Griffies (2004) (Chap. 15) for a
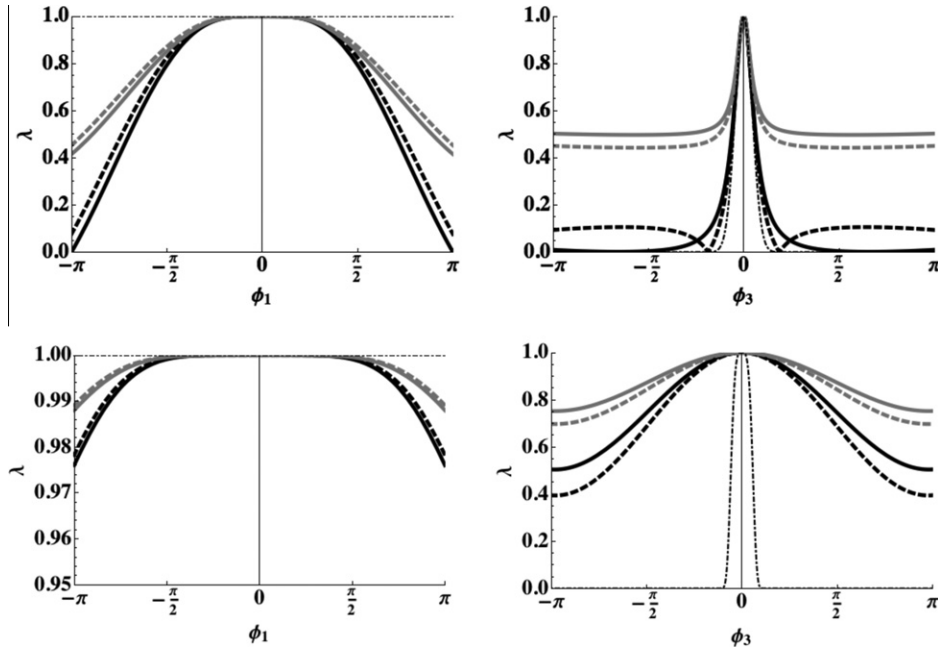
Fig. 8. Amplification factor of the rotated Laplacian operator along the line $D_1 = 0$ (top, left) and $D_2 = 0$ (top, right), and of the rotated biharmonic operator along $D_1 = 0$ (bottom, left) and $D_2 = 0$ (bottom, right) for $s_1 = 10$, $\sigma_1 = 1/4$ and $\sigma_1^{(4)} = 1/4$. The gray lines (resp. black lines) are obtained with a stabilizing diffusivity preventing flip-flops (resp. allowing flip-flops) with the (MSC) scheme. The results obtained with the TRIADS (resp. SW-TRIADS) discretization are represented with thick lines (resp. thick dashed lines). The thin black lines correspond to the exact amplification.
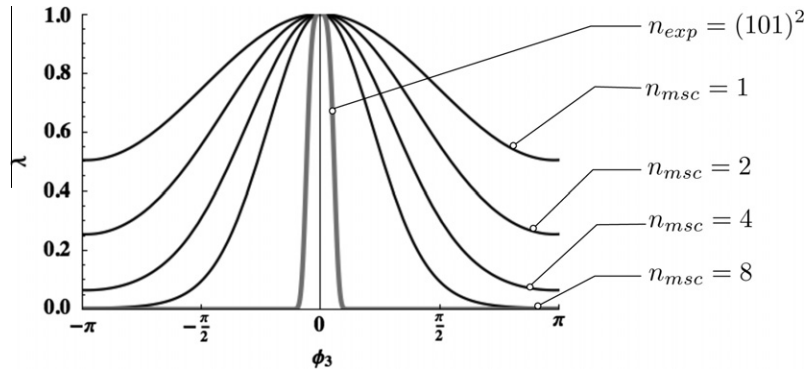

Fig. 9. Amplification factor of the rotated biharmonic operator along the line $D_2 = 0$, for $s_1 = 10$. The results are shown for the TRIADS scheme when a sub-stepping of the operator is used with $n_{\mathrm{msc}} = 1,2,4$ or 8 sub-steps of the (MSC) scheme, and with $n_{\exp} = (1 + s_1^2)^2$ sub-steps of the (EXP) scheme. The case $n_{\mathrm{msc}} = 1$ corresponds to $\sigma_1^{(4)} = 1/4$.

review on this topic through 2003). Those methodologies are generally specifically designed in the framework of the Gent and McWilliams (1990) parameterization to avoid any spurious recirculation in the surface layer when an eddy-induced velocity is used. Indeed, the eddy-induced velocity, parameterizing the effect of mesoscale eddies, is usually defined with respect to the vertical derivative of the neutral slopes, the type of boundary rotation adopted in the surface layer therefore interacts with the parameterization. For this reason, a linear clipping, ensuring a constant eddy-induced velocity in the surface layer, is usually applied to the neutral slopes between the base of the surface boundary layer and the surface (Gnanadesikan et al., 2007; Madec, 2008). However, recent advances in the understanding of the role of eddy fluxes in the mixed layer have led to a redesign of the function responsible for the boundary rotation (Ferrari et al., 2008; Fox-Kemper et al., 2008; Colas et al., 2012). A somehow different way to proceed is presented in Ferrari et al. (2010) where the eddy-induced velocity is computed from a vertical mode decomposition under the assumption that the parameterized eddy-transport is

dominated by low baroclinic modes. In this case, the computation of the eddy-induced velocity does not require any slope limiting or boundary rotation procedure, and those delicacies are transferred to the isoneutral diffusion operator only.

In a more general view, when considering the isoneutral diffusion independently of the eddy-induced velocity, the important term to keep under control is $(\partial_3 \rho)^{-1}$ and no longer the neutral slopes.

5.4. Diffusion slope limit

We provide here a simple example of a procedure to stay consistent with the small slope limit and to satisfy the boundary conditions, although many other procedures might be perfectly valid. We first define the quantity

$$(\partial_1 \rho)^{\max}_{i,j,k+\frac{1}{2}} = \max \left\{ \frac{|\delta_1 \rho_{i-\frac{1}{2}j,k}|}{(\Delta x_1)_{i-\frac{1}{2}j}}, \frac{|\delta_1 \rho_{i+\frac{1}{2}j,k}|}{(\Delta x_1)_{i+\frac{1}{2}j}}, \frac{|\delta_1 \rho_{i-\frac{1}{2}j,k+1}|}{(\Delta x_1)_{i-\frac{1}{2}j}}, \frac{|\delta_1 \rho_{i+\frac{1}{2}j,k+1}|}{(\Delta x_1)_{i+\frac{1}{2}j}} \right\}$$

and the maximum slope $\alpha_{\max}$ allowed. The value of $(\delta_3\rho)^{-1}$, defined at a cell vertical interface, that can be used in practice to compute the neutral slopes is given by

$$\left(\delta_3\rho_{i,j,k+\frac{1}{2}}\right)^{-1} = \max\left\{-\frac{F(x_3)\cdot\alpha_{\max}}{(\Delta x_3)_{i,j,k+\frac{1}{2}}(\partial_1\rho)^{\max}_{i,j,k+\frac{1}{2}}}, \min\left\{-\varepsilon, \left(\delta_3\rho_{i,j,k+\frac{1}{2}}\right)^{-1}\right\}\right\}. \tag{5.6}$$

In the case of an unstable stratification, the enforcement of a minimum stratification ε maintains the diffusion in the horizontal direction. In the case of a stable stratification, but with large slopes, the slope is bounded by a maximum value $\alpha_{\max}$. The procedure (5.6) ensures that the limiting of $(\delta_3\,\rho)^{-1}$ is "felt" the same way when the slopes are computed at u and w points. The analytical function F in (5.6) enables the implementation of a boundary rotation. The value of this function is typically 1 in the oceanic interior and decreases to 0 when approaching the boundaries.

In Section 7, we provide a critical discussion on the choice of the actual slope α_m (as in (5.6)) rather than on the grid slope ratio s_m to maintain the numerical integrity of the isoneutral mixing operators.

5.5. Isoneutral directions

The first implementations of the rotated operators were using the in situ density to compute the $\delta_m\rho$ terms in the rotation tensor (Cox, 1987). As mentioned earlier in Section 2.2.1, an extra horizontal diffusion was generally required to control an instability in the corresponding scheme. The source of this instability was found later in Griffies et al. (1998) (see also Griffies (2004), Chap. 14). They showed that using the in situ density to compute the $\delta_m\rho$ terms leads to a non-linear instability due to an imbalance between the active tracer isoneutral diffusive fluxes. The balance between those fluxes is achieved when the diffusive flux for potential
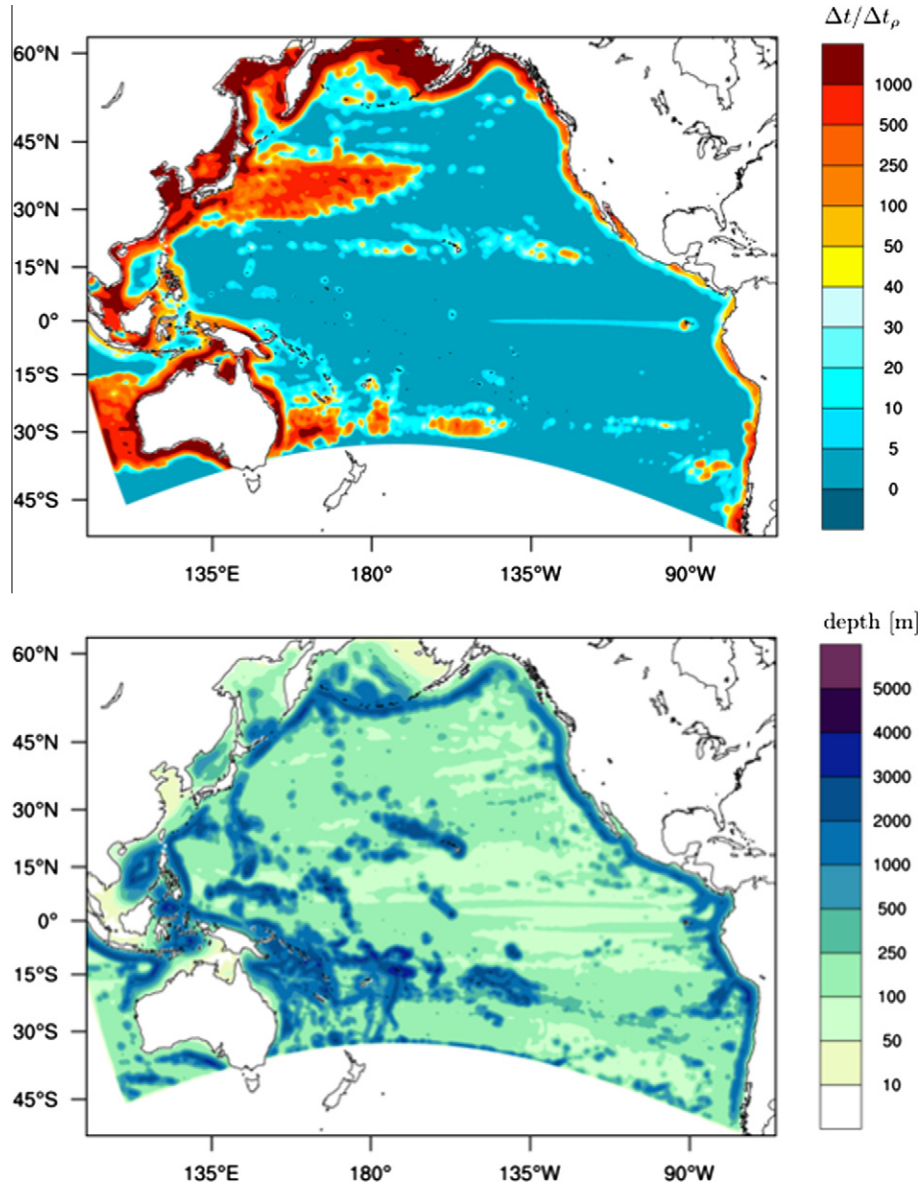

Fig. 10. Annual mean of the maximum value of the ratio $\Delta t/\Delta t_\rho$ for each water column (top), with Δt the time-step of the ROMS model using the (MSC) scheme to advance the rotated biharmonic operator and Δt_ρ the time-step which would be needed to advance the same operator but with the (EXP) scheme. Depth of the maximum (bottom). $\Delta t/\Delta t_\rho$ is first computed using seasonal averages and is then averaged to get the annual mean.

Table 2
Description of the numerical experiments discussed in Section 6. Those experiments are carried out using the rotated Laplacian operator (with $\kappa_1 = 5$ m^2 s^{-1}) and the rotated biharmonic operator (with $B_1 = 5 \times 10^{-1}$ m^4 s^{-1}) with either the SW-TRIADS or the TRIADS spatial discretizations. Δt_ρ is given by the stability limit (3.6) for the Laplacian operator and (4.4) for the biharmonic operator. Δt_0 corresponds to the time step restriction arising from the horizontal component of the rotated operators; i.e., $\Delta t_0 = \Delta x_1^2/2\kappa_1$ for the diffusion, resp. $\Delta t_0 = \Delta x_1^4/8B_1$ for the hyperdiffusion. The ratio $\Delta t_0/\Delta t_\rho$ is given for the LARGE experiments with the rotated Laplacian operator $\mathscr{D}_2$ and for the rotated biharmonic operator $\mathscr{D}_4$.

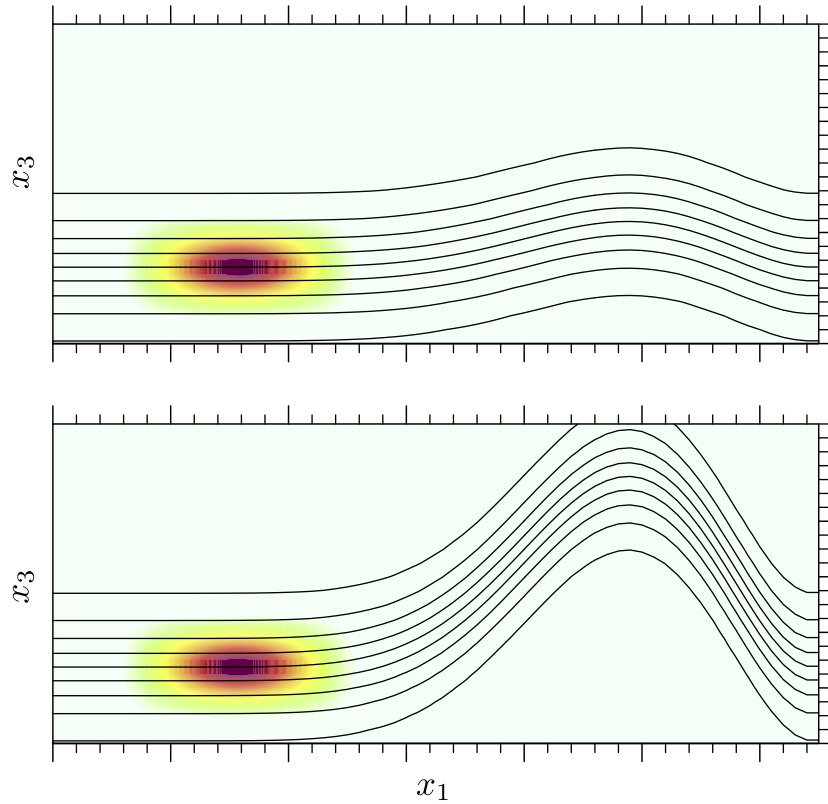| Resolution | Scheme | Time step | Maximum slope parameter (s_1) | | $\Delta t_0/\Delta t_\rho$ | | | |
| | | | Small | Large | Triads | | SW-triads | |
					$\mathscr{D}_2$	$\mathscr{D}_4$	$\mathscr{D}_2$	$\mathscr{D}_4$
1024×96	(EXP)	Δt_ρ	0.08	0.35	1	1	1	1
256×48	(MSC)	Δt_0	0.16	0.70	1.5	2.25	1	1
128×48	(MSC)	Δt_0	0.32	1.4	2.96	9	1.96	3.84
64×24	(MSC)	Δt_0	0.32	1.4	2.96	9	1.96	3.84
32×24	(MSC)	Δt_0	0.64	2.8	8.8	77	7.84	61.5

Fig. 11. Two-dimensional (x_1,x_3) initial conditions for different experiments of a passive tracer (shaded) diffused along a density field (contours) with a moderate slope between the computational grid and the isoneutral direction (top), and with a large slope (bottom).

temperature and salinity combine to give zero locally referenced potential density flux. In Griffies et al. (1998), a procedure to compute the neutral slopes is presented to ensure this constraint. For completeness, we briefly recall the basis of this procedure and express it with our notations. We first note that

$$\delta_m \rho(\Theta, S, x_3) = \rho^{(\Theta)} \delta_m \Theta + \rho^{(S)} \delta_m S, \tag{5.7}$$

where

$$\rho^{(\Theta)} = \left[\frac{\partial \rho}{\partial \Theta}\right]_{S, x_3 = \text{Const}}, \qquad \rho^{(S)} = \left[\frac{\partial \rho}{\partial S}\right]_{\Theta, x_3 = \text{Const}}$$

with Θ the potential temperature and S the salinity. At a discrete level, the natural placement for the $\rho^{(\Theta)}$ and $\rho^{(S)}$ terms is the same as Θ and S, and each triad has a unique associated value of $\rho^{(\Theta)}$ and $\rho^{(S)}$ (corresponding to the central ρ-point of a triad, Fig. 1). For the

potential temperature Θ, the flux (2.13) in the x_1-direction should thus be rewritten as

$$-F^{(1,\text{triads})}_{i+\frac{1}{2},j,k} = \kappa_1 \frac{(\Delta x_2)_{i+\frac{1}{2},j}(\Delta x_3)_{i+\frac{1}{2},j,k}}{(\Delta x_1)_{i+\frac{1}{2},j}} \Big[\delta_1 \Theta_{i+\frac{1}{2},j,k}$$
$$-\frac{1}{4}\Big\{ \delta_3 \Theta_{i,j,k-\frac{1}{2}} \frac{\rho^{(\Theta)}_{i,j,k}\delta_1\Theta_{i+\frac{1}{2},j,k} + \rho^{(S)}_{i,j,k}\delta_1 S_{i+\frac{1}{2},j,k}}{\rho^{(\Theta)}_{i,j,k}\delta_3\Theta_{i,j,k-\frac{1}{2}} + \rho^{(S)}_{i,j,k}\delta_3 S_{i,j,k-\frac{1}{2}}}$$
$$+ \delta_3 \Theta_{i+1,j,k-\frac{1}{2}} \frac{\rho^{(\Theta)}_{i+1,j,k}\delta_1\Theta_{i+\frac{1}{2},j,k} + \rho^{(S)}_{i+1,j,k}\delta_1 S_{i+\frac{1}{2},j,k}}{\rho^{(\Theta)}_{i+1,j,k}\delta_3\Theta_{i+1,j,k-\frac{1}{2}} + \rho^{(S)}_{i+1,j,k}\delta_3 S_{i+1,j,k-\frac{1}{2}}}$$
$$+ \delta_3 \Theta_{i+1,j,k+\frac{1}{2}} \frac{\rho^{(\Theta)}_{i+1,j,k}\delta_1\Theta_{i+\frac{1}{2},j,k} + \rho^{(S)}_{i+1,j,k}\delta_1 S_{i+\frac{1}{2},j,k}}{\rho^{(\Theta)}_{i+1,j,k}\delta_3\Theta_{i+1,j,k+\frac{1}{2}} + \rho^{(S)}_{i+1,j,k}\delta_3 S_{i+1,j,k+\frac{1}{2}}}$$
$$+ \delta_3 \Theta_{i,j,k+\frac{1}{2}} \frac{\rho^{(\Theta)}_{i,j,k}\delta_1\Theta_{i+\frac{1}{2},j,k} + \rho^{(S)}_{i,j,k}\delta_1 S_{i+\frac{1}{2},j,k}}{\rho^{(\Theta)}_{i,j,k}\delta_3\Theta_{i,j,k+\frac{1}{2}} + \rho^{(S)}_{i,j,k}\delta_3 S_{i,j,k+\frac{1}{2}}} \Big\} \Big], \tag{5.8}$$

same rules apply to the salinity flux and to the vertical flux $F^{(3)}$. As a consequence of this methodology, the isoneutral diffusive flux of the locally referenced potential density discretely vanishes triad-by-triad, as long as the (EXP) scheme is used for the time integration. As discussed earlier, the splitting errors associated with the (IMP) time discretization of the isoneutral Laplacian operator reintroduces an imbalance in the active tracer isoneutral diffusive fluxes. The use of the (MSC) scheme is a way to minimize this imbalance because it introduces only the minimum amount of implicit diffusion necessary to stabilize the temporal integration.

In Lemarié et al. (2012), the neutral slopes are computed using the "elementary adiabatic differences" as defined in Shchepetkin and McWilliams (2011) (Eq. (4.8)). In this case, the exact balance between the active tracer isoneutral diffusive fluxes was not satisfied, however the absence of such a balance did not turn out to be problematic for a realistic multi-decadal basin-scale Pacific simulation, although this issue may be more acute elsewhere and for longer timescales.

5.6. Diagnosing the stability condition of the rotated biharmonic operator in a basin-scale model simulation

Based on the prescriptions to handle poorly stratified regions, introduced in (5.6), and on the ROMS Pacific configuration described in Lemarié et al. (2012), we show in Fig. 10 an offline diagnostics of the maximum value of the quantity $\left(\sigma_1^{(4)}(1+s_1^2)+\sigma_2^{(4)}(1+s_2^2)\right)^2/(1/8)$ for each water column. This quantity, derived from the stability condition (4.4) for the rotated biharmonic operator advanced with the (EXP) scheme, provides an estimate of the stiffness of the stability condition for the isoneutral biharmonic operator. To generate the figure, we considered $\Delta t = 4200$ s (i.e., the ROMS baroclinic time-step used in Lemarié et al. (2012) to integrate the Pacific configuration in time), $B_1 = |u|\Delta x_1^3/12$, $B_2 = |v|\Delta x_2^3/12$, $\alpha_{max} = 1/10$, and $F(x_3) = (x_3/h_{bl})^2[3 - 2(x_3/h_{bl})]$ for $x_3 \leqslant h_{bl}$ ($F(x_3) = 1$ otherwise) where h_{bl} is the depth of the surface boundary layer diagnosed by the parameterization of the vertical mixing. For this configuration, the value of Δx_m varies from 50 km at the equator to 35 km at high latitudes. The hyperdiffusivities B_m are those given in Marchesiello et al. (2009) and Lemarié et al. (2012).

As mentioned earlier, it is not unusual to get very stiff stability conditions especially in shallow areas, including coastal regions, and in the Kuroshio extension. The maximum stability constraint is generally found either at the depth of the thermocline (green shaded area in Fig. 10, bottom panel) or at the bottom (blue shaded area in Fig. 10, bottom panel). Fig. 10 is meant to illustrate that even if the time-step of numerical models is generally set by hyperbolic terms, the use of a forward Euler scheme to integrate the rotated biharmonic operator is impractical and would impose a severe restriction on the time-step of the model, as could be expected from our study.

6. Numerical results

In this section, we present a set of idealized experiments to investigate the behavior of the various space–time dicretization schemes we introduced earlier in the paper.

6.1. Experimental setup

We have implemented a two-dimensional (x_1,x_3) testcase defined on the computational domain $\Omega = [0,1] \times [0,1]$ with a time-independent stratification

$$\rho_\xi(x_1,x_3) = -\tanh\left(5\left\{x_3 - \frac{1}{4} - \xi 8\pi^3 x_1^3\left[\sin(\pi x_1) - \frac{1}{2}\sin(2\pi x_1)\right]^2\right\}\right). \tag{6.1}$$

The slope associated with this stratification is

$$\alpha_1 = -\frac{\partial_1 \rho_\xi}{\partial_3 \rho_\xi} = \xi \cdot R(x_1), \tag{6.2}$$

where $R(x) = 64\pi^3 x^2 \cos(\pi x/2)\sin(\pi x/2)^5(2\pi x + 4\pi x\cos(\pi x) + 3\sin(\pi x))$. In (6.1), ξ is a stiffness parameter used to define the amplitude of the angle between the computational grid and the local isoneutral direction. Choosing two values of ξ, we build two set of experiments which are described in Table 2: a first one with a small grid slope ratio between the computational grid and the isoneutral direction (hereafter SMALL) and a second with a large grid slope ratio (hereafter LARGE). The largest value we consider is $s \approx 3$ which, for example, would correspond to $\alpha_1 = 7.5 \times 10^{-4}$, $\Delta x_1 = 100$ km and $\Delta x_3 = 25$ m.

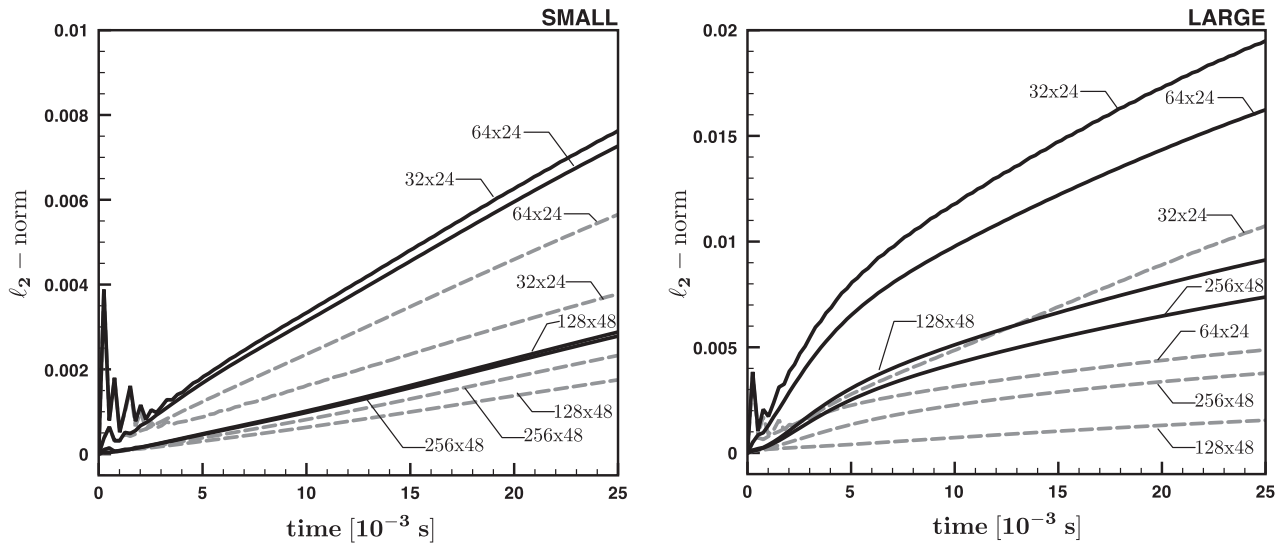The stratification (6.1) is shown in Fig. 11 along with the initial condition

Fig. 12. Time history of the error ℓ_2-norm for different grid resolutions, in the SMALL experiments (left) and in the LARGE experiments (right). The black lines correspond to the results obtained with the TRIADS scheme, and the dashed gray lines to the results obtained with the SW-TRIADS. Note the different vertical axis between the two panels.
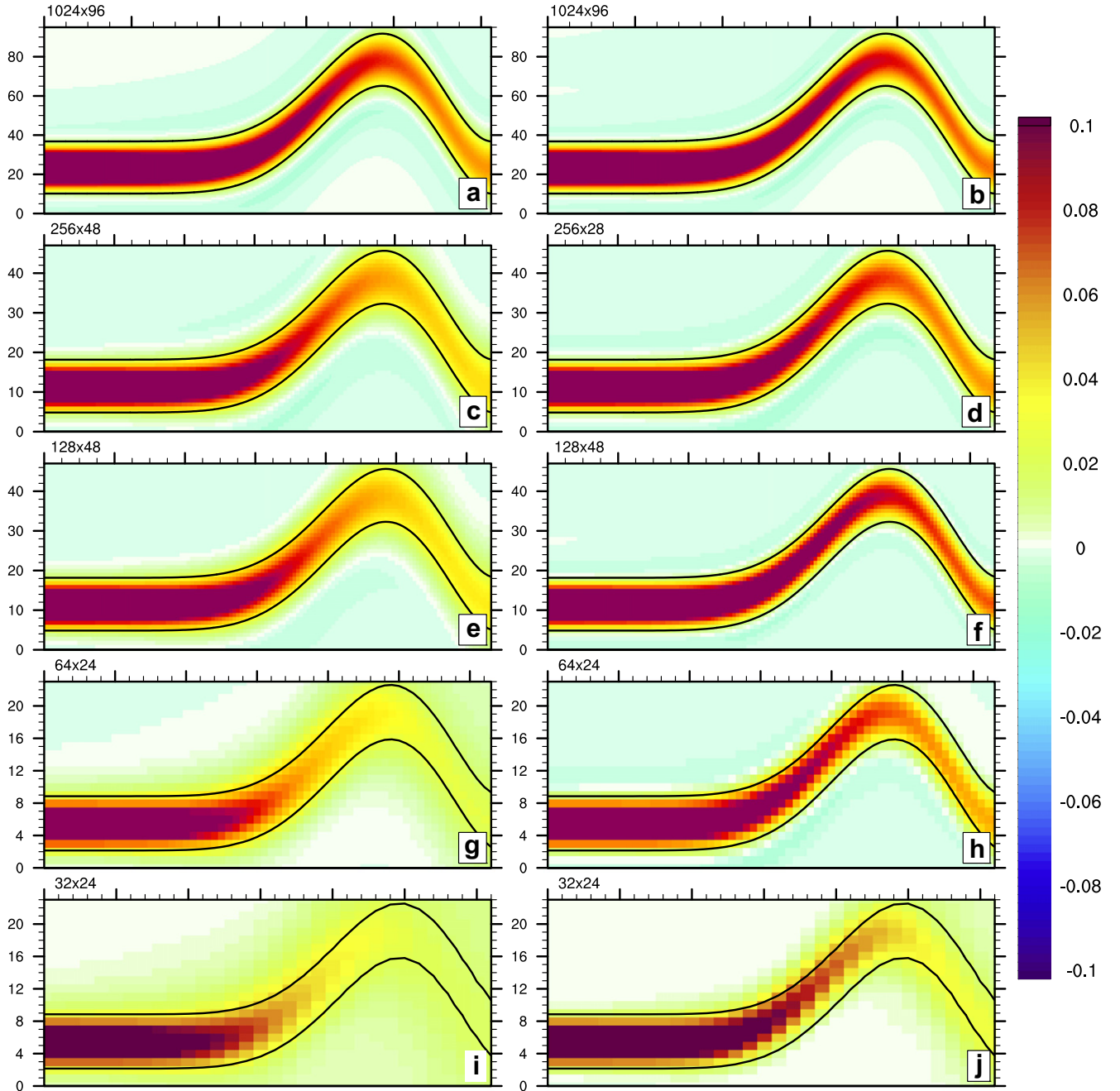
Fig. 13. Snapshots of a passive tracer diffused in the neutral direction after 25×10^{-3} s of integration in the LARGE case. Results obtained with the TRIADS scheme (resp. SW-TRIADS scheme) are shown in the left panels (a), (c), (e), (g) and (i) (resp. the right panels (b), (d), (f), (h) and (j)) for different grid resolutions.

$$q_0(x_1, x_3) = \frac{1}{4} \left[\cos \left((20x_3 - 5) \frac{\pi}{3} \right) + 1 \right]$$
$$\left[\cos \left((20x_1 - 5) \frac{\pi}{3} \right) + 1 \right] \mathbf{I}_{[1/10, 4/10]}(x_1) \mathbf{I}_{[1/10, 4/10]}(x_3), \quad (6.3)$$

where $\mathbf{I}_\Omega(x)$ is the indicator function.[6] All the simulations described in Table 2 are run with the same diffusivity $\kappa_1 = 5$ m² s⁻¹ and hyper-diffusivity $B_1 = 5 \times 10^{-1}$ m⁴ s⁻¹.

6.2. Accuracy of the rotated operators

The accuracy of different space–time discretizations is checked by computing a high resolution solution on a 1024×96 grid using

an explicit Euler scheme in time. This solution is taken as a solution of reference for a set of four coarser grids, 256×48, 128×48, 64×24, and 32×24. With the exception of the reference solution, all the simulations are done using the (MSC) scheme with the stabilizing parameters (3.7), (3.9), (4.5) and (4.7) with $\kappa_2 = 0$ (resp. $B_2 = 0$). To build this hierarchy of grids we have considered that when the horizontal resolution is refined by n^2 the vertical resolution is refined by n (Table 2). This rule is meant to be quite consistent with the usual practice in climate models. Due to the excessive computational cost of the explicit-in-time rotated biharmonic operator on the 1024×96 grid, we use the 256×48 grid as a solution of reference in this case.

The stratification (6.1) and the initial condition (6.3) are first defined on the reference 1024×96 grid and then a coarsening procedure is used to provide it to the entire hierarchy of grids. The same

---

[6] $\mathbf{I}_\Omega(x) = 1$, if $x \in \Omega$; $\mathbf{I}_\Omega(x) = 0$ otherwise.

coarsening procedure is then applied to the solution of reference to compute the ℓ_2-norm of the error for each grid of the hierarchy. This procedure ensures that the error is initially zero. The results obtained for the SMALL and the LARGE experiments are shown in Fig. 12. When using the TRIADS scheme, the error is monotonically decreasing when the grid is refined. For large grid slope ratios this discretization leads to a significant amount of spurious dianeutral diffusion due to discretization errors (Fig. 13(g) and (i)). The SW-TRIADS scheme systematically leads to smaller errors whatever the grid resolution and the grid slope ratio (Fig. 12). However, the evolution of the errors with the resolution is relatively uncommon. For example, in the LARGE experiments, the error is smaller on the 128×48 grid than on the 256×48 grid. This is explained by the fact that the errors of discretization associated with the SW-TRIADS scheme do not monotonically increase when the grid slope ratio s_1 increases, as this is the case for the TRIADS scheme. This point will be further discussed in Section 6.4 but it can be seen from (2.21) that the discretization reduces to the classical $1, -2, 1$ stencil in the oblique direction for $s_1 = 1$, thus explaining why the errors are small for the experiments for which the grid slope ratio is close to one (e.g., for the 64×24 and 128×48 grids in the LARGE case). As far as the biharmonic operator is concerned, the results are very consistent with the one obtained with the rotated Laplacian operator (Fig. 14). The SW-TRIADS performs better than the TRIADS when the grid slope ratio exceeds one, which is an important asset when considering grid cells with a small aspect ratio $\Delta x_3/\Delta x_1$ as it can happen for a σ-coordinate models in shallow areas. For very large values of s_1 the direction of diffusion becomes less and less accurate (Figs. 13(j) and 14(h)) and a larger vertical stencil should potentially be required to lessen the discretization errors.

Monotonicity violations are obvious from Figs. 13 and 14 where the blue-shaded areas correspond to negative values whereas the initial condition has positive values only. When the discretization errors are increasing, thus leading to a spurious dianeutral diffusion, the false extrema are significantly moderated. The biharmonic operator generates large negative values (Fig. 14), however those min–max violations are not necessarily associated with the rotation of the tensor because the horizontal biharmonic operator also produces overshoots with a similar order of magnitude (not shown). It is worth mentioning that the part of the computational domain with a flat stratification coincides with the location of the initial condition (Fig. 11). Most of the overshoots with the biharmonic operator are generated during the initialization, this is the reason why relatively large monotonicity violations are located in this part of the computational domain.
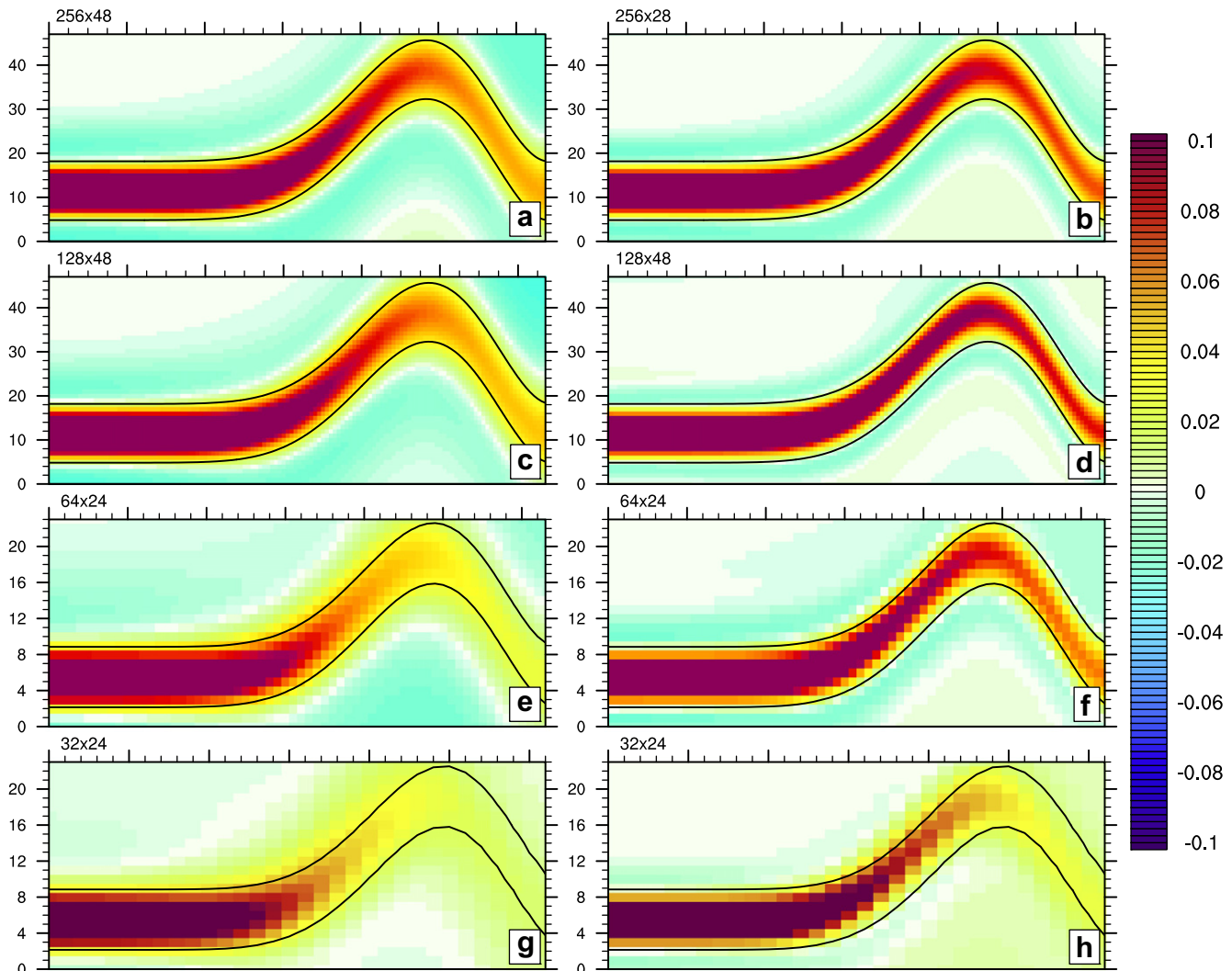

Fig. 14. Snapshots of a passive tracer diffused in the neutral direction with a biharmonic operator after 25×10^{-3} s of integration in the LARGE case. Results obtained with the TRIADS scheme (resp. SW-TRIADS scheme) are shown in the left panels (a), (c), (e), and (g) (resp. the right panels (b), (d), (f) and (h)) for different grid resolutions.

6.3. Overshootings

Mathieu and Deleersnijder (1998) emphasized the non-monotonic behavior of the discretized rotated diffusion operator. This can be seen simply by looking at the diffusion of a dirac signal along a direction non-aligned with the computational grid (Fig. 15). Negative bands are generated on both sides of the isoneutral direction along which the Dirac signal is propagating. The rotated biharmonic operator presents two bands of negative values separated by positive values. We can also see from those figures that the cancellation of the contribution of the dianeutral points in the discretization stencil of the SW-TRIADS scheme leads to a thin signal elongated in the isoneutral direction while the TRIADS scheme produces a thicker signal in both the $s_1 = 1/2$ and $s_1 = 2$ cases. Note that the case $s_1 = 1/2$ corresponds to a maximum of discretization errors for the SW-TRIADS scheme in the limit that $s_1 \leqslant 1$; see discussion in Section 6.4.

Monotonicity is verified at a position (i,k) only if all the coefficients in the discretization stencil of the operator under consider-

ation are positive for points others than (i,k). It can be seen from (2.21) that neither the TRIADS, nor the SW-TRIADS scheme verifies this property. The continuous form of the rotated Laplacian operator has however the property not to amplify existing extrema (Mathieu and Deleersnijder, 1998), this property is lost at the discrete level due to the discretization of the cross-derivatives. We quantify the monotonicity violation associated with the SW-TRIADS and TRIADS schemes by computing

$$\varepsilon_{i,k} = \max\left(q_{i,k}^{n+1} - q_{i,k}^{\max}, 0\right) - \min\left(q_{i,k}^{n+1} - q_{i,k}^{\min}, 0\right), \tag{6.4}$$

where

$$q_{i,k}^{(\min)} = \min\left(q_{i\pm c,k\pm c}^n\right), \qquad q_{i,k}^{(\max)} = \max\left(q_{i\pm c,k\pm c}^n\right), \tag{6.5}$$

with $c = 1$ for the Laplacian operator and $c = 2$ for the biharmonic operator. The evolution of the maximum value of $\varepsilon_{i,k}$ is shown in Fig. 16 for the diffusion of a Dirac signal. This experiment is done on the 256×48 grid with a diffusivity κ_1 and an hyperdiffusivity
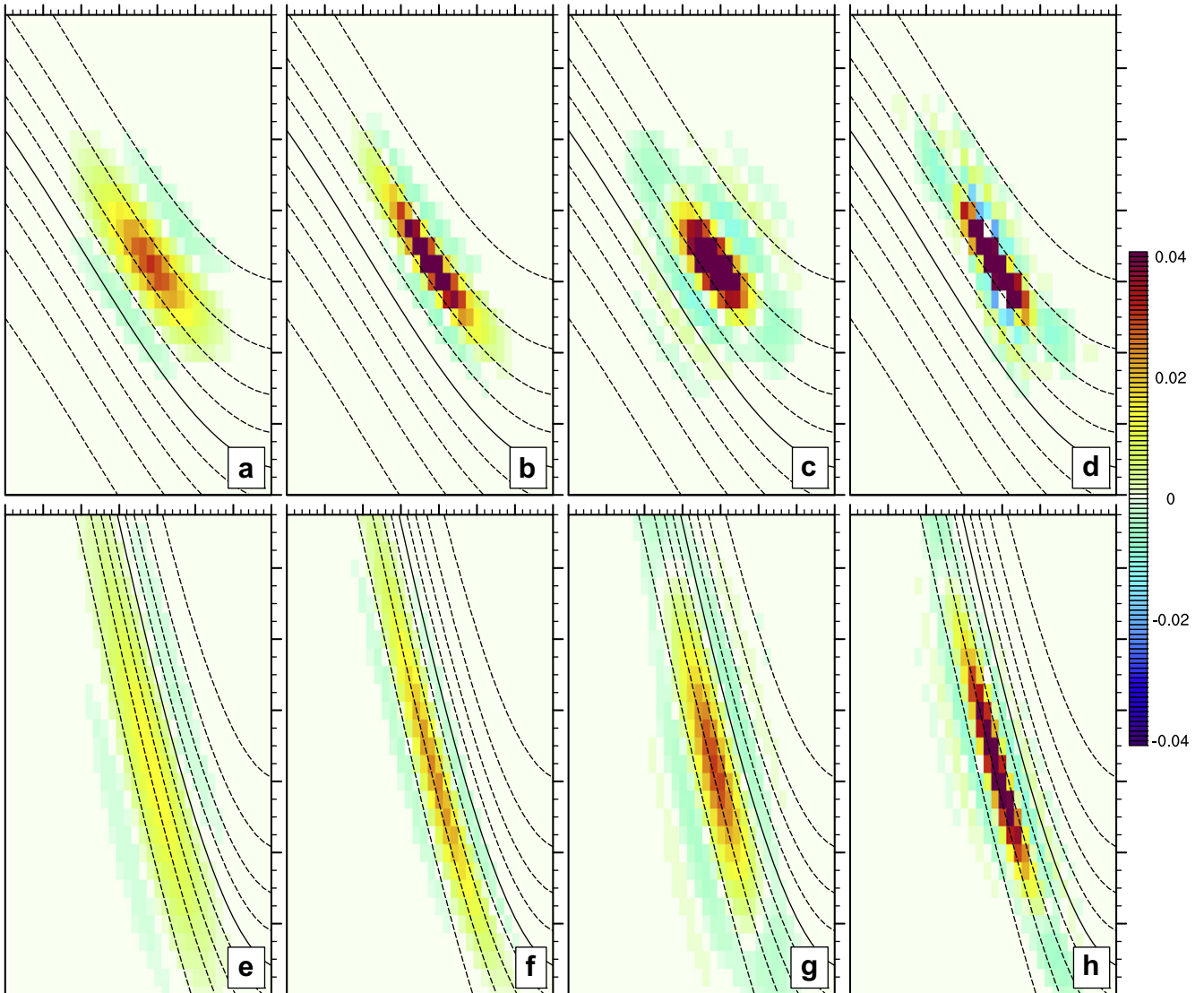

Fig. 15. Diffusion of a Dirac signal in the neutral direction (contours) after $t = 2.5 \times 10^{-4}$ s: (a) and (e) with a rotated Laplacian operator using the TRIADS discretization; (b) and (f) with a rotated Laplacian operator using the SW-TRIADS discretization; (c) and (g) with a rotated biharmonic operator using the TRIADS discretization; (d) and (h) with a rotated biharmonic operator using the SW-TRIADS discretization. The tracer field is deliberately not smoothed, cell-averaged values are shown. Note that blue-shaded areas indicate negative values. The grid slope ratio is $s_1 \approx 1/2$ for panels (a), (b), (c) and (d), and $s_1 \approx 2$ for (e), (f), (g) and (h).
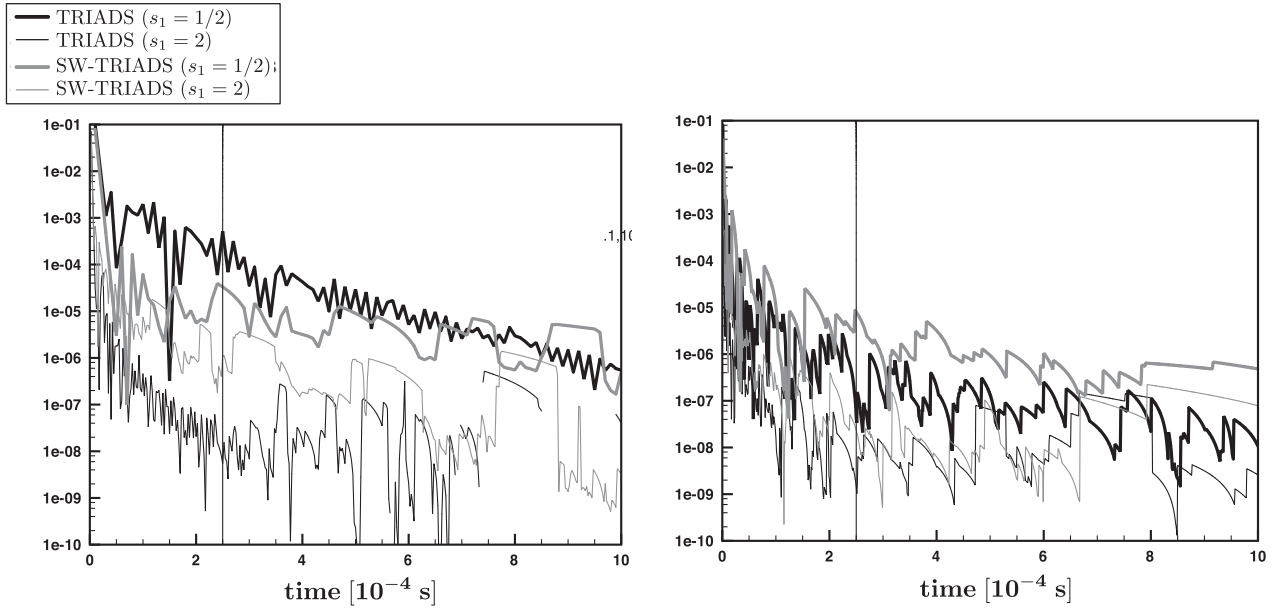
Fig. 16. Magnitude of min–max violations ε for the rotated Laplacian operator (left) and for the rotated biharmonic operator (right) discretized either with the TRIADS scheme (black lines) or the SW-TRIADS scheme (gray lines). The vertical line at $t = 2.5 \times 10^{-4}$ s represents the time corresponding to the plots in Fig. 15.
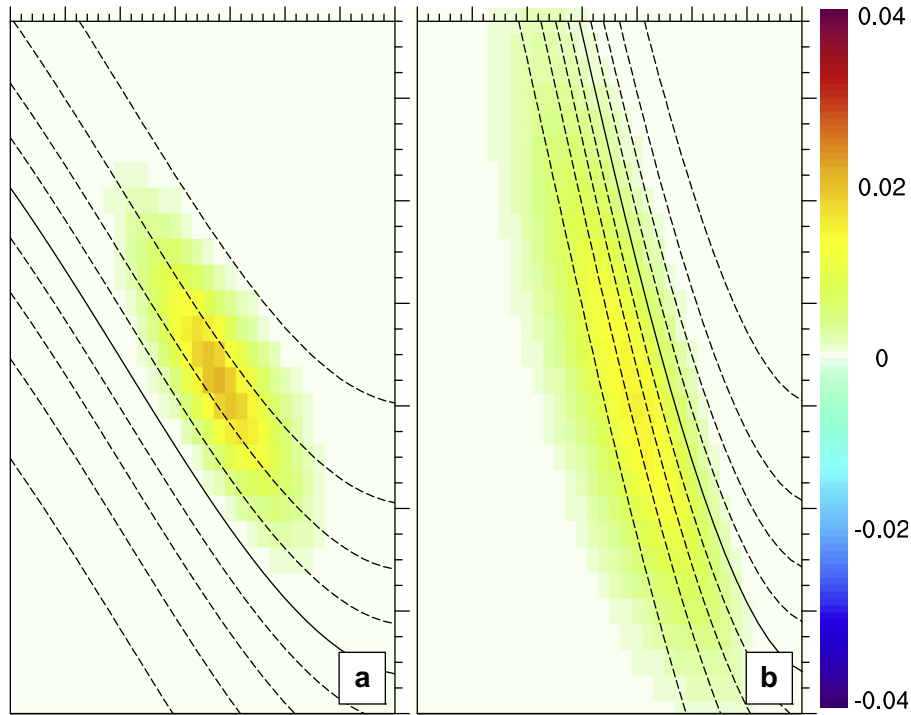

Fig. 17. Diffusion of a Dirac signal (shaded) in the neutral direction (contours) using the SW-TRIADS-COMBI scheme: (a) for $s_1 \approx 1/2$; (b) for $s_1 \approx 2$. The results are shown after 2.5×10^{-4} s of integration. Panel (a) should be compared with Fig. 15(b) and panel (b) with with Fig. 15(f).

B_1 chosen so that it provides the same dissipative time scale at the scale of the grid (i.e., $B_1 = \kappa_1 \Delta x_1^2$).

Fig. 16 shows that the magnitude of the min–max violations is of the same order for the rotated harmonic and biharmonic operators. Even if Fig. 15 suggests that larger negative values are produced by the biharmonic operator, this does not mean that the min–max violations are larger in this case, as we see from Fig. 16. This is explained by the fact that the amount of dianeutral diffusion, associated with discretization errors, is smaller with the

rotated biharmonic operator than with the rotated Laplacian operator and is insufficient to moderate the false extrema.

6.4. SW-TRIADS-COMBI scheme and scaling of the discretization errors

In this paragraph, we borrow the concept of the so-called COM-BI scheme, introduced in Beckers et al. (2000), to assess the evolution of the discretization errors of the SW-TRIADS scheme with respect to s_m. To minimize overshootings, Beckers et al. (2000) pro-

pose an inconsistent COMBI scheme which consists in adding an additional horizontal or vertical diffusion to cancel the negative weights in the stencil (2.21) and thus to maintain monotonicity. With the TRIADS discretization this is not straightforward because the negative weights are systematically in the diagonal direction. For the SW-TRIADS scheme, it is easier to apply the concept of the COMBI scheme; in (2.21) we see that, for s_m positive and $s_m < 1$, it is sufficient to add a vertical diffusion with a coefficient proportional to $s_m(1 - s_m)$ and, for $s_m > 1$, it is sufficient to add an horizontal diffusion with a coefficient proportional to $s_m - 1$. In Fig. 17, we show the diffusion of a Dirac signal using the SW-TRI-ADS-COMBI scheme (defined as the SW-TRIADS scheme combined with the COMBI approach). The scheme seems to behave relatively well for $s_1 \approx 2$, however the amount of spurious dianeutral diffusion is larger compared with the SW-TRIADS scheme. For $s_1 \approx 1/2$, the orientation of the diffusion is less accurate and the dirac signal is propagated too vertically relative to the isoneutral direction. We can show that the extra diffusivity κ_v used for $s_m < 1$ in the SW-TRIADS-COMBI scheme is

$$\kappa_v = \kappa_m \left(\frac{\Delta x_3}{\Delta x_m} |\alpha_m| - \alpha_m^2 \right).$$

The expression of κ_v is also useful to quantify the discretization errors associated with the SW-TRIADS scheme. The minimum of the error is obtained for $\alpha_m = 0$, or $\alpha_m = \Delta x_3/\Delta x_m$ (i.e., $s_m = 1$) because κ_v cancels in those cases, hence the scheme reduces to the classical 1, −2, 1 stencil and is monotonic. The maximum of the discretization error is for $\alpha_m = \Delta x_3/2\Delta x_m$ (i.e., $s_m = 1/2$), which leads to $\kappa_v^{\max} = \frac{\kappa_m}{4} \left(\frac{\Delta x_3}{\Delta x_m} \right)^2$. For $s_m > 1$, the discretization error scales with $s_m - 1$ (which corresponds to the background horizontal diffusivity of the SW-TRIADS-COMBI scheme) and thus keeps increasing with increasing values of s_m.

The value of $\kappa_v^{\max}$ can be compared with the background vertical diffusivity associated with the vertical mixing parameterizations currently in use in ocean models, which is of the order of 10^{-5} m^2 s^{-1} below the mixed layer. We see that it is not unusual, regarding the typical horizontal and vertical resolutions used by climate models, that the background vertical diffusion in the oceanic interior is sufficient to significantly moderate the overshootings associated with the use of a rotated mixing operator discretized with the SW-TRIADS scheme, as long as the grid slope ratio is smaller than one.

7. Conclusion

The use of a mixing operator non-aligned with the computational grid raises difficulties to maintain several properties of the non-rotated operators: numerical stability, strict global tracer variance dissipation, monotonicity (in the case of the Laplacian operator), and accuracy when the slopes steepen to greater than the grid aspect ratio. In this paper, we present a set of conservative space–time discretizations to investigate those delicacies. Since we do not want the numerical models to be penalized by diffusive processes, we consider only linear spatial discretizations and first-order accurate temporal integrations. We do not strive to design higher order schemes because the diffusive terms are used either for numerical or physical closure (or both) and are thus supposed to vanish anyway for sufficiently high resolution.

In the same spirit as the methods commonly used for multi-dimensional parabolic problems with mixed derivatives, we introduce a simple time-stepping scheme and we show its relevance to handle the time-integration of the rotated harmonic and biharmonic operators. This method, which is known as Method of Stabilizing Corrections (MSC), consists of a multi-stage approach: at the first stage, a consistent (explicit) approximation of the

rotated operator is evaluated, while all succeeding stages serve only to improve the stability. For both the rotated harmonic and biharmonic operators, the stabilizing step is done using a vertical Laplacian operator whose diffusivity is chosen through linear stability analysis. The proposed scheme is made to enable the rotated operators to be advanced with the same time step as the non-rotated ones. For large grid slope ratios, the scheme can however suffer from a lack of damping of the smallest resolved scales in the vertical. To alleviate this problem a time-splitting of the diffusion could be used with a few (typically of the order of 4) small time steps using the (MSC) scheme within a larger baroclinic time step. This approach would still be significantly more computationally efficient than using an explicit Euler scheme.

As noted previously in Beckers et al. (2000), all the consistent linear spatial discretizations of the rotated operators produce false dianeutral mixing and min–max violations. This issue is cumbersome because, in general, min–max violations are larger for schemes with small inherent dianeutral mixing, and conversely schemes with a larger dianeutral mixing associated with discretization errors tend to moderate the overshootings. The rotated biharmonic operator does not seem to generate significantly larger monotonicity violations than the rotated Laplacian operator and than the non-rotated biharmonic operator. Furthermore, we show that different spatial discretizations of the rotated operators can lead to a quite different behavior of the solution especially for large grid slope ratios. A compact discretization (referred to as SW-TRIADS) whose stencil adapts to the orientation of the slope provides more accuracy, hence has less spurious dianeutral mixing, for situations where the neutral slope is greater than the vertical to horizontal aspect ratio. However, this discretization does not damp very efficiently small-scale noise, and dispersive errors could thus go uncontrolled with this approach. As shown in Beckers et al. (2000), the SW-TRIADS scheme can easily be made monotonic by adding a vertical background diffusion (as long as the grid slope ratio is less than one) at the expense of a larger dianeutral contribution. However, under some circumstances, the order of magnitude of this background diffusivity is expected to be of the same order as the physically admissible dianeutral diffusivity.

When using the isoneutral mixing operators under realistic conditions, a specific procedure is required to maintain the consistency with the small slope approximation made at a continuous level to derive the rotation tensor, and to properly satisfy the boundary conditions. To do so, we consider a clipping or tapering based on a maximum value of the neutral slope α_m, as done traditionally in numerical climate models. However, our study shows that the stability and the accuracy of the rotated operators are much more dependent on the grid slope ratio s_m rather than on the actual slope α_m. This remark suggests that a clipping on the local value of s_m could be more appropriate. One drawback of this approach would be to allow the violation of the small slope approximation when large values of α_m are associated with small values of s_m. Considering that the small slope limit is valid for $\alpha_m^2 \ll 1$, a slope $\alpha_m = 1/10$ would imply a 1% error which suggests some flexibility in the choice of $\alpha_{\max}$. It is therefore not clear whether violating the small-slope approximation (which may happen with a limiting acting on s_m) is much more damaging for the stratification than the loss of accuracy for large values of the grid slope ratio (which may happen with a limiting acting on α_m). A definitive answer to this question would require numerical experiments under fully-realistic conditions. This point is left for a future study, but this question certainly deserves more attention.

We show that rotated operators must be used with care if we rely on those operators to efficiently smooth grid-scale noise along the computational grid. Adding a background vertical, as it is

commonly done through the vertical mixing parameterization, or horizontal diffusion is a way to erase the deficiencies in terms of smoothing but at the expense of additional numerically-induced spurious dianeutral mixing. The requirements in terms of noise control are tied to the numerical schemes used to handle the tracer advection. When low-order schemes are used, larger dispersive errors are expected and an operator providing an efficient numerical filtering is crucial. In this case, the TRIADS scheme would be recommended. An unexplored possibility could be to formulate the advection in an isoneutral framework hence the numerical noise would be prominently in the isoneutral direction and rotated operators would be more adequate to control this noise.

Besides the idealized configurations studied in the present paper, it is shown in Lemarié et al. (2012) that a rotated biharmonic operator advanced with the (MSC) scheme in time and using the SW-TRIADS discretization performs well for a realistic coarse-resolution basin-scale simulation with the Regional Oceanic Modelling System (ROMS, Shchepetkin and McWilliams, 2005) σ-coordinate model. Using this space–time discretization, we have demonstrated that the use of an isoneutral biharmonic operator significantly improves the conservation of intermediate water properties and leads to a tightening of the thermocline compared to an iso-σ biharmonic operator. Because the grid slope ratio with a σ-coordinate is generally larger than with a z-level model we took advantage of the gain of accuracy provided by the SW-TRIADS scheme.

Acknowledgements

Appendix A. Upper bound on $\varphi_m^\theta = \varphi_m - 2\theta y_{m3}^2$

The aim of this appendix is to derive an upper bound for the function φ_m^θ introduced in Section 3. We keep the notations previously used in the paper, and for convenience we introduce the parameters $X_m = \tan(\phi_m/2)$, $X_m \in \mathbb{R}$ ($m = 1, 3$); so that the expression of φ_m^θ transforms to

$$\varphi_m^\theta = 2\sigma_m \left(\frac{\left[(X_m + s_m X_3)^2 + (1 + s_m^2) X_m^2 X_3^2 \right]}{\left(1 + X_m^2 \right)\left(1 + X_3^2 \right)} - 2\theta s_m^2 \frac{X_3^2}{1 + X_3^2} \right).$$
(A.1)

In the remaining of this section we successively study the behavior of φ_m^θ with respect to X_m and then to X_3. We first get

$$\text{Sign}\left(\frac{\partial \varphi_m^\theta}{\partial X_m} \right) = \text{Sign}\left(s_m X_3 \left(1 - X_m^2 \right) + X_m \left(1 + X_3^2 \right) \right),$$
(A.2)

where the roots of the second order polynomial in X_m are

$$X_m^{(\pm)} = \frac{1 + X_3^2 \pm \sqrt{\left(1 + X_3^2 \right)^2 + (2s_m X_3)^2}}{2s_m X_3}.$$
(A.3)

$\frac{\partial \varphi_m^\theta}{\partial X_m}$ is positive for $X_m^{(-)} \leqslant X_m \leqslant X_m^{(+)}$ which is sufficient to show that φ_m^θ reaches its maximum either for $X_m = X_m^{(+)}$ or $X_m \to -\infty$. In (A.1), we see that the asymptotic limit of φ_m^θ for X_m going to infinity either by positive or negative values is the same; the maximum of

φ_m^θ is therefore obtained for $X_m = X_m^{(+)}$. Substituting X_m by $X_m^{(+)}$ in (A.1) leads to

$$\varphi_m^\theta \leqslant \varphi_m^\theta\left(X_m^{(+)} \right) = \bar{\varphi}_m^\theta$$

$$= 2\sigma_m \left(1 + 2s_m^2(1 - 2\theta) \frac{X_3^2}{1 + X_3^2} + \sqrt{1 + 4s_m^2 \frac{X_3^2}{1 + X_3^2} \left(1 - \frac{X_3^2}{1 + X_3^2} \right)} \right).$$
(A.4)

After some algebra, we find

$$\text{Sign}\left(\frac{\partial \bar{\varphi}_m^\theta}{\partial X_3} \right) = \text{Sign}\left((1 - 2\theta)\sqrt{1 + 4s_m^2 \widetilde{X}_3 (1 - \widetilde{X}_3)} + (1 - 2\widetilde{X}_3) \right),$$

$$\widetilde{X}_3 = \frac{X_3^2}{1 + X_3^2} \in [0, 1].$$
(A.5)

This derivative cancels for

$$\widetilde{X}_3 = \widetilde{X}_3^{(\pm)} = \frac{1}{2} \left[1 \pm \sqrt{\frac{(1 - 2\theta)^2 (1 + s_m^2)}{1 + (1 - 2\theta)^2 s_m^2}} \right].$$
(A.6)

The maximum of $\bar{\varphi}_m^\theta$ is reached for $\widetilde{X}_3 = \widetilde{X}_3^{(+)}$ if $\theta \leqslant 1/2$ and $\widetilde{X}_3 = \widetilde{X}_3^{(-)}$ otherwise. In both cases the maximum is the same and provides the following upper bound for φ_m^θ

$$\varphi_m^\theta \leqslant 2\sigma_m \cdot \mathcal{M}(\theta, s_m),$$
(A.7)

where

$$\mathcal{M}(\theta, s_m) = 1 + s_m^2(1 - 2\theta) + \sqrt{\left(1 + s_m^2 \right)\left(1 + s_m^2(1 - 2\theta)^2 \right)}.$$
(A.8)

Appendix B. Stability analysis with the SW-TRIADS scheme

In this section, we extend the results found in Sections 3 and 4 for the TRIADS scheme to the SW-TRIADS discretization. The function φ_m^θ (with $m = 1, 2$) defined in (3.22) for $\beta_m = 0$ (i.e., the TRIADS scheme) becomes

$$\varphi_m^{\theta,\text{sw}} = 2\sigma_m \left(\frac{\left[(X_m + s_m X_3)^2 + (s_m - 1)^2 X_m^2 X_3^2 \right]}{\left(1 + X_m^2 \right)\left(1 + X_3^2 \right)} - 2\theta s_m^2 \frac{X_3^2}{1 + X_3^2} \right)$$
(B.1)

for $\beta_m = 1$ (i.e., the SW-TRIADS scheme with $s_m \geqslant 0$). In this appendix, we consider only the case $s_m \geqslant 0$, it is straightforward to extend by symmetry the results to the case $s_m \leqslant 0$. As we did in Appendix A for φ_m^θ, we study here the behavior of $\varphi_m^{\theta,\text{sw}}$ with respect to X_m and X_3. After some algebra, we get

$$\text{Sign}\left(\frac{\partial \varphi_m^{\theta,\text{sw}}}{\partial X_m} \right) = \text{Sign}\left(s_m X_3 \left(1 - X_m^2 \right) + X_m \left(1 + X_3^2(1 - 2s_m) \right) \right),$$
(B.2)

where the roots of the second order polynomial in X_m are

$$X_m^{(\pm)} = \frac{1 + X_3^2(1 - 2s_m) \pm \sqrt{\left(1 + X_3^2(1 - 2s_m) \right)^2 + (2s_m X_3)^2}}{2s_m X_3}.$$
(B.3)

We can easily show that the maximum of $\varphi_m^{\theta,\text{sw}}$ is for $X_m = X_m^{(+)}$ which leads to

$$\varphi_m^{\theta,\text{sw}} \leqslant \varphi_m^{\theta,\text{sw}}\left(X_m^{(+)} \right) = \bar{\varphi}_m^{\theta,\text{sw}}$$

$$= 2\sigma_m \left(1 + 2(s_m(s_m - 1) - 2\theta s_m^2) \frac{X_3^2}{1 + X_3^2} \right.$$

$$\left. + \sqrt{1 + 4s_m(s_m - 1) \frac{X_3^2}{1 + X_3^2}} \right).$$
(B.4)

The sign of the derivative of this function with respect to X_3 reads

$$\mathrm{Sign}\left(\frac{\partial \bar{\varphi}_m^{\theta,\mathrm{sw}}}{\partial X_3}\right) = \mathrm{Sign}\left((s_m - 1)\left(1 + \sqrt{1 + 4s_m(s_m - 1)\widetilde{X}_3}\right)\right.$$
$$\left. -2s_m\theta\sqrt{1 + 4s_m(s_m - 1)\widetilde{X}_3}\right), \qquad (\mathrm{B.5})$$

where $\widetilde{X}_3 = X_3^2/\left(1 + X_3^2\right)$.

B.1. Rotated Laplacian operator

We recall that the space–time discretization under consideration is stable for $\varphi_1^{\theta,\mathrm{sw}} + \varphi_2^{\theta,\mathrm{sw}} \leqslant 2$. In (B.5), we see that for $s_m \leqslant 1$, $\partial \bar{\varphi}_m^{\theta,\mathrm{sw}}/\partial X_3$ is negative, hence the maximum is for $\widetilde{X}_3 = 0$ which translates into $\varphi_m^{\theta,\mathrm{sw}} \leqslant 4\sigma_m$ in (B.4). This shows that, in this case, the scheme is stable for $\sigma_1 + \sigma_2 \leqslant 1/2$ which corresponds to the stability condition of the non-rotated operator. Moreover, for $s_m > 1$, taking $\theta = (s_m - 1)/s_m$ still ensures that $\partial \bar{\varphi}_m^{\theta,\mathrm{sw}}/\partial X_3$ is negative, and thus leads to the same stability constraint. This last remark is sufficient to conclude that the stability condition of the rotated Laplacian operator discretized using the SW-TRIADS scheme in space and the (MSC) scheme in time is equivalent to the stability condition of the non-rotated Laplacian operator for

$$\theta = \theta^{\mathrm{sw}} = \max\left\{\frac{|s_1| - 1}{|s_1|}, \frac{|s_2| - 1}{|s_2|}, 0\right\}. \qquad (\mathrm{B.6})$$

If $|s_1|$ and $|s_2|$ are both smaller than 1 we get $\theta = 0$, and for $|s_m| \to \infty$, $\theta \to 1$ which also shows that the (IMP) scheme is stable as long as the horizontal terms of the tensor are stable.

B.2. Rotated biharmonic operator

Using (B.6), and following the methodology used in Section 4.3 to derive an expression for the stabilizing diffusivity $\tilde{\sigma}^{\mathrm{sw}}$, we find that

$$\tilde{\sigma} = \tilde{\sigma}^{\mathrm{sw}} = 8(S_1\sigma_1 + S_2\sigma_2)((1 + S_1)\sigma_1 + (1 + S_2)\sigma_2), \qquad S_m$$
$$= \max\left\{s_m^2 - |s_m|, 0\right\}. \qquad (\mathrm{B.7})$$

Note that $\tilde{\sigma}^{\mathrm{sw}}$ vanishes when $|s_1|$ and $|s_2|$ are smaller than one.

References

Andreev, V.B., 1967. Splitting operator difference schemes for general second order p-dimensional parabolic equations with mixed derivatives. USSR Comput. Math. Math. Phys. 7, 92–104.

Beckers, J.M., Burchard, H., Campin, J.M., Deleersnijder, E., Mathieu, P.P., 1998. Another reason why simple discretizations of rotated diffusion operators cause problems in ocean models: Comments on Isoneutral diffusion in a z-coordinate ocean model. J. Phys. Oceanogr. 28, 1552–1559.

Beckers, J.M., Burchard, H., Deleersnijder, E., Mathieu, P.P., 2000. Numerical discretization of rotated diffusion operators in ocean models. Mon. Weather Rev. 128, 2711–2733.

Colas, F., Capet, X., McWilliams, J.C., Li, Z., 2012. Mesoscale eddy buoyancy flux and eddy-induced circulation in eastern-boundary upwelling systems. J. Phys. Oceanogr. Under review.

Cox, M.D., 1987. Isopycnal diffusion in a z-coordinate ocean model. Ocean Modell. (unpublished manuscripts) 74, 1–5.

Craig, I., Sneyd, A., 1988. An alternating-direction implicit scheme for parabolic equations with mixed derivatives. Comput. Math. Appl. 16, 341–350.

Cushman-Roisin, B., Beckers, J.M., 2011. Introduction to Geophysical Fluid Dynamics: Physical and Numerical Aspects. Academic Press.

Danabasoglu, G., McWilliams, J.C., 1995. Sensitivity of the global ocean circulation to parameterizations of mesoscale tracer transports. J. Clim. 8, 2967–2987.

Danabasoglu, G., McWilliams, J.C., Gent, P.R., 1994. The role of mesoscale tracer transports in the global ocean circulation. Science 264, 1123–1126.

Delhez, E.J., Deleersnijder, E., 2007. Overshootings and spurious oscillations caused by biharmonic mixing. Ocean Modell. 17, 183–198.

Douglas, J., 1962. Alternating direction methods for three space variables. Numer. Math. 4, 41–63.

Douglas, J., Gunn, J.E., 1964. A general formulation of alternating direction methods. Numer. Math. 6, 428–453.

Ferrari, R., Griffies, S.M., Nurser, A.J.G., Vallis, G.K., 2010. A boundary-value problem for the parameterized mesoscale eddy transport. Ocean Modell. 32, 143–156.

Ferrari, R., McWilliams, J.C., Canuto, V., Dubovikov, M., 2008. Parameterization of eddy fluxes near oceanic boundaries. J. Clim. 21, 2770–2789.

Fox-Kemper, B., Ferrari, R., Hallberg, R., 2008. Parameterization of mixed layer eddies. part i: Theory and diagnosis. J. Phys. Oceanogr. 38, 1145–1165.

Gent, P.R., 2011. The Gent-McWilliams parameterization: 20/20 hindsight. Ocean Modell. 39, 2–9.

Gent, P.R., McWilliams, J.C., 1990. Isopycnal mixing in ocean circulation models. J. Phys. Oceanogr. 20, 150–155.

Gnanadesikan, A., Griffies, S.M., Samuels, B.L., 2007. Effects in a climate model of slope tapering in neutral physics schemes. Ocean Modell. 16, 1–16.

Goosse, H., Campin, J.M., Deleersnijder, E., Fichefet, T., Mathieu, P.P., Morales Maqueda, M.A., Tartinville, B., 2008. Description of the CLIO model version 3.0, 7 December 2008 http://www.astr.ucl.ac.be/research/CLIO/clio30.pdf.

Griffies, S.M., 2004. Fundamentals of Ocean Climate Models. Princeton University Press, Princeton, NJ, USA.

Griffies, S.M., 2010. Elements of MOM4p1, in: GFDL Ocean Group Technical Report No. 6. NOAA/GFDL, February 19, 2010. 444 pp.

Griffies, S.M., Gnanadesikan, A., Pacanowski, R.C., Larichev, V., Dukowicz, J.K., Smith, R.D., 1998. Isoneutral diffusion in a z-coordinate ocean model. J. Phys. Oceanogr. 28, 805–830.

Hallberg, R., Adcroft, A., 2009. Reconciling estimates of the free surface height in lagrangian vertical coordinate ocean models with mode-split time stepping. Ocean Modell. 29, 15–26.

Hecht, M.W., 2010. Cautionary tales of persistent accumulation of numerical error: dispersive centered advection. Ocean Modell. 35, 270–276.

Hofmeister, R., Burchard, H., Beckers, J.M., 2010. Non-uniform adaptive vertical grids for 3d numerical ocean models. Ocean Modell. 33, 70–86.

Hundsdorfer, W., 2002. Accuracy and stability of splitting with stabilizing corrections. Appl. Numer. Math. 42, 213–233.

in 't Hout, K., Welfert, B., 2009. Unconditional stability of second-order ADI schemes applied to multi-dimensional diffusion equations with mixed derivative terms. Appl. Numer. Math. 59, 677–692.

Leclair, M., Madec, G., 2011. z-–coordinate, an arbitrary lagrangian-eulerian coordinate separating high and low frequency motions. Ocean Modell. 37, 139–152.

Lemarié, F., Kurian, J., Shchepetkin, A.F., Molemaker, M.J., Colas, F., McWilliams, J.C., 2012. Are there inescapable issues prohibiting the use of terrain-following coordinates in climate models? Ocean Modell. 42, 57–79.

Lengaigne, M., Madec, G., Menkes, C., 2003. Impact of isopycnal mixing on the tropical ocean circulation. J. Geophys. Res., 108.

Madec, G., 2008. NEMO ocean engine, in: Note du Pole de modélisation No. 27. Institut Pierre-Simon Laplace (IPSL), France.

Manfredi, G., Ottaviani, M., 1999. Finite-difference schemes for the diffusion equation. In: Leach, P., Bouquet, S., Rouet, J.L., Fijalkow, E. (Eds.), Dynamical Systems, Plasmas and Gravitation, Lecture Notes in Physics, vol. 518. Springer, Berlin/Heidelberg, pp. 82–92.

Marchesiello, P., Debreu, L., Couvelard, X., 2009. Spurious diapycnal mixing in terrain-following coordinate models: The problem and a solution. Ocean Modell. 26, 159–169.

Mathieu, P.P., Deleersnijder, E., 1998. What is wrong with isopycnal diffusion in world ocean models? Appl. Math. Modell. 22, 367–378.

Mathieu, P.P., Deleersnijder, E., Beckers, J.M., 1999. Accuracy and stability of the discretised isopycnal-mixing equation. Appl. Math. Lett. 12, 81–88.

McDougall, T.J., 1987. Neutral surfaces. J. Phys. Oceanogr. 17, 1950–1964.

Redi, M.H., 1982. Oceanic isopycnal mixing by coordinate rotation. J. Phys. Oceanogr. 12, 1154–1158.

Shchepetkin, A., McWilliams, J.C., 2005. The regional oceanic modeling system: a split-explicit, free-surface, topography-following-coordinate ocean model. Ocean Modell. 9, 347–404.

Shchepetkin, A.F., McWilliams, J.C., 2011. Accurate Boussinesq oceanic modeling with a practical, "stiffened" equation of state. Ocean Modell. 38, 41–70.

Smith, R.D., Gent, P.R., 2004. Anisotropic Gent–McWilliams parameterization for ocean models. J. Phys. Oceanogr. 34, 2541–2564.

Smith, R.D., Jones, P., Briegleb, B., Bryan, F., Danabasoglu, G., Dennis, J., Dukowicz, J., Eden, C., Fox-Kemper, B., Gent, P., Hecht, M., Jayne, S., Jochum, M., Large, W., Lindsay, K., Maltrud, M., Norton, N., Peacock, S., Vertenstein, M., Yeager, S., 2010. The Parallel Ocean Program (POP) Reference Manual, 23 March 2010, LAUR-10-01853.

Solomon, H., 1971. On the representation of isentropic mixing in ocean circulation models. J. Phys. Oceanogr. 1, 233–234.

Treguier, A.M., Held, I.M., Larichev, V.D., 1997. On the parameterization of quasi-geostrophic eddies in primitive equation ocean models. J. Phys. Oceanogr., 567–580.

van der Houwen, P., Verwer, J., 1979. One-step splitting methods for semi-discrete parabolic equations. Computing 22, 291–309.

Chapter 8

Multigrid solvers and multigrid preconditioners for the solution of variational data assimilation problems, *QJRMS (2015)*

Multigrid solvers and multigrid preconditioners for the solution of variational data assimilation problems

Laurent Debreu [a]*Emilie Neveu[a] Ehouarn Simon[b] François-Xavier Le Dimet[a] Arthur Vidard[a]

[a]*INRIA Grenoble Rhône-Alpes and Laboratoire Jean Kuntzmann (LJK), Grenoble, France*

[b]*Université de Toulouse, INP, IRIT, Toulouse, France*

*Correspondence to: Laboratoire Jean Kuntzmann, 51 rue des Mathematiques, 38400 Saint Martin d'Heres, France. E-mail: Laurent.Debreu@inria.fr

In order to lower the computational cost of the variational data assimilation process, we investigate the use of multigrid methods to solve the associated optimal control system. In a linear advection equation, we study the impact of the regularization term on the optimal control and the impact of discretization errors on the efficiency of the coarse grid correction step. We show that even if the optimal control problem leads to the solution of an elliptic system, numerical errors introduced by the discretization can alter the success of the multigrid method. The view of multigrid iteration as a preconditioner for a Krylov optimization method leads to a more robust algorithm. A scale dependent weighting of the multigrid preconditioner and the usual background error covariance matrix based preconditioner is proposed and brings significant improvements.

1. Introduction

Data assimilation methods are a way of combining different sources of information: a priori information (background), observations and numerical models according to error statistics for these sources. Data assimilation methods can be divided into two groups: sequential and variational methods. Sequential methods like the ensemble Kalman filter (Evensen 2006) are based on the estimation theory and evolve the state vector in time along with its error statistics. Variational methods (Le Dimet

and Talagrand 1986) are based on optimal control techniques and minimize a cost function $J(\mathbf{x})$ that measures the distance between the model trajectory and observations. Both methods have huge computational costs and need simplification for operational purposes. The two approaches are well known to be equivalent in the linear case and in absence of model error. In this paper, we focus on variational data assimilation methods in the context of geophysical fluids. Assuming $\mathbf{x}$ is the control vector, the necessary condition of optimality at $\mathbf{x}^\star$ is given by the equation $\nabla_{\mathbf{x}} J(\mathbf{x}^\star) = \mathbf{0}$. It leads to the solution of a large unconstrained minimization

problem. This paper attempts to use multigrid methods for solving the resulting system.

In the optimal control framework, several attempts have been made to apply multigrid methods, either for linear or non linear optimization (see Borzì and Schulz (2009) for a review). Lewis and Nash (2005) focus on the control of the initial condition for a linear advection equation with a specific cost function and discretization scheme that renders the problem fully elliptic (i.e. large scale components of the error are more efficiently reduced on a coarser grid) and thus well suited for multigrid methods. In the framework of variational data assimilation, more specifically the problem of computing the observation impact on the solution of the minimization problem, Cioaca *et al.* (2013) reported relatively good performances of a basic multigrid algorithm applied to the resolution of a linear system for which the matrix is the Hessian of the cost function (evaluated at the optimal point). However, this study does not investigate or provide a theoretical basis for an efficient (or not) use of multigrid methods for the solution of the variational data assimilation problem.

In this paper, multigrid methods are applied to a simple 2D (1D in space, 1D in time) variational assimilation problem using a cost function $J(\mathbf{x})$ that mimics those used in more realistic applications in the context of geophysical fluids. The model is linear and leads to a quadratic cost function. Most of the actual implementations of variational data assimilation use a truncated Gauss Newton (also known as incremental) approach where a succession of minimizations of quadratic cost functions is performed. This study follows previous works of Neveu *et al.* (2011) on the application of multigrid methods to the solution of the 1D variational assimilation problem, and notably the impact of the model discretization and the regularization term in the cost function on the ellipticity of the discrete Hessian. We provide here a detailed study of the approximation property (i.e. the differences between the gradients computed on the coarse and fine grids) and its impact on the convergence (or divergence) of the multigrid algorithm.

In section 2, the variational data assimilation problem is described and its characteristics (in particular its ellipticity) are derived. Section 3 introduces the multigrid algorithm and the convergence criteria. Its application to variational data assimilation is studied in

section 4 where the main ingredients of the multigrid algorithms are discussed: smoothing property, design of transfer operators and approximation property. The effect of the background error correlation matrix on the ellipticity is studied as well as the impact of numerical model errors on the approximation property. Numerical experiments are performed in section 5 for 1D and 2D variational problems and illustrate the behavior of the multigrid algorithm for different parameters of the cost function and of the numerical model. The direct application of the multigrid method as a solver for data assimilation problems may lead to non-convergence in particular cases where the approximation property is strongly violated. For this reason, we also investigate the view of the multigrid method as a preconditioner for a conjugate gradient algorithm. This adds more robustness and leads to performance results that significantly outperform traditional unigrid methods based on the background error covariance matrix (or its square root). We show how to design a preconditioner that tries to take advantage of both types of methods. To the best of our knowledge, this preconditioner differs from other multigrid preconditioners used in PDE-constrained optimization problems. First, it applies to the whole Hessian matrix of the (possibly linearized) quadratic cost function which can be non elliptic. Thus, it does not target specific blocks of the system matrix (saddle-point structure) that have the ellipticity property (and are associated with an elliptic PDE) as the preconditioning strategies suggested by Rees *et al.* (2008) for instance. Second, it does not require smoothing steps that can be computationally expensive.

2. Variational data assimilation and associated linear system

We consider the time evolution of a system governed by the following equation:

$$
\begin{aligned}
\frac{\mathrm{d}X}{\mathrm{d}t} &= F(X) \\
X(t = t_0) &= \mathbf{x}
\end{aligned}
\tag{1}
$$

$\mathbf{x}$ is the initial condition at time $t = t_0$ and is our control parameter. The variational data assimilation problem consists of finding the minimum of a cost function $J(\mathbf{x})$ that measures the

distance of the model predicted state to the observations and includes a regularization term associated to background $\mathbf{x}_b$:

$$J(\mathbf{x}) = \frac{1}{2} (\mathbf{x} - \mathbf{x}_b)^T \mathbf{B}^{-1} (\mathbf{x} - \mathbf{x}_b)$$
$$+ \frac{1}{2} (H(X(\mathbf{x}, t)) - \mathbf{y})^T \mathbf{R}^{-1} (H(X(\mathbf{x}, t)) - \mathbf{y}). \quad (2)$$

Here $\mathbf{y}$ are the observations. H is the observation operator from model space to observation space, $\mathbf{R}$ and $\mathbf{B}$ are respectively the observation and background error covariance matrices. When observations are available at a number N_{obs} of different times t_i, the cost function can be more precisely written as:

$$J(\mathbf{x}) = \frac{1}{2} \|\mathbf{x} - \mathbf{x}_b\|^2_{\mathbf{B}^{-1}}$$
$$+ \frac{1}{2} \sum_{i=0}^{N_{\mathrm{obs}}-1} (H_i(X(\mathbf{x}, t_i)) - \mathbf{y}_i)^T \mathbf{R}_i^{-1} (H_i(X(\mathbf{x}, t_i)) - \mathbf{y}_i).$$
$$(3)$$

At a minimum $\mathbf{x}^\star$ of J, the gradient is zero

$$\nabla_{\mathbf{x}} J(\mathbf{x}^\star) = 0. \quad (4)$$

When the model F and the observations operator H are linear, the cost function is quadratic and the solution of (4) is equivalent to the solution of

$$\mathbf{A}\mathbf{x}^\star = \mathbf{b} \quad (5)$$

where $\mathbf{A}$ is the Hessian of the cost function:

$$\mathbf{A} = \mathbf{B}^{-1} + \mathbf{G}^T \mathbf{R}^{-1} \mathbf{G}$$

where $\mathbf{G}$ is a compact representation that includes both the model and the observation operators and the right hand side $\mathbf{b}$ is given by

$$\mathbf{b} = \mathbf{B}^{-1} \mathbf{x}_b + \mathbf{G}^T \mathbf{R}^{-1} \mathbf{y}.$$

The solution of (5) can thus be written:

$$\mathbf{x}^\star = \left(\mathbf{B}^{-1} + \mathbf{G}^T \mathbf{R}^{-1} \mathbf{G}\right)^{-1} \left(\mathbf{B}^{-1} \mathbf{x}_b + \mathbf{G}^T \mathbf{R}^{-1} \mathbf{y}\right)$$

or

$$\mathbf{x}^\star = \mathbf{x}_b + \left(\mathbf{B}^{-1} + \mathbf{G}^T \mathbf{R}^{-1} \mathbf{G}\right)^{-1} \mathbf{G}^T \mathbf{R}^{-1} (\mathbf{y} - \mathbf{G}\mathbf{x}_b)$$

Using the Sherman-Morrison-Woodbury formula

$$\left[\mathbf{A}^{-1} + \mathbf{B}^T \mathbf{C}^{-1} \mathbf{B}\right]^{-1} \mathbf{B}^T \mathbf{C}^{-1} = \mathbf{A}\mathbf{B}^T \left[\mathbf{C} + \mathbf{B}\mathbf{A}\mathbf{B}^T\right]^{-1},$$

we can also express the solution as

$$\mathbf{x}^\star = \mathbf{x}_b + \mathbf{B}\mathbf{G}^T \left(\mathbf{R} + \mathbf{G}\mathbf{B}\mathbf{G}^T\right)^{-1} (\mathbf{y} - \mathbf{G}\mathbf{x}_b) \quad (6)$$

Eq. (6) shows that a correction is first computed in observation space weighted by the sum of the observation error covariance matrix and the background error covariance matrix in observation space, transformed back to model state using $\mathbf{G}^T$ and then spatially distributed according to the $\mathbf{B}$ matrix. In practice, the minimization is conducted using $\mathbf{x}_b$ as a starting point. The scales of the final correction $(\mathbf{x}^\star - \mathbf{x}_b)$ are thus largely governed by the correlation scales in the $\mathbf{B}$ matrix. The main idea here is to solve the system (5) by multigrid methods and to evaluate the main characteristics of the problem that impact convergence and robustness. Among these characteristics, those of the background error covariance matrix are most important.

2.1. Definition of the background error covariance matrix B, preconditioning and implicit solver

The background error covariance matrix $\mathbf{B}$ is a symmetric and positive definite matrix that can be factored as $\mathbf{B} = \boldsymbol{\Sigma}\mathbf{C}\boldsymbol{\Sigma}$ where $\boldsymbol{\Sigma}$ is a diagonal matrix of background error standard deviations and $\mathbf{C}$ a symmetric matrix of background error correlations. The correlations can be modeled by applying a diffusion operator (Weaver and Courtier 2001). Indeed, pseudo-time integration over the interval $[0, \tau]$ of the diffusion equation

$$\frac{\partial \eta}{\partial s} = \varkappa \Delta \eta \quad (7)$$

where s is the pseudo-time coordinate, Δ is the Laplacian operator, approximates a Gaussian correlation function, $g(x) = e^{-\frac{x^2}{2L_{\mathrm{corr}}^2}}$, of length L_{corr} where $L_{\mathrm{corr}}^2 = 2\varkappa\tau$ is the square

of a length scale. Let $\mathcal{L}$ be the operator that evolves η from time 0 to pseudo-time τ:

$$\eta(\tau) = \mathcal{L}\,\eta(0).$$

A diagonal normalization matrix $\boldsymbol{\Lambda}$ is then computed so that $\mathbf{C}$ written under the form

$$\mathbf{C} = \boldsymbol{\Lambda}\mathcal{L}\boldsymbol{\Lambda}$$

has ones along its diagonal. Assuming the square root of the operator $\mathcal{L}$ is available (it corresponds to applying the diffusion operator over half the pseudo-time interval), the coefficients of $\boldsymbol{\Lambda}$ can be computed using the relation

$$\mathbf{e}_i^T \mathbf{C} \mathbf{e}_i = 1 \qquad \Leftrightarrow (\mathcal{L}^{1/2}\boldsymbol{\Lambda}\mathbf{e}_i)^T (\mathcal{L}^{1/2}\boldsymbol{\Lambda}\mathbf{e}_i) = 1, \quad \forall i$$

If Λ_{ii} is the i-th diagonal element of the diagonal matrix $\boldsymbol{\Lambda}$ ($\Lambda_{ii}\mathbf{e}_i = \boldsymbol{\Lambda}\mathbf{e}_i$), we have:

$$\Lambda_{ii} = \sqrt{(\mathcal{L}^{1/2}\mathbf{e}_i)^T (\mathcal{L}^{1/2}\mathbf{e}_i)}.$$

2.1.1. Preconditioning

The performance of an iterative minimization method for the solution of (5) is linked to the condition number of this system. The system matrix $\mathbf{A}$ being symmetric and positive definite, the condition number can be defined as $\mathcal{K}(\mathbf{A}) = \frac{\lambda_{\max}(\mathbf{A})}{\lambda_{\min}(\mathbf{A})}$ where $\lambda_{\min}(\mathbf{A})$ and $\lambda_{\max}(\mathbf{A})$ are the smallest and largest eigenvalues of $\mathbf{A}$. In general, the larger the condition number, the slower the rate of convergence. When matrix $\mathbf{B}$ and its square root are available as in the preceding derivation (where $\mathbf{B}^{1/2} = \boldsymbol{\Sigma}\boldsymbol{\Lambda}\mathcal{L}^{1/2}$), an alternative, symmetrically preconditioned, form of (5) can be deduced (see Courtier (1997)):

$$\mathbf{B}^{T/2}\mathbf{A}\mathbf{B}^{1/2}\mathbf{z}^\star = \mathbf{B}^{T/2}\mathbf{b} \qquad (8)$$

where $\mathbf{x}^\star = \mathbf{B}^{1/2}\mathbf{z}^\star$ and $\mathbf{B}^{T/2}$ stands for transpose of the square root of $\mathbf{B}$. The preconditioned system matrix is given by:

$$\mathbf{B}^{T/2}\mathbf{A}\mathbf{B}^{1/2} = \mathbf{I} + (\mathbf{G}\mathbf{B}^{1/2})^T\mathbf{R}^{-1}(\mathbf{G}\mathbf{B}^{1/2}).$$

$\mathbf{B}^{T/2}\mathbf{A}\mathbf{B}^{1/2}$ has its smallest eigenvalue superior or equal (if H or G is low rank) to 1 and its condition number $\mathcal{K}(\mathbf{B}^{T/2}\mathbf{A}\mathbf{B}^{1/2})$ is bounded.

2.1.2. Explicit/implicit solution

If (7) is integrated with an explicit Euler scheme using M_{lap} time steps, the discrete form writes

$$\eta(\tau) = \mathcal{L}_+^{M_{\mathrm{lap}}}\eta(0), \qquad \mathcal{L}_+ = [\mathbf{I} + \varkappa\Delta t\,\Delta] \qquad (9)$$

where $M_{\mathrm{lap}}\Delta t = \tau$, $\varkappa\Delta t = \frac{L_{\mathrm{corr}}^2}{2M_{\mathrm{lap}}}$. When associated with a second order centered approximation of the Laplacian, the operator $\mathcal{L}_+$ is constrained by the stability condition $\varkappa\Delta t/\Delta x^2 \leq 1/2$ which leads to

$$M_{\mathrm{lap}} \geq \left(\frac{L_{\mathrm{corr}}}{\Delta x}\right)^2. \qquad (10)$$

At very high resolution, the stability constraint (10) of the diffusion operator can lead to a large increase of the corresponding cost due to the required number of time steps. In order to alleviate the cost, the diffusion equation can be integrated in time using an implicit scheme (Carrier and Ngodock (2010); Mirouze and Weaver (2010)). In that case, (9) is rewritten as

$$\eta(\tau) = \mathcal{L}_-^{-M_{\mathrm{lap}}}\eta(0), \qquad \mathcal{L}_- = [\mathbf{I} - \varkappa\Delta t\,\Delta]$$

This formulation has been adopted in practical applications. Note that each step now requires the inversion of the Laplacian operator that is also potentially computationally expensive. However Gratton *et al.* (2013) have shown that it can be efficiently solved by a multigrid scheme. In the following, we will use this formulation which also leads to a very fast and explicit computation of $\mathbf{B}^{-1}$ used in the non-preconditioned system:

$$\mathbf{B}^{-1} = \boldsymbol{\Sigma}^{-1}\boldsymbol{\Lambda}^{-1}\mathcal{L}_-^{M_{\mathrm{lap}}}\boldsymbol{\Lambda}^{-1}\boldsymbol{\Sigma}^{-1}. \qquad (11)$$

It will allow us to easily compare the non-preconditioned to the preconditioned version.

2.2. Design of the numerical experiments

In order to study the eigenpairs of our data assimilation problem, we introduce some of the parameters of our idealized test case. The domain is a one dimensional periodic domain of size L. The uniform grid is composed of N cells of stepsize Δx.

The distance between two observation points is denoted by L_{obs} so that the observations are evenly located every $L_{\text{obs}}/\Delta x$ grid points. The observation operator H is a simple selection operator at corresponding grid points. As in most of the practical applications, the error correlation matrix $\mathbf{R}$ is assumed to be a diagonal matrix with constant standard deviation equal to σ_{obs}.

The background error correlation matrix is based on the implicit form of the diffusion operator and the number M_{lap} of iterations is equal to 4 which provides a good compromise between the computational costs and the accuracy of the approximation of the explicit form of the correlation matrix. The matrix $\mathbf{B}$ has a constant variance ($\mathbf{\Sigma} = \sigma_b \mathbf{I}$).

The numerical model approximates the solution of a linear advection equation:

$$\frac{\partial u}{\partial t} + c\,\frac{\partial u}{\partial x} = 0, \text{ with } c > 0, x \in [0, L], t \in [0, T], \qquad (12)$$

using the initial condition $u(x, t = 0) = u^0(x)$ which represents our control parameter. The numerical values of the following parameters are fixed:

$$c = 1\text{m.s}^{-1}, L = 100\text{m}, T = 78.125\text{s}.$$

For the sake of simplicity, the value $T = 78.125\text{s}$ is chosen to guarantee that the times of the observations correspond to model temporal grid points at the different grid levels (no time interpolation of the observations). The discretization of (12) is achieved using a Lax Wendroff scheme (Lax and Wendroff 1960) which is second order accurate both in time and space. An important parameter of the numerical model is the Courant number $\mu = c\,\dfrac{\Delta t}{\Delta x}$ where Δt is the time step. This parameter controls the accuracy of the discretization. The discretization is stable if $\mu \le 1$ and for $\mu < 1$ implicit diffusion is introduced by the numerical scheme. The special value of $\mu = 1$ leads to a

numerical solution that coincides with the exact solution.

2.3. Eigenstructure of the data assimilation problem

The convergence of the optimization problem or equivalently the solution of the linear system $\mathbf{Ax} = \mathbf{b}$ using iterative methods is known to be dependent on the conditioning of the matrix and the spectrum of its eigenvalues. We recall that matrix $\mathbf{A}$ is given by

$$\mathbf{A} = \mathbf{A}^{NP} = \mathbf{B}^{-1} + \mathbf{G}^T \mathbf{R}^{-1} \mathbf{G}$$

in non-preconditioned (*NP*) mode and by

$$\mathbf{A} = \mathbf{A}^{P} = \mathbf{I} + (\mathbf{GB}^{1/2})^T \mathbf{R}^{-1}(\mathbf{GB}^{1/2})$$

in preconditioned (*P*) mode.

Several results on the condition number of these matrices can be found in Haben *et al.* (2011). Here, we summarize the main characteristics of the systems and illustrate them - eigenvalue spectrum and condition number for both the non-preconditioned and preconditioned versions - in a 1DVAR case ($N_{\text{obs}} = 1$, the observations being at initial time t_0) and in a 2DVAR - 1D in space and 1D in time - case (observations are located at several times t_i with $t_{i+1} = t_i + T_{\text{obs}}$ where T_{obs} is fixed to $7.8125s$). In both cases, the number of grid cells N is equal to 128.

1. If we focus only on the background term ($\mathbf{A}^{NP} = \mathbf{B}^{-1}$) in our periodic domain, simple computations lead to the following condition number:

$$\mathcal{K}(\mathbf{B}^{-1}) = \left[1 + \frac{2}{M_{\text{lap}}} \left(\frac{L_{\text{corr}}}{\Delta x} \right)^2 \right]^{M_{\text{lap}}}.$$

Note that $\mathcal{K}(\mathbf{B}^{-1}) = \mathcal{K}(\mathcal{L}_{-}^{M_{\text{lap}}})$ since, due to periodicity, $\mathbf{\Sigma}$ and $\mathbf{\Lambda}$ are multiples of the identity matrix. The expression of the condition number differs from Gratton *et al.* (2013) who assumed a closed domain with Dirichlet boundary conditions. Due to the assumption of a periodic domain, zero becomes an eigenvalue of the Laplacian operator, and so the minimum eigenvalue of $\mathbf{B}^{-1}$ is one. Note that this expression would also hold for

closed domain with a Neumann boundary condition. This condition number can be relatively high and increases when the resolution ($\Delta x \searrow$) or when the correlation length L_{corr} increases. These results are in agreement with the findings of Haben *et al.* (2011) obtained in a different framework.

2. The preconditioning by $\mathbf{B}^{1/2}$ ensures that the smallest eigenvalues of $\mathbf{A}^P$ are bounded from below by 1 (Courtier, 1997). Obviously, the preconditioning is effective when the relative weight of the background term is not negligible in comparison with the weight on the observation error. This weight is dependent on the ratio of the standard error deviations $\sigma_b/\sigma_{\text{obs}}$ and on the ratio $L_{\text{obs}}/\Delta x$. Thus, Haben *et al.* (2011) showed that the condition number of the preconditioned Hessian is "likely to increase when the observations are accurate and dense or when the background error correlation lengthscales are large." In the trivial case where the model and the observation operator are the identity ($\mathbf{G} = \mathbf{I}$) and the observation error covariance matrix $\mathbf{R}$ is a diagonal matrix with constant variance equal to σ_{obs}^2, the eigenvalues of the preconditioned and non-preconditioned matrices are given by

$$\lambda(\mathbf{A}^{NP}) = \frac{1}{\sigma_{\text{b}}^2}\lambda(\mathbf{C}^{-1}) + \frac{1}{\sigma_{\text{obs}}^2},$$

$$\lambda(\mathbf{A}^P) = 1 + \frac{\sigma_{\text{b}}^2}{\sigma_{\text{obs}}^2}\lambda(\mathbf{C}),$$

and satisfy

$$\mathcal{K}(\mathbf{A}^{NP}) = \frac{\frac{1}{\sigma_{\text{b}}^2}\lambda_{\max}(\mathbf{C}^{-1}) + \frac{1}{\sigma_{\text{obs}}^2}}{\frac{1}{\sigma_{\text{b}}^2}\lambda_{\min}(\mathbf{C}^{-1}) + \frac{1}{\sigma_{\text{obs}}^2}} = \frac{\lambda_{\max}(\mathbf{C}^{-1}) + \frac{\sigma_{\text{b}}^2}{\sigma_{\text{obs}}^2}}{\lambda_{\min}(\mathbf{C}^{-1}) + \frac{\sigma_{\text{b}}^2}{\sigma_{\text{obs}}^2}}$$

$$(13)$$

$$\mathcal{K}(\mathbf{A}^P) = \frac{1 + \frac{\sigma_{\text{b}}^2}{\sigma_{\text{obs}}^2}1/\lambda_{\min}(\mathbf{C}^{-1})}{1 + \frac{\sigma_{\text{b}}^2}{\sigma_{\text{obs}}^2}1/\lambda_{\max}(\mathbf{C}^{-1})} = \frac{\lambda_{\max}(\mathbf{C}^{-1})}{\lambda_{\min}(\mathbf{C}^{-1})}\frac{1}{\mathcal{K}(\mathbf{A}^{NP})}.$$

So that

$$\mathcal{K}(\mathbf{A}^{NP})\mathcal{K}(\mathbf{A}^P) = \mathcal{K}(\mathbf{C}^{-1}) = \mathcal{K}(\mathbf{B}^{-1}), \qquad (14)$$

which shows that for a fixed background error correlation matrix, the condition number of the non-preconditioned system decreases when the condition number of the preconditioned system increases. We note a similar behavior of both condition numbers (see Table (1) for the 1DVAR case and Table (2) for the 2DVAR case) even if the systems are not fully observed.

3. If the system is not fully observed ($\mathbf{G}^T\mathbf{G} \neq \mathbf{I}$), but there is one observation point every $L_{\text{obs}}/\Delta x$ grid points, the eigenvalues may become clustered if the background error correlation length is relatively small. This phenomenon is illustrated in Figures (1,2) which present the eigenvalue spectrum of both the unpreconditioned and preconditioned versions of the algorithm for the 1DVAR case. Indeed, in this case the eigenvalue problem can be approximated by L/L_{obs} similar eigenvalue problems between two observation points. The clustering of eigenvalues improves the convergence rate of an iterative algorithm. Indeed, in exact arithmetic, the conjugate gradient (CG) algorithm converges in a number of iterations at most equal to the number of distinct eigenvalues of the matrix.

4. For the time dependent problem, extending the length of the assimilation windows increases the weight of the observation term and so decreases the relative weight of the background term. This renders the background term based preconditioner less efficient. This can be seen in table (2) and in figure (3) which represents the eigenvalues for a different number of observations in time ($N_{\text{obs}} = 1$ (i.e. 1DVAR), $N_{\text{obs}} = 5$ and $N_{\text{obs}} = 10$) in the 2DVAR case. For the non-preconditioned version, the extension of the length of the assimilation window is associated with an increase of the smallest eigenvalues due to the larger weight of the observation term, the largest eigenvalues still coincide with those of the $\mathbf{B}^{-1}$ matrix. This is in agreement with relation (13) that was derived in the simple case of an identity observation operator. Thus, globally the condition number decreases. For the preconditioned version, the smallest eigenvalue is still one while the largest eigenvalues increase with the

weight of the observation term. Globally the condition number increases. This result is in agreement with the works of Haben *et al.* (2011); Desroziers and Berre (2012) who noted a similar increase of the condition number of the preconditioned Hessian when assimilating dense and accurate observations.
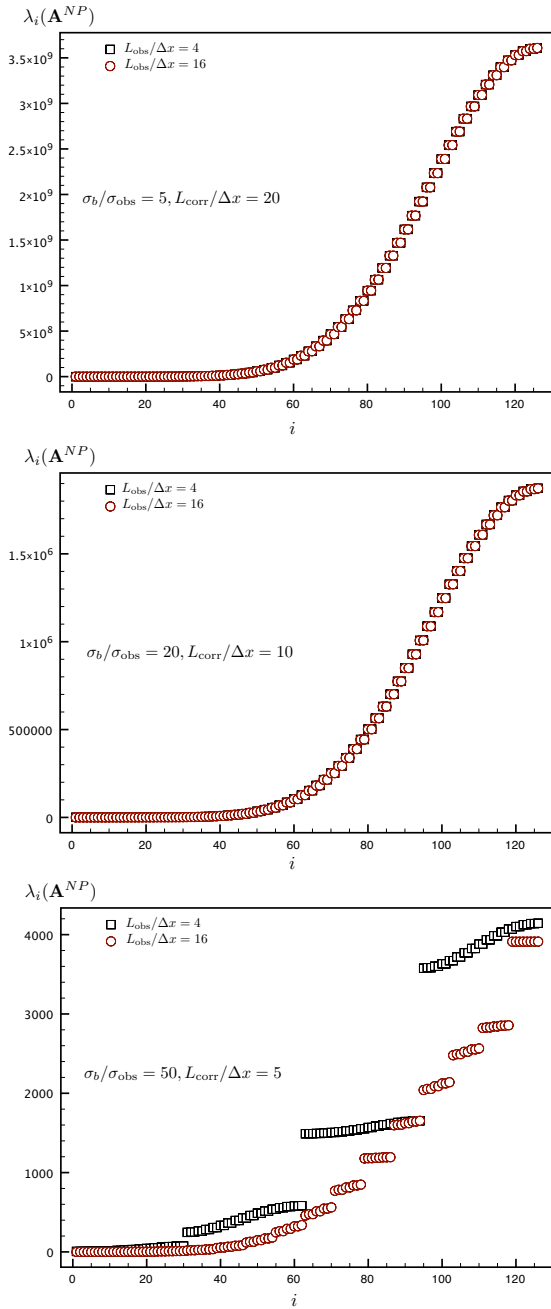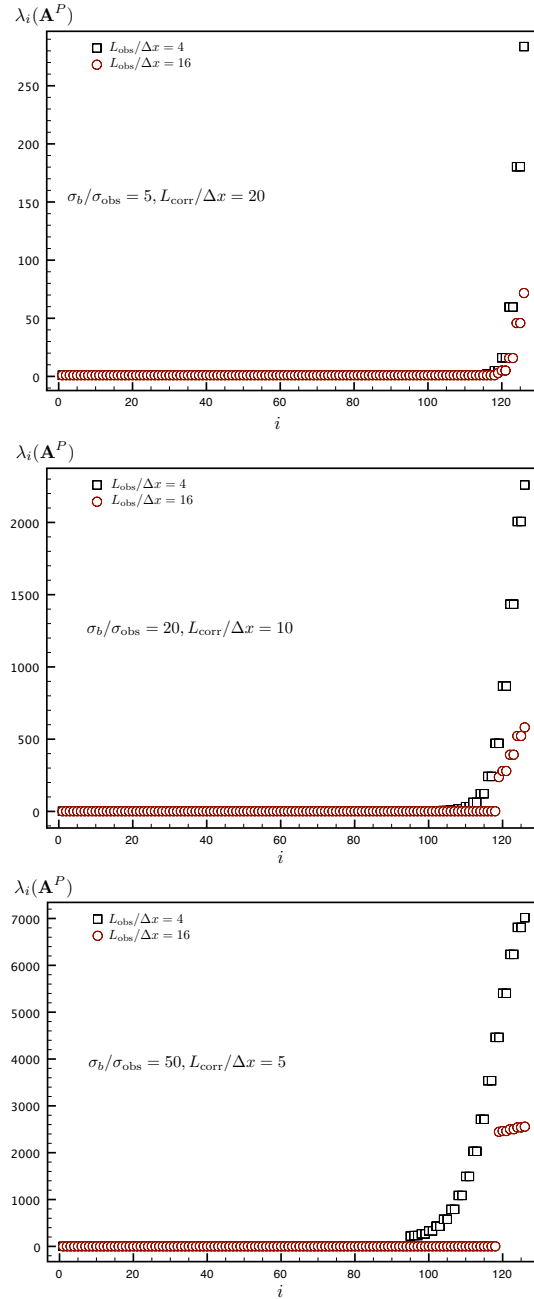

Figure 1. Eigenvalue spectrum $(\lambda_i(\mathbf{A}^{NP}), i = 1 \ldots N)$ of the non-preconditioned version for the 1DVAR case $(N_{\text{obs}} = 1)$ and for $\sigma_b/\sigma_{\text{obs}} = 5, L_{\text{corr}}/\Delta x = 20$ (top), $\sigma_b/\sigma_{\text{obs}} = 20, L_{\text{corr}}/\Delta x = 10$ (middle) and $\sigma_b/\sigma_{\text{obs}} = 50, L_{\text{corr}}/\Delta x = 5$ (bottom)

In the rest of the paper, $L_{\text{obs}}/\Delta x$ is fixed and equal to 16.

Figure 2. Eigenvalue spectrum $(\lambda_i(\mathbf{A}^P), i = 1 \ldots N)$ of the preconditioned version for the 1DVAR case $(N_{\text{obs}} = 1)$ and for $\sigma_b/\sigma_{\text{obs}} = 5, L_{\text{corr}}/\Delta x = 20$ (top), $\sigma_b/\sigma_{\text{obs}} = 20, L_{\text{corr}}/\Delta x = 10$ (middle) and $\sigma_b/\sigma_{\text{obs}} = 50, L_{\text{corr}}/\Delta x = 5$ (bottom)

$\sigma_b/\sigma_{\text{obs}}$	$L_{\text{corr}}/\Delta x$	$L_{\text{obs}}/\Delta x$	NP	P
5	20	4	5741850	284
5	20	16	23454000	71
20	10	4	3030	2260
20	10	16	1136080	580
50	5	4	695	7017
50	5	16	26830	2555

Table 1. 1DVAR Condition numbers for the non-preconditioned (NP) version and for the preconditioned (P) version

Ellipticity

In a typical optimization method, the error relative to large eigenvalues of $\mathbf{A}$ will be removed faster than the one relative to

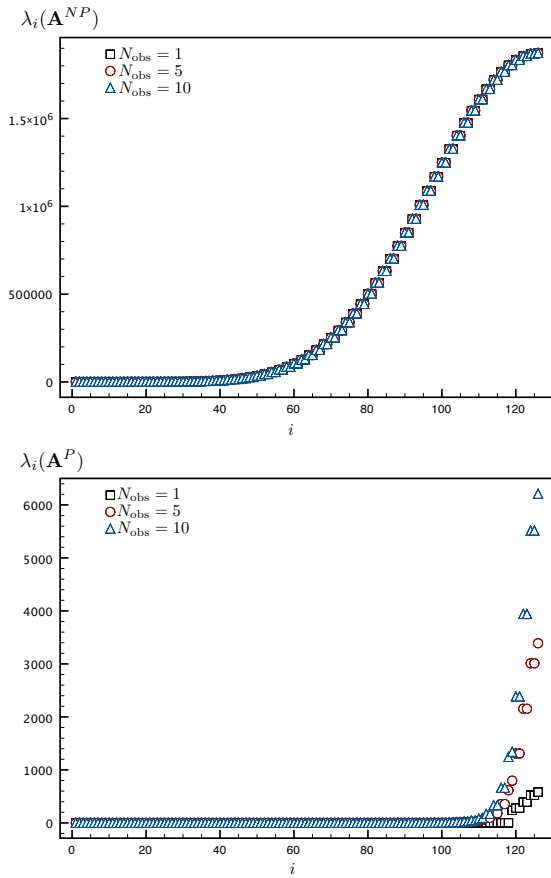$\lambda_i(\mathbf{A}^{NP})$

$\lambda_i(\mathbf{A}^P)$

Figure 3. Eigenvalue spectrum for the 2DVAR case for $\sigma_b/\sigma_{\mathrm{obs}} = 10$, $L_{\mathrm{corr}}/\Delta x = 20$. Non-preconditioned (top), preconditioned (bottom). Note that the vertical axis differ by several order of magnitude.

N_{obs}	Non-preconditioned	Preconditioned
1	14427643	284
5	1029078	1697
10	530060	3110

Table 2. 2DVAR Condition numbers, $\sigma_b/\sigma_{\mathrm{obs}} = 20$, $L_{\mathrm{obs}}/\Delta x = 16$, $L_{\mathrm{corr}}/\Delta x = 20$

small eigenvalues of $\mathbf{A}$ - see for instance Briggs *et al.* (2000). This is because a matrix-vector product based iterative method uses as a basic ingredient the residual $(\mathbf{A}\mathbf{x} - \mathbf{b} = \mathbf{A}(\mathbf{x} - \mathbf{x}^\star))$ which is small for small eigenvalues even if the error $(\mathbf{x} - \mathbf{x}^\star)$ itself has a large amplitude. So it is important to identify the scales relative to the eigenvectors. These scales are defined here using a filtering based on interpolation and restriction operators. If $\mathbf{v}$ is an eigenvector of $\mathbf{A}$, then the measured quantity is

$$\xi(\mathbf{v}) = \frac{\|(\mathbf{I} - \mathbf{I}_c^f \mathbf{I}_f^c)\mathbf{v}\|_2}{\|\mathbf{v}\|_2}$$

where $\mathbf{I}_f^c$ is a restriction operator from the current grid Ω_f to a twice coarser resolution grid Ω_c and $\mathbf{I}_c^f$ is an interpolation operator

from Ω_c to Ω_f. By construction, $\xi(v)$ is small at large scales and close to one at small scales. In figure (4), $\xi(v_i)$ is plotted for the N eigenvectors ($N = 128$) of the non-preconditioned and the preconditioned version. The interpolation and restriction operators are defined accordingly to the eight order interpolation and restriction operators introduced in §4.1. The eigenvectors $\mathbf{v}_i$ are ordered according to increasing eigenvalue.
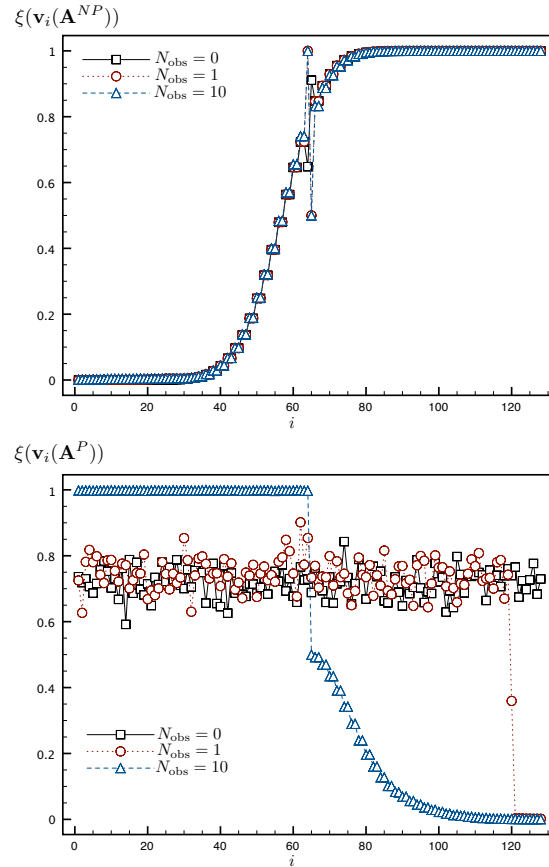
$\xi(\mathbf{v}_i(\mathbf{A}^{NP}))$

$\xi(\mathbf{v}_i(\mathbf{A}^P))$

Figure 4. Scales of eigenvectors for $\sigma_b/\sigma_{\mathrm{obs}} = 10$, $L_{\mathrm{corr}}/\Delta x = 20$ and for different number of observation times. $N_{\mathrm{obs}} = 0$ corresponds to the background term only, $N_{\mathrm{obs}} = 1$ to observations only at initial time (1DVAR). Non-preconditioned (top), preconditioned (bottom)

The properties of the non-preconditioned version with small eigenvalues (seen in figure (3)) corresponding to large scales (seen in figure (4)) (and vice versa) is characteristic of an *elliptic* system (for a precise definition of the concept of ellipticity on a discrete grid (h-ellipticity) see Trottenberg *et al.* (2000), §4.7.1). In our data assimilation problem, this characteristic mainly comes from the background (or regularization) term which enables control of the small scales of the initial condition, a control that could not be performed with the observation term only, particularly in the case of a partially observed system. Ellipticity is at the base of the use of multigrid methods that are introduced in the next section for

general linear systems.

In figure (4), it can be seen that the preconditioning removes the ellipticity of the original matrix. The large scales correspond to large eigenvalues so that the large scale component of the error will be first reduced. Note that when the length of the assimilation windows is extended (i.e. when $N_{\rm obs}$ is increased), it has almost no effect on the eigenvectors of the non-preconditioned version while it has a strong impact on those of the preconditioned version. In particular, it can be seen (Figure (4, bottom) that the number of large scale modes is increased. For $N_{\rm obs} = 10$ (blue dashed curve), eigenvectors from approximately 65 to 100 now correspond to medium to large scales. Because they are still associated with small eigenvalues (cf figure (3)), the reduction of error components along these eigenvectors will be slow and can benefit from the use of a coarser resolution grid.

The principal idea of the multigrid method is that if there are some large scale components that are slow to converge on the high resolution grid, they are reduced faster and at a smaller cost on a coarser resolution grid.

3. Multigrid methods

3.1. Multigrid methods: algorithm

Readers can refer to Briggs *et al.* (2000) for an excellent introduction to the subject. The general idea is to begin by reducing the small scale components of the error on the current (high resolution) grid Ω_f. This is called the pre-smoothing step and should be achieved in a few iterations according to the ellipticity of the system (large eigenvalues at small scales). The error is then smooth and can be appropriately computed on a coarse resolution grid Ω_c during the coarse grid correction step. The correction is then interpolated back to the fine grid. Since the interpolation operator can in turn produce small scale error components, a post-smoothing step is finally applied.

The basic algorithm with two grid levels can be written: MULTIGRID(ν_1,ν_2,Ω_f,$\mathbf{x}_f$,b_f)

1. Pre-smoothing: Apply ν_1 steps of an iterative method $\mathbf{S}_1$ on a fine grid for the solution of $\mathbf{A}_f\mathbf{x}_f = \mathbf{b}_f$. During pre-smoothing, the error $\mathbf{e}_f = \mathbf{x}_f - \mathbf{x}^*$ evolves as:

$$\mathbf{e}_f \leftarrow \mathbf{S}_1^{\nu_1}\mathbf{e}_f.$$

2. Coarse grid correction

   • Transfer the residual onto a coarser grid

   $$\mathbf{r}_c = \mathbf{I}_f^c(\mathbf{b}_f - \mathbf{A}_f\mathbf{x}_f), \quad I_f^c : \text{ restriction operator}$$

   • Solve the problem on the coarse grid

   $$\mathbf{A}_c\delta\mathbf{x}_c = \mathbf{r}_c. \tag{15}$$

   • Transfer the correction onto the fine grid

   $$\mathbf{x}_f = \mathbf{x}_f + \mathbf{I}_c^f\delta\mathbf{x}_c, \quad \mathbf{I}_c^f : \text{ interpolation operator}$$

3. Post-smoothing: Apply ν_2 steps of an iterative method $\mathbf{S}_2$ (most of the time identical to $\mathbf{S}_1$) onto a fine grid for the solution of $\mathbf{A}_f\mathbf{x}_f = \mathbf{b}_f$. During post-smoothing, the error $\mathbf{e}_f = \mathbf{x}_f - \mathbf{x}^*$ evolves as:

$$\mathbf{e}_f \leftarrow \mathbf{S}_2^{\nu_2}\mathbf{e}_f.$$

The extension of this two grid algorithm to a multi grid algorithm is done recursively by solving eq. 15 by a multigrid algorithm. Eq. 15 is replaced by

$$\text{For } n = 1\ldots\gamma, MULTIGRID(\nu_1, \nu_2, \Omega_c, \delta\mathbf{x}_c, \mathbf{r}_c)$$

The number γ of recursive calls determines the kind of multigrid algorithms: the best known being the V-cycle ($\gamma = 1$) and W-cycle ($\gamma = 2$) and are depicted in figure (5).
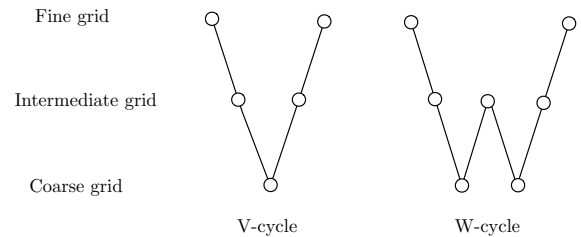

Figure 5. V-cycle and W-cycle algorithms in the case of three grid levels

3.2. Full Approximation Scheme variant

In the multigrid algorithm introduced above, the coarse grid correction seeks a solution for the error $\delta\mathbf{x}_c$ (eq. 15). It is possible

to rewrite the algorithm in an equivalent form where a coarse solution is searched for instead. This is the Full Approximation Scheme (FAS) (Brandt 1982) which has a natural extension to non linear operators and also permits the recursive use of multigrid acceleration techniques that will be introduced in (5.4). The coarse grid correction step is obtained by expressing the coarse grid correction $\delta\mathbf{x}_c$ as $\mathbf{x}_c - I_f^c\mathbf{x}_f$ and the problem is solved for the full approximation $\mathbf{x}_c$ instead of the correction $\delta\mathbf{x}_c$:

- Solve the problem on the coarse grid

$$\mathbf{A}_c\mathbf{x}_c = \mathbf{b}_c \qquad (16)$$

where

$$\mathbf{b}_c = \mathbf{r}_c + \mathbf{A}_c\mathbf{I}_f^c\mathbf{x}_f = \mathbf{I}_f^c\mathbf{b}_f + \left(\mathbf{A}_c\mathbf{I}_f^c - \mathbf{I}_f^c\mathbf{A}_f\right)\mathbf{x}_f.$$

- Transfer the correction onto the fine grid

$$\mathbf{x}_f = \mathbf{x}_f + \mathbf{I}_c^f\left(\mathbf{x}_c - \mathbf{I}_f^c\mathbf{x}_f\right).$$

3.3. Ingredients of convergence: the smoothing and approximation properties

We refer to Hackbusch (2003) for a detailed explanation of the different ingredients of the convergence proof.

3.3.1. Smoothing property

The relation between the error $\mathbf{e}_f = \mathbf{x}_f - \mathbf{x}^*$ before ($\mathbf{e}_f^{\text{before}_{\text{cc}}}$) and after ($\mathbf{e}_f^{\text{after}_{\text{cc}}}$) the coarse grid correction step is given by:

$$\mathbf{e}_f^{\text{after}_{\text{cc}}} = \left(\mathbf{I} - \mathbf{I}_c^f\mathbf{A}_c^{-1}\mathbf{I}_f^c\mathbf{A}_f\right)\mathbf{e}_f^{\text{before}_{\text{cc}}}.$$

Including the smoothing steps (and assuming only pre-smoothing is applied ($\nu_1 = \nu, \nu_2 = 0$),

$$\mathbf{e}_f^{k+1} = \left(\mathbf{I} - \mathbf{I}_c^f\mathbf{A}_c^{-1}\mathbf{I}_f^c\mathbf{A}_f\right)\mathbf{S}^\nu\mathbf{e}_f^k .$$

The smoothing steps $\mathbf{S}^\nu$ should remove most of the error at small scales while the coarse grid correction step should remove the large scale error. These two properties enable us to show

that the spectral radius of the multigrid iteration matrix $\mathbf{\Phi} = \left(\mathbf{I} - \mathbf{I}_c^f\mathbf{A}_c^{-1}\mathbf{I}_f^c\mathbf{A}_f\right)\mathbf{S}^\nu$ can be made less than one if a sufficient number of smoothing steps ν are applied.

3.3.2. Order of transfer operators and the approximation property

The coarse grid correction matrix is defined by $\left(\mathbf{I} - \mathbf{I}_c^f\mathbf{A}_c^{-1}\mathbf{I}_f^c\mathbf{A}_f\right)$. Let $q(\mathbf{A})$ be the order of the differential operator that leads to the matrix $\mathbf{A}$. The order of a restriction operator ($\mathbf{I}_f^c$) (on a grid of size Δx) is defined as the largest integer $m \geq 0$ so that

$$\widehat{\mathbf{I}_f^c}(k\Delta x) = 1 + \mathcal{O}((k\Delta x)^m), \quad \text{for } k\Delta x \to 0$$

where $\widehat{\mathbf{I}_f^c}(k\Delta x)$ is the Fourier component associated with the wavenumber k. A similar definition holds for the order of a prolongation operator (see Hemker (1990)). The following conditions on the order of the restriction ($\mathbf{I}_f^c$) and prolongation ($\mathbf{I}_c^f$) operators must hold:

$$order(\mathbf{I}_f^c) \geq q(\mathbf{A}), \quad order(\mathbf{I}_c^f) \geq q(\mathbf{A}). \qquad (17)$$

Relations (17) correspond to strong conditions implying that the norm of the error amplification matrix (the coarse grid correction matrix) and also the norm of the residual amplification matrix are bounded. These conditions are more restrictive than the usual ones $order(\mathbf{I}_f^c) + order(\mathbf{I}_c^f) \geq q(\mathbf{A})$, which only imply that the small scale components of the error are not amplified during one coarse grid correction step.

In addition, the approximation property states that the coarse grid matrix $\mathbf{A}_c$ is close to the fine grid matrix $\mathbf{A}_f$ and induces a reduction of large scale error components. This property is maintained by the underlying discretization order of the differential operator. Another approach is to use where possible the so called Galerkin approximation to deduce the coarse grid matrix $\mathbf{A}_c$. In this approximation, the restriction and interpolation operators are adjoints:

$$\mathbf{I}_c^f = (\mathbf{I}_f^c)^*, \qquad (18)$$

and the coarse grid matrix is defined by:

$$\mathbf{A}_c = \mathbf{I}_f^c \mathbf{A}_f \mathbf{I}_c^f. \tag{19}$$

In (18), the restriction and interpolations operators are adjoints with respect to the discrete form of the L_2 inner products on fine and coarse grids. Explicitly, we have $\mathbf{I}_c^f = \mathbf{W}_f^{-1}(\mathbf{I}_f^c)^T \mathbf{W}_c$ where $\mathbf{W}_f$ and $\mathbf{W}_c$ are diagonal matrices containing the grid weights (constant in this study).

It can be shown that if these conditions are fullfilled, the components of the error that lie in the range of the interpolation operator before the coarse grid correction step are completely removed by the coarse grid correction step.

4. Application to data assimilation problems

We look at the main characteristics of the data assimilation problem in the light of the notions previously introduced: order of transfer operators, approximation property, ellipticity. In all our experiments (except the last one), the refinement factor between the different grids is equal to 2 both in space and time. In this section, only the non-preconditioned version of the data assimilation problem is addressed since we have seen that the preconditioning breaks the ellipticity of the original system. The study of the preconditioned version will be reintroduced in section (5) where the multigrid method is used as a preconditioner instead of a solver.

4.1. Order of transfer operators

We now look at the conditions that have to fulfill the transfer operators according to our definition of the background error covariance matrix $\mathbf{B}$. With M_{lap} equal to 4 in (11), the order of the differential operator corresponding to $\mathbf{B}^{-1}$ is equal to 8 (four applications of a Laplacian operator). Therefore, the order of transfer operators must be greater than 8. Here we use generalized Shapiro low pass filters (Purser 1987) based on the following formula for a restriction operator of order $2p$:

$$\mathbf{I}_f^c \mathbf{x} = \mathbf{R}_f^c \left[\mathbf{I}_d + \sum_{k=p}^{k=2p-1} \alpha_k \Delta^k \right] \mathbf{x} \tag{20}$$

where $\mathbf{R}_f^c$ is the trivial injection operator (see Briggs *et al.* 2000). The interpolation operators are taken to be the adjoints, with respect to a discrete form of the L^2-inner product, of the restriction operators : $\mathbf{I}_c^f = \rho(\mathbf{I}_f^c)^T$, ρ being the mesh refinement factors between 2 grid levels ($\rho = 2$ in all our experiments). The coefficients α_k are computed so that both the restriction and the interpolation operator are of order $2p$. This is equivalent to saying that both the primary (large scale) and secondary (small scale) orders of the restriction operator $\mathbf{I}_f^c$ are equal to $2p$ (see Hemker (1990)).

4.2. Approximation property

For our data assimilation problem, we use the Galerkin condition (19) for the definition of the inverse of the background error covariance matrix at coarse resolution:

$$\mathbf{B}_c^{-1} = \mathbf{I}_f^c \mathbf{B}_f^{-1} \mathbf{I}_c^f.$$

Application of the Galerkin condition for the observation term is not affordable since it would require running the model at high resolution on each grid in the hierarchy. We begin by studying only the term that corresponds to the regularization operator $\mathbf{B}^{-1}$. Figure (6) represents the application of the coarse grid correction matrix $\left(\mathbf{I} - \mathbf{I}_c^f \mathbf{A}_c^{-1} \mathbf{I}_f^c \mathbf{A}_f \right)$ (with $\mathbf{A} = \mathbf{B}^{-1}$) to the discrete Fourier modes (here computed with $N = 64$). The vertical axis corresponds to $\dfrac{\|(\mathbf{I} - \mathbf{I}_c^f \mathbf{A}_c^{-1} \mathbf{I}_f^c \mathbf{A}_f)\mathbf{e}_f^m\|}{\|\mathbf{e}_f^m\|}$ with $\mathbf{e}_f^m = \cos(m\mathbf{x}/L)$ being a discrete Fourier mode.

The necessity of using high order transfer operators to correctly reduce the large scale components of the error (left part of the figure) is clearly seen.

We now evaluate the approximation property when the observation term is present. We take a number of $N_{\mathrm{obs}} = 10$ observations in time. An important parameter of the numerical discretization is the Courant number. For a Courant number equal to one, the numerical model is exact. For smaller values, numerical viscosity is added and, as can be seen in figure (7), it greatly impacts the correctness of the coarse grid correction step.

The dissipative properties of the numerical model at coarse resolution breaks the approximation property and some of the large scale components of the error are not well reduced by the
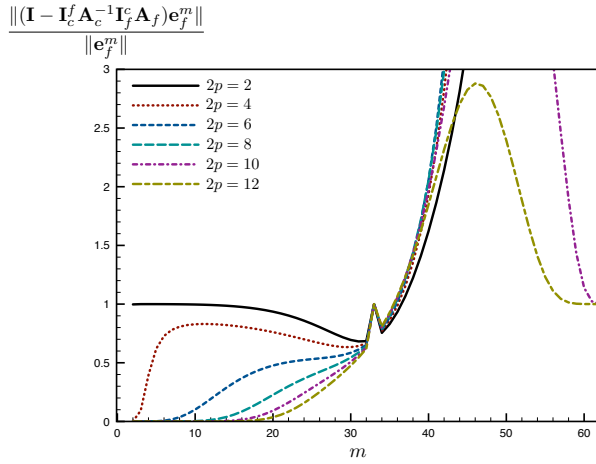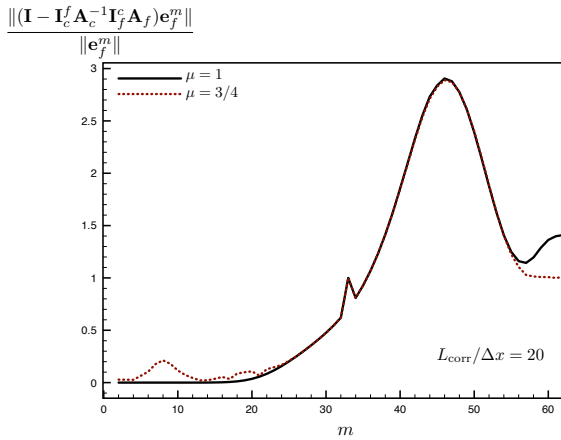
$$\frac{\|(\mathbf{I} - \mathbf{I}_c^f \mathbf{A}_c^{-1} \mathbf{I}_f^c \mathbf{A}_f)\mathbf{e}_f^m\|}{\|\mathbf{e}_f^m\|}$$

Figure 6. Approximation property for $\mathbf{A} = \mathbf{B}^{-1}$, $M_{\text{lap}} = 4$, $N = 64$, $L_{\text{corr}}/\Delta x = 20$. The left part (resp. right part) of the picture corresponds to the large scale (resp. small scale) eigenvectors. The vertical axis corresponds to $\frac{\|(\mathbf{I} - \mathbf{I}_c^f \mathbf{A}_c^{-1} \mathbf{I}_f^c \mathbf{A}_f)\mathbf{e}_f^m\|}{\|\mathbf{e}_f^m\|}$ with $\mathbf{e}_f^m = \cos(m\mathbf{x}/L)$ being a discrete Fourier mode.

$$\frac{\|(\mathbf{I} - \mathbf{I}_c^f \mathbf{A}_c^{-1} \mathbf{I}_f^c \mathbf{A}_f)\mathbf{e}_f^m\|}{\|\mathbf{e}_f^m\|}$$

Figure 7. Approximation property for a Courant number equal to 1 (exact numerical model) and for a Courant number equal to 3/4 for $N = 128$, $L_{\text{corr}}/\Delta x = 20$, $2p = 12$. The vertical axis corresponds to $\frac{\|(\mathbf{I} - \mathbf{I}_c^f \mathbf{A}_c^{-1} \mathbf{I}_f^c \mathbf{A}_f)\mathbf{e}_f^m\|}{\|\mathbf{e}_f^m\|}$ with $\mathbf{e}_f^m = \cos(m\mathbf{x}/L)$ being a discrete Fourier mode.

coarse grid correction step. The problem is amplified when the mesh is refined ($N = 256$) and/or when the background error correlation length is reduced (Figure (8)).

This will, of course, affect the performance of the multigrid method as can be seen in section (5).

4.3. Smoothers

We now look at the different possibilities for the choice of a smoother for our data assimilation problem. We are exclusively concerned with black box smoothers where the only available information is the matrix-vector product. For the solution of the symmetric positive definite system (5), the conjugate gradient (CG) method is often the method of choice. However, it is well
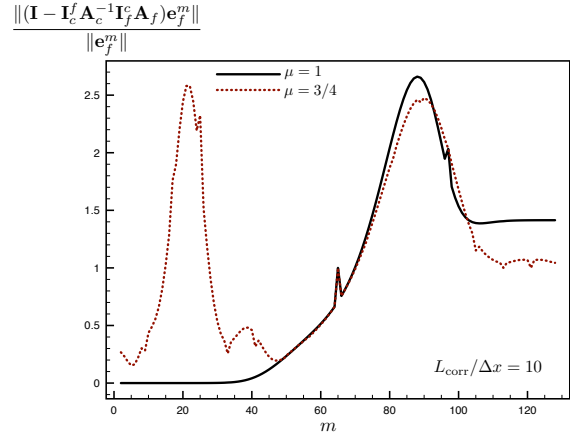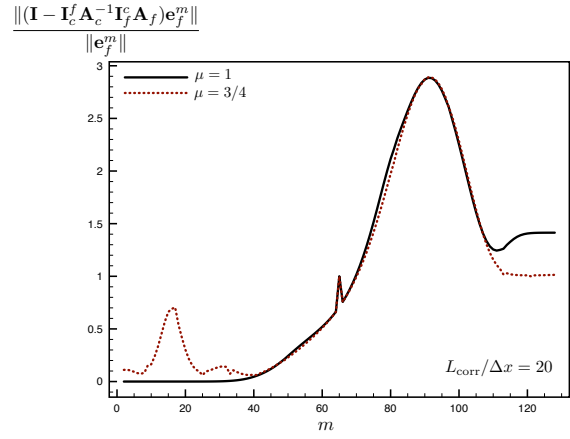
$$\frac{\|(\mathbf{I} - \mathbf{I}_c^f \mathbf{A}_c^{-1} \mathbf{I}_f^c \mathbf{A}_f)\mathbf{e}_f^m\|}{\|\mathbf{e}_f^m\|}$$

$$\frac{\|(\mathbf{I} - \mathbf{I}_c^f \mathbf{A}_c^{-1} \mathbf{I}_f^c \mathbf{A}_f)\mathbf{e}_f^m\|}{\|\mathbf{e}_f^m\|}$$

Figure 8. Approximation property for a Courant number equal to 1 (exact numerical model) and for a Courant number equal to 3/4 for $N = 256$, for $L_{\text{corr}}/\Delta x = 20$ (top) and $L_{\text{corr}}/\Delta x = 10$ (bottom), all with $2p = 12$. The vertical axis corresponds to $\frac{\|(\mathbf{I} - \mathbf{I}_c^f \mathbf{A}_c^{-1} \mathbf{I}_f^c \mathbf{A}_f)\mathbf{e}_f^m\|}{\|\mathbf{e}_f^m\|}$ with $e_f^m = \cos(m\mathbf{x}/L)$ being a discrete Fourier mode.

known that this algorithm cannot be considered as a smoother (Shewchuk 1994). Indeed, the CG minimizes the $\mathbf{A}^{-1}$ norm of the residual $\mathbf{r}$ ($= \mathbf{A}x - \mathbf{b}$): $< \mathbf{r}, \mathbf{A}^{-1}\mathbf{r} >$ and thus for an elliptic system can produce after a few iterations residuals with large amplitudes at small scales. Even if these residuals actually correspond to errors with small amplitudes, the restriction of these residuals to the coarse resolution grid can be aliased and accordingly produce wrong large scale correction of the control itself. As the CG algorithm, the minimal residual method (MINRES) is also based on a Lanczos iteration but produces iterates that minimize the Euclidian norm of the residual instead of the $\mathbf{A}^{-1}$ norm for CG. In general, this will lead to better smoothing properties than the conjugate gradient method. The MINRES method is the smoother used in the following.

More complex smoothers, that may require high computational cost, exist and could be effective particularly when the same (or

similar) matrix is used for successive minimizations, as would be the case if the multigrid algorithm was used inside an incremental assimilation approach. As an example, sparse approximate smoothers based on the minimization of the Frobenius norm could be derived (see Tang and Wan (2000)).

5. Numerical experiments

5.1. Design of the assimilation experiments

The background x_b is taken to be

$$\mathbf{x}_b = 0.3 + \sin 2\pi \frac{x}{L},$$

while the true state is obtained by adding a Gaussian white noise corresponding to the $\mathbf{B}$ matrix:

$$\mathbf{x}_{true} = \mathbf{x}_b + \mathbf{B}^{1/2}\mathbf{u}, \qquad \mathbf{u} \sim \mathcal{N}(\mathbf{0}, \mathbf{I}).$$

The standard deviation of the diagonal observation error covariance matrix is equal to $\sigma_{\text{obs}} = 0.02m \approx 1.5\%$ of its maximum value. The stopping criterion of all the experiments will be

$$\frac{\|\mathbf{x} - \mathbf{x}^\star\|_2}{\|\mathbf{x}^\star\|_2} \leq 10^{-4}$$

where $\mathbf{x}^\star$ is the solution of the assimilation problem (previously computed with a unigrid optimization).

5.2. 1DVAR experiments

For 1DVAR experiments, the numerical model is replaced by the identity and only one set of observations at time t_0 is used. We run the unigrid and multigrid algorithm for different values of the ratio $\sigma_{\text{b}}/\sigma_{\text{obs}}$ and $L_{\text{corr}}/\Delta x$. For this first series of experiments, only two grid levels are used. Our main focus is on the number of fine grid iterations. The required number of iterations on the coarse grid is shown for information only and will be discussed later.

Table (3) shows the number of iterations to attain convergence for the unigrid preconditioned (P) and non-preconditioned (NP) cases and for the multigrid non-preconditioned ($MGNP$) case. The experiments are run using $V(1, 1)$ cycles (i.e. one pre- and one post-smoothing steps) and the number of fine grid cells is here

equal to $N = 128$. In table (3), the numbers between parentheses indicate the number of iterations on the coarse grid.

$L_{\text{corr}}/\Delta x$ $\sigma_{\text{b}}/\sigma_{\text{obs}}$	20			10		
	P	NP	$MGNP$	P	NP	$MGNP$
5	5	330	2 (5)	2	167	2 (4)
20	5	473	2 (5)	2	179	6 (34)

Table 3. Number of iterations for $N = 128$ using $V(1, 1)$ cycles, 2 grid levels

The number of fine grid iterations required by the unigrid preconditioned and multigrid algorithms are very small in this simple 1DVAR experiment. We note that since the correction is in the range of the $\mathbf{B}$ matrix, if the correlation length is large ($L_{\text{corr}}/\Delta x = 20$), then the optimal solution can be captured by only one multigrid cycle (2 fine grid iterations).

For the rest of the paper, the ratio $\sigma_b/\sigma_{\text{obs}}$ is taken equal to 20. As noted in Table (3), it corresponds to the most difficult case for all the algorithms, except for the preconditioned algorithm which is less sensitive.

5.3. Numerical experiments: 2DVAR assimilation

We now evaluate the behavior of the multigrid algorithm in a 2DVAR context. The observations are generated from the numerical solution starting from the true initial state. The model is integrated over a period of $T = 78.125$ seconds and observations are taken each 7.8125 seconds, so that a number of 10 observation times are used, and each 16 grid points. No noise is added to the true state, so the observations are perfect. The fine grid resolution is increased by choosing $N = 256$ leading to a more difficult test in the case of model errors. Two experiments are performed: the first with a model free of numerical errors (the Courant number μ is unity) and the second with a Courant number of $\mu = 3/4$ which leads to both dissipative and dispersive errors that affect the approximation property. The number of iterations required for convergence is indicated in table (4) below.

$L_{\text{corr}}/\Delta x$ μ	20			10		
	P	NP	$MGNP$	P	NP	$MGNP$
1	32	345	4 (54)	40	93	6 (109)
3/4	44	439	26 (411)	68	130	$\times$

Table 4. Number of fine grid iterations for $N_{\text{obs}} = 10$, $N = 256$ for a perfect model ($\mu = 1$) and with numerical errors ($\mu = 3/4$)

In the case of a perfect model ($\mu = 1$), the performance of the multigrid method is clearly superior to that of the preconditioned

version, with only a few fine grid iterations to converge. However, the number of coarse grid iterations is not negligible and introduces computational costs which are not evaluated in this experiment. Because the non-preconditioned Hessian is elliptic (see section 2.3) and the approximation property holds (perfect model), a solution for reducing the computational cost associated to the coarse grid iterations consists in using more than two grid levels as illustrated in section 5.4. When numerical errors are introduced ($\mu = 3/4$) all the algorithms are affected and the number of iterations increase. The introduction of diffusive error impacts the controllability of the initial state. As was demonstrated in section (4.2), the multigrid algorithm also suffers from a less accurate approximation property and its behavior drastically degrades. In the case of a relatively small correlation length ($L_{\mathrm{corr}}/\Delta x = 10$), the algorithm diverges. As previously mentioned, results presented here have been done using the MINRES algorithm as a smoother but are worse with the CG method (not shown). Figure (9) represents the true solution and evolution of the control after the first multigrid cycles. It is clear that at the scales where the approximation property is not valid, the error increases from one cycle to another.
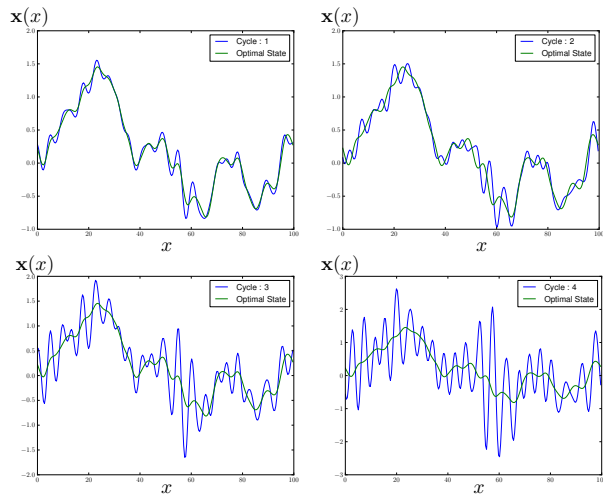
Figure 9. Evolution of the multigrid solution during the four first cycles and comparison with the true solution of the optimal control problem.

It is of course possible to make the process converge by increasing the number of pre- and post-smoothing steps, i.e. using $V(\nu, \nu)$ cycles with $\nu > 1$ to maintain convergence - see for instance Cioaca *et al.* (2013). The main difficulty derives from the fact that, during these fine grid smoothing steps not only the small scales of the error have to be reduced but also the scales where

the approximation property is not valid and these are difficult to predict so that ν can become quite large. This scheme clearly lacks robustness. In addition, our aim is to use more than 2 levels but the approximation property degrades further as the number of levels is increased. A solution to make the process more robust is using the multigrid iteration as a preconditioner for an optimization method instead of as a direct solver. This is the subject of the next section.

5.4. *Multigrid as a preconditioner*

As seen previously, the multigrid method applied to our toy data assimilation problem suffers from lack of robustness due to several problems: the ellipticty of the $\mathbf{B}^{1/2}$-preconditioned version is not ensured, particularly when the background error correlation length is small; some of the errors of the numerical model (typically implicit diffusion) render the approximation property less accurate. These problems are also common to several fields of application of multigrid methods (e.g. convection-diffusion problems with upwind discretizations see (Trottenberg *et al.* 2000, chap. 7)) and can sometimes be solved using specialized smoothers. Other methods have been developed to improve behavior in this context. Multigrid acceleration techniques like the minimal residual method (Zhang 1998) or more general recombination of iterates of the multigrid process have been developed (Trottenberg *et al.* 2000, chap. 7). Another possibility is to integrate one multigrid cycle as a preconditioner for a Krylov minimization method. The original system $\mathbf{Ax} = \mathbf{b}$ can be left preconditioned as

$$\mathbf{K}^{-1}\mathbf{Ax} = \mathbf{K}^{-1}\mathbf{b}$$

where $\mathbf{K}^{-1}$ is an approximation of the inverse of $\mathbf{A}$ that will be given by one multigrid iteration. Following Tatebe (1993), one idea is to choose $\mathbf{K}^{-1}$ as an operator which corresponds to one multigrid cycle. Let $\mathbf{x}_k$ be the current estimate of the solution $\mathbf{x}^\star$ at iteration k of the minimization and let $\mathbf{r}_k$ be the residual $\mathbf{r}_k = \mathbf{A}(\mathbf{x}^\star - \mathbf{x}_k)$. The application of the multigrid preconditioner to the residual $\mathbf{r}_k$ to compute a correction ($\mathbf{z}_k = \mathbf{K}^{-1}\mathbf{r}_k$) is obtained by performing one multigrid cycle for the solution of $\mathbf{Az}_k^\star = \mathbf{r}_k$.

In one multigrid iteration the evolution of the error is given by :

$$\mathbf{e}^{\text{after}} = \mathbf{\Phi}\mathbf{e}^{\text{before}}, \quad \text{where } \mathbf{\Phi} = \mathbf{S}_2^{\nu_2}\left(\mathbf{I} - \mathbf{I}_\mathbf{c}^\mathbf{f}\mathbf{A}_\mathbf{c}^{-1}\mathbf{I}_\mathbf{f}^\mathbf{c}\mathbf{A}_\mathbf{f}\right)\mathbf{S}_1^{\nu_1} \tag{21}$$

where $\mathbf{e}^{\text{before}} = \mathbf{0} - \mathbf{z}_k^\star$ (starting from a null initial guess for $\mathbf{z}_k^\star$) and $\mathbf{e}^{\text{after}} = \mathbf{z}_k - \mathbf{z}_k^\star$. We can thus deduce that $\mathbf{z}_k = (\mathbf{I} - \mathbf{\Phi})\mathbf{z}_\mathbf{k}^\star = (\mathbf{I} - \mathbf{\Phi})\mathbf{A}^{-1}\mathbf{r_k}$ leading to the following expression of $\mathbf{K}^{-1}$:

$$\mathbf{K}^{-1} = (\mathbf{I} - \mathbf{\Phi})\,\mathbf{A}^{-1}. \tag{22}$$

Ideally, the error is completely removed in one multigrid cycle ($\mathbf{\Phi} = \mathbf{0}$) so that $\mathbf{K}^{-1}$ corresponds exactly to the inverse of $\mathbf{A}$. In the general case, the matrix $\mathbf{K}^{-1}\mathbf{A}$ is given by $\mathbf{I} - \mathbf{\Phi}$. The application of the conjugate gradient to this matrix requires $\mathbf{I} - \mathbf{\Phi}$ to be symmetric positive definite which in turn requires ν_1 to be strictly positive for the definiteness while the symmetry can be ensured if $\nu_2 = \nu_1$, $\mathbf{S}_2 = \mathbf{S}_1$ corresponding to a linear relaxation method (Tatebe (1993)). These conditions are quite restrictive but the algorithm has been successfully applied with relaxed conditions, in particular with $\nu_2 = 0$ (no post-smoothing) and ν_1 small (typically one) Bouwmeester *et al.* (2012)). An alternative is to use the multigrid preconditoning for a GMRES method (Oostelee and Washio 1998) that allows the use of non symmetric preconditioners. However, several evaluations of the matrix vector product on the fine grid are still needed and we choose to avoid it. When neither pre- or post-smoothing steps are applied ($\mathbf{S}_1^{\nu_1} = \mathbf{S}_2^{\nu_2} = I$), $\mathbf{K}^{-1}$ is given by $\mathbf{K}^{-1} = \mathbf{I}_c^f\mathbf{A}_c^{-1}\mathbf{I}_f^c$, a matrix which is clearly not definite positive. Looking for alternatives to define a symmetric positive definite preconditioner, we propose a weighting of the multigrid iteration with the standard $\mathbf{B}$ preconditioning as follows:

$$\mathbf{K}^{-1} = \mathbf{I}_c^f\mathbf{A}_c^{-1}\mathbf{I}_f^c + (\mathbf{I} - \mathbf{P}_c^f\mathbf{I}_f^c)^T\mathbf{B}_f(\mathbf{I} - \mathbf{I}_c^f\mathbf{I}_f^c) \tag{23}$$

where $\mathbf{P}_c^f$ is an interpolation operator. The symmetric positive definiteness of $\mathbf{A}_c$ and $\mathbf{B}_f$ implies the same properties for $\mathbf{K}^{-1}$. Indeed, $\mathbf{K}^{-1}$ is trivially positive and symmetric. Furthermore,

using (18), one has:

$$\begin{aligned} <\mathbf{K}^{-1}\mathbf{X}_f, \mathbf{X}_f> \quad = \quad & <\mathbf{I}_f^f\mathbf{A}_c^{-1}\mathbf{I}_f^c\mathbf{X}_f, \mathbf{X}_f> \\ & + <(\mathbf{I} - \mathbf{P}_c^f\mathbf{I}_f^c)^T\mathbf{B}_f(\mathbf{I} - \mathbf{P}_c^f\mathbf{I}_f^c)\mathbf{X}_f, \mathbf{X}_f> \\ = \quad & <\mathbf{A}_c^{-1}\mathbf{I}_f^c\mathbf{X}_f, \mathbf{I}_f^c\mathbf{X}_f> \\ & + <\mathbf{B}_f(\mathbf{I} - \mathbf{P}_c^f\mathbf{I}_f^c)\mathbf{X}_f, (\mathbf{I} - \mathbf{P}_c^f\mathbf{I}_f^c)\mathbf{X}_f> . \end{aligned}$$

So that the positive definiteness of $\mathbf{A}_c^{-1}$ and $\mathbf{B}_f$ implies that $\left\langle\mathbf{K}^{-1}\mathbf{X}_f, \mathbf{X}_f\right\rangle = 0$ if and only if $\mathbf{I}_f^c\mathbf{X}_f = 0$ and $\left(\mathbf{I} - \mathbf{P}_c^f\mathbf{I}_f^c\right)\mathbf{X}_f = 0$, which in turn implies $\mathbf{X}_f = 0$. An obvious choice for the operator $\mathbf{P}_c^f$ is the one which leads to the multigrid iteration matrix when the approximation property is valid and to the $\mathbf{B}_f$ preconditioning when it is not. This leads to the following choice of $\mathbf{P}_c^f$:

$$\mathbf{P}_c^f = \mathbf{A}_f\mathbf{I}_c^f\mathbf{A}_c^{-1} \tag{24}$$

and we recognize in $(\mathbf{I} - \mathbf{P}_c^f\mathbf{I}_f^c) = \mathbf{I} - \mathbf{A}_f\mathbf{I}_c^f\mathbf{A}_c^{-1}\mathbf{I}_f^c$ nothing else than the coarse grid amplification matrix for the residual. However, this definition of $\mathbf{P}_c^f$ introduces two applications of $\mathbf{A}_f$ and so has an important cost. In (24) the full matrix $\mathbf{A}$ can be approximated by the part which corresponds to the background term ($\mathbf{B}$) and a still simpler expression is the one based only on the interpolation operator for which we have:

$$\mathbf{P}_c^f = \mathbf{I}_c^f. \tag{25}$$

The objective of the preconditioner defined by (23,25) is clear: the large scale components of the residual (for which $\mathbf{P}_c^f\mathbf{I}_f^c \approx \mathbf{I}_d$) are preconditioned by the multigrid iteration matrix while its small scale components (for which $\mathbf{P}_c^f\mathbf{I}_f^c \approx \mathbf{0}$) are preconditioned by $\mathbf{B}_f$ (remarking that at small scales the background term is the dominant one in the $\mathbf{A}_f$ matrix). This preconditioner is symmetric positive definite - the proof is the same as the one used for the multigrid preconditioner (23) - and does not require any relaxation step at high resolution. In the following, this choice of $\mathbf{P}_c^f$ (eq. 25) is made.

Note that the advantage of the multigrid preconditioned algorithm is that it can also be applied to the preconditioned version of the system ($\mathbf{A}^P$). When the multigrid algorithm is applied as a solver for $\mathbf{A}^P$, the non ellipticity of the problem implies that

the small scale error is not quickly reduced by the minimization method and this leads, through aliasing on the coarse grid, to a divergence of the multigrid cycles. When the multigrid algorithm is used inside a Krylov method as a preconditioner, the small scale amplification by the multigrid cycle does not lead to a globally divergent algorithm and the large scale error is reduced at a lower cost on coarser resolution grids. In that case, the multigrid preconditioner (23) should be replaced by

$$\mathbf{K}^{-1} = \mathbf{I}_c^f \mathbf{A}_c^{-1} \mathbf{I}_f^c + (\mathbf{I} - \mathbf{P}_c^f \mathbf{I}_f^c)^T (\mathbf{I} - \mathbf{P}_c^f \mathbf{I}_f^c) \qquad (26)$$

where the obvious difference is that the small scale term has already been preconditioned so that the $\mathbf{B}$ matrix needs to be removed. The second term on the right hand side is only there to make matrix $\mathbf{K}^{-1}$ non singular.

In the following, the usual multigrid preconditioner given by (22) is denoted $\mathbf{K}_{MG}^{-1}$ while the weighting of the multigrid preconditioner with the $\mathbf{B}$ term is written $\mathbf{K}_{BMG}^{-1}$. Two versions of both preconditioners are tested depending on if the original system was preconditioned (using $\mathbf{A}^P$) or not (using $\mathbf{A}^{NP}$).

Eigenvalues of the multigrid preconditioned matrix

The eigenvalues of the multigrid preconditioned matrix $\mathbf{K}^{-1}\mathbf{A}$ are plotted in figure (10) for the different expressions of the multigrid preconditioner $\mathbf{K}^{-1}$. The number of pre- and post-smoothing steps for the multigrid only preconditioner ($\mathbf{K}_{MG}^{-1}$) are indicated in brackets on the figure. Following Bouwmeester *et al.* (2012), only one or two pre-processing steps are applied and no post-smoothing is done. Even if it leads to a non symmetric (still definite positive) preconditioner, it does not affect the results (post-smoothing steps do not improve the performances (not shown)) and save computational costs and time associated with the high resolution smoothing steps.

The hybrid preconditioners ($\mathbf{K}_{BMG}^{-1}$) clearly have lower condition numbers than the $\mathbf{K}_{MG}^{-1}$ preconditioners. In particular, the latter still have very small eigenvalues. These small eigenvalues can be shown to be associated with small scale eigenvectors. For the $\mathbf{K}_{MGNP}^{-1}$ preconditioner, increasing the number of pre smoothing steps efficiently increases the smallest eigenvalues. This is not true for the $\mathbf{K}_{MGP}^{-1}$ preconditioner since the pre smoothing
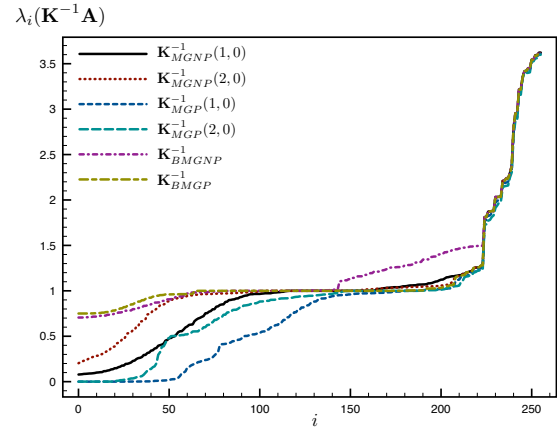

Figure 10. Eigenvalue spectrum for the multigrid preconditioner ($\mathbf{K}_{MG}^{-1}\mathbf{A}$) for one and two presmoothing steps and for the hybrid multigrid / $\mathbf{B}$ preconditioned system ($\mathbf{K}_{BMG}^{-1}\mathbf{A}$). $L_{\mathrm{corr}}/\Delta x = 10$, $N = 256$, $N_{\mathrm{obs}} = 10$, $\mu = 3/4$

relaxation steps done on $\mathbf{A}^P$ mainly concentrate on the large scale components of the error.

This hybrid preconditioner results in very small condition numbers of $\mathcal{K}(\mathbf{K}_{BMGNP}^{-1}\mathbf{A}^{NP}) = 5.1$ and $\mathcal{K}(\mathbf{K}_{BMGP}^{-1}\mathbf{A}^P) = 4.8$, when their unigrid non-preconditioned and preconditioned equivalents have a condition number equal to $\mathcal{K}(\mathbf{A}^{NP}) = 2187$ and $\mathcal{K}(\mathbf{A}^P) = 6213$.

Choice of the number of iterations on the coarse grid level(s)

For an efficient algorithm, the coarse grid problem is not solved exactly in practice. Using the FAS formulation (cf 3.1), the multigrid preconditioned conjugate gradient can be recursively extended to the case of more than two grid levels. At each grid level, the multigrid preconditioned CG is used to (approximately) solve the corresponding system. In the following, we limit the number of iterations of the CG algorithm at each coarse grid level(s). When applied to an original non-preconditioned system ($\mathbf{A}^{NP}$), the numbers of iterations at each level can be very low and similar to the typical ones used when the multigrid method is used as a solver. This comes from the ellipticity of the $\mathbf{A}^{NP}$ matrix. The situation is different for the originally preconditioned system ($\mathbf{A}^P$). Here the coarse grid level(s) are mainly present to solve the large scale errors at a lower computation cost. But on the coarser grids the rate of convergence is not smaller, so that more CG iterations are required. Note, however, that in general the cost of these coarse grid iterations is much cheaper and is often fully negligible in comparison with the cost of the finer grid integrations.

The use of approximate computations of $\mathbf{A}_c^{-1}$ in the expression of $\mathbf{K}^{-1}$ renders this preconditioner not constant over the conjugate gradient iterations. For this reason, we use the flexible form of the conjugate gradient algorithm (Notay 2000).

Numerical results of the multigrid preconditioned experiments

Tables (5,6) show the results of the multigrid preconditioned experiments for 2 and 3 grid levels when applied to $\mathbf{A}^{NP}$ (table 5) and $\mathbf{A}^P$ (table 6). The number of CG iterations on the coarse grids is limited to 30 in the 2 grid level case. In the three grid level case, it is limited to 3 when working on $\mathbf{A}^{NP}$, while for $\mathbf{A}^P$ it is limited to 5 on the second level and to 10 on the third level. These limitations have been hand tuned and can probably be improved/adjusted using advanced control of the error between two successive grid levels (e.g. Thekale *et al.* 2010). However, the chosen values reflect (as mentioned above) that the application of multigrid preconditioning to an originally non-preconditioned system ($\mathbf{A}^{NP}$) benefits from the ellipticity of this system, while the application of $\mathbf{A}^P$ requires more coarse grid iterations.

$L_{\text{corr}}/\Delta x$	20	10
Unigrid	353	98
Multigrid Precon 2-levels	5 (150)	6 (180)
Multigrid Precon 3-levels	3 (9, 27)	7 (21, 63)

Table 5. Multigrid as a preconditioner on $\mathbf{A}^{NP}$ (original system under non-preconditioned form): Number of fine and coarse grid iterations for $N_{\text{obs}} = 10$, $N = 256$ and $\mu = 3/4$

$L_{\text{corr}}/\Delta x$	20	10
Unigrid	27	51
Multigrid Precon 2-levels	3 (89)	6 (180)
Multigrid Precon 3-levels	6 (30, 300)	6 (30, 300)

Table 6. Multigrid as a preconditioner on $\mathbf{A}^P$ (original system under $\mathbf{B}^{1/2}$ preconditioned form): Number of fine and coarse grid iterations for $N_{\text{obs}} = 10$, $N = 256$ and $\mu = 3/4$

First, all the algorithms converged towards the solution of the data assimilation problem $\mathbf{x}^*$ (with a relative error lower than the stopping criterion 10^{-4}). Secondly, the good behavior of the multigrid preconditioned algorithms is confirmed. The number of required fine grid iterations is much less than the unigrid experiments. This means that in a more realistic 3D application with a higher ratio between the computational costs of coarse and fine grids, the performance in terms of computation time is expected to be much less for the

multigrid algorithms. While the use of 3 grid levels is clearly an advantage for the application of the multigrid preconditioning on $\mathbf{A}^{NP}$, it is less clear on $\mathbf{A}^P$ probably due to fundamental differences in their elliptic characteristics.

Increase of resolution and length of assimilation windows:
In the last experiments, the number of grid points is increased and the length of assimilation windows is extended to $T = 234s$ so that there are 30 observation times. In addition, we experiment with the use of a higher refinement factor of $\rho = 3$. In order to avoid complex restriction/interpolation operators, the number of fine grid points have to be a multiple of $\rho^{l_{\max}}$ where $l_{\max}$ the number of coarse grid levels is set to 3 in these experiments. Thus N is set to $N = 4096$ when $\rho = 2$ and set to $N = 5184$ when $\rho = 3$. For $\rho = 2$ (resp. $\rho = 3$), figure (11) (resp. figure (12)) shows the evolution of the error $\dfrac{\|\mathbf{x} - \mathbf{x}^\star\|_2}{\|\mathbf{x}^\star\|_2}$ as a function of the number of iterations on the fine grid and the total computational time, including the time spent on coarse grid levels and during grid interactions.
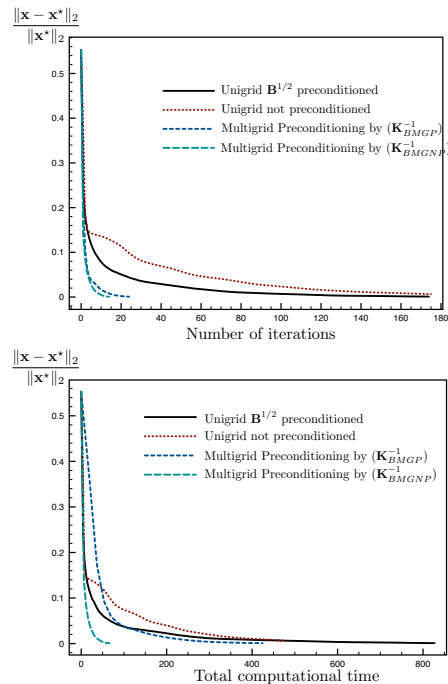

Figure 11. Refinement factor $\rho = 2$. Evolution of the error $\left(\dfrac{\|\mathbf{x} - \mathbf{x}^\star\|_2}{\|\mathbf{x}^\star\|_2}\right)$ as a function of the number of fine grid iterations (top) and of the total computational time in seconds (bottom) for $L_{\text{corr}}/\Delta x = 10$ and with three grid levels.

The number of required iterations for unigrid cases has greatly increased and is now close to 200. One order of magnitude less iterations is required for the multigrid preconditioned
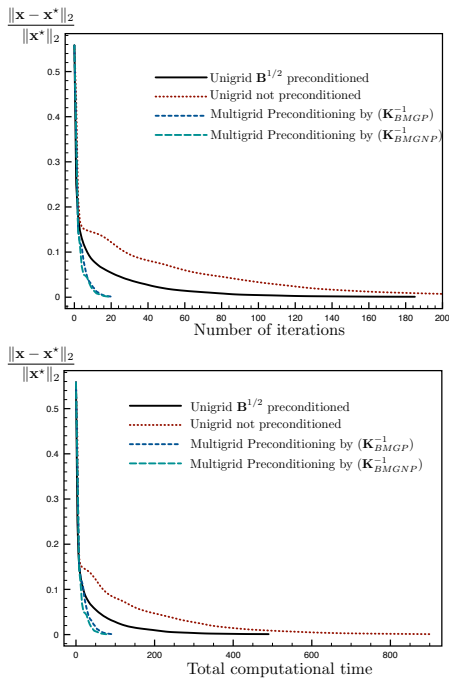
Figure 12. Refinement factor $\rho = 3$. Evolution of the error $\left(\dfrac{\|\mathbf{x} - \mathbf{x}^\star\|_2}{\|\mathbf{x}^\star\|_2} \right)$ as a function of the number of fine grid iterations (top) and of the total computational time in seconds (bottom) for $L_{\mathrm{corr}}/\Delta x = 10$ and with three grid levels.

experiments. In terms of total computational cost, the minimum is for the multigrid preconditioning applied to $\mathbf{A}^{NP}$ and is less than one-tenth the cost of unigrid cases.

When applied to $\mathbf{A}^P$, the multigrid method suffers from the number of required coarse grid iterations (remember that when applied to $\mathbf{A}^P$, the multigrid algorithm requires more smoothing steps on the coarse grid levels due to the lack of ellipticity). When the refinement factor is set to 2, the cost of the coarse grid iterations is not negligible as can be seen in figure (11). Indeed, with the chosen limitations on the number of iterations at each grid level, the number of total iterations during one fine grid step is given by 1 (fine grid) + 5 (second grid level) + 5 $\times$ 10 (third grid level). With a refinement ratio of 2 in space and time, this means that the computational cost associated with one fine grid iteration of the multigrid preconditioned algorithm is $1 + \frac{5}{2\times2} + \frac{5\times10}{(2\times2)\times(2\times2)} = 5.375$ times the cost of a unigrid iteration. This additional cost decreases when the refinement factor is set to 3 and figure (12) shows that the total computational costs of the two multigrid versions become similar. As previously mentioned, this cost should still decrease in a more realistic application in higher dimension. Figure (12) also shows that the multigrid

preconditioned algorithms are robust to an increase of the mesh refinement factor.

6. Conclusion and perspectives

This paper has focused on the application of multigrid methods to the solution of variational data assimilation problems. Using a cost function with characteristics similar to the ones typically used in geophysical applications, we showed the important role played by the background error covariance matrix and preconditioning of the ellipticity problem. Then, for the model problem of a transport equation, the quality of approximation of the fine grid system by one with a coarser resolution has been investigated. Numerical errors, in particular those of a dissipative nature, alter the quality of this approximation. Robustness and efficiency have been achieved by using multigrid iterations inside the preconditioning step of a conjugate gradient algorithm. The final results are very encouraging and show that the gain can be up to one order of magnitude both in terms of iterations and total computational time.

The obvious next step is to experiment in a more complex model setting. The behavior of the approximation property is interesting to study when the problem has a less advective nature than our transport equation. In addition, when the multigrid method is used as a solver, it is worth studying the design of more complex and specifically adapted smoothers. In the context of data assimilation for non linear problems, the incremental approach leads to a series of similar systems that may benefit from these advanced smoothers. When the multigrid method is used as a preconditioner, the choice of the underlying minimization method, here a conjugate gradient algorithm, may also be important. The number of observations and their spatial repartition are other aspects that can affect the minimisation efficiency. Indeed in the unigrid case, less observations leads to a decrease of the condition number in the preconditioned case and an increase in the non-preconditioned one. This in turn may affect the benefit of using multigrid approaches in case of sparse data, and further study is required to quantify this impact. Additionally, observations often suffer from a sporadic distribution with, on the one hand, over-observed areas, and, on the other hand, unobserved areas. Moreover they generally suffer from correlated

errors. The proper solution is to account for these correlations with the off-diagonal terms of the observation error covariance matrix, but due to non trivial algorithmic difficulties, one tends to retain a diagonal matrix and to adopt simpler sub-optimal solutions (subsampling or superobbing). In any case this choice affects the conditioning of the minimisation and therefore its interaction with the multigrid approaches needs to be studied thoroughly. Finally, the multigrid preconditioner has been coupled here with traditional preconditioning based on the square root of the background error covariance matrix. Hybridization of the multigrid preconditioner with a more advanced preconditioner is also of prime interest.

Acknowledgements

References

Borzì A, Schulz V. 2009. Multigrid methods for pde optimization. *SIAM Rev.* **51**(2): 361–395, doi:10.1137/060671590, URL http://dx.doi.org/10.1137/060671590.

Bouwmeester H, Dougherty A, Knyazev AV. 2012. Nonsymmetric multigrid preconditioning for conjugate gradient methods. *CoRR* **abs/1212.6680**.

Brandt A. 1982. Guide to multigrid development. In: *Multigrid Methods*, *Lecture Notes in Mathematics*, vol. 960, Hackbusch W, Trottenberg U (eds), Springer Berlin Heidelberg, ISBN 978-3-540-11955-5, pp. 220–312, doi:10.1007/BFb0069930, URL http://dx.doi.org/10.1007/BFb0069930.

Briggs WL, Henson VE, McCormick SF. 2000. *A multigrid tutorial, second edition*. Society for Industrial and Applied Mathematics, second edn, doi:10.1137/1.9780898719505, URL http://epubs.siam.org/doi/abs/10.1137/1.9780898719505.

Carrier MJ, Ngodock H. 2010. Background-error correlation model based on the implicit solution of a diffusion equation. *Ocean Modelling* **35**(1–2): 45 – 53, doi:10.1016/j.ocemod.2010.06.003, URL http://www.sciencedirect.com/science/article/pii/S1463500310000855.

Cioaca A, Sandu A, de Sturler E. 2013. Efficient methods for computing observation impact in 4D-Var data assimilation. *Comput. Geosci.* **17**: 975–990.

Courtier P. 1997. Dual formulation of four-dimensional variational assimilation. *Quarterly Journal of the Royal Meteorological Society*

123(544): 2449–2461, doi:10.1002/qj.49712354414, URL http://dx.doi.org/10.1002/qj.49712354414.

Desroziers G, Berre L. 2012. Accelerating and parallelizing minimizations in ensemble and deterministic variational assimilation. *Quarterly Journal of the Royal Meteorological Society* **138**: 1599–1610.

Evensen G. 2006. *Data assimilation: The ensemble kalman filter*. Springer-Verlag New York, Inc.: Secaucus, NJ, USA, ISBN 354038300X.

Gratton S, Toint PL, Tshimanga J. 2013. Conjugate gradients versus multigrid solvers for diffusion-based correlation models in data assimilation. *Quarterly Journal of the Royal Meteorological Society* : n/a–n/adoi:10.1002/qj.2050, URL http://dx.doi.org/10.1002/qj.2050.

Haben S, Lawless A, S N. 2011. Conditioning of incremental variational data assimilation, with application to the met office system. *Tellus A* **63**: 782–792.

Hackbusch W. 2003. *Multi-grid methods and applications*. Springer Series in Computational Mathematics, Springer, ISBN 9783540127611, URL http://books.google.fr/books?id=ObBmg6ab-ukC.

Hemker P. 1990. On the order of prolongations and restrictions in multigrid procedures. *Journal of Computational and Applied Mathematics* **32**(3): 423 – 429, doi:10.1016/0377-0427(90)90047-4, URL http://www.sciencedirect.com/science/article/pii/0377042790900474.

Lax P, Wendroff B. 1960. Systems of conservation laws. *Communications on Pure and Applied Mathematics* **13**(2): 217–237, doi:10.1002/cpa.3160130205, URL http://dx.doi.org/10.1002/cpa.3160130205.

Le Dimet FX, Talagrand O. 1986. Variational algorithms for analysis and assimilation of meteorological observations: theoretical aspects. *Tellus A* **38A**(2): 97–110, doi:10.1111/j.1600-0870.1986.tb00459.x, URL http://dx.doi.org/10.1111/j.1600-0870.1986.tb00459.x.

Lewis RM, Nash SG. 2005. Model problems for the multigrid optimization of systems governed by differential equations. *SIAM J. Sci. Comput.* **26**(6): 1811–1837, doi:10.1137/S1064827502407792, URL http://dx.doi.org/10.1137/S1064827502407792.

Mirouze I, Weaver AT. 2010. Representation of correlation functions in variational assimilation using an implicit diffusion operator. *Quarterly Journal of the Royal Meteorological Society* **136**(651): 1421–1443, doi:10.1002/qj.643, URL http://dx.doi.org/10.1002/qj.643.

Neveu E, Debreu L, Le Dimet FX. 2011. Multigrid methods and data assimilation, convergence study and first experiments on non-linear equations. *ARIMA* **14**: 63–80.

Notay Y. 2000. Flexible conjugate gradients. *SIAM J. Sci. Comput.* **22**(4): 1444–1460, doi:10.1137/S1064827599362314, URL http://dx.doi.org/10.1137/S1064827599362314.

Oostelee C, Washio T. 1998. On the use of multigrid as a preconditioner. In: *Ninth International Conference on Domain Decomposition Methods*. Bergen.

Purser RJ. 1987. The filtering of meteorological fields. *Journal of Climate and Applied Meteorology* **26**(12): 1764–1769, doi:10.1175/1520-0450(1987) 026⟨1764:TFOMF⟩2.0.CO;2, URL http://dx.doi.org/10.1175/ 1520-0450(1987)026<1764:TFOMF>2.0.CO;2.

Rees T, Dollar HS, Wathen AJ. 2008. Optimal solvers for PDE-Constrained Optimization. Technical Report NA-08/10, Oxford University Computing Laboratory.

Shewchuk JR. 1994. An introduction to the conjugate gradient method without the agonizing pain. Technical report, Carnegie Mellon University, Pittsburgh, PA, USA.

Tang W, Wan W. 2000. Sparse approximate inverse smoother for multigrid. *SIAM Journal on Matrix Analysis and Applications* **21**(4): 1236–1252, doi:10.1137/S0895479899339342, URL http://epubs.siam.org/ doi/abs/10.1137/S0895479899339342.

Tatebe O. 1993. The multigrid preconditioned conjugate gradient method. In: *Proc. of Sixth Copper Moutain Conference on Multigrid Methods*. NASA Conference Publication 3224, pp. 612–634.

Thekale A, Gradl T, Klamroth K, Rüde U. 2010. Optimizing the number of multigrid cycles in the full multigrid algorithm. *Numerical Linear Algebra with Applications* **17**(2-3): 199–210, doi:10.1002/nla.697, URL http: //dx.doi.org/10.1002/nla.697.

Trottenberg U, Oosterlee C, Schuller A. 2000. *Multigrid*. Elsevier Science, ISBN 9780080479569, URL http://books.google.fr/books? id=9ysyNPZoR24C.

Weaver A, Courtier P. 2001. Correlation modelling on the sphere using a generalized diffusion equation. *Quarterly Journal of the Royal Meteorological Society* **127**(575): 1815–1846, doi:10.1002/qj.49712757518, URL http://dx.doi.org/10.1002/qj.49712757518.

Zhang J. 1998. Multi-level minimal residual smoothing: a family of general purpose multigrid acceleration techniques. *Journal of Computational and Applied Mathematics* **100**(1): 41 – 51, doi:10. 1016/S0377-0427(98)00133-2, URL http://www.sciencedirect. com/science/article/pii/S0377042798001332.

Bibliography

Debreu, Laurent, Florian Lemarié, and Eric Blayo (2014). "Schwarz waveform relaxation for heterogeneous cluster computing and applications". In: *43th SPEEDUP Workshop on High-Performance Computing*. Geneva, Switzerland. URL: https://hal.inria.fr/hal-01062959.

Debreu, Laurent, Florian Lemarié, and Patrick Marchesiello (2014). "Numerical delicacies associated with the use of isoneutral mixing operators in ocean models". In: *The workshop on Partial Differential Equations on the Sphere*. Boulder, United States. URL: https://hal.inria.fr/hal-01062955.

Demange, Jérémie (2014). "Numerical advection and internal waves propagation schemes for ocean circulation models". Theses. Université de Grenoble. URL: https://hal.inria.fr/tel-01104703.

Doyen, D. and P. H. Gunawan (2014). "An Explicit Staggered Finite Volume Scheme for the Shallow Water Equations". In: *Finite Volumes for Complex Applications VII-Methods and Theoretical Aspects*. Vol. 77. Springer International Publishing, pp. 227–235. DOI: 10.1007/978-3-319-05684-5{_}21. URL: http://dx.doi.org/10.1007/978-3-319-05684-5_21.

Ducousso, Nicolas, Julien Le Sommer, Jean-Marc Molines, Gurvan Madec, Laurent Debreu, and Florian Lemarié (2014). "Caveats in using the EEN momentum advection scheme: illustration with idealized experiments and sensitivity of ORCA025 solutions". In: *DRAKKAR/MYOCEAN 2014 Annual Workshop*. Grenoble, France. URL: https://hal.inria.fr/hal-00941032.

Eden, Carsten, Lars Czeschel, and Dirk Olbers (2014). "Toward Energetically Consistent Ocean Models". In: *Journal of Physical Oceanography* 44.12, pp. 3160–3184. DOI: 10.1175/JPO-D-13-0260.1. URL: http://dx.doi.org/10.1175/JPO-D-13-0260.1.

Haut, Terry and Beth Wingate (2014). "An Asymptotic Parallel-in-Time Method for Highly Oscillatory PDEs". In: *SIAM Journal on Scientific Computing* 36.2, A693–A713. DOI: 10.1137/130914577. URL: http://dx.doi.org/10.1137/130914577.

Lemarié, Florian, Laurent Debreu, Gurvan Madec, Marc Honnorat, and Jean-Marc Molines (2014). "Stability constraints for oceanic numerical models: implications for the formulation of space-time discretizations". In: *2014 AGU Ocean Sciences Meeting*. Honolulu, United States. URL: https://hal.inria.fr/hal-00957238.

Lemarié, Florian, Patrick Marchesiello, Laurent Debreu, and Eric Blayo (2014). *Sensitivity of Ocean-Atmosphere Coupled Models to the Coupling Method : Example of Tropical Cyclone Erica*. Research Report RR-8651. INRIA Grenoble, p. 32. URL: https://hal.inria.fr/hal-00872496.

Majda, Andrew and Ian Grooms (2014). "New perspectives on superparameterization for geophysical turbulence". In: *Journal of Computational Physics* 271. Frontiers in Compu-

tational PhysicsModeling the Earth System, pp. 60–77. DOI: http://dx.doi.org/10.1016/j.jcp.2013.09.014. URL: http://www.sciencedirect.com/science/article/pii/S0021999113006190.

Mémin, Etienne (2014). "Fluid flow dynamics under location uncertainty". In: *Geophysical & Astrophysical Fluid Dynamics* 108.2, pp. 119–146. DOI: 10.1080/03091929.2013.836190. URL: http://dx.doi.org/10.1080/03091929.2013.836190.

Rebollo, Tomas Chacon and Roger Lewandowski (2014). *Mathematical and Numerical Foundations of Turbulence Models and Applications*. Springer.

Thuburn, John, James Kent, and Nigel Wood (2014). "Cascades, backscatter and conservation in numerical models of two-dimensional turbulence". In: *Quarterly Journal of the Royal Meteorological Society* 140.679, pp. 626–638. DOI: 10.1002/qj.2166. URL: http://dx.doi.org/10.1002/qj.2166.

Danilov, Sergey (2013). "Ocean modeling on unstructured meshes". In: *Ocean Modelling* 69, pp. 195–210. DOI: http://dx.doi.org/10.1016/j.ocemod.2013.05.005. URL: http://www.sciencedirect.com/science/article/pii/S1463500313000905.

Debreu, Laurent (2013). "Schwarz waveform relaxation for heterogeneous cluster computing: Application to numerical weather prediction". In: *DD22 - 22nd International Conference on Domain Decomposition Methods - 2013*. Lugano, Switzerland. URL: https://hal.inria.fr/hal-00932898.

Fox-Kemper, B. and D. Menemenlis (2013). "Can Large Eddy Simulation Techniques Improve Mesoscale Rich Ocean Models?" In: *Ocean Modeling in an Eddying Regime*. American Geophysical Union, pp. 319–337. DOI: 10.1029/177GM19. URL: http://dx.doi.org/10.1029/177GM19.

Lemarié, Florian, Laurent Debreu, and Patrick Marchesiello (2013). "Numerical delicacies associated with the use of isoneutral mixing operators in ocean models". In: *European Geosciences Union General Assembly 2013*. EGU. Vienna, Austria. URL: https://hal.inria.fr/hal-00826006.

Maday, Yvon, Mohamed-Kamel Riahi, and Julien Salomon (2013). "Parareal in Time Intermediate Targets Methods for Optimal Control Problems". English. In: *Control and Optimization with PDE Constraints*. Ed. by Kristian Bredies, Christian Clason, Karl Kunisch, and Gregory von Winckel. Vol. 164. International Series of Numerical Mathematics. Springer Basel, pp. 79–92. DOI: 10.1007/978-3-0348-0631-2_5. URL: http://dx.doi.org/10.1007/978-3-0348-0631-2_5.

Vidard, Arthur, Laurent Debreu, and Emilie Neveu (2013a). "Multi Resolution Variational Data Assimilation Schemes With Application to a Realistic Ocean Model". In: *Sixth WMO Symposium on Data Assimilation*. College Park, United States. URL: https://hal.inria.fr/hal-00877893.

— (2013b). "Multi resolution variational data assimilation system for the ocean". In: *EGU 2013 - European Geosciences Union General Assembly 2013*. Vienne, Austria. URL: https://hal.inria.fr/hal-00877890.

Desroziers, Gérald and Loïk Berre (2012). "Accelerating and parallelizing minimizations in ensemble and deterministic variational assimilations". In: *Quarterly Journal of the Royal Meteorological Society* 138.667, pp. 1599–1610. DOI: 10.1002/qj.1886. URL: http://dx.doi.org/10.1002/qj.1886.

Gratton, Serge, Vincent Malmedy, and Philippe L. Toint (2012). "Using approximate secant equations in limited memory methods for multilevel unconstrained optimization".

English. In: *Computational Optimization and Applications* 51.3, pp. 967–979. DOI: 10.1007/s10589-011-9393-3. URL: http://dx.doi.org/10.1007/s10589-011-9393-3.

Illicak, Mehmet, Alistair J. Adcroft, Stephen M. Griffies, and Robert W. Hallberg (2012). "Spurious dianeutral mixing and the role of momentum closure". In: *Ocean Modelling* 45-46, pp. 37–58.

Kent, James, John Thuburn, and Nigel Wood (2012). "Assessing implicit large eddy simulation for two-dimensional flow". In: *Quarterly Journal of the Royal Meteorological Society* 138.663, pp. 365–376. DOI: 10.1002/qj.925. URL: http://dx.doi.org/10.1002/qj.925.

Lemarié, Florian, Jaison Kurian, Alexander F. Shchepetkin, M. Jeroen Molemaker, François Colas, and James C. McWilliams (2012). "Are there inescapable issues prohibiting the use of terrain-following coordinates in climate models?" In: *Ocean Modelling* 42.0, pp. 57–79. DOI: http://dx.doi.org/10.1016/j.ocemod.2011.11.007. URL: http://www.sciencedirect.com/science/article/pii/S1463500311001831.

Melet, Angelique, Jacques Verron, and Jean-Michel Brankart (2012). "Potential outcomes of glider data assimilation in the Solomon Sea: Control of the water mass properties and parameter estimation". In: *Journal of Marine Systems* 94.0, pp. 232–246. DOI: http://dx.doi.org/10.1016/j.jmarsys.2011.12.003. URL: http://www.sciencedirect.com/science/article/pii/S0924796311002934.

Cushman-Roisin, Benoit and Jean-Marie Beckers (2011). *Introduction to Geophysical Fluid Dynamics: Physical and Numerical Aspects*. Academic Press. Academic Press. URL: https://books.google.fr/books?id=3KS8sD5ky9kC.

Debreu, Laurent, Ehouarn Simon, and Eric Blayo (2011). *4D variational data assimilation for locally nested models: optimality system and preliminary experiments*. Research Report RR-7675, p. 19. URL: https://hal.inria.fr/inria-00607177.

Gent, Peter R. (2011). "The Gent–McWilliams parameterization: 20/20 hindsight". In: *Ocean Modelling* 39.1–2, pp. 2–9. DOI: http://dx.doi.org/10.1016/j.ocemod.2010.08.002. URL: http://www.sciencedirect.com/science/article/pii/S1463500310001253.

Gratton, Serge, A. Sartenaer, and J. Tshimanga (2011). "On A Class of Limited Memory Preconditioners For Large Scale Linear Systems With Multiple Right-Hand Sides". In: *SIAM Journal on Optimization* 21.3, pp. 912–935. DOI: 10.1137/08074008. URL: http://dx.doi.org/10.1137/08074008.

Lemarié, Florian, Laurent Debreu, and Eric Blayo (2011). "Optimized Schwarz Methods in the Context of Ocean-Atmosphere Coupling". In: *DD 20 - 20th International Conference on Domain Decomposition Methods*. San Diego, United States. URL: https://hal.archives-ouvertes.fr/hal-00749195.

Maddison, J. R., D.P. Marshall, C.C. Pain, and M.D. Piggott (2011). "Accurate representation of geostrophic and hydrostatic balance in unstructured mesh finite element ocean modelling". In: *Ocean Modelling* 39.3–4, pp. 248–261. DOI: http://dx.doi.org/10.1016/j.ocemod.2011.04.009. URL: http://www.sciencedirect.com/science/article/pii/S1463500311000825.

Marchesiello, Patrick, Xavier Capet, Christophe Menkes, and Sean C. Kennan (2011). "Submesoscale dynamics in tropical instability waves". In: *Ocean Modelling* 39.1–2. Modelling and Understanding the Ocean Mesoscale and Submesoscale, pp. 31–46. DOI: http://dx.doi.org/10.1016/j.ocemod.2011.04.011. URL: http://www.sciencedirect.com/science/article/pii/S1463500311000849.

Neveu, Emilie (2011). "Multigrids methods applied to variationnal data assimilation in geophysics models". Theses. Université de Grenoble. URL: https://tel.archives-ouvertes.fr/tel-00574221.

Shchepetkin, Alexander F. and James C. McWilliams (2011). "Accurate Boussinesq oceanic modeling with a practical, "Stiffened" Equation of State". In: *Ocean Modelling* 38.1–2, pp. 41–70. DOI: http://dx.doi.org/10.1016/j.ocemod.2011.01.010. URL: http://www.sciencedirect.com/science/article/pii/S146350031100014X.

Sidorenko, D., Q. Wang, Sergey Danilov, and J. Schröter (2011). "FESOM under coordinated ocean-ice reference experiment forcing". In: 61 (7), pp. 881–890.

Verron, Jacques, Pierre Brasseur, Jean-Michel Brankart, Emmanuel Cosme, Eric Blayo, Laurent Debreu, and Arthur Vidard (2011). "Assimilation of SARAL/AltiKa data for physical ocean prediction and ecosystem monitoring". In: *Second SARAL/AltiKa Science Workshop*. Ahmedabad, India. URL: https://hal.inria.fr/hal-00769114.

Deleersnijder, Eric, V. Legat, and P. F. J. Lermusiaux (2010). "Mutil-scale modelling of coastal, shelf and global ocean dynamics". In: 60, pp. 1357–1359.

Mason, Evan, Jeroen Molemaker, Alexander F. Shchepetkin, Francois Colas, James C. McWilliams, and Pablo Sangrà (2010). "Procedures for offline grid nesting in regional ocean models". In: *Ocean Modelling* 35.1–2, pp. 1–15. DOI: http://dx.doi.org/10.1016/j.ocemod.2010.05.007. URL: http://www.sciencedirect.com/science/article/pii/S146350031000082X.

Neveu, Emilie, Laurent Debreu, and François-Xavier Le Dimet (2010a). "Méthodes multi-grilles pour le 4D-VAR". In: *Colloque National sur l'Assimilation de Données*. Grenoble, France. URL: https://hal.inria.fr/hal-00788218.

— (2010b). "Multigrid methods and data assimilation applied to a linear advection equation". In: *CARI'10 - African Conference on Research in Computer Science and Applied Mathematics*. Yamoussoukro, Côte d'Ivoire. URL: https://hal.inria.fr/hal-00788216.

Borzì, Alfio and Volker Schulz (2009). "Multigrid Methods for PDE Optimization". In: *SIAM Rev.* 51.2, pp. 361–395. DOI: 10.1137/060671590. URL: http://dx.doi.org/10.1137/060671590.

Ciarlet, P.G., Roger Temam, and J. Tribbia (2009). *Computational Methods for the Atmosphere and the Oceans: Special Volume*. Handbook of Numerical Analysis. Elsevier Science. URL: https://books.google.fr/books?id=2LSH9TUFaNoC.

Ham, David A., Christopher C. Pain, Emmanuel Hanert, Julie Pietrzak, and Jens Schröter (2009). *Special Issue: The sixth international workshop on unstructured mesh numerical modelling of coastal, shelf and ocean flows. Imperial College London, September 19-21, 2007*. Vol. 28. Elsevier, pp. 1–1.

Kamenkovich, V.M. and D.A. Nechaev (2009). "On the time-splitting scheme used in the Princeton Ocean Model". In: *Journal of Computational Physics* 228.8, pp. 2874–2905. DOI: http://dx.doi.org/10.1016/j.jcp.2008.12.033. URL: http://www.sciencedirect.com/science/article/pii/S0021999109000059.

Shchepetkin, Alexander F. and James C. McWilliams (2009). "Computational Kernel Algorithms for Fine-Scale, Multiprocess, Longtime Oceanic Simulations". In: *Handbook of Numerical Analysis*. Ed. by P.G. Ciarlet. Vol. 14. Handbook of Numerical Analysis. Elsevier, pp. 121–183. DOI: http://dx.doi.org/10.1016/S1570-8659(08)01202-0. URL: http://www.sciencedirect.com/science/article/pii/S1570865908012020.

Simon, Ehouarn, Laurent Debreu, and Eric Blayo (2009). "4D-Variational data assimilation for locally nested numerical models". In: *European Geophysical Union General Assembly 2009*. Vienna, Austria. URL: https://hal.archives-ouvertes.fr/hal-00795819.

Bennis, A.-C., T. Chacón Rebollo, M. Gomez Marmol, and R. Lewandowski (2008). "Stability of some turbulent vertical models for the ocean mixing boundary layer". In: *Applied Mathematics Letters* 21.2, pp. 128–133. DOI: http://dx.doi.org/10.1016/j.aml.2007.02.016. URL: http://www.sciencedirect.com/science/article/pii/S0893965907001061.

Biastoch, A., C. W. Boning, and J. R. E. Lutjeharms (2008). "Agulhas leakage dynamics affects decadal variability in Atlantic overturning circulation". In: *Nature* 456.7221, pp. 489–492. URL: http://dx.doi.org/10.1038/nature07426.

Chanut, Jérôme, Bernard Barnier, William Large, Laurent Debreu, Thierry Penduff, Jean-Marc Molines, and Pierre Mathiot (2008b). "Mesoscale eddies in the Labrador Sea and their contribution to convection and re-stratification". In: *Phys. Oceanogr* 38, pp. 1617–1643. URL: https://hal.archives-ouvertes.fr/hal-00266980.

Deleersnijder, Eric, Emmanuel Hanert, Hans Burchard, and HenkA. Dijkstra (2008). "On the mathematical stability of stratified flow models with local turbulence closure schemes". English. In: *Ocean Dynamics* 58.3-4, pp. 237–246. DOI: 10.1007/s10236-008-0145-6. URL: http://dx.doi.org/10.1007/s10236-008-0145-6.

Jouanno, Julien, Julio Sheinbaum, Bernard Barnier, Jean-Marc Molines, Laurent Debreu, and Florian Lemarié (2008). "The mesoscale variability in the Caribbean Sea. Part I: Simulations and characteristics with an embedded model". In: *Ocean Modelling* 23.3-4, pp. 82–101. DOI: 10.1016/j.ocemod.2008.04.002. URL: https://hal.inria.fr/hal-00658107.

Lemarié, Florian (2008). "Schwarz algorithms and ocean-atmosphere coupling". Theses. Université Joseph-Fourier - Grenoble I. URL: https://tel.archives-ouvertes.fr/tel-00343501.

Lemarié, Florian, Laurent Debreu, and Eric Blayo (2008a). *Optimized global-in-time Schwarz algorithm for diffusion equations with discontinuous and spatially variable coefficients*. Research Report RR-6663, p. 45. URL: https://hal.inria.fr/inria-00324533.

— (2008b). "Optimized Schwarz methods in the context of ocean-atmosphere coupling". In: *ESCO 2008 - European Seminar on Coupled Problems*. Jetrichovice, Czech Republic. URL: https://hal.inria.fr/inria-00344508.

Morel, Yves, Remy Baraille, and Annick Pichon (2008). "Time splitting and linear stability of the slow part of the barotropic component". In: *Ocean Modelling* 23.3-4, pp. 73–81. DOI: http://dx.doi.org/10.1016/j.ocemod.2008.04.001. URL: http://www.sciencedirect.com/science/article/pii/S1463500308000474.

Simon, Ehouarn, Eric Blayo, and Laurent Debreu (2008). "4D-Variational data assimilation for locally nested numerical models". In: *GODAE Final Symposium*. Nice, France. URL: https://hal.inria.fr/inria-00344507.

Barth, A., A. Alvera-Azcárate, Jean-Marie Beckers, M. Rixen, and L. Vandenbulcke (2007a). "Multigrid state vector for data assimilation in a two-way nested model of the Ligurian Sea". In: *Journal of Marine Systems* 65.1–4, pp. 41–59. DOI: http://dx.doi.org/10.1016/j.jmarsys.2005.07.006. URL: http://www.sciencedirect.com/science/article/pii/S0924796306002843.

— (2007b). "Multigrid state vector for data assimilation in a two-way nested model of the Ligurian Sea". In: *Journal of Marine Systems* 65.1–4, pp. 41–59. DOI: http://dx.doi.

org/10.1016/j.jmarsys.2005.07.006. URL: http://www.sciencedirect.com/science/article/pii/S0924796306002843.

Blayo, Eric, Laurent Debreu, Franck Dumas, Valérie Garnier, Joel Marin, Céline Robert, and Frédéric Vandermeirsch (2007). "Investigation of 2-D and 3-D characteristic-based open boundary conditions for regional ocean models". In: *European Geophysical Union General Assembly*. Vienne, Austria. URL: https://hal.archives-ouvertes.fr/hal-00385256.

Debreu, Laurent (2007). "Two-way nesting". In: *Workshop on Numerical Methods in Ocean Models*. Bergen, Norway. URL: https://hal.archives-ouvertes.fr/hal-00795799.

Gander, M. J. and L. Halpern (2007). "Optimized Schwarz waveform relaxation methods for advection reaction diffusion problems". In: *SIAM J. Numer. Anal.* 45.2, pp. 666–697.

Griffiths, S. D. and R. H. J. Grimshaw (2007). "Internal Tide Generation at the Continental Shelf Modeled Using a Modal Decomposition: Two-Dimensional Results". In: 37.3, pp. 428–451. DOI: 10.1175/JPO3068.1. URL: http://dx.doi.org/10.1175/JPO3068.1.

Grinstein, F.F., L.G. Margolin, and W.J. Rider (2007). *Implicit Large Eddy Simulation: Computing Turbulent Fluid Dynamics*. Cambridge University Press. URL: http://books.google.fr/books?id=Xk-eb9kPgXsC.

Lemarié, Florian and Laurent Debreu (2007). "NEMO/AGRIF, theoretical and practical aspects". In: *Workshop on the DRAKKAR global ocean model at 1/4° resolution*. Brest, France. URL: https://hal.archives-ouvertes.fr/hal-00795803.

Lemarié, Florian, Laurent Debreu, and Eric Blayo (2007). "Méthodes mathématiques et numériques pour le couplage océan-atmosphère à échelle régionale". In: *SMAI 2007 - 3e congrès national de mathématiques appliquées et industrielles*. Praz-sur-Arly, France. URL: https://hal.archives-ouvertes.fr/hal-00795355.

Simon, Ehouarn (2007). "Assimilation variationnelle de données pour des modèles emboîtés". Theses. Université Joseph-Fourier - Grenoble I. URL: https://tel.archives-ouvertes.fr/tel-00194593.

Blayo, Eric, Laurent Debreu, Franck Dumas, Véronique Garnier, Joël Marin, Céline ROBERT, and F. Vandermeirsch (2006). "Investigation of 2-D and 3-D characteristic open boundary conditions for regional ocean models". In: *Coastal Operational Oceanography conference*. Brest, France. URL: https://hal.archives-ouvertes.fr/hal-00171630.

Levin, C., M. Iskandarani, and D.B. Haidgovel (2006). "To continue or discontinue: Comparisons of continuous and discontinuous Galerkin formulations in a spectral element ocean model". In: 15, pp. 56–70.

Ngnepieba, Pierre Désiré, M.Yussuf Hussaini, and Laurent Debreu (2006). "Optimal Control and Stochastic Parameter Estimation". In: *Monte Carlo Methods and Applications*. DOI: 10.1515/156939606779329062. URL: https://hal.inria.fr/inria-00592665.

Parrenin, Frédéric et al. (2006). "Conjonction de modèles de données pour l'étude des calottes polaires". In: *Colloque national sur l'assimilation de données*. Toulouse, France. URL: https://hal.archives-ouvertes.fr/hal-00171646.

Sagaut, P., S. Deck, and M. Terracol (2006). *Multiscale and Multiresolution Approaches in Turbulence*. Imperial College Press. URL: http://books.google.fr/books?id=1oHxzXPFOwoC.

Simon, Ehouarn, Laurent Debreu, and Eric Blayo (2006a). "4D variational data assimilation for locally nested models". In: *European Geophysical Union General Assembly*. Vienne, Austria. URL: https://hal.archives-ouvertes.fr/hal-00171657.

— (2006b). "Assimilation de données variationnelle pour des modèles multi-échelles". In: *Colloque national sur l'assimilation de données*. Toulouse, France. URL: https://hal. archives-ouvertes.fr/hal-00171642.

— (2006c). "Assimilation de données variationnelle pour des modèles multi-grilles". In: *Colloque national sur l'assimilation de données*. Toulouse, France. URL: https://hal. archives-ouvertes.fr/hal-00171710.

Thuburn, John (2006). "Vertical discretizations giving optimal representation of normal modes: Sensitivity to the form of the pressure-gradient term". In: *Quarterly Journal of the Royal Meteorological Society* 132.621, pp. 2809–2825. DOI: 10.1256/qj.06.10. URL: http://dx.doi.org/10.1256/qj.06.10.

Lewis, Robert Michael and Stephen G. Nash (2005). "Model Problems for the Multigrid Optimization of Systems Governed by Differential Equations". In: *SIAM J. Sci. Comput.* 26.6, pp. 1811–1837. DOI: 10.1137/S1064827502407792. URL: http://dx.doi.org/10. 1137/S1064827502407792.

Shchepetkin, Alexander F. and James C. McWilliams (2005). "The regional oceanic modeling system (ROMS): a split-explicit, free-surface, topography-following-coordinate oceanic model". In: *Ocean Modelling* 9.4, pp. 347–404. DOI: http://dx.doi.org/10.1016/j. ocemod.2004.08.002. URL: http://www.sciencedirect.com/science/article/pii/ S1463500304000484.

Sheng, Jinyu, RichardJ. Greatbatch, Xiaoming Zhai, and Liqun Tang (2005). "A new two-way nesting technique for ocean modeling based on the smoothed semi-prognostic method". English. In: *Ocean Dynamics* 55.3-4, pp. 162–177. DOI: 10.1007/s10236-005-0005-6. URL: http://dx.doi.org/10.1007/s10236-005-0005-6.

Griffies, S.M. (2004). *Fundamentals of Ocean Climate Model*. Princeton University Press, Princeton, NJ, USA.

Hanert, Emmanuel, D. Y. Le Roux, V. Legat, and Eric Deleersnijder (2004). "Advection schemes for unstructured grid ocean modelling". In: 7 (1-2), pp. 39–58.

Smith, Richard D. and Peter R. Gent (2004). "Anisotropic Gent–McWilliams Parameterization for Ocean Models". In: *Journal of Physical Oceanography* 34.11, pp. 2541–2564. DOI: 10.1175/JPO2613.1. URL: http://dx.doi.org/10.1175/JPO2613.1.

Hackbusch, W. (2003). *Multi-Grid Methods and Applications*. Springer Series in Computational Mathematics. Springer. URL: http://books.google.fr/books?id=ObBmg6ab-ukC.

Lengaigne, M., G. Madec, C. Menkes, and G. Alory (2003). "Impact of isopycnal mixing on the tropical ocean circulation". In: *Journal of Geophysical Research: Oceans* 108.C11. 3345, n/a–n/a. DOI: 10.1029/2002JC001704. URL: http://dx.doi.org/10.1029/ 2002JC001704.

Debreu, Laurent and Eric Blayo (2002). *AGRIF: Adaptive Grid Refinement In Fortran*. Research Report RT-0262, p. 16. URL: https://hal.inria.fr/inria-00069912.

Kundu, P. K. and I. M. Cohen (2002). *Fluid Mechanics*. Second. Academic Press.

Lions, Jacques-Louis, Yvon Maday, and Gabriel Turinici (2001). "A parareal in time discretization of PDEs". In: *C.R. Acad. Sci., Paris, Sér. I, Math.* 332.7, pp. 661–668.

Weaver, Anthony and Philippe Courtier (2001). "Correlation modelling on the sphere using a generalized diffusion equation". In: *Quarterly Journal of the Royal Meteorological Society* 127.575, pp. 1815–1846. DOI: 10.1002/qj.49712757518. URL: http://dx.doi.org/10. 1002/qj.49712757518.

Baden, S.C., N.P. Chrisochoides, D.B. Gannon, and M.L. Norman, eds. (2000). *Structured Adaptive Mesh Refinement (SAMR) Grid Methods.* Vol. 117. The IMA Volumes in Mathematics and its Applications. Springer New York. DOI: 10.1007/978-1-4612-1252-2.

Beckers, Jean-Marie, Hans Burchard, Eric Deleersnijder, and Pierre-Philippe Mathieu (2000). "Numerical Discretization of Rotated Diffusion Operators in Ocean Models". In: *Monthly Weather Review* 128.8, pp. 2711–2733. DOI: 10.1175/1520-0493(2000)128<2711:NDORDO>2.0.CO;2. URL: http://dx.doi.org/10.1175/1520-0493(2000)128%3C2711:NDORDO%3E2.0.CO;2.

Briggs, William L., Van Emden Henson, and Steve F. McCormick (2000). *A Multigrid Tutorial, Second Edition.* Second. Society for Industrial and Applied Mathematics. DOI: 10.1137/1.9780898719505. URL: http://epubs.siam.org/doi/abs/10.1137/1.9780898719505.

Blayo, Eric, Laurent Debreu, Grégory Mounié, and Denis Trystram (1999). "Dynamic Load Balancing for Ocean Circulation Model with Adaptive Meshing". In: ed. by Daniel Ruiz. Lecture Notes in Computer Science (LNCS) 1685. Springer Verlag, pp. 303–312. URL: https://hal.archives-ouvertes.fr/hal-00003948.

Delcayre, F. (1999). "Etude par simulation des grandes échelles d'un écoulement décollé : la marche descendante". PhD thesis. Institut National Polytechnique de Grenoble.

Mathieu, Pierre-Philippe, Eric Deleersnijder, and Jean-Marie Beckers (1999). "Accuracy and stability of the discretised isopycnal-mixing equation". In: *Applied Mathematics Letters* 12.4, pp. 81–88. DOI: http://dx.doi.org/10.1016/S0893-9659(99)00039-7. URL: http://www.sciencedirect.com/science/article/pii/S0893965999000397.

Beckers, Jean-Marie, Hans Burchard, J. M. Campin, Eric Deleersnijder, and Pierre-Philippe Mathieu (1998). "Another Reason Why Simple Discretizations of Rotated Diffusion Operators Cause Problems in Ocean Models: Comments on "Isoneutral Diffusion in a z-Coordinate Ocean Model"". In: *Journal of Physical Oceanography* 28.7, pp. 1552–1559. DOI: 10.1175/1520-0485(1998)028<1552:ARWSDO>2.0.CO;2. URL: http://dx.doi.org/10.1175/1520-0485(1998)028%3C1552:ARWSDO%3E2.0.CO;2.

Griffies, S.M., A. Gnanadeskian, R. C. Pacanowski, V. Larichev, J. K. Dukowicz, and Smith R. D. (1998). "Isoneutral diffusion in a z-coordinate ocean model." In: *Journal of Physical Oceanography* 28, pp. 805–830.

Hunt, J.C.R., A.A. Wray, and P. Moin (1998). *Eddies, stream and convergence zones in turbulent flows.* Tech. rep. CTR-S88:193. Center for Turbulence Research report.

Mathieu, Pierre-Philippe and Eric Deleersnijder (1998). "What is wrong with isopycnal diffusion in world ocean models?" In: *Applied Mathematical Modelling* 22.4–5, pp. 367–378. DOI: http://dx.doi.org/10.1016/S0307-904X(98)10008-2. URL: http://www.sciencedirect.com/science/article/pii/S0307904X98100082.

Cullen, M. J.P., T. Davies, M. H. Mawson, J. A. James, S. C. Coulter, and A. Malcolm (1997). "An Overview of Numerical Methods for the Next Generation U.K. NWP and Climate Model". In: *Atmosphere-Ocean* 35.sup1, pp. 425–444. DOI: 10.1080/07055900.1997.9687359. URL: http://dx.doi.org/10.1080/07055900.1997.9687359.

Hallberg, Robert (1997). "Stable Split Time Stepping Schemes for Large-Scale Ocean Modeling". In: *Journal of Computational Physics* 135.1, pp. 54–65. DOI: http://dx.doi.org/10.1006/jcph.1997.5734. URL: http://www.sciencedirect.com/science/article/pii/S002199919795734X.

Higdon, Robert L. and Roland A. de Szoeke (1997). "Barotropic-Baroclinic Time Splitting for Ocean Circulation Modeling". In: *Journal of Computational Physics* 135.1, pp. 30–

53. DOI: http://dx.doi.org/10.1006/jcph.1997.5733. URL: http://www.sciencedirect.com/science/article/pii/S0021999197957338.

Nadiga, B.T., M.W. Hecht, L.G. Margolin, and P.K. Smolarkiewicz (1997). "On Simulating Flows with Multiple Time Scales Using a Method of Averages". English. In: *Theoretical and Computational Fluid Dynamics* 9.3-4, pp. 281–292. DOI: 10.1007/s001620050045. URL: http://dx.doi.org/10.1007/s001620050045.

Danabasoglu, Gokhan and James C. Mc Williams (1995). "Sensitivity of the Global Ocean Circulation to Parameterizations of Mesoscale Tracer Transports". In: *Journal of Climate* 8.12, pp. 2967–2987. DOI: 10.1175/1520-0442(1995)008<2967:SOTGOC>2.0.CO;2. URL: http://dx.doi.org/10.1175/1520-0442(1995)008%3C2967:SOTGOC%3E2.0.CO;2.

Danabasoglu, Gokhan, James C. McWilliams, and Peter R. Gent (1994). "The Role of Mesoscale Tracer Transports in the Global Ocean Circulation". In: *Science* 264.5162, pp. 1123–1126. URL: http://www.sciencemag.org/content/264/5162/1123.abstract.

Leslie, L.M. and R.J. Purser (1992). "A comparative study of the performance of various vertical discretization schemes". English. In: *Meteorology and Atmospheric Physics* 50.1-3, pp. 61–73. DOI: 10.1007/BF01025505. URL: http://dx.doi.org/10.1007/BF01025505.

Lions, Jacques-Louis, Roger Temam, and Shouhong Wang (1992). "On the equations of the large-scale ocean". In: *Nonlinearity* 5.5, p. 1007.

Germano, Massimo, Ugo Piomelli, Parviz Moin, and William H. Cabot (1991). "A dynamic subgrid scale eddy viscosity model". In: *Physics of Fluids A: Fluid Dynamics (1989-1993)* 3.7, pp. 1760–1765. DOI: http://dx.doi.org/10.1063/1.857955.

Killworth, Peter D., David J. Webb, David Stainforth, and Stephen M. Paterson (1991). "The Development of a Free-Surface Bryan–Cox–Semtner Ocean Model". In: *Journal of Physical Oceanography* 21.9, pp. 1333–1348. DOI: 10.1175/1520-0485(1991)021<1333:TDOAFS>2.0.CO;2. URL: http://dx.doi.org/10.1175/1520-0485(1991)021%3C1333:TDOAFS%3E2.0.CO;2.

Gent, Peter R. and James C. Mcwilliams (1990). "Isopycnal Mixing in Ocean Circulation Models". In: *Journal of Physical Oceanography* 20.1, pp. 150–155. DOI: 10.1175/1520-0485(1990)020<0150:IMIOCM>2.0.CO;2. URL: http://dx.doi.org/10.1175/1520-0485(1990)020%3C0150:IMIOCM%3E2.0.CO;2.

Arakawa, Akio and Shrinivas Moorthi (1988). "Baroclinic Instability in Vertically Discrete Systems". In: *Journal of the Atmospheric Sciences* 45.11, pp. 1688–1708. DOI: 10.1175/1520-0469(1988)045<1688:BIIVDS>2.0.CO;2. URL: http://dx.doi.org/10.1175/1520-0469(1988)045%3C1688:BIIVDS%3E2.0.CO;2.

Cox, M.D. (1987). "Isopycnal diffusion in a z-coordinate ocean model". In: *Ocean Modelling* 74, pp. 1–5.

Le Dimet, François-Xavier and Olivier Talagrand (1986). "Variational algorithms for analysis and assimilation of meteorological observations: theoretical aspects". In: *Tellus A* 38A.2, pp. 97–110. DOI: 10.1111/j.1600-0870.1986.tb00459.x. URL: http://dx.doi.org/10.1111/j.1600-0870.1986.tb00459.x.

Berger, Marsha J and Joseph Oliger (1984). "Adaptive mesh refinement for hyperbolic partial differential equations". In: *Journal of Computational Physics* 53.3, pp. 484–512. DOI: http://dx.doi.org/10.1016/0021-9991(84)90073-1. URL: http://www.sciencedirect.com/science/article/pii/0021999184900731.

Brandt, Achi (1982). "Guide to multigrid development". In: *Multigrid Methods*. Ed. by W. Hackbusch and U. Trottenberg. Vol. 960. Lecture Notes in Mathematics. Springer Berlin

Heidelberg, pp. 220–312. DOI: 10.1007/BFb0069930. URL: http://dx.doi.org/10. 1007/BFb0069930.

Redi, Martha H. (1982). "Oceanic Isopycnal Mixing by Coordinate Rotation". In: *Journal of Physical Oceanography* 12.10, pp. 1154–1158. DOI: 10.1175/1520-0485(1982) 012<1154:OIMBCR>2.0.CO;2. URL: http://dx.doi.org/10.1175/1520-0485(1982) 012%3C1154:OIMBCR%3E2.0.CO;2.

Harten, Amiram and Peter D. Lax (1981). "A Random Choice Finite Difference Scheme for Hyperbolic Conservation Laws". In: *SIAM Journal on Numerical Analysis* 18.2, pp. 289– 315. URL: http://www.jstor.org/stable/2156505.

Houwen, P.J. van der and J.G. Verwer (1979). "One-step splitting methods for semi-discrete parabolic equations". English. In: *Computing* 22.4, pp. 291–309. DOI: 10.1007/BF02265311. URL: http://dx.doi.org/10.1007/BF02265311.